Multiphase field modelling of ferroelectric materials near the polymorphic phase boundary

---

A thesis

submitted in partial fulfilment

of the requirements for the degree of

DOCTOR OF PHILOSOPHY

MECHANICAL ENGINEERING

by

OSCAR A. TORRES MATHEUS

University of Canterbury

February 2020

To my sweet little Lizzie.

Preface

This thesis is submitted as a partial requirement for the degree of Doctor of Philosophy in Mechanical Engineering in the University of Canterbury. This research was conducted under the supervision of senior supervisor Associate Professor Catherine M. Bishop, co-supervisor Professor R. Edwin García (Purdue University) and associate supervisor Associate Professor Stefanie Gutschmidt in the Mechanical Engineering Department, University of Canterbury, New Zealand, between March 2015 and February 2020.

Acknowledgements

I would like to acknowledge the following people and organisations that made this research possible:

- Associate Professor Catherine M. Bishop for her supervision, encouragement, and for sharing her vast knowledge, which helped and inspired me to complete this work. Thank you for your confidence in me, and for giving me the opportunity to provide a better future for my family.
- Professor R. Edwin García for his co-supervision, quick feedback and technical support. Thank you for challenging me to become a better researcher and improve the quality of my work.
- The University of Canterbury for granting me the College of Engineering PhD Scholarship, and the Mechanical Engineering Department administrative staff for their friendly support.
- Dr Aaron Beardsley for his friendship and all the laughter. Thank you for proofreading my work and for reminding me to enjoy life all the time. You became part of my family. Who would have thought!?
- Shaun Mucalo for his friendship and all those good discussions and meals. Thank you for sharing your programming skills. They were vital for completing my work.
- Alice Young for her friendship and the good moments sharing ideas during lunch or morning tea. Thank you for helping me with my writing, even when you were busy with your own work.
- Jeannie, Kate, Jackie, Trish and all the team at the childcare centre for taking such good care of my Lizzie while I was working on this project.
- All my friends, old and new, inside and outside the university, who in one way or another helped me during this journey; my Kiwi family, Maggie, Blair, Andrew, Linda, Antonio, Raquel, Andrea and Are; and my Costa Rican family, Javier, Catalina and Alberto; thank you for the precious memories.
- Carolina, Carlos, Ethan and Emma for giving me a place to call home. Thank you for taking us in when we needed it the most, and for helping us to get back on our feet in this country.
- My parents, brother and extended family for their unconditional love and support that made me the person that I am today. In particular, my mother, for teaching me the value of hard work and for giving me someone that I can admire.
- Lastly, I want to thank my wife, Keidy, and my daughter, Elizabeth, for sharing their life with me, for giving me a reason to continue working and for supporting me in my worst moments. You two mean the world to me. This achievement is yours as much as mine.

Abstract

Lead toxicity has motivated the search for Pb-free ferroelectrics to replace lead zirconate titanate (PZT). This solid solution has been the most widely used piezoelectric material, due to its high electromechanical performance at compositions around its morphotropic phase boundary. Despite the multiple interpretations of the structural state near this compositionally-driven interferroelectric phase transition, it is commonly accepted that the optimal properties are associated with reduction of the crystallographic anisotropy of the free energy. Existing modelling methodologies artificially couple the free energies of the different ferroelectric phases by using a single Landau-Devonshire potential to describe the ferroelectric behaviour of the entire material. This approach inherently limits the accuracy of predicted properties in the bulk phases, and near the interferroelectric transitions in particular. Thus, the structural states and mechanisms responsible for the enhanced electromechanical response near this region of phase space are not able to be properly examined.

In this work, a novel multiphase field (MPF) framework was established to describe systems with multiple interferroelectric phase transitions. The MPF approach naturally couples the free energy densities of the coexisting phases, each one defined by its own Landau coefficients. Consequently, the properties of the ferroelectric phases are allowed to vary independently, enabling a more accurate and thermodynamically consistent description of the bulk phases and interferroelectric phase transitions. Based on the MPF framework, a model was developed for systems with a single, temperature-induced, polymorphic phase boundary (PPB). The model was demonstrated for the BZT-BCT system, $(1-x)\mathrm{Ba}(\mathrm{Zr}_{0.2}\mathrm{Ti}_{0.8})\mathrm{O}_3$-$x(\mathrm{Ba}_{0.7}\mathrm{Ca}_{0.3})\mathrm{TiO}_3$, assuming a phase diagram with a single PPB between the tetragonal and rhombohedral phases. Specifically, the model was demonstrated for coarse-grained BZT-40 BCT in 1-D and 2-D, and for a [00l]-oriented BZT-50 BCT single crystal in 2-D. For the latter, anisotropic Landau coefficients were determined using a combination of single-crystal and polycrystalline experimental data.

Predictions for BZT-40 BCT and BZT-50 BCT are consistent with experimental observations of a tetragonal + rhombohedral coexistence region. Further, the combined energetic and kinetic analysis of the metastable coexistence of the tetragonal and rhombohedral phases can explain the stabilization of the purported orthorhombic phase in the vicinity of the PPB. The MPF model predicts a thermodynamic upper limit for coexistence that agrees with the apparent orthorhombic-tetragonal phase boundary. At low temperatures, results reveal that coexistence is kinetically limited, providing a rationale for the apparent rhombohedral-orthorhombic phase boundary. Near the coexistence thermal limit, the MPF model also demonstrates a vanishing energy barrier between variants in the metastable rhombohedral phase. This automatically predicts the formation of small metastable domains that facilitate polarization switching between stable tetragonal domains through a phase transformation-induced polarization rotation mechanism. This interfacial stabilization of the metastable R phase

can explain the higher electromechanical response reported experimentally for the BZT-BCT system along its purported orthorhombic-tetragonal phase boundary.

For the entire temperature range of metastable coexistence, the MPF model predicts microstructures with faceted domain walls and curved tetragonal-rhombohedral phase interfaces that are consistent with experiments. The formation of curved interfaces to accommodate domains of different phases was attributed to the relatively low anisotropy of the interfacial energy compared to that of domain walls. Also, miniaturization of the domain structure to the nanoscale, commonly observed near interferroelectric transitions, was connected to low interfacial energies and the volume fraction of the metastable ferroelectric phase. The latter produces a pinning effect on the motion of stable domain walls that retards the coarsening rate for domains of the stable ferroelectric phase. Further, a metastable equilibrium regime, characterized by a vanishing driving force for phase transformation, was identified in the vicinity of the PPB in the single-crystal analysis of BZT-50 BCT. The existence of this regime can explain the formation of typically observed domain configurations that produce a metastable equilibrium at the interface intersections and stabilize the ferroelectric microstructure. Moreover, a method was developed for the quantitative analysis of domain structures using the MATLAB™ toolbox MTEX, which can improve our understanding of interferroelectric phase transitions.

The MPF model and analysis tools developed in this work can be readily used to validate competing theories regarding the structural state and enhanced properties near PPBs in the search for lead-free materials.

Deputy Vice-Chancellor's Office

Postgraduate Office

UNIVERSITY OF CANTERBURY
Te Whare Wānanga o Waitaha
CHRISTCHURCH NEW ZEALAND

Co-Authorship Form

This form is to accompany the submission of any thesis that contains research reported in co-authored work that has been published, accepted for publication, or submitted for publication. A copy of this form should be included for each co-authored work that is included in the thesis. Completed forms should be included at the front (after the thesis abstract) of each copy of the thesis submitted for examination and library deposit.

Please indicate the chapter/section/pages of this thesis that are extracted from co-authored work and provide details of the publication or submission from the extract comes:

The content from Chapters 2 and 3 has been published in the following journal article:

- Oscar A. Torres-Matheus, R. Edwin García and Catherine M. Bishop. Phase coexistence near the polymorphic phase boundary. *Acta Materialia*, 164: 577-585, 2019, DOI: 10.1016/j.actamat.2018.10.041.

Please detail the nature and extent (%) of contribution by the candidate:

All work and analysis was performed by the PhD candidate. The article was written by the candidate and edited by the co-authors. An estimated 90% of the work was performed by the candidate.

Certification by Co-authors:

If there is more than one co-author then a single co-author can sign on behalf of all.
The undersigned certifies that:

- The above statement correctly reflects the nature and extent of the PhD candidate's contribution to this co-authored work
- In cases where the candidate was the lead author of the co-authored work he or she wrote the text

Name: *Catherine Bishop*	Signature: Catherine Bishop	Date: *24-2-2020*

Contents

List of Figures

List of Tables

List of Symbols

A	Helmholtz thermodynamic potential (Chapter 2) or domain size (Chapter 4)
a_{CW}	Curie-Weiss constant
$c_\circ$	Bulk composition
$c_N^{Z_N}$	Mole fraction of the N-th charged chemical species within the ionic solid
$\vec{D}$	Electric displacement
$\vec{E}$	Electric field
$\vec{E}_c$	Coercive field
$\vec{E}_o$	Maximum applied electric field
F	Total free energy functional
f	Free energy density
g	Double-well potential
h	Weight function
K	Gradient energy coefficient
k	Avrami constant (Chapters 3 and 6) or domain coarsening constant (Chapter 4)
L	Size of single-crystal sample
M	Mobility
M_o	Pre-exponential factor in the Arrhenius Equation for mobility
n	Avrami exponent
$\vec{P}$	Polarization
$\vec{P}_r$	Remnant polarization
$\vec{P}_s$	Spontaneous polarization
$\vec{P}_c$	Polarization at coercive field

Q	Activation energy in the Arrhenius Equation for mobility
R	Universal gas constant
r	Rate of phase transformation
T	Temperature
T_C	Curie temperature
T_{CW}	Curie-Weiss temperature
T_{max}	Temperature beyond which the ferroelectric phase is unstable for a first order paraelectric-ferroelectric transition
t	Time
$\vec{u}$	Dimensionless polarization
V	Volume of solid
V_E	Electrostatic potential
W	Double-well coefficient
α	Landau coefficients
Δf	Energy barrier between stable domains
Δf_{min}	Driving force for transformation of ferroelectric phases
$\overleftrightarrow{\varepsilon}$	Elastic strain tensor
$\overleftrightarrow{\epsilon}$	Dielectric permittivity
ϵ_o	Vacuum permittivity
η	Ratio of spontaneous polarization in the rhombohedral phase to the spontaneous polarization in the tetragonal phase
θ	Polar angle
ξ	Interfacial width
σ	Interfacial energy
ϕ	Phase field variable
$\overline{\phi}$	Mean phase field
χ_c	Electric susceptibility at coercive field
ψ	Fraction transformed of ferroelectric phases
ω	Experimental cycling frequency

List of Abbreviations

AFM	Atomic force microscopy
BKT	Bismuth potassium titanate
BNT	Bismuth sodium titanate
BT	Barium titanate
BZT-BCT	Barium zirconate titanate-barium calcium titanate
C	Cubic
CBED	Convergent beam electron diffraction
DW	Domain wall
EBSD	Electron back scatter diffraction
ECD	Equivalent circle diameter
FE	Ferroelectric
FEM	Finite element method
JMAK	Johnson-Mehl-Avrami-Kolmogorov
KNN	Potassium sodium niobate
MPB	Morphotropic phase boundary
MPF	Multiphase field
O	Orthorhombic
ODF	Orientation distribution function
P-FE	Paraelectric-ferroelectric
PDFO	Probability density function of orientation
PPB	Polymorphic phase boundary
PZT	Lead zirconate titanate

R	Rhombohedral
RDW	Rhombohedral domain wall
RMSE	Root mean square error
T	Tetragonal
TCP	Tricritical point
TDW	Tetragonal domain wall
TEM	Transmission electron microscopy
TTT	Time-temperature-transformation
XRD	X-ray diffraction

Chapter 1

Introduction

This chapter provides an introduction to the research project. It begins with the general background of the field, which serves as motivation for this research and includes key concepts that will be used and further developed. The chapter also outlines the scope and objectives of the project and a list of research achievements, including conference presentations and journal publications. Finally, it presents an overview of how the thesis is structured, and a list of the novel contributions.

1.1 General background

1.1.1 Ferroelectric materials

Ferroelectric (FE) materials can be defined as special dielectrics with a spontaneous polarization that can be reversed by the application of an external electric field[1–3]. Dielectric materials are well known electric insulators that can be polarized. In these materials, upon the application of an electric field, the centres of positive and negative electric charges at atomic level shift slightly, forming induced electric dipoles. This displacement, or induced polarization, increases with the applied electric field, and it vanishes when the electric field is removed[3]. FE materials, on the other hand, are characterized by a spontaneous polarization in the absence of an external electric field due to the formation of permanent electric dipoles below the Curie temperature. Upon cooling below this critical temperature, these materials undergo a structural phase transition, denoted by a change or distortion in the crystal structure, transforming from a high-temperature paraelectric phase into a low-temperature FE phase[1,2], Figure 1.1. Since the permanent electric dipoles in the FE phase are coupled to its crystal structure, they can only lie in one crystallographic direction. Moreover, any stimuli that changes the material's lattice, such as force and temperature, will also change the strength of the dipoles and, consequently, the spontaneous polarization and associated spontaneous strain. Therefore, all ferroelectrics are also piezoelectric and pyroelectric materials[1].

When a FE material is cooled below its Curie temperature, the electric dipoles group themselves into regions with uniformly oriented spontaneous polarization, known as ferroelectric domains. These domains form within the material to minimize the electrostatic energy associated with depolarizing fields and the elastic energy due to mechanical constraints[1]. The interface between two domains is called a domain wall (DW). In polycrystalline ferroelectrics, all domains have initially different

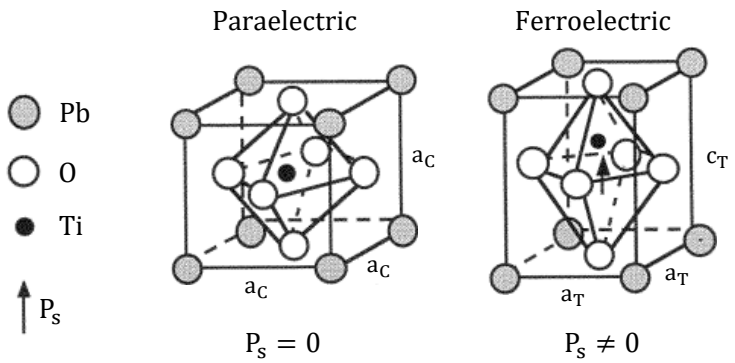

Figure 1.1: Paraelectric-ferroelectric (P-FE) phase transition illustrated for $PbTiO_3$. The high-temperature paraelectric phase has a cubic crystal structure and the low-temperature FE phase has a tetragonal crystal structure. Figure adapted from Damjanovic[4].

polarization orientations due to the complex set of electric and elastic conditions at the grain boundaries[4]. As explained above, these polarization states are restricted by the crystal orientation of each grain. This results in zero net polarization and no pyroelectric and piezoelectric effects. Upon the application of small electric fields, the net polarization of the material increases linearly with the applied field. As the magnitude of the electric field increases, the ferroelectric domains switch in the direction of the field. At this stage, the net polarization rises rapidly until saturation is reached. This process is called poling and it is applied to a FE material only once, after which it will behave as shown in Figure 1.2. The value of polarization extrapolated back from the saturation limit is the spontaneous polarization, P_s, the value at zero electric field is the remnant polarization, P_r, and the field at which the polarization switches from one state to another is the coercive field, E_c. At saturation, polarization is proportional to the applied electric field. The dashed line in Figure 1.2 corresponds to the extrapolated linear segment that describes this linear behaviour.

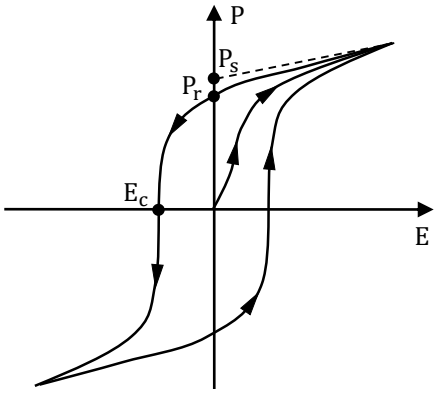

Figure 1.2: Ferroelectric hysteresis loop showing the spontaneous polarization, P_s, remnant polarization, P_r, and coercive field, E_c.

In single-crystal ferroelectrics, a single-domain state can be achieved by poling[4], in which case the spontaneous and remnant polarizations may have the same value. Conversely, in polycrystalline materials, P_r is always smaller than P_s, and its maximum value depends on the available polarization states in the FE phase, in accordance with its crystal structure[4]. For example, in a tetragonal (T) phase with six available polarization states, $P_{r,max} = 0.8312P_s$; while in a rhombohedral (R) phase with eight available polarization states, $P_{r,max} = 0.8660P_s$ [4–10].

1.1.2 Ferroelectric ceramics

Ferroelectric materials are ubiquitous in modern society. Their applications range from high-dielectric-constant capacitors[11]; electromechanical devices, such as sensors, actuators, transducers, micropositioning systems, piezoelectric fuel injectors and printing machines[12]; and, more recently, non-volatile memories[11]. The number of industrial and commercial applications increased significantly after the development of FE ceramics. In the context of this field, the use of ceramics is of particular importance because of the ability to adjust their properties for different applications by using a wide range of compositions[1].

Essentially, the development of ferroelectric ceramics started during World War II with the discovery of the unusually high permittivity in ceramic barium titanate ($BaTiO_3$) capacitors. Soon after, it was established that the origin of this unusually high permittivity in $BaTiO_3$ was its ferroelectric nature, i.e. the presence of permanent electric dipoles[13]. These two discoveries were pivotal in the development of FE ceramics for a number of reasons[1]. On the one hand, $BaTiO_3$ was of significant practical utility: high chemical and mechanical stability, ferroelectric at room temperature, and readiness to use in ceramic form. On the other hand, the simplicity of its perovskite lattice structure enabled significant progress in understanding and interpreting ferroelectricity in a microscopic and macroscopic way. Also, the ferroelectric nature of $BaTiO_3$ led to the discovery of the poling process, which allowed converting an inert ferroelectric into an electromechanically active ceramic with a large number of applications[13]

In addition, $BaTiO_3$ was the first material with more than one FE phase, Figure 1.3. This led to the notion of interferroelectric phase boundaries, as opposed to paraelectric-ferroelectric phase boundaries[14–16]. The phase transformation regimes are traditionally summarized in composition-temperature maps, or phase diagrams. A phase boundary representing a compositionally driven interferroelectric transition is referred to as a morphotropic phase boundary (MPB); while a phase boundary representing an interferroelectric transition driven by changes in temperature is referred to as a polymorphic phase boundary (PPB)[16,17].

Another important FE ceramic is lead zirconate titanate (PZT), or $Pb(Zr_{1-x}Ti_x)O_3$. This material also has a perovskite crystal structure and more than one FE phase. Further, its phase diagram features an MPB between the T and R ferroelectric phases, Figure 1.4. This solid solution exhibits a wide range of properties depending on the different compositions between lead titanate and lead zirconate. In particular, PZT has been the most widely used piezoelectric material due its high electromechanical performance near its MPB compositions ($x \approx 0.48$)[11,12,18].

According to Heitmann and Rossetti[15], the structural state in the vicinity of the MPB has been a subject of considerable debate. However, they have also noted that, regardless of its structural nature, the enhanced electromechanical properties are related to the reduced anisotropy of the free energy surface in this region. The latter has been linked to miniaturization of the domain structure to the nanoscale, due to a reduction in the DW energy[20], and to an easy path for polarization rotation / extension[21,22].

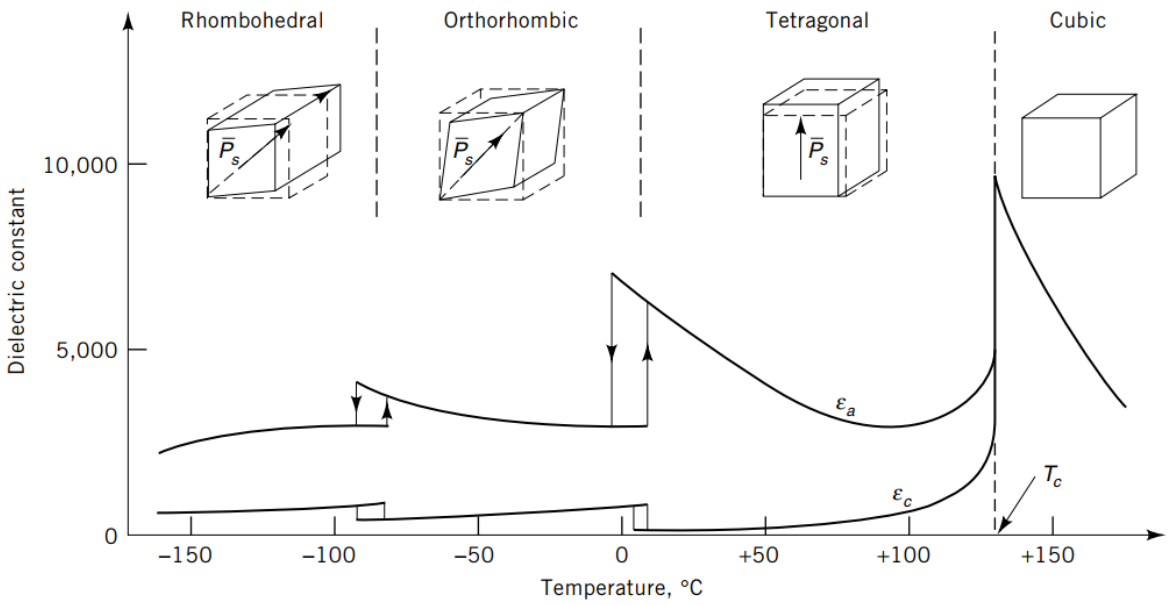

Figure 1.3: Paraelectric and ferroelectric phases in $BaTiO_3$, as reported by Jang[3]. The transition temperatures are denoted by anomalies in the dielectric permittivity. For each FE phase, the direction of the spontaneous polarization and associated distortion of the unit cell are shown.

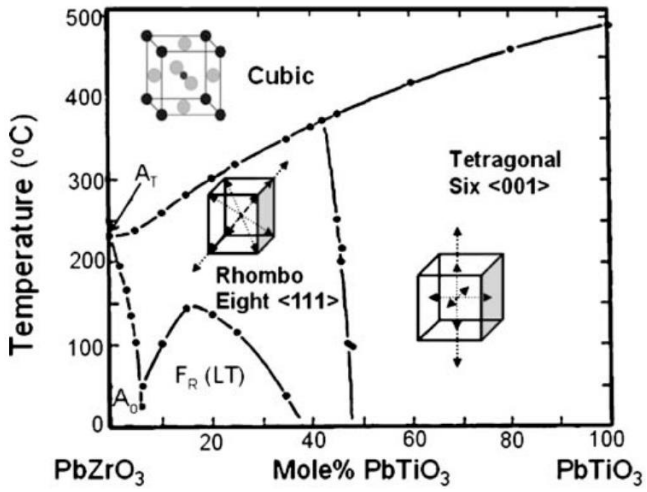

Figure 1.4: PZT pseudo-binary phase diagram, as shown in Shrout and Zhang[19].

Despite being the dominant piezoelectric material for the last decades, recent environmental restrictions on the use of lead have motivated extensive research on lead-free ferroelectrics[12,18,19,23]. The search for lead-free alternatives that demonstrate the same versatility as PZT has proven to be a challenge. Suitable replacement materials have been found only for specific applications[12,18,19,23].

1.1.3 Lead-free ferroelectrics

According to Bell[11], the search for new lead-free materials to replace PZT relies on understanding the origin of its outstanding electromechanical performance, which is known to be related to the presence of an MPB but whose nature has been under debate[12]. Further, it has been established that the presence of lead is not essential for having an MPB, and that the free-energy flattening (or reduced

anisotropy) associated with the properties enhancement near this region is also observed in lead-free materials[18]. Hence, despite unreached consensus regarding the origin of the large piezoelectric response near the MPB, significant research has focused on solid solutions exhibiting interferroelectric phase boundaries.

In general, the following lead-free systems have been investigated: electrostrictive or relaxor-based materials, such as strontium sodium bismuth titanate (SBNT); non-perovskite ferroelectric structures, such as bismuth layer-structured ferroelectrics (BLSF) and tungsten-bronze type ferroelectrics; and perovskite ferroelectric structures[12,23]. Materials in the latter group constitute the most promising candidates and can be categorized into three main families: the barium titanate (BT) system, $BaTiO_3$; the potassium sodium niobate (KNN) system, $(K_{1-x}Na_x)NbO_3$; and the bismuth sodium titanate (BNT) system, $(Bi_{0.5}Na_{0.5})TiO_3$[12,18,19,23].

Although the lead-free perovskite ferroelectrics were discovered (and some discarded for piezoelectric applications) more than fifty years ago, current developments have focussed on modifying their chemical composition and improving their processing[18]. In the case of $BaTiO_3$, for instance, its use has been limited for practical piezoelectric applications due to its low Curie temperature ($T_c = 120\,°C$)[23]. However, this system has been widely studied recently as part of binary and ternary systems[12,18,19,23]. The KNN system, on the other hand, is a solid solution regarded as one of the best and most investigated lead-free piezoelectric candidates[23]. The major drawbacks traditionally associated with this system are its difficult processing, inferior properties compared to those of PZT, and relatively complex phase diagram with multiple PPBs[12,18,19], Figure 1.5(a). As for the BNT system, it represents the main candidate among the bismuth-based materials, which also includes the bismuth potassium titanate (BKT) system. These ceramics are important as end members for several promising binary and tertiary solid solutions, such as: BNT-BT, BKT-BT, BNT-BKT and BNT-BKT-BT[12,19,23]. All these solid solutions have a phase diagram similar to that of PZT, with an MPB between the T and R ferroelectric phases. However, they experience poor temperature stability due to a relatively low depolarization temperature and the polymorphic character of the MPB[12,19], Figure 1.5(b). Further information regarding chemical modification and processing, as well as the positive attributes, shortcomings and current state of these lead-free perovskite materials have been extensively reviewed and documented[12,18,19,23].

In 2009, Liu and Ren[24] reported a new lead-free FE ceramic, barium zirconate titanate-barium calcium titanate (BZT-BCT), $(1-x)Ba(Zr_{0.2}Ti_{0.8})O_3$-$x(Ba_{0.7}Ca_{0.3})TiO_3$, with outstanding piezoelectric response ($d_{33} > 600\,pC/N$). In contrast to the materials mentioned above, the BZT-BCT system is remarkably similar to PZT. It has a phase diagram with a single interferroelectric phase boundary ending at a tricritical point (TCP) where the T and R ferroelectric phases meet with a paraelectric cubic (C) phase, Figure 1.6(a). However, Keeble *et al.*[25] have speculated the existence of an additional orthorhombic (O) phase and revised its phase diagram, Figure 1.6(b). This initiated an ongoing debate regarding the true structural state near the original PPB of the BZT-BCT system, refer to Section 3.1 for a full discussion.

Regardless of the structural nature of BZT-BCT, its high piezoelectric response has attracted considerable attention. Numerous studies have been conducted to address some limitations of this system

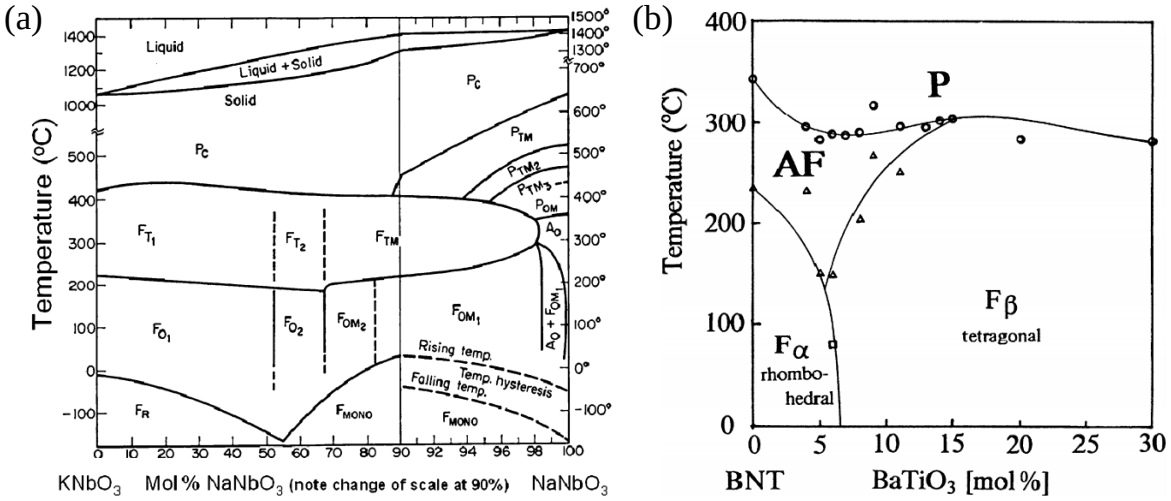

Figure 1.5: Pseudo-binary phase diagrams of the (a) KNN and (b) BNT-BT systems, as shown in Shrout and Zhang [19]. For the BNT-BT system, an anti-ferroelectric phase (AF) causes depolarization at temperatures below its Curie temperature.

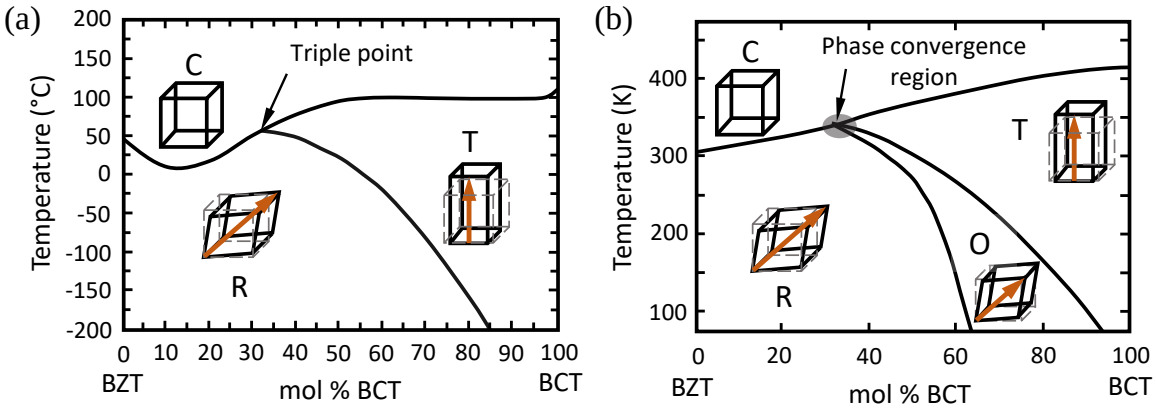

Figure 1.6: (a) Original and (b) revised pseudo-binary phase diagrams for the BZT-BCT system, adapted from Liu and Ren [24] and Keeble *et al.* [25], respectively.

for practical applications, namely: poor temperature stability due to the inclined interferroelectric phase boundary, relatively low P-FE transition temperatures, and the composition with the highest piezoelectric coefficient (d_{33}) has a Curie point close to room temperature [18]. Further, substantial experimental work has been carried out to characterize the microstructure and obtain the full set of elastic, dielectric and piezoelectric properties for different compositions. Detailed information regarding the processing, properties and microstructure of the BZT-BCT system can be found in recent review articles by Acosta *et al.* [16] and Gao *et al.* [17].

From the theoretical point of view, Damjanovic *et al.* [18] have noted that BZT-BCT represents a convenient system to investigate factors associated with the enhanced electromechanical properties. These factors include composition and temperature effects on the flattening of the free energy density, mechanisms controlling the polarization rotation / extension, and contributions from the motion of domain walls.

1.1.4 Modelling of ferroelectric materials

Computational work on ferroelectrics includes first-principles[26–31], atomic-level[32–37], and phase field modelling and simulations[38–55]. First-principles approaches are typically based on the density functional theory[26], and have been successfully used to determine intrinsic material properties[26,27], as well as to study domain walls[28] and domain patterns in nanowires[29], ultrathin films[30] and single crystals[31].

Further, shell model molecular dynamics have been used to investigate domain nucleation and switching dynamics in single crystals[32], size and strain effects on electric field-induced domain evolution in ultrathin films[35], and energetics of surfaces and domain walls[36]. In addition, molecular dynamics simulations based on effective Hamiltonians have been employed to investigate the mechanisms of polarization switching[34]. Nanoscale domain configurations and their evolution have also been studied by combining the shell model and the atomic-scale finite element method to improve computational performance[37].

Moreover, since ferroelectricity is a structural phase transition, phase field models have been used extensively to study different aspects of the ferroelectric phenomenon. Most studies have focused on the ferroelectric behaviour in single-phase regions of the materials' phase diagram. This includes microstructural evolution and domain configurations in single-crystals[38–45], polycrystals[46–48], as well as in thin films[49,50]. Recent works have used the phase field method to investigate phase coexistence and the mechanisms responsible for the enhanced electromechanical properties near the MPB[51–56]. These models rely on a single Landau-Devonshire thermodynamic potential with coefficients fitted to macroscopic properties to describe the FE behaviour, see Section 1.1.5. When there is more than one FE phase, all Landau coefficients cannot be fitted to experimental data from all the phases. Instead, they are generally fitted to properties from specific FE phases in an orderly manner, *i.e.,* some coefficients are fitted to properties from one phase, then they are held constant while other coefficients are fitted to data from another phase, and so on until all coefficients are estimated. Although significant effort can be invested on the fitting procedure, the use of a single Landau-Devonshire potential to describe more than one FE phase inherently limits the accuracy of predicted properties in the bulk phases and, particularly, near interferroelectric transitions, see *e.g.,* Figure 1.7[57–59].

1.1.5 The phase field method

The phase field method is a mathematical model traditionally used to solve interfacial problems. It has been applied in materials science as a computational approach for modelling a wide range of cases involving microstructure evolution, such as solidification, solid-state phase transformations, grain growth and coarsening, among others[60–63]. In the traditional sharp-interface description, the regions representing different compositional or structural domains are separated by zero-thickness interfaces, which are explicitly tracked during the microstructure evolution using a set of boundary conditions[60,64]. In contrast, the phase field method has a diffuse-interface approach which allows the entire microstructure to be described by one or more variables that vary continuously at the interfaces,

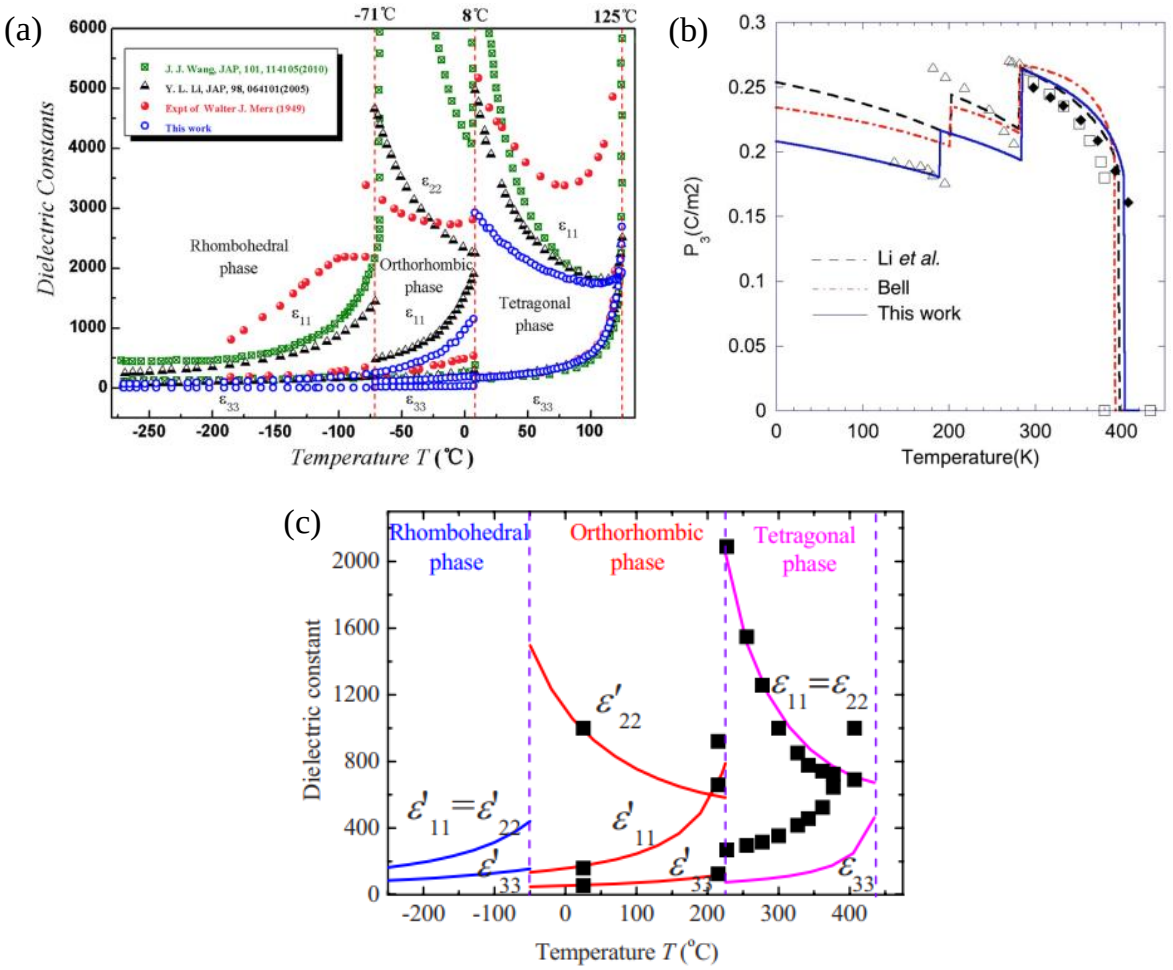

Figure 1.7: (a) Predicted relative dielectric permittivity for single-crystal $BaTiO_3$, as reported by Ma *et al.*[58]. (b) Predicted spontaneous polarization for single-crystal $BaTiO_3$, as reported by Wang *et al.*[59]. (c) Predicted relative dielectric permittivity for single-crystal $KNbO_3$, as reported by Liang *et al.*[57]. In subfigure (a) the experimental data is represented by red markers, while the other markers indicate predictions from different models. In subfigures (b) and (c) the experimental data is represented by markers, while lines correspond to predicted values. In all cases, the accuracy of the prediction is compromised for some properties and/or phases.

Figure 1.8. In particular, since the phase field method does not involve the explicit tracking of the moving interfaces between domains, it is more practical and suitable than the traditional approach for complicated multidimensional simulations and complex morphologies[60–62,64].

In the phase field method, the microstructure is described by a single free energy functional, expressed in terms of the phase-field variables and their gradients. This functional is derived based on phenomenological theories that lean on the laws of thermodynamics and kinetics to explain phase transitions without regard to the microscopic factors[1]. The use of this theory allows introducing material-specific properties into the model by estimating the phenomenological parameters using measurable macroscopic quantities. Additionally, the phase field method can account for different driving forces for the microstructure evolution by including volumetric, gradient, electrostatic and elastic terms in the total free energy functional[60].

Moreover, the equations that govern the microstructure evolution are derived using variational

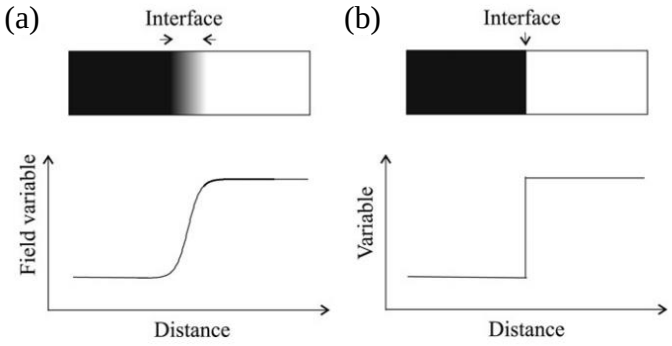

Figure 1.8: (a) Diffuse-interface approach showing continuous transition of a field variable across the interface, and (b) sharp-interface approach showing discontinuity of a field variable at the interface, adapted from Moelans *et al.* [60].

techniques and irreversible (non-equilibrium) thermodynamics, *i.e.,* it is assumed that the rate of evolution is proportional to the total driving force [64]. Depending on the conserved or non-conserved nature of the phase-field variables, the microstructure evolution is controlled by Cahn-Hilliard or Allen-Cahn type equations, respectively [60,61,64]. Thus,

$$\frac{\partial c}{\partial t} = \nabla \cdot M \nabla \frac{\delta F}{\delta c} \tag{1.1}$$

$$\frac{\partial \phi}{\partial t} = -M \nabla \frac{\delta F}{\delta \phi} \tag{1.2}$$

where F is the total free energy functional, M is the interface mobility, c represents a conserved or composition variable, and ϕ represents a non-conserved variable. Equation 1.1 is a Cahn-Hilliard equation, and Equation 1.2 is an Allen-Cahn equation. In general, all the phase-field variables depend on time and position, and the free energy functional can be a function of both conserved and non-conserved variables. According to Moelans *et al.* [60], conserved variables are normally associated with local composition such as molar fractions, mass fractions or concentrations; while non-conserved variables can be divided into order parameters and phase fields. The former are generally related to crystal structure and orientation. The latter refers to phenomenological variables without well-defined physical meaning, used to specify the region in spatial space where a phase is locally stable.

Further, phase field models have been categorized into two main types depending on their application. In one type, mainly applied to solidification, non-conserved phenomenological phase fields are used to avoid tracking the interfaces; while in the other type, the variables are related to well-defined physical quantities, such as conserved variables for phase separation and non-conserved order parameters for order-disorder transformations [60–62]. The latter category embodies the phase field models commonly applied to solid-state transformations involving symmetry reduction, such as ferroelectric transitions.

The phase field models applied to ferroelectrics differ substantially depending on the specific formulation of the total free energy functional. The volumetric free energy density is described by a Landau-Devonshire potential, *i.e.,* a Taylor expansion in terms of the polarization order parameter, generally expressed up to the sixth order to describe first- and second-order ferroelectric transi-

tions[65,66]. Further, heterogeneous structures, such as DWs, can be taken into account by introducing a gradient energy term for changes in polarization. Similarly to the Landau-Devonshire potential, this term must also consider the anisotropic nature of the FE material. For a cubic crystal symmetry, the gradient free energy density can be written using Voigt notation as[67]

$$\begin{aligned} f_{gradient} = &\frac{1}{2}g_{11}\left(P_{1,1}^2 + P_{2,2}^2 + P_{3,3}^2\right) + g_{12}\left(P_{1,1}P_{2,2} + P_{1,1}P_{3,3} + P_{2,2}P_{3,3}\right) \\ &+ \frac{1}{2}g_{44}\left[(P_{1,2} + P_{2,1})^2 + (P_{1,3} + P_{3,1})^2 + (P_{2,3} + P_{3,2})^2\right] \end{aligned} \tag{1.3}$$

where $P_{i,j} = \partial P_i / \partial x_j$ with $i, j = 1, 2, 3$ are the spatial derivatives of the polarization vector; and $g_{11} = g_{1111}$, $g_{12} = g_{1122}$ and $g_{44} = g_{1212}$ are the gradient energy coefficients. Alternatively, the following equivalent expression has been proposed[68]

$$\begin{aligned} f_{gradient} = &\frac{1}{2}g_{11}\left(P_{1,1}^2 + P_{2,2}^2 + P_{3,3}^2\right) + g_{14}\left(P_{1,1}P_{2,2} + P_{1,1}P_{3,3} + P_{2,2}P_{3,3}\right) \\ &+ \frac{1}{2}g_{44}\left[P_{1,2}^2 + P_{2,1}^2 + P_{2,3}^2 + P_{3,2}^2 + P_{3,1}^2 + P_{1,3}^2\right] \end{aligned} \tag{1.4}$$

where $g_{14} = g_{12} + g_{44} \neq g_{1123}$. Equation 1.3 is analogous to the expression for elastic free energy density, while Equation 1.4 has a simpler interpretation in discrete form that facilitates its numerical implementation[68]. Further, if an isotropic gradient energy coefficient is assumed, such that $K_P = K_{1111}$, the expression can be reduced to[47,48]

$$f_{gradient} = \frac{1}{2}K_P(P_{1,1}^2 + P_{2,2}^2 + P_{1,2}^2 + P_{2,1}^2 + P_{3,2}^2 + P_{3,1}^2) \tag{1.5}$$

Finally, phase field models applied to ferroelectrics commonly include elastic and electrostrictive terms into the total free energy functional, see *e.g.,*[49,65]. In this case, the local elastic strains can be calculated by solving the mechanical equilibrium equation. Similarly, an electrostatic contribution to the total free energy can be introduced to consider charged defects, see *e.g.,*[69], and dipole-dipole interactions, see *e.g.,*[38,70]. In this case, the local electrostatic field can be calculated for any distribution of charges and dipoles by solving Coulomb's Equation.

1.2 Scope and objectives

The aim of this research project is to develop a novel multiphase field (MPF) model to study FE materials with a single PPB. The MPF approach considers the homogeneous free energy density of the individual FE phases, with Landau coefficients fitted only to their own properties, enabling a better description of the single-phase regions of the material. This allows a thermodynamically correct and more accurate analysis in the vicinity of the interferroelectric phase transitions. The model will be applied to the BZT-BCT system to elucidate the mechanisms responsible for the coexistence of FE phases and enhanced electromechanical properties reported by experiments near its PPB. In particular, the domain structures and transformation kinetics of the coexisting FE phases will be analysed. The research scope is limited to the computational modelling and analysis of single-crystal ferroelectrics

in one and two spatial dimensions, with no changes in composition, strain effects or charged defects. The following list contains objectives or milestones with increasing complexity in the development and application of the MPF model:

- Derivation of a general multiphase field framework for systems with multiple FE phases.
- Derivation of a MPF model for FE systems with a single PPB.
- Model formulation in one spatial dimension.
- Application of the one-dimensional MPF model to coarse-grained BZT-40 BCT.
- Extension of the model to two spatial dimensions.
- Application of the two-dimensional MPF model to coarse-grained BZT-40 BCT.
- Fitting of anisotropic Landau coefficients for the T and R phases of the BZT-50 BCT system.
- Application of the two-dimensional MPF model to a BZT-50 BCT single crystal.

1.3 Research achievements

This section lists the conference presentations and journal publications related to this work in chronological order.

- Oscar A. Torres-Matheus, R. Edwin García and Catherine M. Bishop. Coexistence and domain dynamics of ferroelectric phases in vicinity of the MPB. Presented by Oscar A. Torres-Matheus at the *Materials Science and Technology 2017* conference, Pittsburgh, PA, United States of America.
- Catherine M. Bishop, Oscar A. Torres-Matheus and R. Edwin García. Charged grain boundaries and ferroelectric phase transitions. Presented by Catherine M. Bishop at the *Gordon Research Conference 2018 on Solid State Studies in Ceramics* (selected by organisers for a Late Breaking Science talk), South Hadley, MA, United States of America.
- Oscar A. Torres-Matheus, R. Edwin García and Catherine M. Bishop. Phase field modelling of ferroelectric materials near the polymorphic phase boundary. Presented by Oscar A. Torres-Matheus at the *Materials@UC 2018* conference, Christchurch, New Zealand.
- Oscar A. Torres-Matheus, R. Edwin García and Catherine M. Bishop. Phase coexistence near the polymorphic phase boundary. *Acta Materialia*, 164: 577-585, 2019, DOI: 10.1016/j.actamat.2018.10.041.
- Catherine M. Bishop, Oscar A. Torres-Matheus and R. Edwin García. TTT relations for ferroelectrics near the polymorphic phase boundary: Insights from a new model for BZT-BCT. Presented by Catherine M. Bishop at the *European Materials Research Society 2019* spring meeting, Nice, France.
- Catherine M. Bishop, Oscar A. Torres-Matheus and R. Edwin García. Multi-phase field formulation for ferroelectrics near the polymorphic phase boundary: insights into BZT-BCT. Presented by Catherine M. Bishop at the *XVI European Ceramics Society* conference, 2019, Torino, Italy.

– Catherine M. Bishop, Oscar A. Torres-Matheus and R. Edwin García. TTT relations for ferroelectrics near the polymorphic phase boundary: Insights from a new model for BZT-BCT. Presented by Catherine M. Bishop at the *Materials Science and Technology 2019* conference (invited talk), Portland, OR, United States of America.

1.4 Thesis chapter overviews

This section summarizes the content of each chapter and appendix that appears in this thesis.

Chapter 1 - Introduction: this chapter provides an introduction to the research project. It begins with the general background of the field, which serves as motivation for this research and includes key concepts that will be used and further developed. The chapter also outlines the scope and objectives of the project and a list of research achievements, including conference presentations and journal publications. Finally, it presents an overview of how the thesis is structured, and a list of the novel contributions.

Chapter 2 - Multiphase field theory: in this chapter, a new theory based on a MPF formulation is proposed to describe systems with multiple FE phases considering their individual free energy densities, *i.e.,* individual Landau-Devonshire potentials. The MPF framework is then used to develop a two-FE-phase model for systems with a single PPB. Finally, based on an assessment of the thermodynamic P-FE transition of the individual FE phases, predictions are made about the coexistence and stability of phases in the vicinity of the PPB.

Chapter 3 - Application to coarse-grained BZT-40 BCT polycrystal in 1-D: in this chapter, the MPF model is applied to the lead-free BZT-40 BCT system assuming a phase diagram with a single PPB between the T and R phases. For each FE phase, the Landau coefficients are obtained from polycrystalline properties using a coarse-grained approach. A one-dimensional study is performed to demonstrate the mechanisms controlling the stabilization of the apparent O phase near the T-R phase boundary, and to elucidate the driving forces that determine their long-term dynamics.

Chapter 4 - Application to coarse-grained BZT-40 BCT polycrystal in 2-D: in this chapter, the MPF model is demonstrated in two dimensions for a coarse-grained BZT-40 BCT polycrystal. This enables access to additional degrees of freedom, or polarization configurations, to minimize the free energy of the system. The additional spatial dimension yields more realistic domain configurations that affect the equilibrium states and transformation dynamics of the coexisting FE phases in the vicinity of the PPB. Further, the two-dimensional model allows assessment of the effect of local electric fields within the material on the FE domain structures and the kinetics of phase transformation.

Chapter 5 - Fitting of Landau coefficients for BZT-50 BCT: in this chapter, a procedure is outlined for estimating the Landau parameters for the R and T phases of single-crystal $(Ba_{0.85}Ca_{0.15})(Zr_{0.10}Ti_{0.90})$, also known as $Ba(Zr_{0.2}Ti_{0.8})O_3$-50 $(Ba_{0.7}Ca_{0.3})TiO_3$ or BZT-50 BCT. This has been the most widely studied composition of this system, which allows comparison of the results with simulations and/or experiments found in the literature on BZT-50 BCT. The developed procedure uses single-crystal and polycrystalline experimental information available in the literature. Equations for calculating the

intrinsic electromechanical properties of ceramics are used to relate the single-crystal and polycrystalline data. This allows the use of measurements from polycrystalline samples to complement the required information for the fitting of Landau parameters.

Chapter 6 - Application to BZT-50 BCT single crystal in 2-D: in this chapter, the MPF model is demonstrated for a BZT-50 BCT single crystal, characterized by the spatial distribution of a three-component polarization order parameter. Simulations are performed on a 2-D computational domain parallel to the (001) plane of the pseudocubic crystal structure. The anisotropic Landau coefficients determined in Chapter 5 are used to examine the intrinsic effects of ferroelectric coexistence on the phase transformation kinetics and domain morphology. The chapter also presents a method for the quantitative analysis of FE domains and their interfaces in the MATLAB™ toolbox MTEX.

Chapter 7 - Conclusions and future work: this chapter summarizes the main findings and predictions of the developed model, as well as their implications for the analysis of similar FE systems. The chapter also outlines a potential trajectory for future work in the field. This includes possible applications of the MPF model and recommendations for its further development.

Appendix A - Mobility calculations for the BZT-*x* BCT system: this appendix contains mobility calculations for different compositions of the BZT-*x* BCT system. The calculation method is detailed in Section 3.3.2. However, the procedure is summarized here for completeness.

Appendix B - Publications: this appendix provides a copy of an article published during the course of this research. The article was published in the journal Acta Materialia and was adapted in this work for non-commercial use only. Specifically, its content was included and further developed in Chapters 2 and 3. The article has the following citation:

- Oscar A. Torres-Matheus, R. Edwin García and Catherine M. Bishop. Phase coexistence near the polymorphic phase boundary. *Acta Materialia*, 164: 577-585, 2019, DOI: 10.1016/j.actamat.2018.10.041.

1.5 Novel contributions

- Developed a new multiphase field model for ferroelectrics.
- Obtained anisotropic Landau parameters for the BZT-50 BCT system.
- Developed a tool to analyse quantitatively ferroelectric microstructures in MATLAB™.
- Developed a method to study the kinetics of phase transformation in two-FE-phase systems using time-temperature-transformation (TTT) diagrams.
- Explained the coexistence range of FE phases observed around the PPB in the BZT-BCT system.

Chapter 2

Multiphase field theory

The content of this chapter has been published as: Oscar A. Torres-Matheus, R. Edwin García and Catherine M. Bishop. Phase coexistence near the polymorphic phase boundary. *Acta Materialia*, 164: 577-585, 2019, DOI: 10.1016/j.actamat.2018.10.041, and adapted here for non-commercial use only.

2.1 Introduction

Phase field formulations are traditionally built upon the Landau-Devonshire thermodynamic potential to describe the paraelectric-ferroelectric phase transition, and a polarization gradient energy penalty to account for domain walls[71]. Phase field descriptions have been extensively used for single-phase ferroelectrics to investigate microstructural evolution and domain configurations in single-crystals[38–45], polycrystals[46–48], as well as in thin films[49,50]. For the region near the interferroelectric phase boundary, phenomenological approaches commonly split the Landau coefficients into isotropic and anisotropic contributions to facilitate the thermodynamic analysis[15,20,72]. Structure symmetry is determined by identifying the direction of the polarization vector that minimises the volumetric free energy density[20]. Landau coefficients are commonly fitted to experimental data of specific ferroelectric (FE) phases, and the accuracy of predicted properties is limited near interferroelectric transitions and bulk phases, *e.g.,* [57–59].

In spite of significant progress, the thermodynamic state and the material properties in the vicinity of the interferroelectric phase boundary remain under considerable debate[15]. Existing approaches cannot directly assess the thermodynamic conditions for the stable and metastable coexistence of FE phases, nor the impact of the transformation kinetics of the multiple coexisting phases. This limitation can be overcome by considering the homogeneous free energy density of coexisting FE phases separately[73], each with independent Landau coefficients obtained from experimental data for the respective phase.

In this chapter, a new theory based on a multiphase field (MPF) formulation is proposed to consider the thermodynamics of multiple FE phases. The MPF framework is then used to develop a two-FE-phase model for systems with a single polymorphic phase boundary (PPB). Finally, based on

an assessment of the thermodynamic paraelectric-ferroelectric (P-FE) transition of the individual FE phases, predictions are made about the coexistence and stability of phases in the vicinity of the PPB.

2.2 Multiphase field formulation for ferroelectric systems

The total Helmholtz free energy of a multiphase FE system on a domain of volume V is defined herein as

$$\begin{aligned} F[\vec{P}, \overleftrightarrow{\varepsilon}, \{c_N^{Z_N}\}, \{\phi_m\}; \vec{E}, T, c_\circ] = \int_V \Bigg\{ & f(\vec{P}, \overleftrightarrow{\varepsilon}, \{c_N^{Z_N}\}, \{\phi_m\}; \vec{E}, T, c_\circ) \\ & + \frac{1}{2} \sum_{k,l=1}^{3} \sum_{i,j=1}^{3} K_{ijkl} \frac{\partial P_k}{\partial x_i} \frac{\partial P_l}{\partial x_j} \\ & + \sum_{m=1}^{q} \sum_{n=m+1}^{q} \left[\frac{K_{mn}}{2} |\phi_m \nabla \phi_n - \phi_n \nabla \phi_m|^2 \right] \Bigg\} dV \end{aligned} \tag{2.1}$$

where T and $c_\circ$ are the temperature and bulk composition of interest; $\vec{P}$ is the polarization; $\overleftrightarrow{\varepsilon}$ is the elastic strain tensor; $\vec{E}$ is the electric field; $\{c_N^{Z_N}\}$ is the mole fraction of the N-th charged chemical species integrating the ionic solid, as defined by Vikrant *et al.*[69]; $\{\phi_m\}$ is the set of phase fields describing the interacting phases; and q is the number of distinguishable FE phases. Each phase field, $0 \leq \phi_m \leq 1$, specifies the region in (spatial) space where the m-th phase is locally stable, and is subjected to the geometrical constraint $\phi_1 + \phi_2 + \ldots + \phi_q = 1$.

The first term on the right side of Equation 2.1 is the volumetric free energy density of the FE system, a continuous function of the controlling variables at the temperature and composition of interest. The second term is the gradient energy penalty to create a domain wall (a polarization domain interface). K_{ijkl} is the $ijkl$-th gradient energy coefficient contribution for a polarization domain wall. The third term is the phase gradient energy penalty to create an interface between two phases. K_{mn} is the mn-th gradient energy coefficient contribution for a phase boundary. Interphase interfacial energies have contributions from both the polarization and phase gradient energy terms. In the traditional approach, these energies are fully coupled. In the new approach, the interphase and domain wall energies can be varied independently.

Based on analogous phase field models for transformations that involve more than two phases, such as multiphase solidification in eutectic, peritectic and monotectic alloys; or evolution of polycrystalline structures (*e.g.,* grain growth)[60,74,75]; the volumetric free energy density is defined herein as

$$f(\vec{P}, \overleftrightarrow{\varepsilon}, \{c_N^{Z_N}\}, \{\phi_m\}; \vec{E}, T, c_\circ) = \sum_{m=1}^{q} h(\phi_m) f_m + \sum_{m=1}^{q} \sum_{n=m+1}^{q} W_{mn} \phi_m^r \phi_n^r \tag{2.2}$$

where the first term represents an interpolation function that combines the volumetric free energies of the coexisting phases, f_m, into a single expression using weight functions, $h(\phi_m)$; and the second term can be formulated as a multi-well potential ($r = 2$) or as a multi-obstacle potential ($r = 1$), with coefficients, W_{mn}, related to properties of the interface between phases m and n[60,63].

The MPF framework enables the thermodynamically correct analysis of systems with multiple FE phases considering the volumetric free energy density of each phase. Particularly, it allows the description of systems with two FE phases separated by a single PPB, or systems with a third intervening FE phase and two PPBs (*e.g.,* $BaTiO_3$ and $KNbO_3$). Hence, the proposed approach can be used to elucidate current debate regarding the structural nature of FE systems in the vicinity of interferroelectric phase boundaries and validate competing theories.

2.3 Model for systems with a single polymorphic phase boundary

For a strain-free, two-phase FE system, where a polymorphic phase boundary occurs at $T = T_{PPB}$ for a specific composition, Equation 2.1 reduces to

$$F[\vec{P},\phi;\vec{E},T] = \int_V \left\{ f(\vec{P},\phi;\vec{E},T) + \frac{1}{2}\sum_{k,l=1}^{3}\sum_{i,j=1}^{3} K_{ijkl}\frac{\partial P_k}{\partial x_i}\frac{\partial P_l}{\partial x_j} + \frac{1}{2}\sum_{i,j=1}^{3} K_{ij}\frac{\partial \phi}{\partial x_i}\frac{\partial \phi}{\partial x_j} \right\} dV \tag{2.3}$$

where ϕ is a phase field variable that specifies the region in space where each FE phase is locally stable. The low-temperature phase is set as $\phi = 0$ and the high-temperature phase is set as $\phi = 1$.

The volumetric free energy density of the system is defined as

$$f(\vec{P},\phi;\vec{E},T) = f_0(\vec{P};\vec{E},T)[1-h(\phi)] + f_1(\vec{P};\vec{E},T)h(\phi) + Wg(\phi) \tag{2.4}$$

where $h(\phi) = \phi^3(6\phi^2 - 15\phi + 10)$ is a function that interpolates between the free energy densities of the two phases, f_0 and f_1; $g(\phi) = \phi^2(1-\phi)^2$ is a double-well potential that prevents unphysical phase transitions and its coefficient, W, controls the depth of the double-well potential, see *e.g.,* [76]. The double-well potential acts as an energy barrier for phase transformations, which effectively leads to an increase in the volumetric free energy density associated with phase interfaces.

For each phase, the volumetric free energy density is described by the Helmholtz thermodynamic potential, A, (a Landau-Devonshire potential) with respect to the cubic paraelectric phase, *i.e.,* [1]

$$A(\vec{P};\vec{E},T) = A(\vec{0};\vec{0},T) + \frac{1}{2}\alpha_i P_i^2 + \frac{1}{4}\alpha_{ij}P_i^2P_j^2 + \frac{1}{6}\alpha_{ijk}P_i^2P_j^2P_k^2 - P_iE_i \tag{2.5}$$

where P_i is the i-th polarization component (with $i,j,k = 1,2,3$), and α_i, α_{ij}, and α_{ijk} are the Landau coefficients. The leading coefficient is $\alpha_i = a_{CW}(T - T_{CW})$, where T_{CW} is the Curie-Weiss temperature and $a_{CW} > 0$ [1].

The free energy density is defined herein, without loss of generality, as $f(\vec{P};\vec{E},T) = A(\vec{P};\vec{E},T) - A(\vec{0};\vec{0},T_{CW,1})$, where $A(\vec{0};\vec{0},T_{CW,1})$ is the Helmholtz free energy of the cubic reference state. Thus,

$$f_1(\vec{P};\vec{E},T) = \frac{1}{2}\alpha_{i,1}(T)P_i^2 + \frac{1}{4}\alpha_{ij,1}P_i^2P_j^2 + \frac{1}{6}\alpha_{ijk,1}P_i^2P_j^2P_k^2 - P_iE_i \tag{2.6}$$

$$f_0(\vec{P};\vec{E},T) = \frac{1}{2}\alpha_{i,0}(T)P_i^2 + \frac{1}{4}\alpha_{ij,0}P_i^2P_j^2 + \frac{1}{6}\alpha_{ijk,0}P_i^2P_j^2P_k^2 - P_iE_i + \Delta f_{PPB} \tag{2.7}$$

According to Heitmann and Rossetti[15], the interferroelectric phase transitions are all of first order. Thus, $\Delta f_{PPB} = A_1(\vec{P}_{s1};\vec{0},T_{PPB}) - A_0(\vec{P}_{s0};\vec{0},T_{PPB})$, where $\vec{P}_{s1}$ is the spontaneous polarization of the high-temperature phase and $\vec{P}_{s0}$ is the spontaneous polarization of the low-temperature phase at the polymorphic phase boundary temperature.

The proposed model is reference frame invariant and can be readily extended to describe polycrystalline systems, see *e.g.,* [47]. The model can also be adapted to include strain effects, see *e.g.,* [49]; and charged defects, see *e.g.,* [69].

2.4 Thermodynamic predictions: phase coexistence and stability in PPB ferroelectrics

The MPF model naturally captures the structural FE-FE phase transformation energetics, polarization energetics, and polarization-structural phase transformation interactions. Further, the coexistence and stability of phases near the PPB depend on the order of the two P-FE transitions, which are independently described by the free energy density of the individual FE phases with their own Landau coefficients.

Figure 2.1 depicts the field-free phase coexistence and stability analysis for a FE system with a single PPB as a function of the two P-FE phase transitions. Since each P-FE transition is either of first or second order[15], four possible combinations are shown with the respective characteristic temperatures, identified as cases (a), (b), (c) and (d). The thermodynamic conditions for phase coexistence and stability are given by the characteristic temperatures. Accordingly, regions of stability (black arrow), metastability (grey arrow), or instability can be easily identified for each phase. Corresponding free energy curves are sketched for select temperatures to further illustrate phase stability. Variants of these four main scenarios are also shown in Figure 2.1 depending on the relative values of the characteristic temperatures. For all cases, the cubic (C) paraelectric phase is stable at $T > T_{C,1}$, the high-temperature FE phase ($\phi = 1$) is stable at $T_{PPB} < T < T_{C,1}$, and the low-temperature FE phase ($\phi = 0$) is stable at $T < T_{PPB}$. In the vicinity of a triple point, the three phases are expected to be in thermodynamic equilibrium at $T_{C,0} \sim T_{C,1} \sim T_{PPB}$.

Figure 2.1 predicts a thermal upper limit for the metastable coexistence of the two FE phases. Its extent is a function of the underlying Landau coefficients. In most cases, the predicted upper limit for ferroelectric coexistence is controlled by the low-temperature FE phase depending on the maximum temperature at which it is metastable. For a second order P-FE transition, the coexistence limit is $T = T_{C,0}$, the maximum temperature at which the low-temperature FE phase is stable as there is no metastability for these systems, Figure 2.1(a) and (b). For a first order P-FE transition, the maximum coexistence temperature is generally $T = T_{max,0}$ given that $T_{max,0} < T_{C,1}$, Figure 2.1(c) and (d).

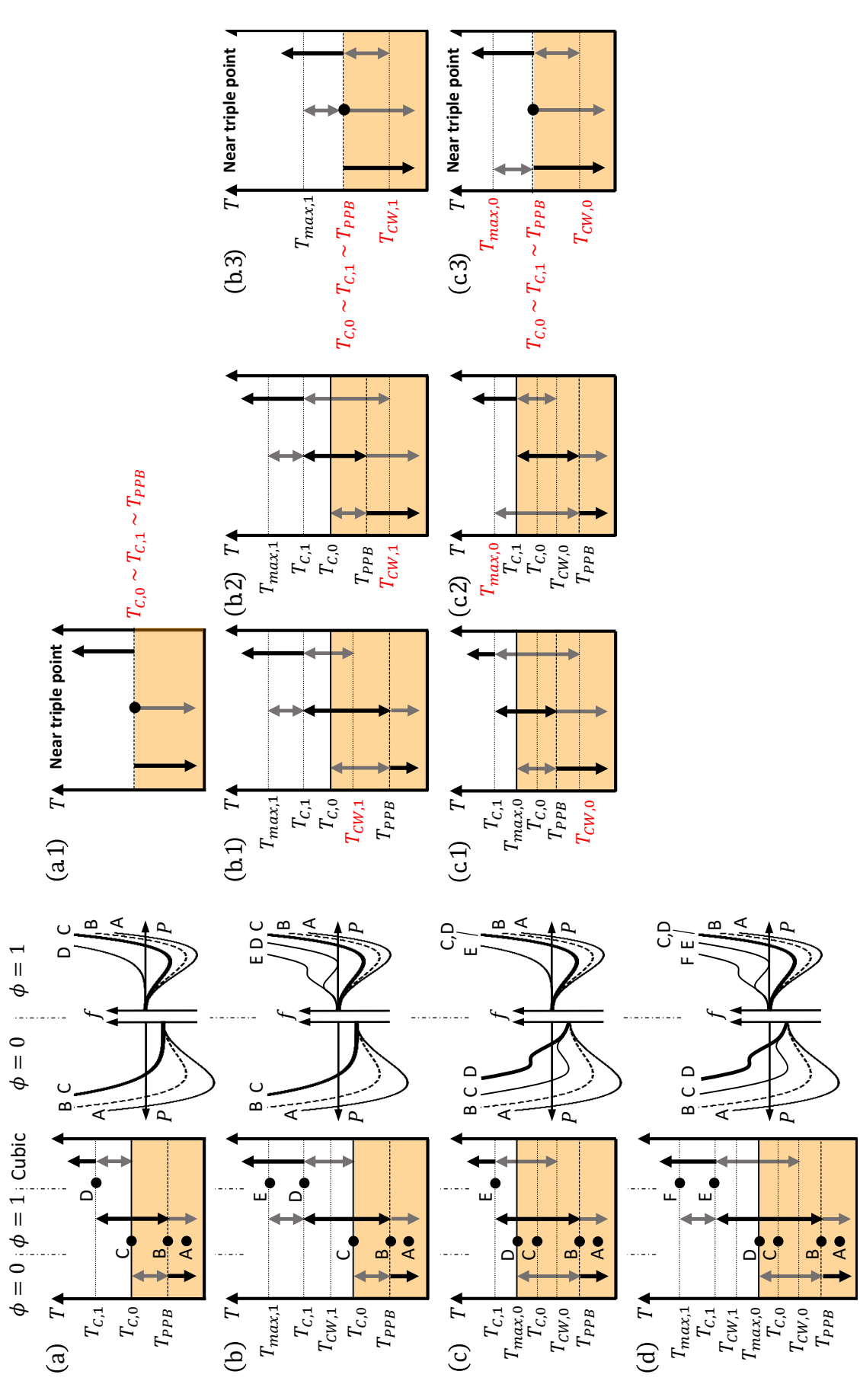

Figure 2.1: Field-free phase coexistence and stability analysis as a function of P-FE phase transition. Two FE phases are shown: a low-temperature FE phase ($\phi = 0$) and a high-temperature FE phase ($\phi = 1$). Subfigures show (a) second order–second order, (b) second order–first order, (c) first order–second order, and (d) first order–first order interactions. Black arrows indicate regions where a particular phase is stable and grey arrows indicate regions where the phase is metastable. Highlighted area indicates metastable coexistence of the FE phases accessible upon heating or cooling. Free energy curves are sketched on the right for selected temperatures. Additional possible scenarios are illustrated depending on the relative values of the characteristic temperatures. T_C and T_{CW} correspond to the Curie and Curie-Weiss temperatures, respectively. Changes with respect to the base case(s) are highlighted in red.

The model also predicts the possibility of metastable coexistence of the FE and C phases, which enables polarization switching mechanisms that have been associated with the enhancement of electromechanical properties[18,22]. When both FE phases display a second order P-FE transition, the paraelectric phase is always unstable within the PPB region where the FE phases coexist, Figure 2.1(a). However, if the high-temperature FE phase exhibits a first order P-FE transition, the paraelectric phase will be metastable for temperatures as low as $T = T_{CW,1}$, allowing the possibility of metastable coexistence of the FE and C phases, Figure 2.1(b). Similarly, if the low-temperature FE phase exhibits a first order P-FE transition, the paraelectric phase will be metastable for temperatures as low as $T = T_{CW,0}$ and coexistence of all phases is possible, Figure 2.1(c).

For the barium zirconate titanate-barium calcium titanate (BZT-BCT) system, coexistence of the rhombohedral (R) and tetragonal (T) ferroelectric phases and the C paraelectric phase has been experimentally reported near its tricritical point[77]. Similarly, paraelectric-ferroelectric phase coexistence has been observed in transmission electron microscopy (TEM) studies near the Curie temperature of $BaTiO_3$[78], see *e.g.,* Figure 2.2. Damjanovic *et al.*[18,22] have argued that the P-FE phase coexistence observed in these chemistries (and others similar) enables a polarization extension mechanism along the paraelectric-ferroelectric path of the energy profile that, together with polarization rotation (FE-FE), lead to their enhanced electromechanical properties.

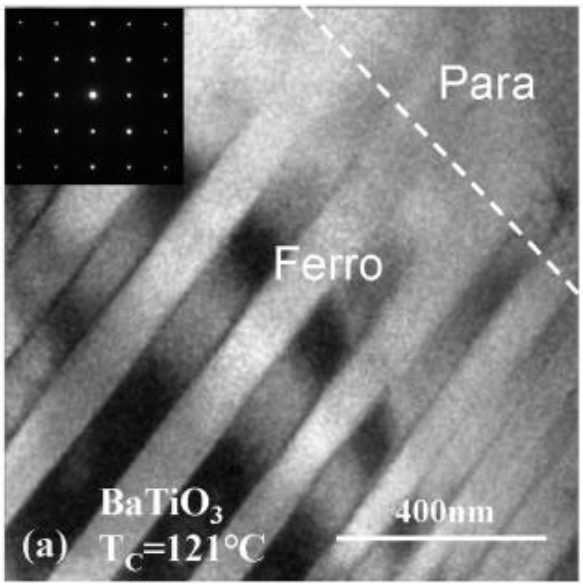

Figure 2.2: TEM image of paraelectric + ferroelectric phase coexistence observed in $BaTiO_3$ near its Curie temperature, as reported by Gao *et al.*[78].

Chapter 3

Application to coarse-grained BZT-40BCT polycrystal in 1-D

The content of this chapter has been published as: Oscar A. Torres-Matheus, R. Edwin García and Catherine M. Bishop. Phase coexistence near the polymorphic phase boundary. *Acta Materialia*, 164: 577-585, 2019, DOI: 10.1016/j.actamat.2018.10.041, and adapted here for non-commercial use only.

3.1 Introduction

As explained in Sections 1.1.2 and 1.1.3, lead toxicity has motivated the search for lead-free ferroelectrics to replace lead zirconate titanate (PZT), which exhibits optimal properties near its inter-ferroelectric transition. One promising lead-free candidate is $(1-x)Ba(Zr_{0.2}Ti_{0.8})O_3$-$x(Ba_{0.7}Ca_{0.3})TiO_3$ or BZT-x BCT, which features a PPB between the tetragonal (T) and rhombohedral (R) phases[24], Figure 3.1. Recently, the existence of an intervening orthorhombic (O) phase has been speculated via high-resolution X-ray diffraction (XRD) and Rietveld refinement[25,79], Raman spectroscopy[80], and elastic, dielectric and piezoelectric measurements[81,82]. However, other works have reported instead a region of R + T phase coexistence using similar experimental techniques, such as temperature-dependent dielectric permittivity, Raman and XRD measurements[77,83,84], micro-Raman scattering[85], convergent beam electron diffraction (CBED)[86], and high-resolution XRD and Rietveld analysis[87]. Moreover, Gao *et al.*[17] have argued that the presence of the orthorhombic phase is inconclusive due to the narrow region of phase space in which the purported O phase appears and the negligible difference in lattice parameter of the surrounding R and T phases. The splitting of XRD reflections (or intensity peaks) associated with the structural change to an orthorhombic phase coincides with the peak splitting expected due to R + T phase coexistence. This superposition of the two diffractograms has led to contradictory interpretations of XRD results[86].

The identification of three FE phases (R, O and T) would imply the existence of two PPBs in the system as opposed to one, see Figure 3.1. It should be noted that at fixed composition, temperature and pressure the classic Gibbs phase rule states that the maximum number of phases in coexistence is three. The existence of an additional O phase would produce forbidden R + O + T + C coexistence at the intersection of the two PPBs. Hence, the revised BZT-x BCT pseudo-binary phase

diagram, presented by Keeble *et al.*[25], refers to this particular intersection as a phase convergence region. Nevertheless, the presence of any one PPB is the origin of enhanced material properties[17], commonly associated with free energy flattening and low polarization anisotropy[15,20,72]. The latter results in minimal domain wall energy that causes miniaturization of the domain structure near the interferroelectric phase boundaries[88], and facilitates polarization rotation/extension[22].

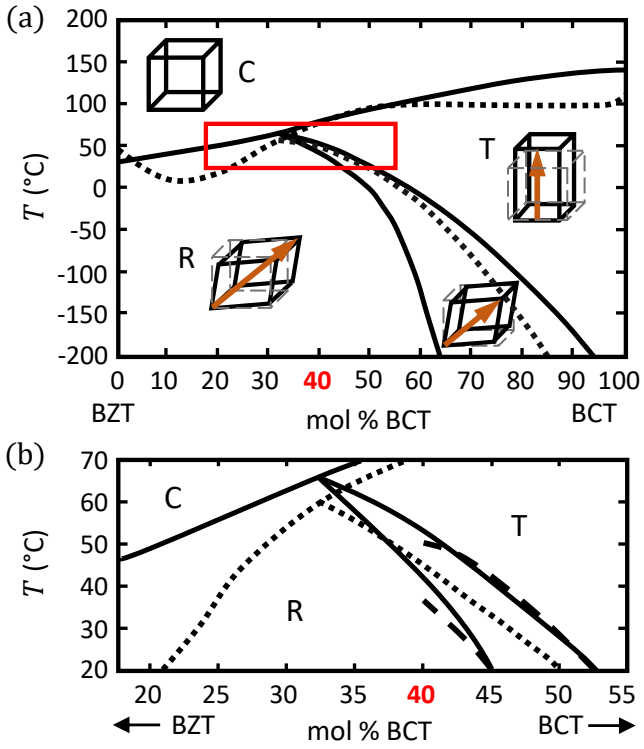

Figure 3.1: (a) BZT-x BCT pseudo-binary phase diagram, and (b) region of interest. Dotted lines correspond to single PPB between R and T phases, as reported by Liu and Ren[24]. Continuous lines indicate a purported O phase between the R and T phases (or the region of R + T coexistence), as reported by Keeble *et al.*[25]. Dashed lines are detailed phase boundaries depicted in region of interest, according to Ehmke[89].

In the previous chapter, a novel MPF framework was proposed and applied to the particular case of FE systems with a single PPB. In this chapter, the model is applied to the lead-free BZT-40 BCT system assuming a phase diagram with a single PPB between the T and R phases. A one-dimensional study is performed to demonstrate the mechanisms controlling the stabilization of the apparent O phase near the T-R phase boundary, and to elucidate the driving forces that determine their long-term dynamics.

3.2 Model formulation

The following formulation is based on the framework established in Section 2.3. For the BZT-x BCT system, the high-temperature FE phase ($\phi = 1$) has a tetragonal crystal structure and the low-temperature FE phase ($\phi = 0$) has a rhombohedral crystal structure. Hence, subscripts 'T' and 'R' are used hereafter to denote each phase.

For a system that undergoes polarization switching events along one direction, say $\hat{\imath}$, with an electric field applied along the same direction, we define $\vec{P} = P\hat{\imath}$ and $\vec{E} = E\hat{\imath} = -\partial V_E/\partial x$, where V_E is the electrostatic potential[90]. The volumetric free energy density of each FE phase, given by Equations 2.6 and 2.7, transform into

$$f_T(P;E,T) = \frac{1}{2}\alpha_{1,T}(T)P^2 + \frac{1}{4}\alpha_{11,T}P^4 + \frac{1}{6}\alpha_{111,T}P^6 - PE \tag{3.1}$$

$$f_R(P;E,T) = \frac{1}{2}\alpha_{1,R}(T)P^2 + \frac{1}{4}\alpha_{11,R}P^4 + \frac{1}{6}\alpha_{111,R}P^6 - PE + \Delta f_{PPB} \tag{3.2}$$

where α_1, α_{11} and α_{111} are the Landau coefficients, and $\alpha_1 = a_{CW}(T - T_{CW})$. Furthermore, the free energy density due to gradients in polarization and phase field are calculated in this model as

$$\frac{1}{2}\sum_{k,l=1}^{3}\sum_{i,j=1}^{3} K_{ijkl}\frac{\partial P_k}{\partial x_i}\frac{\partial P_l}{\partial x_j} = \frac{1}{2}K_P\left(\frac{\partial P}{\partial x}\right)^2 \tag{3.3}$$

$$\frac{1}{2}\sum_{i,j=1}^{3} K_{ij}\frac{\partial \phi}{\partial x_i}\frac{\partial \phi}{\partial x_j} = \frac{1}{2}K_\phi\left(\frac{\partial \phi}{\partial x}\right)^2 \tag{3.4}$$

where $K_P = K_{1111}$ and $K_\phi = K_{11}$.

The polarization switching dynamics are described by two coupled Allen-Cahn equations,

$$\frac{\partial P}{\partial t} = -M_P\left\{\frac{\partial f_R(P;T)}{\partial P}[1-h(\phi)] + \frac{\partial f_T(P;T)}{\partial P}h(\phi) + \frac{\partial V_E}{\partial x} - K_P\frac{\partial^2 P}{\partial x^2}\right\} \tag{3.5}$$

$$\frac{\partial \phi}{\partial t} = -M_\phi\left\{[f_T(P;T) - f_R(P;T)]\frac{\mathrm{d}h(\phi)}{\mathrm{d}\phi} + W\frac{\mathrm{d}g(\phi)}{\mathrm{d}\phi} - K_\phi\frac{\partial^2 \phi}{\partial x^2}\right\} \tag{3.6}$$

where M_P is the polarization mobility and M_ϕ is the phase mobility. We set $M_P = M_\phi = M(\phi;T) = M_R(T)[1-h(\phi)] + M_T(T)h(\phi)$, with the mobility of each phase given by $M(T) = M_o\exp(-Q/RT)$.

The electrostatic field distribution is given by Coulomb's Equation in its differential form, $\partial D/\partial x = 0$. The electric displacement is related to the total polarization via the constitutive relation $D = \epsilon_o E + P$, where ϵ_o is the vacuum permittivity[90]. Therefore,

$$-\epsilon_o\frac{\partial^2 V_E}{\partial x^2} + \frac{\partial P}{\partial x} = 0 \tag{3.7}$$

The model is normalized using $\hat{x} = x/L$, $\hat{t} = t/\tau$, $u = P/|P_{sT}|$, and $\hat{E} = E/|E_{cT}|$; where L is the size of the bulk sample, P_{sT} is the spontaneous polarization of the T phase, E_{cT} is the coercive field of the T phase, and $\tau = 1/\left(\alpha_{111,T}P_{sT}^4 M_T(T)\right)$. Thus, Equations 3.5 through 3.7 are cast in dimensionless form as

$$\frac{1}{\mu}\frac{\partial u}{\partial \hat{t}} = \gamma\hat{\nabla}^2 u - \left\{\frac{\partial \hat{f}_R(u;T)}{\partial u}[1-h(\phi)] + \frac{\partial \hat{f}_T(u;T)}{\partial u}h(\phi) + \hat{E}_{cT}\frac{\partial \hat{V}_E}{\partial \hat{x}}\right\} \tag{3.8}$$

$$\frac{1}{\nu}\frac{\partial \phi}{\partial \hat{t}} = \gamma\lambda\hat{\nabla}^2\phi - \left\{[\hat{f}_T(u;T) - \hat{f}_R(u;T)]\frac{\mathrm{d}h(\phi)}{\mathrm{d}\phi} + \hat{W}\frac{\mathrm{d}g(\phi)}{\mathrm{d}\phi}\right\} \tag{3.9}$$

$$0 = -\hat{\epsilon}_o \frac{\partial^2 \hat{V}_E}{\partial \hat{x}^2} + \frac{\partial u}{\partial \hat{x}} \tag{3.10}$$

where the following dimensionless parameters are identified: $\mu = M(\phi;T)/M_T(T)$, $\nu = P_{sT}^2 \mu$, $\gamma = K_P/(L^2 \alpha_{111,T} P_{sT}^4)$, $\lambda = K_\phi/(K_P P_{sT}^2)$, $\hat{W} = W/(\alpha_{111,T} P_{sT}^6)$, $\hat{E}_{cT} = \left|E_{cT}/(\alpha_{111,T} P_{sT}^5)\right|$, and $\hat{\epsilon}_o = \epsilon_o \left|E_{cT}/P_{sT}\right|$.

Further, $\hat{f}_T(u;T)$ and $\hat{f}_R(u;T)$ are given by

$$\hat{f}_T(u;T) = \frac{1}{6}u^6 + \frac{B_T - 1}{4}u^4 - \frac{B_T}{2}u^2 \tag{3.11}$$

$$\hat{f}_R(u;T) = \rho\left[\frac{1}{6}u^6 + \frac{B_R - \eta^2}{4}u^4 - \frac{B_R \eta^2}{2}u^2\right] + \Delta\hat{f}_{PPB} \tag{3.12}$$

where $B_T = 1 + \alpha_{11,T}/(\alpha_{111,T} P_{sT}^2)$, $B_R = \eta^2 + \alpha_{11,R}/(\alpha_{111,R} P_{sT}^2)$, $\eta = P_{sR}/|P_{sT}|$, $\rho = \alpha_{111,R}/\alpha_{111,T}$, and $\Delta\hat{f}_{PPB} = \Delta f_{PPB}/(\alpha_{111,T} P_{sT}^6)$. In this model, the order of the P-FE phase transitions depend on the values of B_T, B_R and η.

The spontaneous polarization and coercive field of the T phase, required to determine the dimensionless parameters of the model, are calculated as

$$P_{sT} = \pm\left[\frac{-\alpha_{11,T} + \sqrt{\alpha_{11,T}^2 - 4\alpha_{1,T}\alpha_{111,T}}}{2\alpha_{111,T}}\right]^{1/2} \tag{3.13}$$

$$E_{cT} = \left.\frac{\partial f_T(P;T)}{\partial P}\right|_{P=P_{cT}} = \alpha_{1,T} P_{cT} + \alpha_{11,T} P_{cT}^3 + \alpha_{111,T} P_{cT}^5 \tag{3.14}$$

where P_{cT} is the polarization at the coercive field and is obtained from $\partial^2 f_T(P;T)/\partial P^2\big|_{P=P_{cT}} = 0$.

The formulation developed herein can be readily extended to 2-D, see Chapter 4. It can also include the effects of mechanical compatibility from the individual ferroelectric variants and interfaces between coexisting phases, see *e.g.,* [49,70].

3.3 Model parameters

In contrast to traditional phase field models, the proposed MPF model requires a set of Landau coefficients and mobility data for each FE phase. In this study, the BZT-40 BCT composition is selected based on the availability of experimental data in the unambiguously T and R regions of the phase diagram to estimate the Landau coefficients and domain mobilities in each phase. All the parameters estimated for this model are summarized in Table 3.1.

The PPB temperature is estimated for this model as $T_{PPB} \sim (T_{O-T} + T_{R-O})/2 = 43\,^\circ\text{C}$, using $T_{R-O} = 37\,^\circ\text{C}$ and $T_{O-T} = 49\,^\circ\text{C}$, as reported by Ehmke[89]. The estimated T_{PPB} is approximately equal to the value determined by Liu and Ren[24], see Figure 3.1(b). The dimensionless gradient energy coefficients, $\gamma = 3 \times 10^{-5}$ and $\lambda = 5.5$, and the double-well coefficient, $\hat{W} = 4$, are established

Table 3.1: Parameters of the one-dimensional MPF model for coarse-grained BZT-40 BCT polycrystal. Landau coefficients and mobilities are fitted to experimental data reported by Ehmke[89]. Gradient energy coefficients and double-well coefficient are estimated after numerical evaluation at $T = T_{PPB} = 43\,°C$.

Symbol	R phase ($\phi = 0$)	T phase ($\phi = 1$)	Units
a_{CW}	5.000×10^4	2.063×10^4	Jm/C^2K
α_{11}	6.314×10^7	-4.229×10^7	Jm^5/C^4
α_{111}	1.263×10^{10}	3.154×10^{10}	Jm^9/C^6
T_{CW}	49.90	69.08	°C
T_C	$T_{CW,R}$	69.60	°C
T_{max}	$T_{CW,R}$	69.77	°C
M_o	1.809×10^{-4}	3.806×10^{-10}	S/m
Q	8561	−25 260	J/mol
K_P	8.051×10^{-13}		Jm^3/C^2
K_ϕ	2.150×10^{-14}		J/m
W	1.444×10^4		J/m^3
Δf_{PPB}	−632.07		J/m^3

via numerical evaluation such that the widths of the rhombohedral domain walls and the phase interfaces, measured in ϕ, are approximately equal at $T = T_{PPB}$, the only temperature where both phases are stable. In qualitative agreement with Jona and Shirane[91], the width of the rhombohedral domain walls is set to 4 nm, *i.e.,* ten times the characteristic lattice parameter. Thus, the size of the bulk sample is determined as $L = 190$ nm. This is smaller than the typical grain size achieved during standard processing of $27 \pm 3\,\mu$m for BZT-40 BCT[89]. However, for this work, it is sufficiently large to enable multiple domains to be investigated. Finally, values for K_P, K_ϕ and W are back-calculated using the sample size and the expressions for the dimensionless parameters, see Table 3.1.

The interfacial widths (ξ) and energies (σ) are calculated for each type of interface, namely: domain wall (DW) and T-R phase interface. Each interfacial energy is calculated via numerical evaluation by $\sigma = \int_0^L [f_{total}(x) - f_{min}]\, dx$ across a computational domain with a single interface, where f_{total} is the total free energy density and f_{min} is the volumetric free energy density corresponding to the stable polarization state(s). The interfacial width of DWs is determined from the slope of the polarization profile across the interface between stable FE domains, $\partial P(x)/\partial x = P'(x)$. Specifically, the width is defined by the intersection of the slope in the middle of the interface ($x = x_\circ$) and the spontaneous polarization (P_s), as $\xi = |2P_s/P'(x_\circ)|$[27,92]. Figure 3.2 illustrates the calculation methods described above using the profiles of polarization and free energies across a single DW (rhombohedral or tetragonal) at a given temperature of interest.

Similarly, the width of T-R phase interfaces is calculated at $T = T_{PPB}$, where both FE phases are stable. For these interfaces, ξ can be estimated using the polarization profile as $\xi = |(P_{sT} - P_{sR})/P'(x_\circ)|$, or using the phase-field profile as $\xi = 1/|\phi'(x_\circ)|$. Values for the interfacial widths (measured in P) and energies are summarized in Table 3.2.

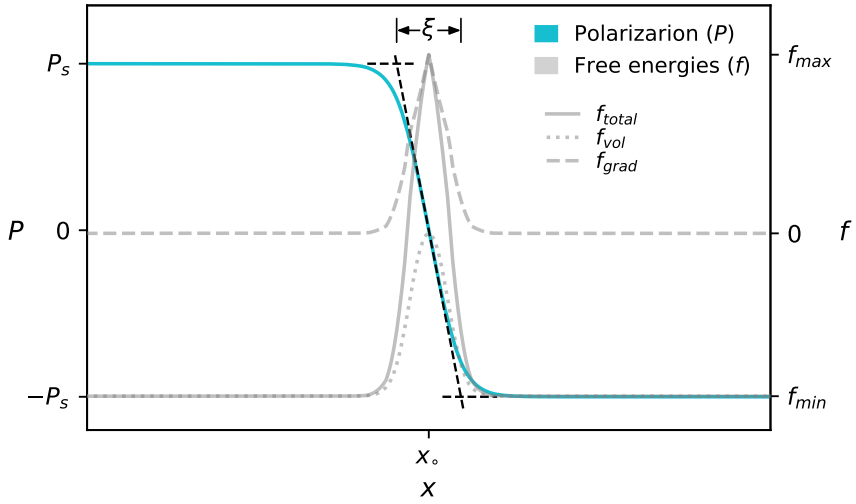

Figure 3.2: Profiles of polarization and free energies across a single, one-dimensional domain wall. The interfacial width calculation method is illustrated, where P_s represents the spontaneous polarization of the T or R phase. The method is valid for domain walls at any temperature of interest. The interfacial energy is calculated as $\sigma = \int_0^L [f_{total}(x) - f_{min}]\, dx$ using the free energy profiles, where f_{vol} is the volumetric free energy density and f_{grad} is the contribution due to gradients in polarization.

Table 3.2: Interfacial widths and energies for the one-dimensional, coarse-grained BZT-40 BCT system calculated at $T = T_{PPB} = 43\,°C$. The interfacial widths are estimated using the polarization profile for all cases to ensure consistency. ξ_{T-R} and σ_{T-R} correspond to phase interfaces between rhombohedral and tetragonal domains with the same polarization orientation.

Symbol	R phase ($\phi = 0$)	T phase ($\phi = 1$)	Units
ξ_{DW}	4.000	2.867	nm
ξ_{T-R}	2.834		nm
σ_{DW}	1.876×10^{-6}	4.063×10^{-6}	J/m^2
σ_{T-R}	4.445×10^{-6}		J/m^2

3.3.1 Microstructurally averaged Landau coefficients

The values for the two sets of Landau coefficients shown in Table 3.1 are determined from experimental hysteresis loops for polycrystalline BZT-40 BCT samples, measured at selected temperatures by Ehmke[89]. A coarse-grained approach is adopted for this model following Zhao, Cao and García[93]. In general, this approach proposes a simplified representation of a system that allows modelling its behaviour without resolving the fine details. Hence, the Landau coefficients obtained here represent microstructurally averaged parameters used to define macroscopic Helmholtz free energy densities. This allows the characterization of the general FE behaviour of polycrystalline ceramics in each region of phase space without resolving fine details, such as grain boundaries and strain effects. Even though the coarse-grained model does not capture the effects of anisotropy in FE materials, it enables detailed analysis of the FE phase coexistence, such as transformation kinetics of coexisting phases and the energetics associated with the FE-FE phase transformation, polarization switching and

polarization-phase transformation interactions. Figure 3.3 shows a detailed flow chart of the fitting procedure used in this study. The procedure described herein can be readily applied to estimate the single-crystal Landau parameters using experimental data measured in single-crystal samples.

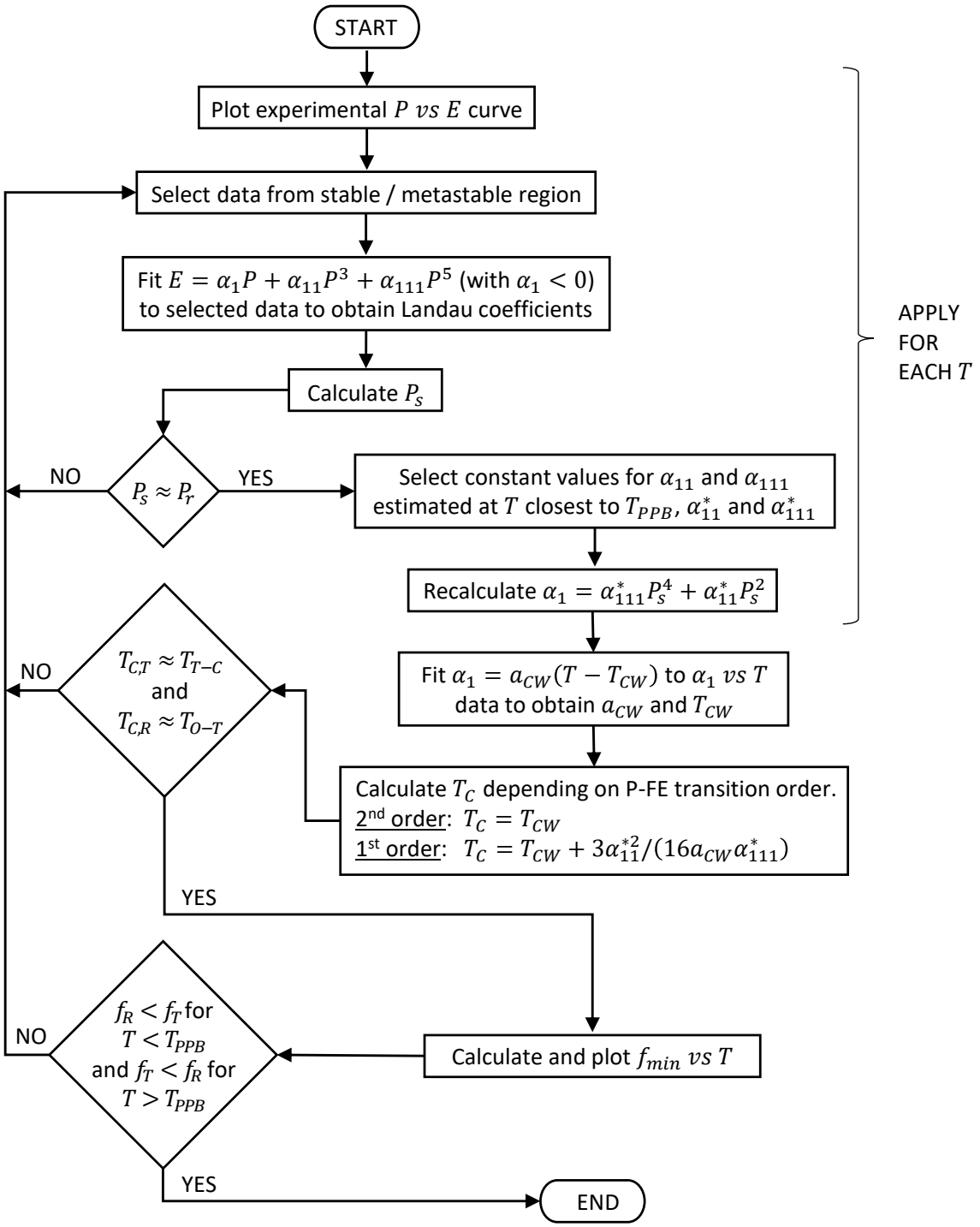

Figure 3.3: Flow chart describing the fitting procedure to estimate the Landau coefficients for one-dimensional, coarse-grained BZT-40 BCT polycrystal. The orthorhombic-tetragonal and tetragonal-cubic transition temperatures used in this procedure are $T_{O-T} = 49\,^{\circ}\text{C}$ and $T_{T-C} = 70\,^{\circ}\text{C}$, as reported by Ehmke[89].

For each FE phase, the Landau coefficients are estimated by fitting the equation $\partial f/\partial P = E = \alpha_1 P + \alpha_{11} P^3 + \alpha_{111} P^5$ to stable and metastable parts of the P vs E curve at different temperatures using

non-linear least squares. In agreement with ferroelectric theory[1], the coefficient α_1 is restricted to negative values.

For the R phase, the spontaneous polarization (P_{sR}) is calculated at each temperature using the fitted $\alpha_{1,R}$, $\alpha_{11,R}$ and $\alpha_{111,R}$ parameters. Since the thermodynamic behaviour of the P *vs* E curve was fitted to experimental hysteresis measurements, the measured remnant polarization (P_{rR}) essentially represents a measured spontaneous polarization. Hence, the calculated P_{sR} can be compared with the measured P_{rR}. In this model, only the leading coefficient is allowed to change with temperature according to the Curie-Weiss equation, $\alpha_{1,R} = a_{CW,R}(T - T_{CW,R})$, where $T_{CW,R}$ is the Curie-Weiss temperature and $a_{CW,R} > 0$. Thus, $\alpha_{11,R}$ and $\alpha_{111,R}$ are considered constant and set equal to the values obtained at the temperature closest to T_{PPB}, $\alpha^*_{11,R}$ and $\alpha^*_{111,R}$. The coefficient $\alpha_{1,R}$ is recalculated at each temperature using the corresponding P_{sR} value and $\alpha^*_{11,R}$ and $\alpha^*_{111,R}$, *i.e.*, $\alpha_{1,R} = -\alpha^*_{111,R}P^4_{sR} - \alpha^*_{11,R}P^2_{sR}$. Finally, the Curie-Weiss equation is re-fitted to the $\alpha_{1,R}$ *vs* T data to obtain $T_{CW,R}$ and $a_{CW,R}$. The same procedure is repeated for the T phase, see Figure 3.4.

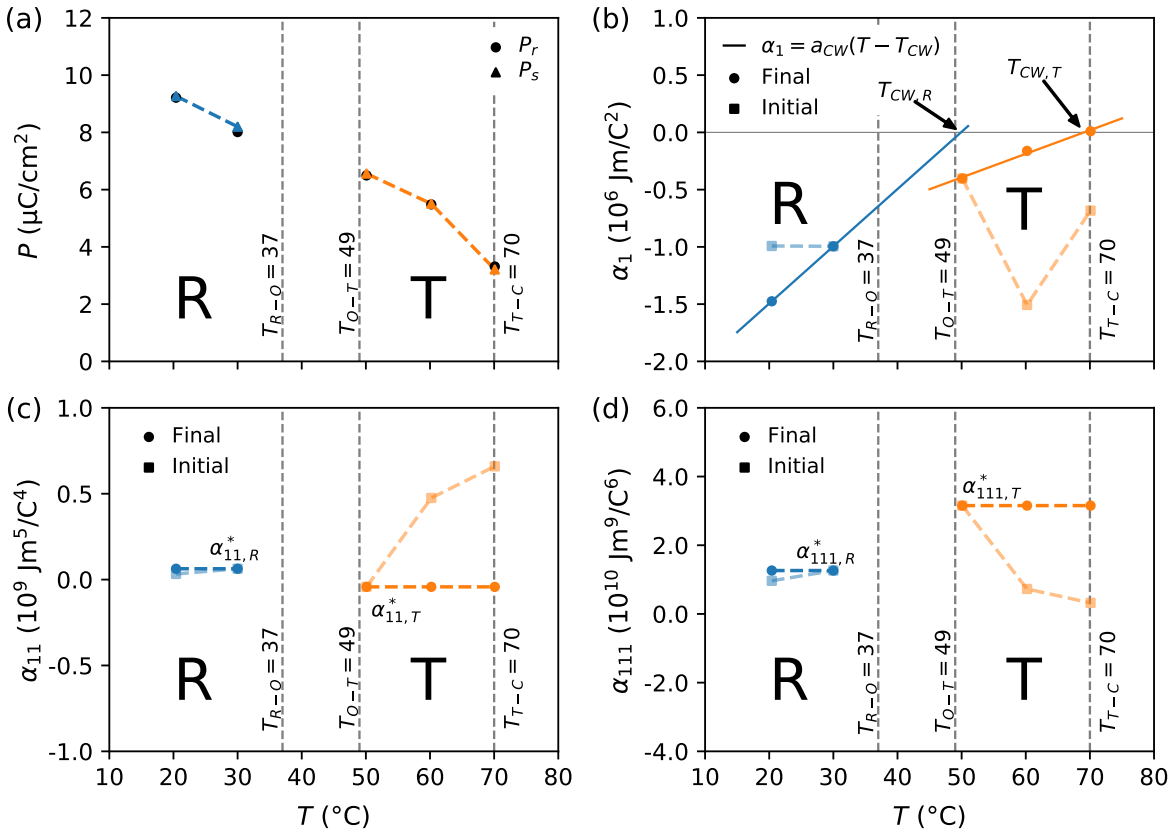

Figure 3.4: Temperature dependence of (a) calculated spontaneous polarization (P_s), and fitted (b) α_1, (c) α_{11} and (d) α_{111} for the R (—) and T (—) phases. Remnant polarization (P_r) and the R-O, O-T and T-C transition temperatures are also shown, as measured by Ehmke[89]. Dashed lines are included as a guide for the eye.

The goodness of fit is calculated using root mean square error (RMSE), which measures the difference (residuals) between the values predicted by $E = \alpha_1 P + \alpha_{11}P^3 + \alpha_{111}P^5$ and the experimental hysteresis data. Thus, RMSE can be used to compare how well different models reproduce experimental data. For each temperature, $\text{RMSE}_{initial}$ is calculated with the Landau coefficients obtained from the first fitting of $E = \alpha_1 P + \alpha_{11}P^3 + \alpha_{111}P^5$ to the stable and metastable parts of the E *vs* P

curve; while RMSE_{final} is calculated with the final Landau coefficients obtained after following the entire procedure described above. Table 3.3 shows the calculated RMSE values at each selected temperature, including the corresponding stable FE phase and the number of experimental data points extracted from each hysteresis loop for fitting.

Table 3.3: Summary of RMSE values measured after initial fitting of Landau coefficients ($\mathrm{RMSE}_{initial}$) and with final model parameters (RMSE_{final}). For each selected temperature, the stable FE phase and the number of experimental data points used for fitting (N) are also included.

T (°C)	Stable phase	N	$\mathrm{RMSE}_{initial}$ (MV/m)	RMSE_{final} (MV/m)
20.4	Rhombohedral	26	1.620×10^{-3}	4.876×10^{-2}
30.0	Rhombohedral	29	4.328×10^{-3}	4.328×10^{-3}
50.1	Tetragonal	49	7.665×10^{-3}	7.731×10^{-3}
60.2	Tetragonal	41	4.120×10^{-3}	9.109×10^{-2}
70.1	Tetragonal	46	1.042×10^{-2}	1.621×10^{-1}

Table 3.3 indicates that the final Landau coefficients give a better fit close to $T = T_{PPB} = 43\,°\mathrm{C}$, where the R and T phases coexist. This is evidenced by the small values of $\mathrm{RMSE}_{final} \approx \mathrm{RMSE}_{initial}$ for the R phase at $T = 30.0\,°\mathrm{C}$ and for the T phase at $T = 50.1\,°\mathrm{C}$. For the rhombohedral phase, $\mathrm{RMSE}_{final} = \mathrm{RMSE}_{initial}$ at $T = 30.0\,°\mathrm{C}$ because there are only two available hysteresis loops at low temperatures where the R phase is stable. For temperatures away from the phase coexistence region of interest, $\mathrm{RMSE}_{final} > \mathrm{RMSE}_{initial}$ due to the restriction of temperature invariance of α_{11} and α_{111} for each phase. In the initial fitting, different α_1, α_{11} and α_{111} coefficients are obtained at each temperature and a good fit is expected between predicted and measured values. In the final fitting, $\alpha_{11} = \alpha_{11}^*$, $\alpha_{111} = \alpha_{111}^*$, and the temperature dependence is included in α_1 only (a typical approach), resulting in higher RMSE values for temperatures away from the T_{PPB}. This relatively poor agreement with experimental data is justified in this case because the study focuses only on the detailed analysis of the FE phase coexistence. However, Table 3.3 shows that the final residuals are still reasonably small.

The fitted Landau coefficients are used to calculate the Curie temperature for each FE phase depending on the order of the P-FE transition. For a second order P-FE transition, $T_C = T_{CW}$; whereas for a first order P-FE transition, $T_C = T_{CW} + 3\alpha_{11}^{*2}/(16 a_{CW} \alpha_{111}^*)$. These results are compared with observed transition temperatures in order to verify that the Landau coefficients correctly reproduce the stable phases, see Figure 3.3 for details. Additionally, the value of Δf_{PPB} is computed and the global stability predictions as a function of temperature are verified, Figure 3.5. The minimum volumetric free energy of each FE phase is calculated by substituting the respective spontaneous polarization into Equations 3.1 and 3.2, and setting $E = 0$. Results are plotted against temperature to confirm that the R phase is stable for $T < T_{PPB}$ and the T phase is stable for $T > T_{PPB}$. If the determined volumetric free energy is not suitable, the hysteresis loop data are resampled until appropriate coefficients are obtained.

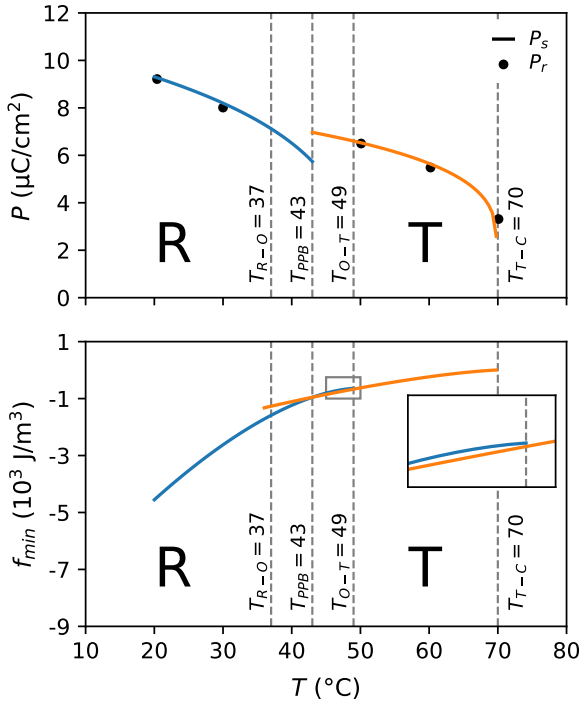

Figure 3.5: Temperature dependence of the spontaneous polarization (P_s) and minimum volumetric free energy density (f_{min}) for the R (—) and T (—) phases. Remnant polarization (P_r) and the R-O, O-T and T-C transition temperatures are also shown, as measured by Ehmke[89]. Inset is a magnified view of the area indicated near the T_{O-T}. For $T > T_{PPB}$, $f_{min,T} < f_{min,R}$, confirming the correct global stability predictions with selected Landau coefficients.

3.3.2 Domain mobility

In accordance with Section 3.2, the mobilities used in this model are defined as an interpolation function, $M_P = M_\phi = M(\phi;T) = M_R(T)[1-h(\phi)] + M_T(T)h(\phi)$, that combines the mobility of each FE phase, M_R and M_T, into a single expression using a weight function, $h(\phi) = \phi^3(6\phi^2 - 15\phi + 10)$. For each phase, the mobility is given by an Arrhenius expression, $M(T) = M_o \exp(-Q/RT)$, where R is the universal gas constant, Q is the activation energy and $M_o > 0$.

To obtain Q and M_o, mobility values are calculated directly from the BZT-40 BCT hysteresis data at selected temperatures using[93]

$$M = 2\pi\omega\chi_c\epsilon_o\sqrt{\left(\frac{E_o}{E_c}\right)^2 - 1} \tag{3.15}$$

where $\omega = 0.1\,\text{Hz}$ is the experimental cycling frequency, $E_o = 1\,\text{MV/m}$ is the maximum applied field during the experiment, χ_c is the electric susceptibility at the experimentally observed coercive field, and $\chi_c\epsilon_o$ corresponds to the slope of the P *vs* E curve at the coercive field. The mobility calculation described above is illustrated in Figure 3.6.

The experimental hysteresis loops are impacted by physical effects such as strain fields, grain boundaries and point defects, among others. Although these effects are not directly included in the model, they are captured by the calculated coarse-grained mobilities. The obtained mobility values

have the same order of magnitude as those reported by Zhao, Cao and García[93] for stress-free, lanthanum-doped PZT, Figure 3.7(a). Further, the model parameters used in this work are validated in Section 3.6.1 by comparing calculated and experimental hysteresis loops at a temperature within the region of phase space in dispute. For each phase, the parameters Q and M_o are estimated by fitting the equation $\ln(M) = \ln(M_o) - (Q/R)(1/T)$ to the calculated $\ln(M)$ *vs* $1/T$ data, see Figure 3.7(b). The final estimated parameters are shown in Table 3.1. The mobility in the T phase has a negative activation energy, likely due to the proximity to the tetragonal-cubic transition. See Appendix A for mobility calculations at different compositions.

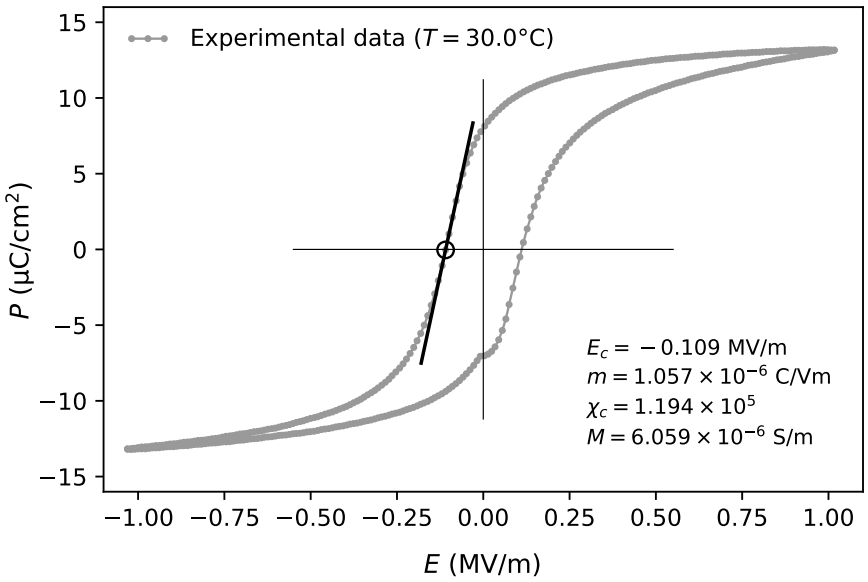

Figure 3.6: Mobility calculation from experimentally observable quantities for the coarse-grained BZT-40 BCT system. The calculation method using Equation 3.15 is demonstrated with data measured by Ehmke[89] at $T = 30.0$ °C with $\omega = 0.1$ Hz and $E_o = 1$ MV/m. The slope, m, corresponds to $\chi_c \epsilon_o$.

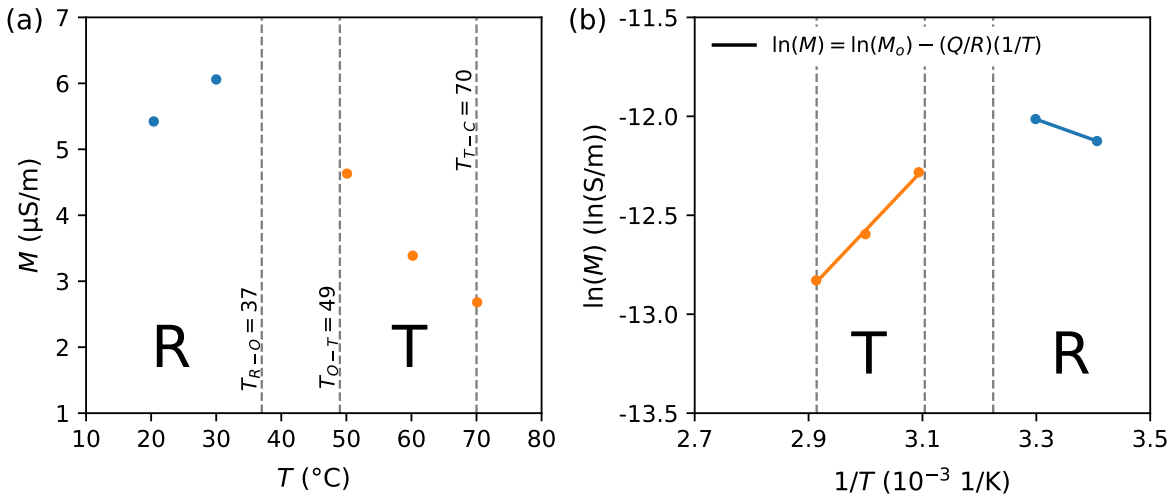

Figure 3.7: Estimated mobilities for the R (—) and T (—) phases of one-dimensional, coarse-grained BZT-40 BCT polycrystal. Subfigures show (a) mobility values extracted from experimental hysteresis data at selected temperatures, and (b) fitting of equation $\ln(M) = \ln(M_o) - (Q/R)(1/T)$ to estimate parameters Q and M_o. The R-O, O-T and T-C transition temperatures are also shown, as measured by Ehmke[89].

3.4 Thermodynamic analysis

According to the Landau coefficients stated in Table 3.1 for BZT-40 BCT, the T phase has a weak first order P-FE transition and the R phase has a second order P-FE transition. This case corresponds to the scenario illustrated in Figure 2.1(a). The Curie temperature for the high-temperature T phase is $T_{C,T} = 69.60\,°C$, which agrees well with the experimentally observed tetragonal-cubic transition temperature, $T_{T-C} \sim 70\,°C$, as reported by Ehmke[89]. Furthermore, the predicted upper limit for metastable coexistence between the R and T phases is $T_{C,R} = 49.90\,°C$, which is approximately equal to $T_{O-T} \sim 49\,°C$, as determined by Ehmke[89], see Figure 3.1(b). This supports the hypothesis of R + T phase coexistence near the PPB, based on data acquired in the unambiguously single phase regions. Notably, the MPF model indicates that there is no thermodynamic lower limit for metastable coexistence of the FE phases.

Figure 3.8 shows contour plots of the volumetric free energy density of the system at different temperatures and normalized polarization states. In all cases by definition, $u = \pm 1$ is the dimensionless spontaneous polarization of the T phase and $u = \pm\eta$ is the dimensionless spontaneous polarization of the R phase at each temperature. For $\hat{E} = 0$, the global minima in the bulk free energy of the system are located at $u = \pm 1$, $\phi = 1$, for $T > T_{PPB}$; and at $u = \pm\eta$, $\phi = 0$, for $T < T_{PPB}$. Results show that direct R↔T transformation between domains with opposing polarization states is inaccessible because of the large energy barrier between antiparallel polarization states. Hence, the MPF model only predicts the formation of phase interfaces separating tetragonal and rhombohedral domains with the same polarization orientation in the one-dimensional system, see Table 3.2.

For $T < T_{PPB}$, the T phase is metastable, see Figure 3.8(a). Thus, both T and R phases coexist through formation of domains of opposite polarization and a weak intervening built-in electric field. Energy barriers for polarization switching are different in each phase; for example, at $T = 39\,°C$ the energy barrier between $u = \pm 1$ in the T phase, $\Delta\hat{f}_T$, is 1.6 times larger than the energy barrier between $u = \pm\eta$ in the R phase, $\Delta\hat{f}_R$. Consequently, the MPF model naturally predicts two possible mechanisms for switching between rhombohedral domains, namely: a) via direct 180° polarization reversals; or b) by performing a R→T transformation (rotation), followed by a 180° reversal while in the tetragonal phase, and finally by transforming back to the rhombohedral phase (rotation), *i.e.,* T→R. The second mechanism favours rotation of the polarization order parameter, but requires the thermal energy of the system to be greater than both $\Delta\hat{f}_T$ and the R→T energy of transformation in order to be accessible.

For $T = T_{PPB}$, four thermodynamic equilibrium states are available, see Figure 3.8(b). The existence of additional polarization states results in a decrease in polarization anisotropy. At the PPB, the domain switching mechanisms described for the R phase at $T < T_{PPB}$ are possible for both phases, *i.e.,* direct 180° polarization reversal or phase transformations plus 180° reversal (polarization rotation mechanism). As temperature increases, the energy barrier in the R phase decreases such that $\Delta\hat{f}_R \approx \Delta\hat{f}_T/3$, favouring the formation of rhombohedral domain walls via the direct 180° reversal mechanism. Since $\Delta\hat{f}_T$ and the T→R energy of transformation are equivalent, the likelihood of observing tetragonal domain walls and T→R transformations is equal. Further, while the polarization

rotation mechanism can occur in both phases, the decrease in $\Delta\hat{f}_R$ favours this mechanism in the T phase.

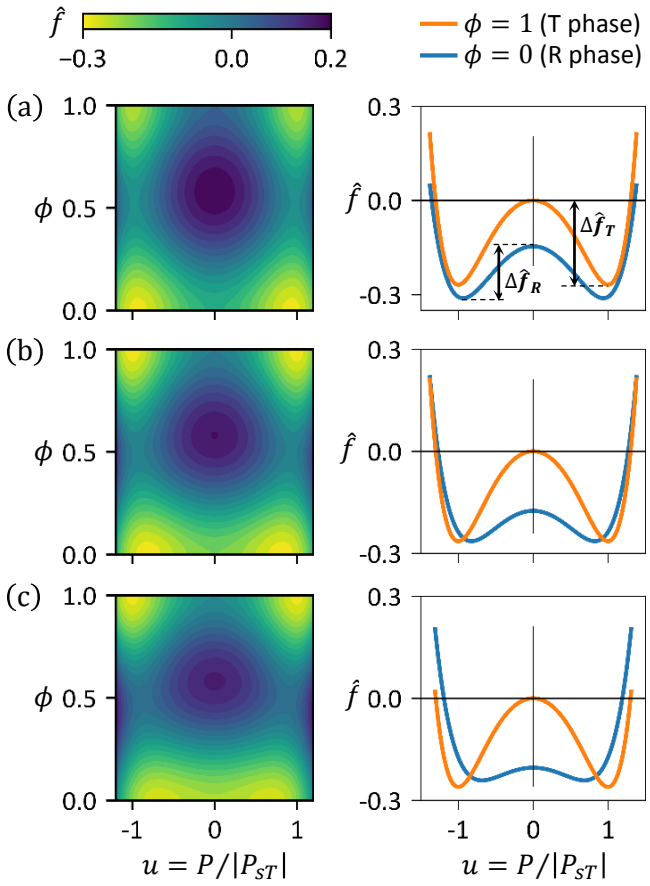

Figure 3.8: Left column: contour plots of the volumetric free energy density, $\hat{f}(u, \phi; \hat{E} = 0, T) = f/(\alpha_{111,T} P_{sT}^6)$. Right column: line plots of the R (—) and T (—) free energy densities. Subfigures correspond to (a) $T = 39\,°C$, (b) $T = T_{PPB} = 43\,°C$, and (c) $T = 46\,°C$. In the absence of an applied electric field, both FE phases are equally stable at $T = T_{PPB}$, but metastably persist for a finite range of temperatures away from the PPB line on the phase diagram.

For $T > T_{PPB}$, the R phase becomes metastable, Figure 3.8(c), and the energy barrier of the R phase further decreases such that $\Delta\hat{f}_R \approx \Delta\hat{f}_T/7$ at $T = 46\,°C$. Here, the additional thermal energy and the low energy barrier will enable the polarization switching plus rotation mechanism proposed herein, allowing the R phase to persist for very long periods of time.

3.5 Simulation cases and numerical implementation

The MPF model was implemented using the finite element method (FEM) in COMSOL Multiphysics® [94]. A 200-element mesh with second-order Lagrange shape functions was used. Simulations took on the order of 25 seconds on an i7-6700 3.4 GHz Quad Core 64 bit processor, with 16 GB of RAM and a Microsoft Windows 7 Enterprise operating system version 6.1.7601.

Hysteretic cycling of BZT-40 BCT was simulated at $T = 40.2\,°C$ to validate the model. Equations 3.8 through 3.10 were solved with a mixed 50%R+50%T initial state. A time-dependent electric

field was applied through the boundary conditions $\hat{V}_E(0,\hat{t}) = 0$ and $\hat{V}_E(1,\hat{t}) = \hat{V}_{E,max}\sin(2\pi\hat{\omega}\hat{t})$, where $\hat{V}_{E,max} = -E_o/|E_{cT}|$ and $\hat{\omega} = \omega\tau$. Zero flux boundary conditions were applied for polarization and for phase field.

The field-free microstructural evolution was simulated at $T = T_{PPB}$ to investigate the phase coexistence of FE phases. Equations 3.8 and 3.9 were solved with initial conditions generated from a uniform random distribution, with $\{\text{mean}, \text{range}\}$, for u $\{0, 2\}$ and ϕ $\{0.5, 1\}$. Periodic boundary conditions were applied for both variables (polarization and phase field).

A time-temperature-transformation (TTT) diagram was constructed for the microstructural evolution of the two-phase ferroelectric towards a stable single phase. The fraction transformed of FE phases was measured by ψ, where $\psi = \overline{\phi}$ at $T > T_{PPB}$, and $\psi = 1 - \overline{\phi}$ at $T < T_{PPB}$. Average transformation times for constant fraction transformed were calculated from fifteen simulations at selected temperatures.

3.6 Results and analysis

3.6.1 Hysteresis loops (model validation)

The model was directly compared against experimental hysteresis data measured from a polycrystalline sample at $T = 40.2\,^{\circ}\text{C} < T_{PPB}$ and $\omega = 0.1\,\text{Hz}$, as reported by Ehmke[89], Figure 3.9. Two different initial conditions were used for the simulations. In one case, a mixed 50%R+50%T initial state was considered. For the other case, it was assumed that only the stable R phase ($\phi = 0$) was present at $\hat{t} = 0$. Figure 3.9 shows that calculations from the mixed-phase initial condition give better agreement with the experiments. The latter further supports the hypothesis of R + T coexistence in the vicinity of the PPB.

Figure 3.10(a) also shows very good agreement between experiments and numerical results considering a mixed-phase initial state. Differences near the tails of the hysteresis loops are a result of the slow polarization switching of the last set of domains pinned by grain boundaries in the experimental data, as discussed by Zhao, Bowman and García[70]. These effects are not captured by the model parameters fitted as described in Sections 3.3.1 and 3.3.2, which give better agreement to experimental data towards the region of interest at low fields of the P-E curves. The grain size effects on the properties of BZT-x BCT have been well investigated. For the BZT-50 BCT composition, increasing the grain size from about $1\,\mu$m to approximately $20\,\mu$m improves the electromechanical response significantly, but larger grain sizes produce little variation in functional properties[16]. In this work, a comprehensive dataset of experimentally measured properties was only available for a BZT-40 BCT sample with a grain size of approximately $27\,\mu$m[89]. Hence, after fitting the model parameters to the available experimental data, the model was validated by comparing the calculated hysteretic response to the experimental P-E curve from the same sample. Further, Figure 3.10(b) shows that the application of a cyclic electric field accelerates the R + T→R transformation, measured by the average phase field $\overline{\phi}$, when $\hat{E} \neq 0$. This suggests that built-in fields in polycrystalline ceramics and poling would reduce the likelihood of observing metastable coexistence states at $T < T_{PPB}$.

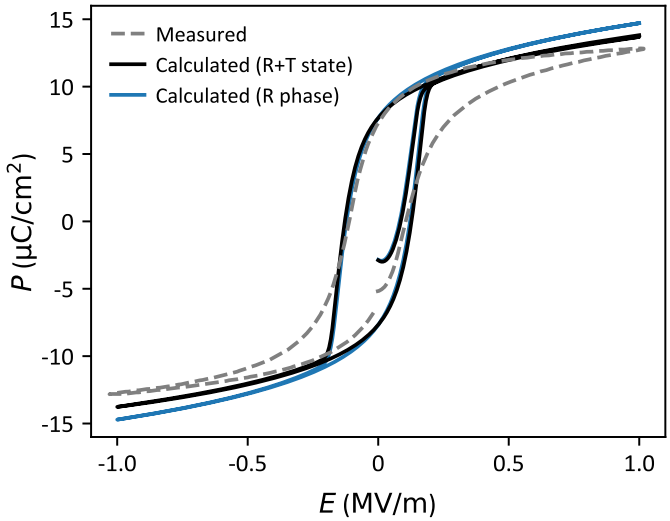

Figure 3.9: Comparison between hysteresis loops measured experimentally[89] (- -) and calculated from single-phase rhombohedral (—) and mixed 50%R+50%T (—) initial conditions for the one-dimensional, coarse-grained BZT-40 BCT system at $T = 40.2\,^{\circ}\mathrm{C}$. Calculations from a mixed-phase initial state give better agreement with experimental data.

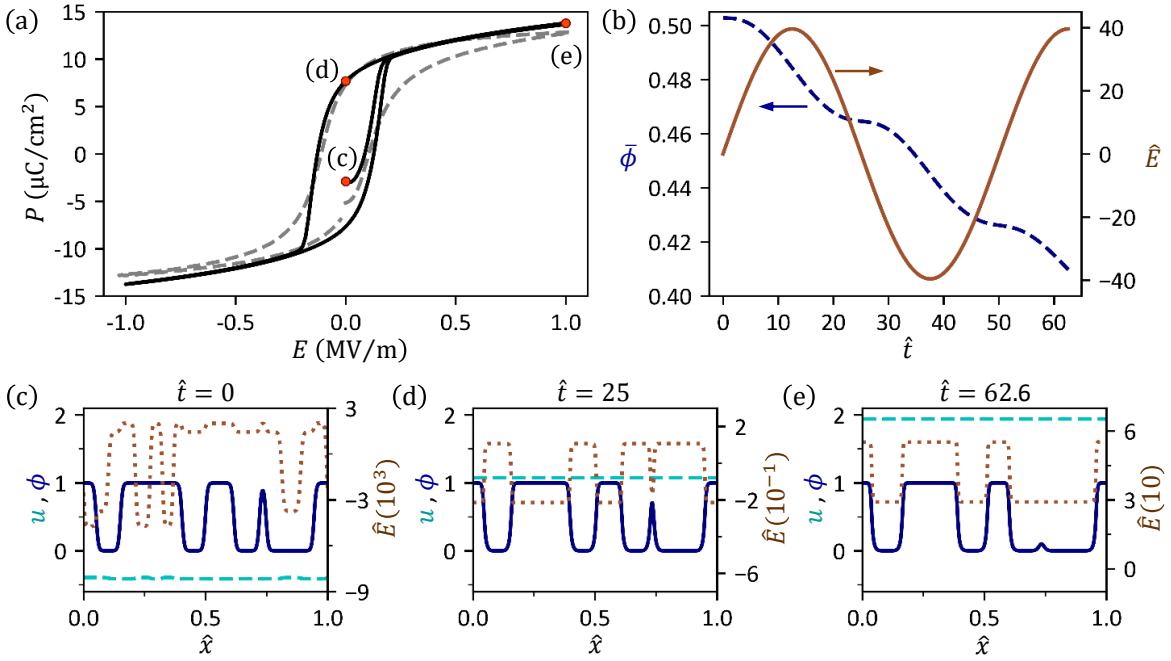

Figure 3.10: (a) Experimental[89] (- -) and calculated (—) hysteresis loops at $T = 40.2\,^{\circ}\mathrm{C}$ with $\omega = 0.1\,\mathrm{Hz}$ and mixed 50%R+50%T initial condition. (b) Effect of sinusoidal electric field (—) on the average phase field, $\overline{\phi}$ (- -). Insets (c) through (e) show the spatial distributions of $u = P/|P_{sT}|$ (- - , left axis), ϕ (—, left axis), and $\hat{E} = E/|E_{cT}|$ (···, right axis) at selected normalized instants $\hat{t} = t/\tau$. Inset (c) shows initial condition ($t = 0$), (d) shows $\hat{t} = 25$ ($t = 5\,\mathrm{s}$), and (e) shows $\hat{t} = 62.6$ ($t = 12.5\,\mathrm{s}$) after one full cycle.

Figure 3.10(c)–(e) illustrate the spatial distribution of polarization, phase field and local electric field over the entire one-dimensional system at different times of the hysteretic cycling. For each case, results reveal that the system adopts an effectively uniform polarization configuration. This unphysical configuration is forced by Coulomb's Equation in the 1-D computational domain, where

$\partial u/\partial \hat{x} \approx 0$ due to $\hat{\epsilon}_o \ll 0$, limiting the microstructural analysis with local electric fields. However, the one-dimensional formulation used herein still allows the calculation of hysteresis loops taking into account local electric fields developed within the material by solving Coulomb's Equation with realistic boundary conditions. The limitation described above is overcome when the model is applied to 2-D and 3-D systems, where the additional degrees of freedom enable access to other polarization directions that lead to realistic domain configurations. The analysis of two-dimensional FE domain structures will be explored in following chapters.

3.6.2 Field-free ferroelectric domain structures

Simulation of the field-free microstructural evolution after quenching shows that rhombohedral and tetragonal domains stably coexist at $T = T_{PPB}$, Figure 3.11. The determined average domain size of 20 nm, within the 10 – 60 nm range as reported by Acosta *et al.*[16], is consistent with miniaturization of the domain structure associated with the decrease in polarization anisotropy[88] and interfacial energy[1] in the vicinity of the PPB.

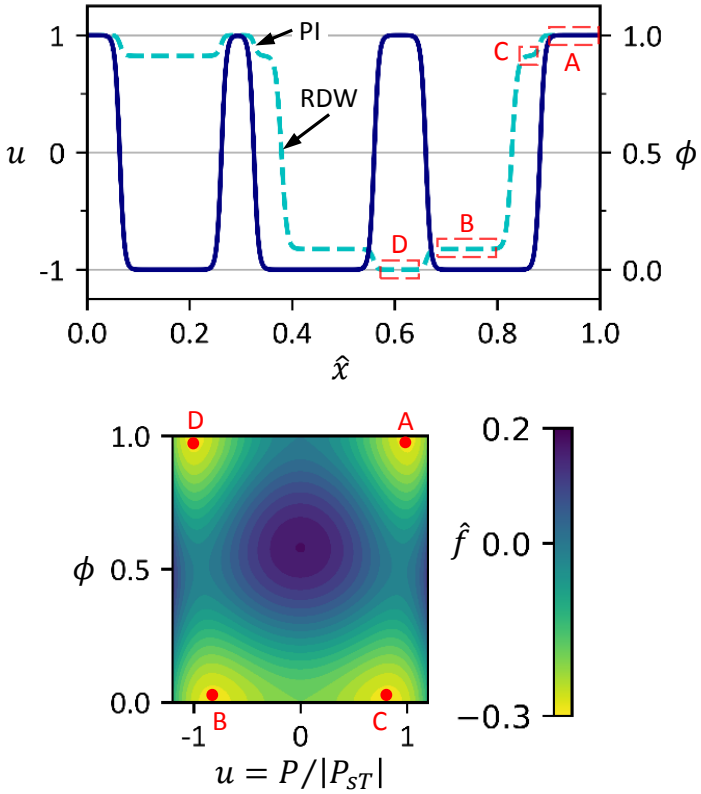

Figure 3.11: Above: spatial distribution of normalized polarization, $u = P/|P_{sT}|$ (- - -), and phase field, ϕ (—), at dimensionless time, $\hat{t} = t/\tau = 40000$, at $T = T_{PPB} = 43\,^{\circ}\text{C}$. Below: contour plot of the volumetric free energy density, $\hat{f}(u, \phi; \hat{E} = 0, T) = f/(\alpha_{111,T} P_{sT}^6)$, at $T = T_{PPB} = 43\,^{\circ}\text{C}$. Rhombohedral domain walls (RDWs) and phase interfaces (PIs) are noted. A, B, C and D represent four equilibrium states. Long-term coexistence of R and T phases is observed at the PPB.

In the absence of an applied electric field, Figure 3.11 demonstrates that the low energy barrier between variants in the R phase facilitates the formation of rhombohedral domain walls between states B and C, and enables the polarization rotation as it transitions between states A and D. As

discussed in Section 3.4, this is explained by equivalent values of σ_{TDW} and σ_{T-R} at $T = T_{PPB}$, see Table 3.2, which yields an equal likelihood of observing tetragonal domain walls and phase interfaces in the 1-D system, enabling the polarization rotation mechanism in the T phase. The results here are consistent with the theoretical observations reported by Yang *et al.*[95] that link the small energy barrier for direct 180° polarization reversal in one phase to easy domain switching and phase transformation (polarization rotation). The latter has been identified as the main origin of the enhanced electromechanical properties near the PPB in lead-free materials[55,96].

Figure 3.11 also shows that R↔T transformations between domains with opposing polarization states, *e.g.,* between states A and B, occur through a phase transformation, from state A to state C, followed by a 180° polarization reversal, from state C to state B. This is a consequence of the large energy barrier between antiparallel polarization states that prohibits direct R↔T transformation, as predicted in Section 3.4. The resulting transformation sequence, *i.e.,* the combination of R↔T reversible transformations and 180° polarization reversals, promotes switching and ferroelectric domain coexistence in the vicinity of the PPB. The presence of local metastable domains, such as those reported herein, have also been simulated by Rao and Wang[51] revealing their role in reducing the total free energy of the system by bridging stable domains.

3.6.3 Time-temperature-transformation (TTT) diagram

Figure 3.12 shows the macroscopic volume fraction transformed from a mixed 50%R+50%T state as a function of time at fixed temperature, *i.e.,* a time-temperature-transformation (TTT) diagram. Calculations show that as $T \rightarrow T_{PPB}$, both phases are more likely to coexist. For $T_{PPB} < T < T_{C,R}$, the low-temperature rhombohedral phase coexists metastably with the high-temperature, thermodynamically stable tetragonal phase as a result of the local R↔T phase transformations that are favoured to accommodate local switching events and metastable domains. In contrast, for $T < T_{PPB}$, a decrease in thermal energy suppresses phase transformations and, hence, suppresses the polarization switching plus rotation mechanism.

It is worth noting that although the phase transformation and polarization reversal pathway between domains is possible at all temperatures where the two FE phases can coexist metastably ($T < T_{C,R}$), it is favoured at $T > T_{PPB}$ due to the high domain wall energy of the stable phase. Further, the likelihood of observing R + T coexistence decreases with temperature as the driving force for transformation to the most stable phase increases, see Figure 3.13(a).

Figure 3.12 indicates that the time to reach 55 % transformed volume fraction is one to three orders of magnitude greater for $T > T_{PPB}$. This is due to the available thermal energy that enables the polarization switching of the individual phases to accommodate opposing polarization states. The latter favours the phase transformation-induced polarization rotation mechanism as a means to extend domain coexistence.

Moreover, Figure 3.12 shows that time for complete R + T→R transformation is on the order of tens of seconds for $T < T_{PPB}$, suggesting that the R + T phase coexistence is kinetically limited at low temperature. Hence, while the MPF model predicts a thermodynamic upper limit for ferroelectric

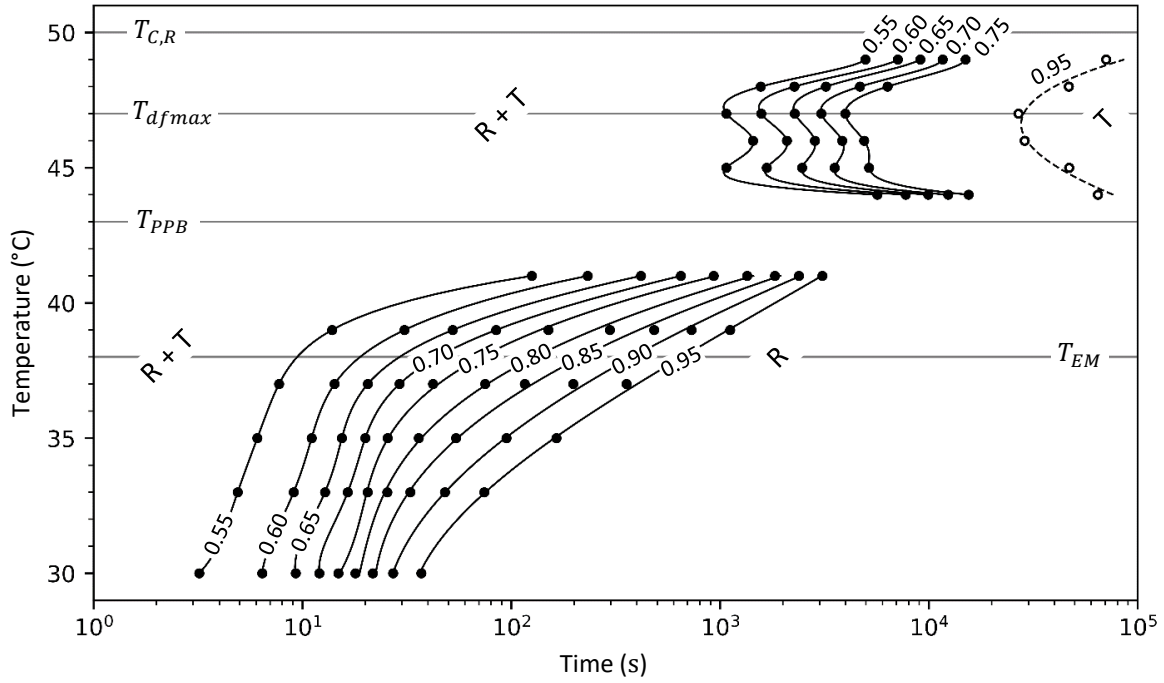

Figure 3.12: TTT diagram for transformation of mixed R + T phase towards stable single phase as $\psi \rightarrow 1$, starting from $\psi = 0.5$ at $t = 0$ at each temperature. Markers represent mean times for constant fraction of phase transformation calculated from fifteen simulations. Splines are included as a guide for the eye. Estimated times for 0.95 fraction transformed to T phase (▪ ▪) are extrapolated from a JMAK analysis at each $T > T_{PPB}$. $T_{df\,max}$ is the temperature at which the driving force for formation of T phase is maximal, and T_{EM} corresponds to a temperature where mobilities of the FE phases are equal, see Figure 3.13. Metastable coexistence persists for longer times at high temperatures compared to shorter times for R + T→R transformation at lower temperatures.

coexistence, its lower limit is determined by the kinetics of phase transformation. These results support experimental observations of R + T coexistence with fine domain structure in the vicinity of the PPB for the BZT-x BCT system[77,83–87], as opposed to the reported intervening O phase[25,79–82]. For PZT systems, it has been shown that the vanishing interfacial energies near the MPB produce nano-domains of the T and R phases, resulting in a domain averaging effect that can mimic the coherent diffraction from a monoclinic phase[14,15,20]. Thus, based on the adaptive martensite theory extended to ferroelectric systems by Jin *et al.* [97], the apparent O phase near the PPB in the BZT-x BCT system can be interpreted as an adaptive FE state of the nanoscale mixture of the T and R phases that causes diffraction artifacts in XRD experiments[16,86]. Results from recent CBED studies[86], which have higher spatial resolution, support the R + T phase coexistence and attribute the apparent O phase to adaptive diffraction of the nano-domain structure of T and R phases.

Macroscopically, for $T < T_{PPB}$, the predicted driving force for transformation to the most stable phase is very large, providing a rationale for the rapid kinetics of phase transformation, Figure 3.13(a). In addition, the phase-averaged mobility of the system increases with decreasing temperature for $\overline{\phi} = 0.5$, further promoting fast phase transformation at $T < T_{PPB}$, Figure 3.13(b). For $T_{PPB} > T > T_{EM}$, mobility increases as the transformation progresses and so does the rate of phase transformation; while for $T < T_{EM}$, phase transformation kinetics are limited by the mobility of the stable R phase, as it has the lower mobility of the two phases.

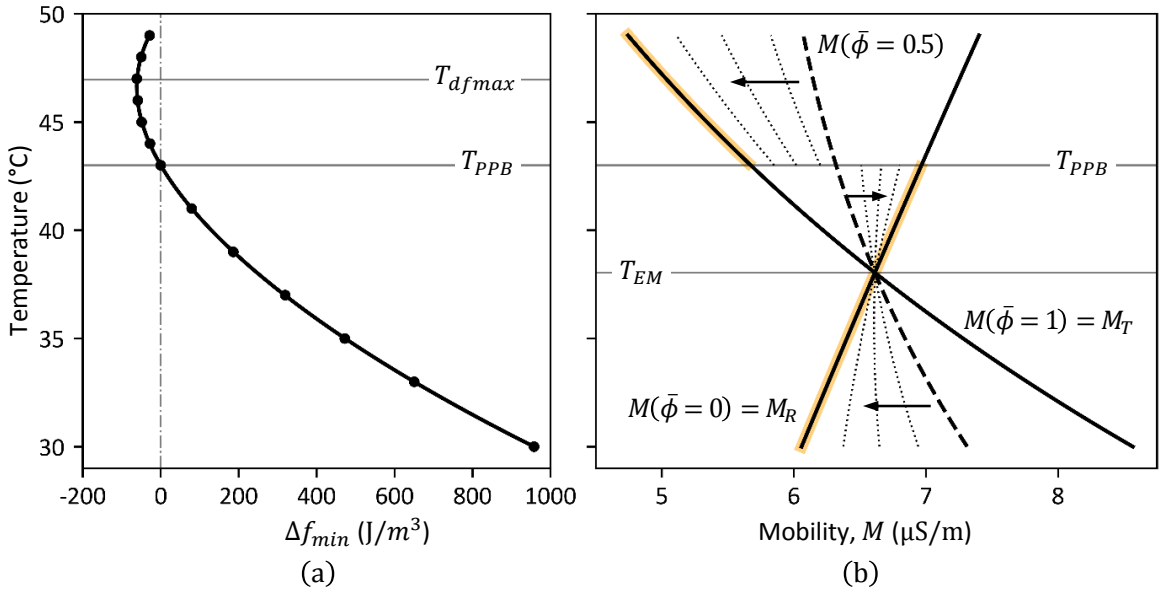

Figure 3.13: Temperature dependence of (a) thermodynamic driving force for transformation of FE phases, $\Delta f_{min} = f_T(P = P_{sT}; E = 0, T) - f_R(P = P_{sR}; E = 0, T)$, and (b) mobility. There is a local maximum in driving force at $T_{df\,max}$ for the R + T→T transformation. The mobilities of the two phases are equal at T_{EM}. Above T_{PPB} and below T_{EM}, the phase-averaged mobility decreases as $\psi \to 1$, but increases in the range $T_{EM} < T < T_{PPB}$.

For $T > T_{PPB}$, comparatively slow transformation kinetics correspond to a much smaller driving force for R→T transformation, which reaches a maximum at $T = T_{df\,max}$, Figure 3.13(a). The rate of phase transformation is again limited by the low mobility of the stable phase, in this case the T phase, with smaller values of mobility being attained than at $T < T_{PPB}$, Figure 3.13(b). Notably, for $T_{df\,max} < T < T_{C,R}$, the coexistence time increases as $T \to T_{C,R}$. This is attributed to vanishing rhombohedral domain wall energy, σ_{RDW}, and vanishing macroscopic driving force, Δf_{min}. The first is a consequence of the second order P-FE transition that occurs for the R phase at $T_{C,R}$. The second is a consequence of the fitted Landau coefficients and the selection of a constant Δf_{PPB}, see inset of Figure 3.5.

For $T > T_{C,R}$, the R phase is no longer metastable and any superheated, mixed R + T state is expected to relax to the equilibrium T phase rapidly, in agreement with the phase diagram. No simulations were carried out in this temperature range as it is out of the scope of this work.

3.6.4 Avrami (JMAK) analysis

The kinetics of isothermal R + T→T and R + T→R transformations can be fitted to the Johnson-Mehl-Avrami-Kolmogorov (JMAK) model, $\psi = 1 - \exp(-kt^n)$[98]. The analysis is illustrated in Figure 3.14 for $T = 37\,°C$. Results show that the isothermal FE transformation only exhibits the upper section of the characteristic sigmoidal profile that describes typical transformations, *e.g.,* crystallization, Figure 3.14(a). This is consistent with the site-saturated nucleation considered in this study. The Avrami exponent, n, and constant k are obtained by plotting $\ln(-\ln(1-\psi))$ versus $\ln(t)$ and using a linear least-squares method to fit a line of slope n, Figure 3.14(b).

Table 3.4 shows estimated values of n and k for different temperatures. Avrami exponents of $0.29 \leq n \leq 0.56$ were found. In general, the exponent n is related to the transformation morphology (or dimensionality) and to the behaviour of nucleation and growth with respect to time[99,100]. Values of $n \leq 1$ have been reported for other transformations depending on the nucleation type and growth mechanism. For order-disorder transformations, it has been suggested that a value of $n \approx 1$ is consistent with site-saturated nucleation and interface-controlled growth in one dimension[99]. For crystallisation, values of $n < 1$ are characteristic of the late stages of the transformation due to a soft-impingement diffusion mechanism that causes a reduction in the growth rate, with decreasing nucleation rate as a second-order effect[100].

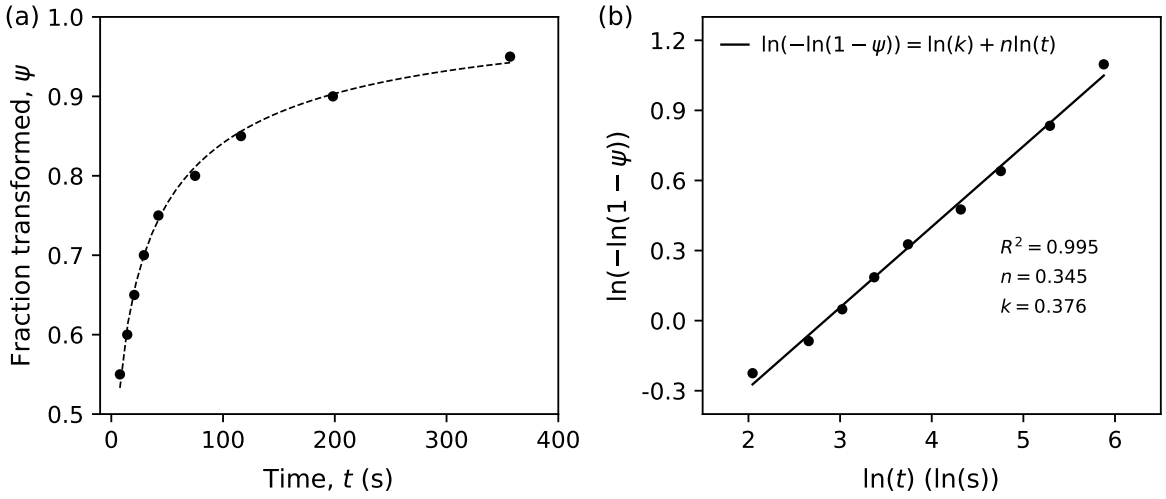

Figure 3.14: (a) Isothermal phase transformation, and (b) JMAK analysis for the one-dimensional, coarse-grained BZT-40 BCT system at $T = 37\,^{\circ}\text{C}$. The volume fraction transformed of FE phases is measured in this case as $\psi = 1 - \overline{\phi}$. Average transformation times are calculated from fifteen simulations. The JMAK equation is plotted using the estimated n and k values (▪ ▪).

Table 3.4: Estimated n and k values of the JMAK equation for the BZT-40 BCT system.

$T < T_{PPB}$				$T > T_{PPB}$			
T (°C)	n	K	R^2	T (°C)	n	K	R^2
41	0.390	1.06×10^{-1}	0.937	44	0.551	6.71×10^{-3}	0.994
39	0.288	3.43×10^{-1}	0.970	45	0.353	6.74×10^{-2}	0.998
37	0.345	3.76×10^{-1}	0.995	46	0.447	3.05×10^{-2}	0.994
35	0.416	3.53×10^{-1}	0.993	47	0.415	4.33×10^{-2}	0.992
33	0.514	3.07×10^{-1}	0.974	48	0.391	4.48×10^{-2}	0.999
30	0.555	3.42×10^{-1}	0.924	49	0.506	1.06×10^{-2}	0.993

3.7 Summary and conclusions

The novel MPF framework for ferroelectric systems, established in Chapter 2, is applied herein to a one-dimensional BZT-40 BCT polycrystal using a coarse-grained approach. A phase diagram with a single PPB between the tetragonal and rhombohedral phases is assumed. The MPF method considers the thermodynamics of the individual FE phases independently in order to assess equilibrium states and phase transformation dynamics of the competing phases. The model naturally identifies thermodynamic conditions for the stable and metastable coexistence of the R and T phases. Further, it predicts a thermodynamic upper limit for metastability, $T_{C,0} = 49.90\,^{\circ}\text{C}$, consistent with experimental observations for the BZT-40 BCT composition.

A TTT diagram for field-free ferroelectric transformation from a mixed R + T initial state is presented. Results demonstrate that coexistence is short lived (on the order of tens of seconds) for $T < T_{PPB}$, whereas it persists from minutes to hours for $T > T_{PPB}$. This suggests that, while a thermodynamic limit for R + T coexistence is predicted at high temperature, its observation is kinetically limited at low temperatures. Results support the hypothesis of R + T coexistence in the vicinity of the PPB, as opposed to the existence of an additional orthorhombic phase in the BZT-x BCT system.

Additionally, results show that metastable coexistence of phases provides access to additional polarization states, which enables a phase transformation-induced polarization rotation mechanism near the interferroelectric phase boundary. The proposed polarization rotation mechanism is a local intervening kinetic step that is partially responsible for the enhancement of ferroelectric properties due to its role in extending domain coexistence and enabling easy polarization switching and rotation.

Due to the fact that this is a one-dimensional study, the solution of Coulomb's Equation forces an unphysical polarization configuration over the entire computational system. This limits the analysis of the effects of local electric fields on microstructural evolution. Further, the coarse-grained approach adopted in this work does not capture the detailed effects of anisotropy in FE materials. These limitations are addressed in the following chapters.

Chapter 4

Application to coarse-grained BZT-40BCT polycrystal in 2-D

A version of this chapter is currently under preparation for journal publication as: Oscar A. Torres-Matheus, R. Edwin García and Catherine M. Bishop. Two-dimensional phase coexistence in multi-phase field model of BZT-40 BCT.

4.1 Introduction

In previous chapters, a novel MPF model was developed for FE systems with a single PPB. The model was applied to a one-dimensional, coarse-grained BZT-40 BCT polycrystal to assess the thermodynamic conditions and transformation dynamics controlling the coexistence of the R and T ferroelectric phases in the vicinity of the PPB. The MPF model was validated by comparing calculated and experimental hysteresis loops in the region of phase space where the FE phases coexist. However, the analysis of domain structures and phase transformation kinetics was limited by the system's spatial dimensionality. In a 1-D system, solving Coulomb's Equation to account for the local electric fields produces an artificial configuration with uniform polarization. Hence, simulations for the microstructural evolution of one-dimensional BZT-40 BCT were carried out ignoring the effect of local electric fields within the material.

In this chapter, the MPF model is demonstrated in two dimensions for a coarse-grained BZT-40 BCT polycrystal. This enables access to additional degrees of freedom, or polarization configurations, to minimize the free energy of the system. The additional spatial dimension yields more realistic domain configurations that affect the equilibrium states and transformation dynamics of the coexisting FE phases in the vicinity of the PPB. Further, the two-dimensional model allows assessment of the effect of local electric fields within the material on the FE domain structures and the kinetics of phase transformation.

4.2 Model formulation

The formulation described herein is based on the theoretical MPF framework presented in Section 2.3 for FE systems with a single PPB. It corresponds to the two-dimensional extension of the model developed in Chapter 3 for one-dimensional BZT-40 BCT, see Section 3.2.

For a system that undergoes polarization switching events in two orthogonal directions, say $\hat{\imath}$ and $\hat{\jmath}$, with an electric field applied along the same directions, we define $\vec{P} = (P_1, P_2)$ and $\vec{E} = (E_1, E_2) = -\nabla V_E$, where $\nabla = (\partial/\partial x_1, \partial/\partial x_2)$ and V_E is the electrostatic potential[90]. A simple Landau-Devonshire expansion is selected to describe the volumetric free energy density of the T and R phases in two dimensions[101]. Thus, Equations 2.6 and 2.7 reduce to

$$f_T(\vec{P};\vec{E},T) = \frac{1}{2}\alpha_{1,T}(P_1^2+P_2^2) + \frac{1}{4}\alpha_{11,T}(P_1^4+P_2^4) + \frac{1}{2}\alpha_{12,T}P_1^2P_2^2 + \frac{1}{6}\alpha_{111,T}(P_1^6+P_2^6) - (P_1E_1+P_2E_2) \tag{4.1}$$

$$f_R(\vec{P};\vec{E},T) = \frac{1}{2}\alpha_{1,R}(P_1^2+P_2^2) + \frac{1}{4}\alpha_{11,R}(P_1^4+P_2^4) + \frac{1}{2}\alpha_{12,R}P_1^2P_2^2 + \frac{1}{6}\alpha_{111,R}(P_1^6+P_2^6) - (P_1E_1+P_2E_2) + \Delta f_{PPB} \tag{4.2}$$

where α_1, α_{11}, α_{12} and α_{111} are the Landau coefficients, and $\alpha_1 = a_{CW}(T - T_{CW})$. Further, the free energy density due to gradients in polarization is obtained as

$$\frac{1}{2}\sum_{k,l=1}^{3}\sum_{i,j=1}^{3} K_{ijkl}\frac{\partial P_k}{\partial x_i}\frac{\partial P_l}{\partial x_j} = \frac{1}{2}K_P(P_{1,1}^2 + P_{2,2}^2 + P_{1,2}^2 + P_{2,1}^2) \tag{4.3}$$

where $P_{i,j} = \partial P_i/\partial x_j$ and $K_P = K_{1111}$ assuming an isotropic gradient energy penalty[47,48]. The free energy density due to gradients in phase field is the same given by Equation 3.4 for the one-dimensional case.

The polarization switching dynamics of the two-dimensional FE system is described by three coupled Allen-Cahn equations,

$$\frac{\partial P_1}{\partial t} = -M_P\left\{\frac{\partial f_R(\vec{P};T)}{\partial P_1}[1-h(\phi)] + \frac{\partial f_T(\vec{P};T)}{\partial P_1}h(\phi) + \frac{\partial V_E}{\partial x_1} - K_P\nabla^2 P_1\right\} \tag{4.4}$$

$$\frac{\partial P_2}{\partial t} = -M_P\left\{\frac{\partial f_R(\vec{P};T)}{\partial P_2}[1-h(\phi)] + \frac{\partial f_T(\vec{P};T)}{\partial P_2}h(\phi) + \frac{\partial V_E}{\partial x_2} - K_P\nabla^2 P_2\right\} \tag{4.5}$$

$$\frac{\partial \phi}{\partial t} = -M_\phi\left\{[f_T(\vec{P};T) - f_R(\vec{P};T)]\frac{\mathrm{d}h(\phi)}{\mathrm{d}\phi} + W\frac{\mathrm{d}g(\phi)}{\mathrm{d}\phi} - K_\phi\nabla^2\phi\right\} \tag{4.6}$$

where $\nabla^2 = \partial^2/\partial x_1^2 + \partial^2/\partial x_2^2$. Mobilities are defined in the same way as detailed in Section 3.3.2, *i.e.*, $M_P = M_\phi = M(\phi;T) = M_R(T)[1-h(\phi)] + M_T(T)h(\phi)$, with M_R and M_T defined as $M(T) = M_o\exp(-Q/RT)$.

The electrostatic field distribution is calculated using the differential form of Coulomb's Equation assuming zero free electric charge density, $\nabla\cdot\vec{D} = 0$. By substituting the constitutive relation

between the electric displacement and the total polarization, $\vec{D} = \vec{P} + \epsilon_o \vec{E}$, where ϵ_o is the vacuum permittivity[90], Coulomb's Equation becomes

$$\nabla \cdot \vec{P} - \epsilon_o \nabla^2 V_E = 0 \tag{4.7}$$

The model is normalized using $\hat{x_i} = x_i/L$, $\hat{t} = t/\tau$, $u_i = P_i/|P_{sT}|$, and $\hat{E}_i = E_i/|E_{cT}|$; where L is the size of a square single-crystal sample, P_{sT} is the spontaneous polarization of the T phase, E_{cT} is the coercive field of the T phase, $\tau = 1/\left(|\alpha_{1,T}|M_T\right)$ and $i = 1, 2$. With these definitions, Equations 4.4 through 4.7 are cast in dimensionless form as

$$\frac{1}{\mu}\frac{\partial u_1}{\partial \hat{t}} = \gamma \hat{\nabla}^2 u_1 - \left\{ \frac{\partial \hat{f}_R(\vec{u};T)}{\partial u_1}[1 - h(\phi)] + \frac{\partial \hat{f}_T(\vec{u};T)}{\partial u_1} h(\phi) + \hat{E}_{cT}\frac{\partial \hat{V}_E}{\partial \hat{x}_1} \right\} \tag{4.8}$$

$$\frac{1}{\mu}\frac{\partial u_2}{\partial \hat{t}} = \gamma \hat{\nabla}^2 u_2 - \left\{ \frac{\partial \hat{f}_R(\vec{u};T)}{\partial u_2}[1 - h(\phi)] + \frac{\partial \hat{f}_T(\vec{u};T)}{\partial u_2} h(\phi) + \hat{E}_{cT}\frac{\partial \hat{V}_E}{\partial \hat{x}_2} \right\} \tag{4.9}$$

$$\frac{1}{\nu}\frac{\partial \phi}{\partial \hat{t}} = \gamma\lambda \hat{\nabla}^2 \phi - \left\{ [\hat{f}_T(\vec{u};T) - \hat{f}_R(\vec{u};T)]\frac{\mathrm{d}h(\phi)}{\mathrm{d}\phi} + \hat{W}\frac{\mathrm{d}g(\phi)}{\mathrm{d}\phi} \right\} \tag{4.10}$$

$$0 = \hat{\nabla} \cdot \vec{u} - \hat{\epsilon}_o \hat{\nabla}^2 \hat{V}_E \tag{4.11}$$

where the following dimensionless parameters are identified: $\mu = M/M_T$, $\nu = P_{sT}^2\mu$, $\gamma = K_P/(|\alpha_{1,T}|L^2)$, $\lambda = K_\phi/(K_P P_{sT}^2)$, $\hat{W} = W/(|\alpha_{1,T}|P_{sT}^2)$, $\hat{E}_{cT} = \left|E_{cT}/(\alpha_{1,T}P_{sT})\right|$, and $\hat{\epsilon}_o = \epsilon_o\,|E_{cT}/P_{sT}|$.

In addition, $\hat{f}_R(\vec{u};T)$ and $\hat{f}_T(\vec{u};T)$ are obtained by

$$\begin{aligned}\hat{f}_T(\vec{u};T) = \frac{f_T(\vec{u};T)}{\left|\alpha_{1,T}\right|P_{sT}^2} =& \frac{\alpha'_{1,T}}{2}(u_1^2 + u_2^2) + \frac{\alpha'_{11,T}}{4}(u_1^4 + u_2^4) + \frac{\alpha'_{12,T}}{2}u_1^2u_2^2 \\ &+ \frac{\alpha'_{111,T}}{6}(u_1^6 + u_2^6)\end{aligned} \tag{4.12}$$

$$\begin{aligned}\hat{f}_R(\vec{u};T) = \frac{f_R(\vec{u};T)}{\left|\alpha_{1,T}\right|P_{sT}^2} =& \frac{\alpha'_{1,R}}{2}(u_1^2 + u_2^2) + \frac{\alpha'_{11,R}}{4}(u_1^4 + u_2^4) + \frac{\alpha'_{12,R}}{2}u_1^2u_2^2 \\ &+ \frac{\alpha'_{111,R}}{6}(u_1^6 + u_2^6) + \Delta\hat{f}_{PPB}\end{aligned} \tag{4.13}$$

where the following dimensionless Landau coefficients are defined: $\alpha'_{1,T} = \alpha_{1,T}/|\alpha_{1,T}| = -1$, $\alpha'_{11,T} = \alpha_{11,T}P_{sT}^2/|\alpha_{1,T}|$, $\alpha'_{12,T} = \alpha_{12,T}P_{sT}^2/|\alpha_{1,T}|$, $\alpha'_{111,T} = \alpha_{111,T}P_{sT}^4/|\alpha_{1,T}|$, $\alpha'_{1,R} = \alpha_{1,R}/|\alpha_{1,T}|$, $\alpha'_{11,R} = \alpha_{11,R}P_{sT}^2/|\alpha_{1,T}|$, $\alpha'_{12,R} = \alpha_{12,R}P_{sT}^2/|\alpha_{1,T}|$, $\alpha'_{111,R} = \alpha_{111,R}P_{sT}^4/|\alpha_{1,T}|$, and $\Delta\hat{f}_{PPB} = \Delta f_{PPB}/(|\alpha_{1,T}|P_{sT}^2)$.

In this two-dimensional model, spontaneous polarizations are along the ⟨10⟩ family of directions for the T phase, and the ⟨11⟩ family of directions for the R phase. Considering the case of $\vec{P}_T = (P, 0)$, the magnitude of the coercive field in the tetragonal phase, $\vec{E}_{cT} = (E_{cT}, 0)$, is determined by

$$E_{cT} = \left.\frac{\partial f_T(\vec{P}_T;T)}{\partial P}\right|_{P=P_{cT}} = \alpha_{1,T}P_{cT} + \alpha_{11,T}P_{cT}^3 + \alpha_{111,T}P_{cT}^5 \tag{4.14}$$

where P_{cT} corresponds to the magnitude of the polarization at the coercive field, which can be calculated from $\partial^2 f_T(\vec{P}_T;T)/\partial P^2\Big|_{P=P_{cT}} = 0$. Furthermore, the magnitudes of the spontaneous polarization for each FE phase, $\vec{P}_{sT} = P_{sT}(1,0)$ and $\vec{P}_{sR} = P_{sR}(1/\sqrt{2},1/\sqrt{2})$, are given by

$$P_{sT} = \pm\left[\frac{-\alpha_{11,T} + \sqrt{\alpha_{11,T}^2 - 4\alpha_{1,T}\alpha_{111,T}}}{2\alpha_{111,T}}\right]^{1/2} \tag{4.15}$$

$$P_{sR} = \pm\left[\frac{-(\alpha_{11,R} + \alpha_{12,R}) + \sqrt{(\alpha_{11,R} + \alpha_{12,R})^2 - 4\alpha_{1,R}\alpha_{111,R}}}{\alpha_{111,R}}\right]^{1/2} \tag{4.16}$$

4.3 Model parameters

The dimensionless parameters of the two-dimensional MPF model are calculated using the material constants reported in Table 3.1 for the one-dimensional BZT-40 BCT system. This allows to isolate the effect of the additional spatial degree of freedom on the model predictions. Table 4.1 summarizes all the physical parameters used in both models.

Table 4.1: Physical parameters of one- and two-dimensional MPF models for coarse-grained BZT-40 BCT polycrystal. Shaded rows highlight parameters that have the same value in both models, as reported in Table 3.1 for the one-dimensional case.

	1-D case		2-D case		
Symbol	R phase ($\phi = 0$)	T phase ($\phi = 1$)	R phase ($\phi = 0$)	T phase ($\phi = 1$)	Units
a_{CW}	5.000×10^4	2.063×10^4	5.000×10^4	2.063×10^4	$\mathrm{Jm/C^2K}$
α_{11}	6.314×10^7	-4.229×10^7	6.314×10^7	-4.229×10^7	$\mathrm{Jm^5/C^4}$
α_{12}	–	–	0.000	5.000×10^8	$\mathrm{Jm^5/C^4}$
α_{111}	1.263×10^{10}	3.154×10^{10}	1.263×10^{10}	3.154×10^{10}	$\mathrm{Jm^9/C^6}$
T_{CW}	49.90	69.08	49.90	69.08	°C
T_C	$T_{CW,R}$	69.60	$T_{CW,R}$	69.60	°C
T_{max}	$T_{CW,R}$	69.77	$T_{CW,R}$	69.77	°C
M_o	1.809×10^{-4}	3.806×10^{-10}	1.809×10^{-4}	3.806×10^{-10}	S/m
Q	8561	−25 260	8561	−25 260	J/mol
K_P	8.051×10^{-13}		8.051×10^{-13}		$\mathrm{Jm^3/C^2}$
K_ϕ	2.150×10^{-14}		2.150×10^{-14}		J/m
W	1.444×10^4		1.444×10^4		$\mathrm{J/m^3}$
Δf_{PPB}	−632.1		−310.3		$\mathrm{J/m^3}$

For the two-dimensional system, values for the coefficient α_{12} are selected such that the volumetric free energy densities, given by Equations 4.1 and 4.2, reproduce the correct equilibrium phase in the entire temperature range of interest. For the T phase, $\alpha_{12,T} = 5.0 \times 10^8\,\mathrm{Jm^5/C^4}$ is added to stabilize the polarization states along the ⟨10⟩ crystallographic directions. For the R phase, we set

$\alpha_{12,R} = 0\,\mathrm{Jm^5/C^4}$ considering that the coefficients $\alpha_{1,R}$, $\alpha_{11,R}$ and $\alpha_{111,R}$ yield stable states along the ⟨11⟩ directions. The selected Landau coefficients allow to compare results with the one-dimensional calculations without changing other parameters controlling the underlying energetics of the BZT-40 BCT system. Hence, it is possible to explore the specific effect of the additional spatial dimension and the distribution of local electric fields within the material on domain configurations and FE phase coexistence. However, since only one coefficient of the two-dimensional Landau expansion is altered, the calculated spontaneous polarizations in the R phase differ from the experimental values, Figure 4.1(a). Selecting a different (valid) value for $\alpha_{12,T}$ would only affect the energy barrier between perpendicular T variants. As the focus of this chapter is not a comparison to experimental results for BZT-40 BCT ceramics, this is deemed acceptable.

Figure 4.1(b) shows that the global stability predictions are preserved in the region of metastability, $T_{R-O} \leq T \leq T_{O-T}$, where $T_{R-O} = 37\,^{\circ}\mathrm{C}$ and $T_{O-T} = 49\,^{\circ}\mathrm{C}$, according to Ehmke[89]. At $T_{PPB} \sim (T_{O-T} + T_{R-O})/2 = 43\,^{\circ}\mathrm{C}$, the rhombohedral and tetragonal phases are both stable. For the R phase, Figure 4.1(c)-(d) confirms that selected Landau coefficients give minima along the ⟨11⟩ polarization directions. For the T phase, Figure 4.1(e)-(f) shows that selected Landau coefficients stabilize polarization states along the ⟨10⟩ directions.

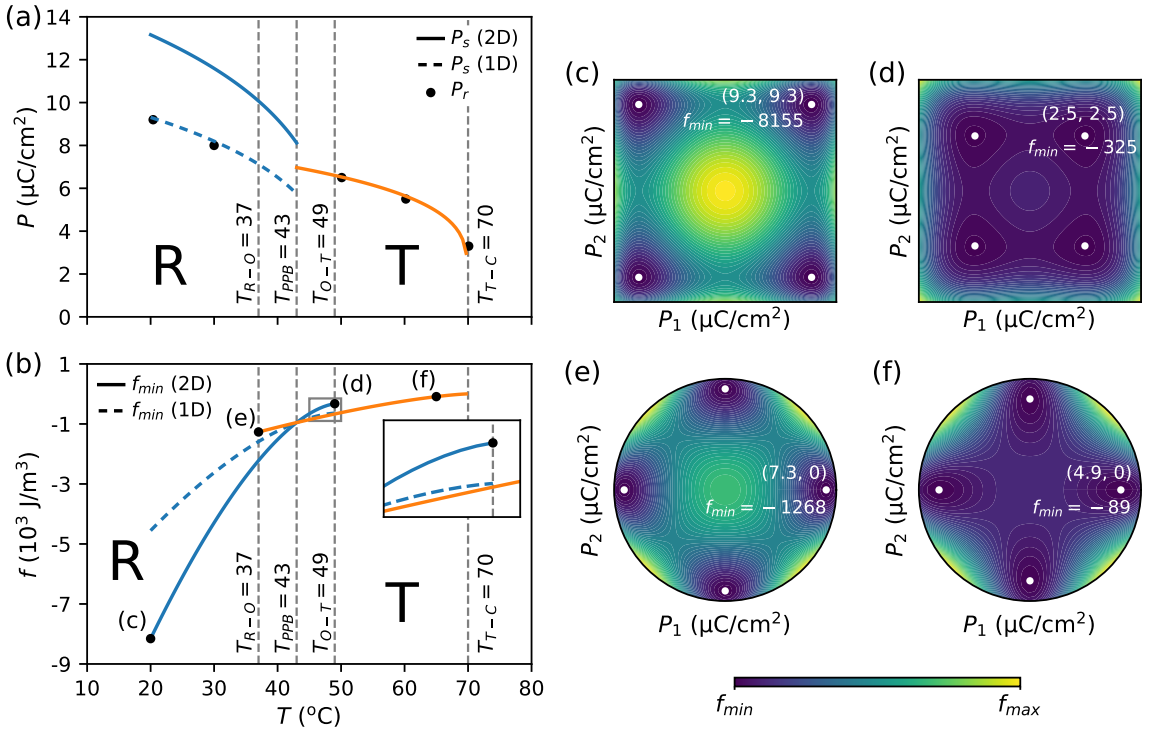

Figure 4.1: Temperature dependence of (a) magnitude of spontaneous polarization, and (b) minimum volumetric free energy density for the R (—) and T (—) phases. Calculated values from the one-dimensional model are also included for comparison. For all temperatures, the spontaneous polarization and minimum free energy density of the T phase are equal in both models due to its crystallographic symmetry. Remnant polarization and the R-O, O-T and T-C transition temperatures are also shown, as measured by Ehmke[89]. Inset corresponds to a magnified view of the area indicated near the T_{O-T}. For $T > T_{PPB}$, $f_{min,T} < f_{min,R}$ in both models, confirming the correct global stability predictions with selected Landau coefficients. Subfigures (c)-(f) illustrate the volumetric free energy density distribution, in $\mathrm{J/m^3}$, and stable polarization states for (c) R phase at $T = 20\,^{\circ}\mathrm{C}$, (d) R phase at $T = 49\,^{\circ}\mathrm{C}$, (e) T phase at $T = 37\,^{\circ}\mathrm{C}$, and (f) T phase at $T = 65\,^{\circ}\mathrm{C}$.

The gradient energy coefficients, K_P and K_ϕ, and the double-well coefficient, W, shown in Table 4.1, allow to calculate the dimensionless parameters λ and $\hat{W}$. Following a procedure similar to that used in Section 3.3, we set $\gamma = 3\times10^{-5}$ via numerical evaluation such that the widths of rhombohedral domain walls and phase interfaces, measured in ϕ, are approximately equal at $T = T_{PPB} = 43\,^{\circ}\text{C}$, where both FE phases are stable. Thus, the crystal size is estimated as $L = 223\,\text{nm}$ from $\gamma = K_P/(L^2\left|\alpha_{1,T}\right|_{T_{PPB}})$, which is similar to the crystal size obtained for the one-dimensional model ($L = 190\,\text{nm}$).

4.4 Simulation cases and numerical implementation

The two-dimensional MPF model was implemented using FEM in COMSOL Multiphysics® [94], on a square computational domain of side L and global coordinates x and y. Interfacial calculations were performed on a 100x100-element mesh and microstructural evolution simulations were carried out on a 75×75-element mesh. For all cases, second-order Lagrange shape functions were used.

The interfacial widths and energies were estimated for different types of tetragonal domain walls (TDWs), rhombohedral domain walls (RDWs) and T-R phase interfaces at selected temperatures. For all cases, Equations 4.8 through 4.11 were solved considering a computational domain with a single interface between two homogeneous FE domains, with $\hat{V}_E(\hat{x},\hat{y},\hat{t}=0) = 0$. All boundaries were electrically grounded ($\hat{V}_E = 0$), while zero flux conditions were applied for u_x, u_y and ϕ.

The microstructural evolution of two-phase FE systems was simulated for selected temperatures in the absence of applied electric fields. Two different scenarios were considered. In one case, Equations 4.8 through 4.10 were solved to investigate the effect of the additional spatial dimension on domain configurations and transformation dynamics of coexisting FE phases. Results were directly compared with those obtained for one-dimensional BZT-40 BCT in Section 3.6.3. For the other case, Equations 4.8 through 4.11 were solved to elucidate the effect of the spatial variation of local electric fields on the domain configurations and phase coexistence. In addition, numerical results from the latter case were used to study the coarsening of ferroelectric domains in the vicinity of the PPB, where the T and R phases coexist. For both scenarios, mixed 50%R+50%T initial conditions were considered using a uniform random distribution function, {mean, range}, for the phase field $\{0.5, 1\}$ and for each polarization component $\{0, 2\}$; and $\hat{V}_E(\hat{x},\hat{y},\hat{t}=0) = 0$. All boundaries were electrically grounded, with periodic boundary conditions for u_x, u_y and ϕ.

Additional simulations were performed for the microstructural evolution of single-phase FE systems in the absence of applied electric fields. Equations 4.8, 4.9 and 4.11 were solved to examine ferroelectric domain coarsening in single-phase conditions. Results were compared with those obtained in mixed R + T phase conditions to elucidate the mechanism controlling domain coarsening in the vicinity of the PPB. Two sets of simulations were carried out: one assuming that only the R phase was present, *i.e.,* $\phi(\hat{x},\hat{y},\hat{t}=0) = 0$, for $T \le T_{PPB}$; and another considering only the T phase, $\phi(\hat{x},\hat{y},\hat{t}=0) = 1$, for $T \ge T_{PPB}$. Random initial conditions were used for each polarization component $\{0, 2\}$, with $\hat{V}_E(\hat{x},\hat{y},\hat{t}=0) = 0$. All boundaries were electrically grounded, with periodic boundary conditions for u_x, u_y and ϕ.

For all cases, the microstructural evolution was evaluated using fifteen simulations at each temperature. A scalar variable was created to output the average phase field $\overline{\phi}$ at every $\hat{t} = 1$; while the solution fields of u_x, u_y and ϕ were stored at selected times for detailed analysis of FE domain structures and coarsening.

4.5 Results and analysis

4.5.1 Interfacial calculations

Values for the interfacial width and energy, ξ and σ, were calculated for six different cases identified in this study, namely: 180TDW, 90TDW, 180RDW, 90RDW, 135T-R and 45T-R. According to this nomenclature, domain walls are described by the polarization rotation between variants that occurs across the interface, and T-R phase interfaces are described by the polarization rotation from one phase to the other. Figures 4.2 through 4.4 show the simulation results at $T = T_{PPB} = 43\,^{\circ}\mathrm{C}$. On the left, the lowest energy configurations of the two-dimensional FE system with a single interface are illustrated. On the right, $\hat{f}$, ϕ and $u_{y'}$ are plotted along a line normal to the resolved interface. For all cases, a local coordinate system is defined with respect to the interface of interest, with x' as the normal direction and y' as the tangential direction.

Since there is no free charge in the system, Coulomb's Equation yields electrically neutral interfaces according to $\hat{\nabla} \cdot \vec{u} - \hat{\epsilon}_o \hat{\nabla}^2 \hat{V}_E = 0$ (Equation 4.11). Further, for planar interfaces, $\partial u_{x'}/\partial y' =$

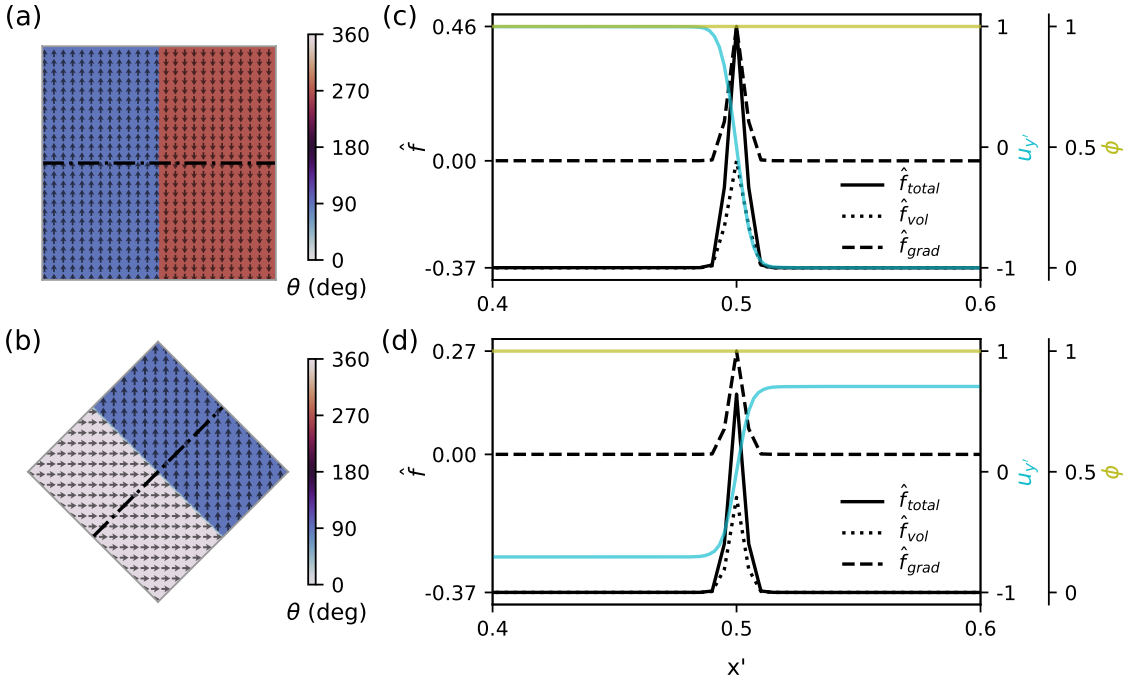

Figure 4.2: Interfacial width and energy calculations for tetragonal domain walls (TDWs) at $T = T_{PPB} = 43\,^{\circ}\mathrm{C}$. Left column: stable configuration for a single (a) 180TDW and (b) 90TDW, shown by vector plot of $\vec{u}$ and contour plot of $\theta = \mathrm{atan2}(u_y, u_x)$, with local coordinates x' and y' in the normal and tangential directions to the interface. Right column: line plot of calculated $\hat{f} = f/(|\alpha_{1,T}|P_{sT}^2)$, $u_{y'} = P_{y'}/|P_{sT}|$ and ϕ along interface normal for the (c) 180TDW and (d) 90TDW.

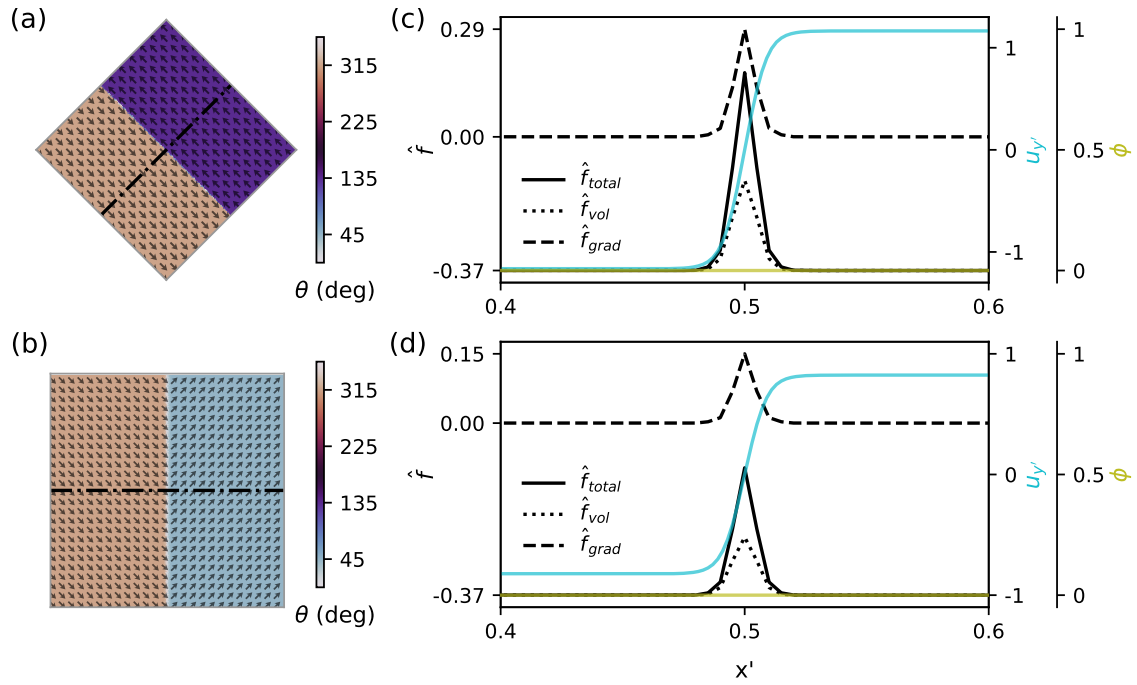

Figure 4.3: Interfacial width and energy calculations for rhombohedral domain walls (RDWs) at $T = T_{PPB} = 43\,^{\circ}\mathrm{C}$. Left column: stable configuration for a single (a) 180RDW and (b) 90RDW, shown by vector plot of $\vec{u}$ and contour plot of $\theta = \mathrm{atan2}(u_y, u_x)$, with local coordinates x' and y' in the normal and tangential directions to the interface. Right column: line plot of calculated $\hat{f} = f/(|\alpha_{1,T}|P_{sT}^2)$, $u_{y'} = P_{y'}/|P_{sT}|$ and ϕ along interface normal for the (c) 180RDW and (d) 90RDW.

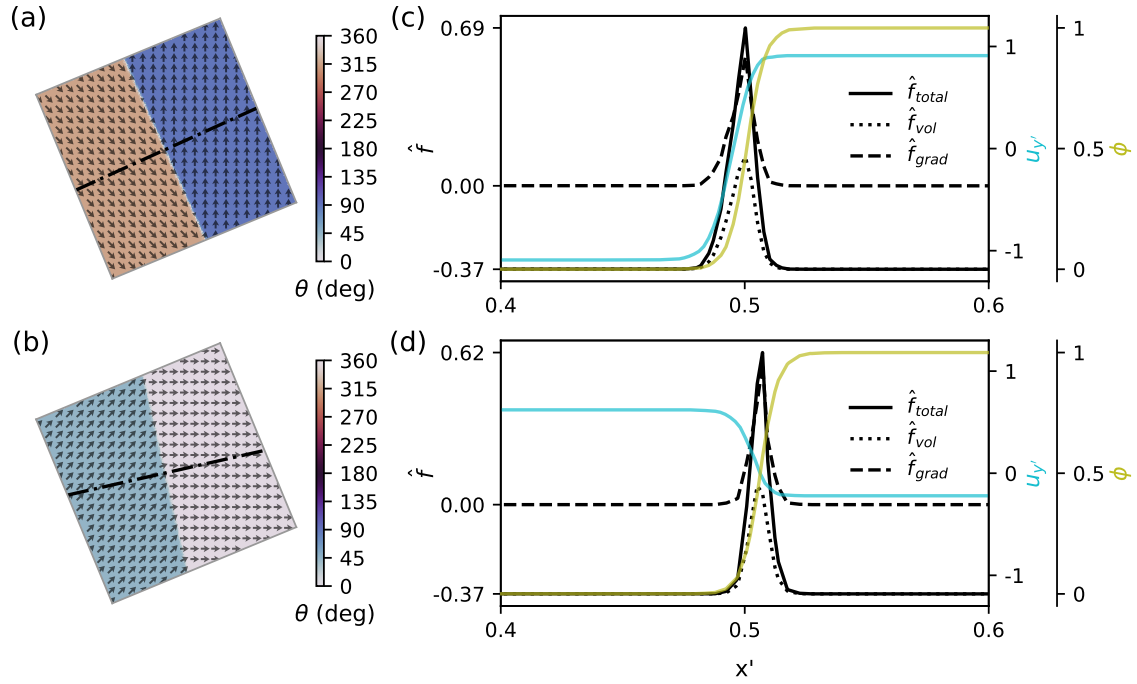

Figure 4.4: Interfacial width and energy calculations for T-R phase interfaces at $T = T_{PPB} = 43\,^{\circ}\mathrm{C}$. Left column: stable configuration for single (a) 135T-R and (b) 45T-R interfaces, shown by vector plot of $\vec{u}$ and contour plot of $\theta = \mathrm{atan2}(u_y, u_x)$, with local coordinates x' and y' in the normal and tangential directions to the interface.. Right column: line plot of calculated $\hat{f} = f/(|\alpha_{1,T}|P_{sT}^2)$, $u_{y'} = P_{y'}/|P_{sT}|$ and ϕ along interface normal for the (c) 135T-R and (d) 45T-R interfaces.

$\partial u_{y'}/\partial y' = \partial \hat{V}_E/\partial y' = 0$. Then, considering that $\hat{\epsilon}_o$ values are very small, it can be shown that only the polarization component perpendicular to the interface normal changes across the boundary[71], *i.e.*, $\partial u_{x'}/\partial x' \approx 0$ and $\partial u_{y'}/\partial x' \neq 0$. Therefore, the interfacial widths were calculated herein using the profile of $u_{y'}$ across the interface; while for the interfacial energies, solutions are given by $\sigma = |\alpha_{1,T}|P_{sT}^2 L \int_0^1 \left[\hat{f}_{total}(x') - \hat{f}_{min}\right] dx'$, as explained in Section 3.3. Results are summarized in Table 4.2 for all interfaces at $T = T_{PPB} = 43\,^{\circ}\text{C}$. The same procedure described above was repeated for calculations at different temperatures.

Table 4.2: Interfacial widths and energies for the two-dimensional, coarse-grained BZT-40 BCT system calculated at $T = T_{PPB} = 43\,^{\circ}\text{C}$. Results from the one-dimensional, coarse-grained model, Table 3.2, are reproduced for ease of comparison.

	1-D case		2-D case		
Symbol	R phase ($\phi = 0$)	T phase ($\phi = 1$)	R phase ($\phi = 0$)	T phase ($\phi = 1$)	Units
ξ_{180DW}	4.000	2.867	4.425	3.313	nm
ξ_{90DW}	–	–	4.425	3.122	nm
ξ_{T-R}	2.834		–		nm
ξ_{135T-R}	–		4.210		nm
ξ_{45T-R}	–		3.358		nm
σ_{180DW}	1.876×10^{-6}	4.063×10^{-6}	3.519×10^{-6}	3.770×10^{-6}	J/m^2
σ_{90DW}	–	–	1.759×10^{-6}	2.034×10^{-6}	J/m^2
σ_{T-R}	4.445×10^{-6}		–		J/m^2
σ_{135T-R}	–		7.111×10^{-6}		J/m^2
σ_{45T-R}	–		5.107×10^{-6}		J/m^2

Table 4.2 shows a comparison of interfacial widths and energies calculated at $T = T_{PPB} = 43\,^{\circ}\text{C}$ for the one- and two-dimensional BZT-40 BCT system. For interfacial widths, it is noted that $\xi^{2D}_{180TDW} \sim \xi^{1D}_{180TDW}$ and $\xi^{2D}_{180RDW} \sim \xi^{1D}_{180RDW}$. These results are in qualitative agreement with the analytical solution obtained considering a sixth-order Landau potential [68,71],

$$\xi = |P_{s,y'}|\sqrt{\frac{2K_P}{\Delta f}} \tag{4.17}$$

where Δf is the energy barrier between stable domains. For the T phase, using the same values for $\alpha_{1,T}$, $\alpha_{11,T}$ and $\alpha_{111,T}$ in the one- and two-dimensional models yields the same results for $P_{s,y'}$ and Δf, see Figure 4.1. Moreover, the same value for K_P is used in both cases, leading to equivalent results for ξ_{180TDW}. For the R phase, although $P_{s,y'}$ and Δf are different in both models, the ratio $|P_{s,y'}|/\sqrt{\Delta f}$ is approximately equal as a consequence of $\alpha_{12,R} = 0$, giving equivalent ξ_{180RDW} values. The latter is evidenced because $P^{2D}_{sR} = \sqrt{2}P^{1D}_{sR}$ and $\Delta f^{2D}_R \approx 2\Delta f^{1D}_R$ at $T = T_{PPB} = 43\,^{\circ}\text{C}$.

For interfacial energies, Table 4.2 indicates that $\sigma^{2D}_{180TDW} \sim \sigma^{1D}_{180TDW}$ and $\sigma^{2D}_{180RDW} \sim 2\sigma^{1D}_{180RDW}$. These results are also explained by the corresponding analytical solution[71]

$$\sigma = \frac{4}{3}C|P_{s,y'}|\sqrt{2K_P\Delta f} \tag{4.18}$$

where C is a correction factor defined as a function of $P_{s,y'}$ and the underlying α_1, α_{11} and α_{111} coefficients. For the T phase, equivalent interfacial energies are obtained in the one- and two-dimensional models as a consequence of the same values for $P_{s,y'}$, Δf and K_P. These values effectively produce similar volumetric and gradient free energy contributions across the 180TDW in both models. For the R phase, larger free energy contributions across the 180RDW are obtained in the two-dimensional model due to higher P_{sR}^{2D} and Δf_R^{2D} values, which result in greater interfacial energy.

The additional degree of freedom in the two-dimensional model allowed calculations for other types of interfaces, such as 90DWs, 45T-R interfaces and 135T-R interfaces. For the T-R interfaces, Table 4.2 reveals that the results from the one-dimensional model most closely resemble those for two-dimensional 45T-R interfaces. This is likely to be a result of the fact that, in both cases, the phase transformation occurs between domains with the same polarization orientation. In the one-dimensional model, direct transformation between rhombohedral and tetragonal domains with opposing polarization states, *i.e.,* a 180T-R interface, was inaccessible due to the large energy barrier between anti-parallel polarization states, see Section 3.4. Hence, results for one-dimensional T-R interfaces, indicated in Table 4.2, correspond to R↔T transformation between domains with the same polarization orientation.

Figure 4.5 illustrates the temperature dependence of the widths and energies of domain walls for the two-dimensional BZT-40 BCT system. For all types of domain walls, the interfacial width increases with temperature, Figure 4.5(a). This behaviour is in qualitative agreement with phenomenological results reported by Marton *et al.*[71] for $BaTiO_3$. Inspection of Equation 4.17 reveals that Δf implicitly depends on $\vec{P}_s$. It is the temperature dependence of the latter that determines the behaviour of the calculated widths. Hence, ξ values increase with temperature as a result of the corresponding decrease of $\|\vec{P}_s\|$. In particular, the widths of RDWs increase considerably as $T \rightarrow T_{C,R}$ (49.90 °C) due to the vanishing spontaneous polarization near the second order P-FE transition that occurs for the R phase at $T_{C,R}$. The latter effectively causes flattening of the free energy density f_R and the consequent vanishing energy barrier between rhombohedral domain states, *i.e.,* $\Delta f_R \rightarrow 0$ as $T \rightarrow T_{C,R}$.

Further, Figure 4.5(a) shows that $\xi_{180TDW} \approx \xi_{90TDW}$. This is attributed to the use of an isotropic polarization gradient energy coefficient K_P, which has been regarded as the most important factor influencing the interfacial width[71]. In fact, the polarization gradient energy coefficient is anisotropic in the general case, and its value depends on the crystallographic direction of the interface normal[71,102]. Notably, Figure 4.5(a) also reveals that $\xi_{180RDW} = \xi_{90RDW}$ for all temperatures. This is a consequence of the selected Landau coefficients for the R phase (with $\alpha_{12,R} = 0$), which yield $P_{s,y',180RDW}/P_{s,y',90RDW} = \sqrt{\Delta f_{180RDW}/\Delta f_{90RDW}}$, giving identical interfacial widths according to Equation 4.17.

Figure 4.5(b) indicates that the interfacial energy decreases with increasing temperature for all types of DWs in the two-dimensional BZT-40 BCT system. This result is attributed to the corresponding decrease of the energy barrier between stable FE domains, see Equation 4.18. For the R phase, the σ values approach zero as $T \rightarrow T_{C,R}$ due to flattening of the rhombohedral free energy density associated with its second order P-FE transition at $T_{C,R}$.

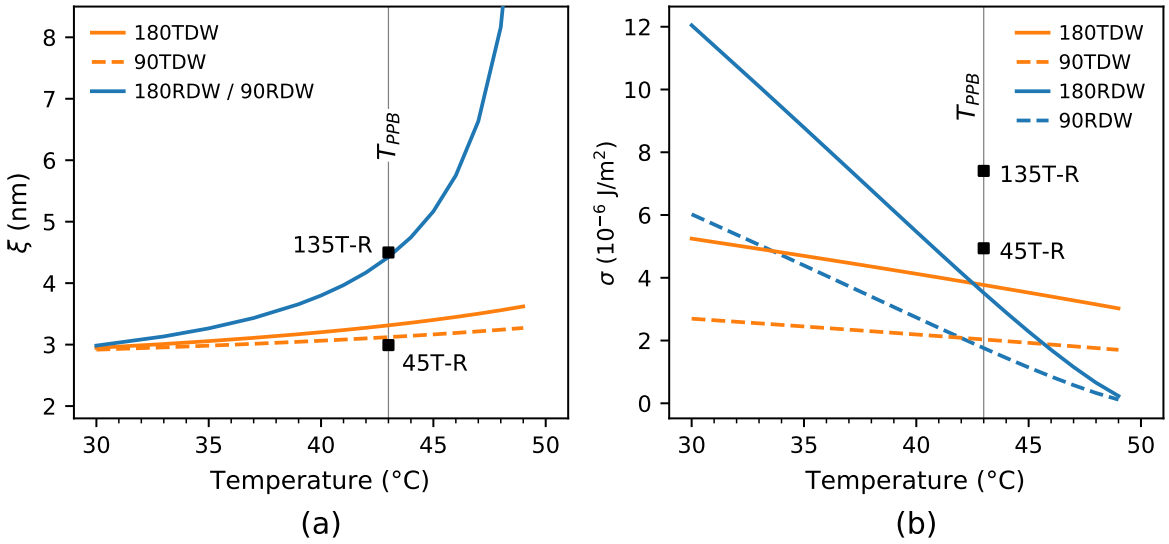

Figure 4.5: Temperature dependence of interfacial (a) widths and (b) energies for the two-dimensional, coarse-grained BZT-40 BCT system. At $T = 42\,^{\circ}\text{C}$, the interfacial energies of 180DWs and 90DWs are approximately equal in each phase, *i.e.*, $\sigma_{180TDW} \approx \sigma_{180RDW}$ and $\sigma_{90TDW} \approx \sigma_{90RDW}$.

For both FE phases, $\sigma_{180DW} > \sigma_{90DW}$ due to greater energy barriers between anti-parallel stable polarization states associated with 180DWs. Moreover, larger polarization switching, $\Delta u_{y'} = \Delta P_{y'}/|P_{sT}|$, is observed across 180DWs compared to that related to 90DWs, Figures 4.2 and 4.3. For the T phase, $\Delta u_{y',180DW} = 2.000$ and $\Delta u_{y',90DW} = 1.414$. For the R phase, $\Delta u_{y',180DW} = 2.330$ and $\Delta u_{y',90DW} = 1.647$. Hence, greater volumetric and gradient free energy contributions are obtained across 180DWs.

Figure 4.5(b) also shows greater energy values associated with T-R interfaces compared to those for domain walls at $T = T_{PPB}$, the only temperature where both phases are stable. Results are explained by changes in the phase field across T-R interfaces that produce additional volumetric and gradient free energy contributions. In this MPF model, the volumetric free energy density of the two-phase FE system includes a double-well potential that acts as an energy barrier for phase transformations, see Equation 2.4. This results in an increased volumetric free energy associated with T-R interfaces. The formulation of the MPF model also includes an additional gradient energy term that penalizes the formation of phase interfaces due to changes in the phase field, see Equation 2.3. Thus, an increased gradient free energy density is obtained across T-R interfaces. The additional phase-field gradient term in the MPF model allows to control the energy associated to phase interfaces separately from that of domain walls in either phase.

4.5.2 Time-temperature-transformation (TTT) diagrams

Two TTT diagrams were constructed using the two sets of simulations for the microstructural evolution of the two-phase FE system in the absence of applied electric fields. The volume fraction transformed of FE phases was measured by ψ, where $\psi = \overline{\phi}$ at $T > T_{PPB}$ and $\psi = 1 - \overline{\phi}$ at $T < T_{PPB}$. Transformation times for constant fraction transformed were calculated as the average from the fifteen simulations at each selected temperature.

Figure 4.6 shows a comparison of the TTT diagrams obtained for one- and two-dimensional BZT-40 BCT without solving Coulomb's Equation. In both cases, the T and R phases are more likely to coexist in the vicinity of the T_{PPB}, and R + T metastable coexistence persists for longer times at $T_{PPB} < T < T_{C,R}$. However, faster transformations towards $\psi \rightarrow 1$ are predicted for all temperatures in the two-dimensional model compared to the 1-D model. This is facilitated by access to additional, low-energy polarization configurations, such as 90DWs, to minimize the free energy of the 2-D system. For $T_{PPB} < T < T_{C,R}$, Figure 4.6 shows that phase transformations are particularly faster in the two-dimensional model. The latter is partly because the phase transformation-induced polarization rotation mechanism, identified in Section 3.6.3 as a means to extend domain coexistence in one-dimensional BZT-40 BCT, is limited in the 2-D model by relatively higher interfacial energy of RDWs and T-R phase boundaries, see Table 4.2.

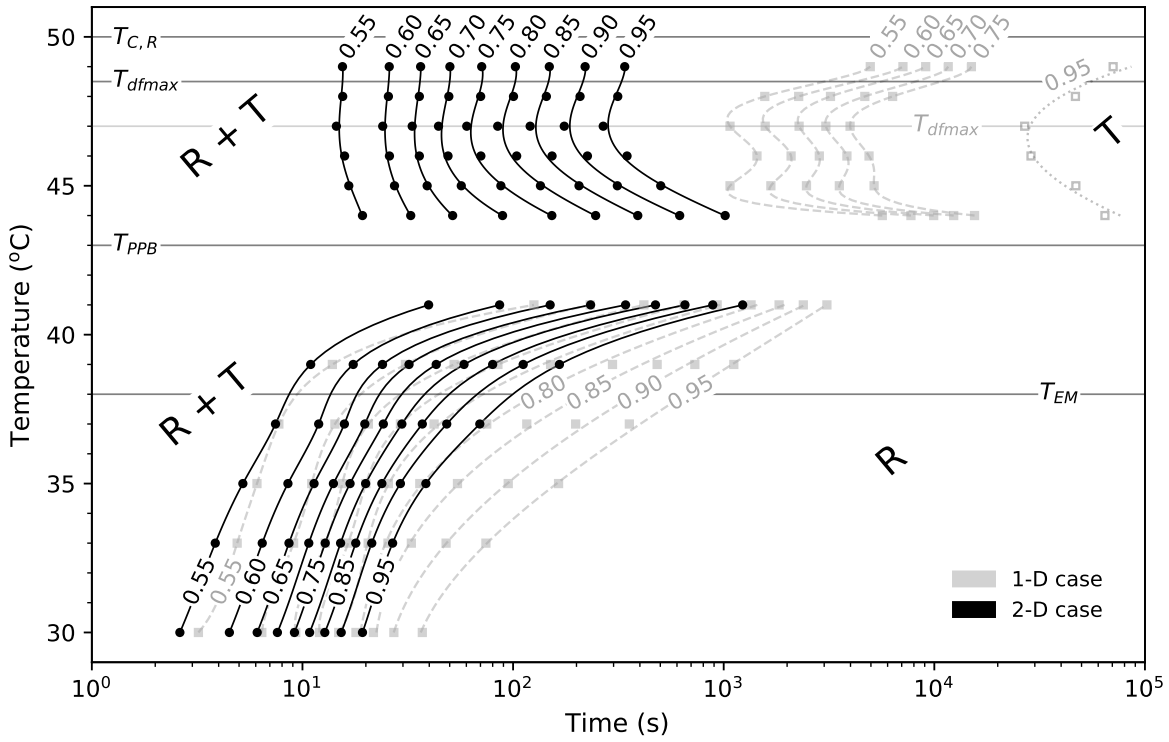

Figure 4.6: Comparison of TTT diagrams for the one- and two-dimensional BZT-40 BCT systems. Local electric fields within the material are not solved, *i.e.,* $V_E(x, y) = 0$. Both diagrams show transformation from mixed 50%R+50%T state towards stable single phase as $\psi \rightarrow 1$ at each temperature. Markers indicate mean times for constant fraction transformed calculated from fifteen simulations, and splines are included as a guide for the eye. The temperature $T_{df\,max}$ at which the driving force for formation of T phase is maximal is shown for each model. T_{EM} is the temperature at which the mobilities of the FE phases are equal. Since the same mobilities are used in each case, T_{EM} is common to both models. Overall, faster transformations are observed in the 2-D system.

In Figure 4.6, no data was reported at $T = 42$ °C because simulations showed occasional relaxation of the metastable T phase, *i.e.,* R+T $\rightarrow$ T, instead of the expected transformation towards the stable R phase. These results are explained by the vanishing macroscopic driving force for FE phase transformation, Figure 4.7(a), and by the equivalent interfacial energies of 180DWs and 90DWs in both phases at $T = 42$ °C, as shown in Figure 4.5(b).

Moreover, Figure 4.7(a) compares the thermodynamic driving force for phase transformation in the one- and two-dimensional models. The additional degree of freedom in the two-dimensional system affects the volumetric free energy density of the stable rhombohedral polarization states, resulting in a greater difference between free energy minima of the T and R phases, Δf_{min}, Figure 4.7(b). Thus, the macroscopic driving force for transformation towards the stable FE phase is greater in the two-dimensional model for all temperatures. The latter explains the rapid kinetics of phase transformation observed in two-dimensional simulations, particularly for $T_{PPB} < T < T_{C,R}$, where the macroscopic driving force is very small in the one-dimensional case.

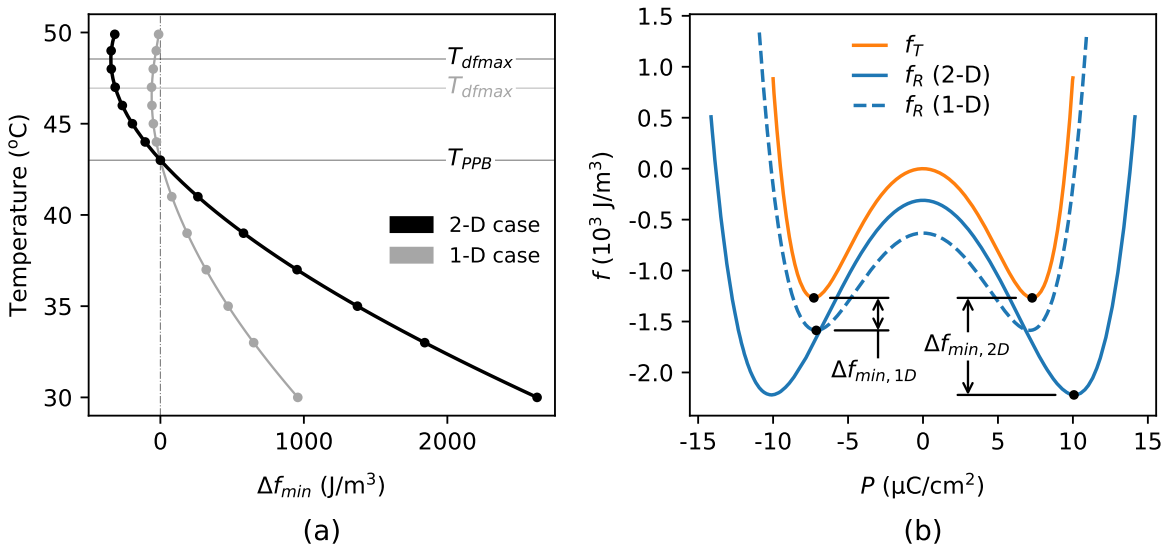

Figure 4.7: (a) Thermodynamic driving force for transformation of FE phases, $\Delta f_{min} = f_T(\vec{P} = \vec{P}_{sT}; \vec{E} = \vec{0}, T) - f_R(\vec{P} = \vec{P}_{sR}; \vec{E} = \vec{0}, T)$, for the one- and two-dimensional BZT-40 BCT systems. (b) Volumetric free energy densities at $T = 37\,°C$, showing calculation of Δf_{min} for the one- and two-dimensional models. For the 2-D case, f_T is calculated along the $\langle 10 \rangle$ directions and f_R is calculated along the $\langle 11 \rangle$ directions. The free energy density of the T phase is equal in both models due to symmetry considerations.

For the one-dimensional model, the coexistence time of FE phases increases considerably in the $T_{df\,max} < T < T_{C,R}$ region as $T \rightarrow T_{C,R}$. In Section 3.6.3, this result was connected to vanishing σ_{RDW}, due to the second order P-FE transition for the R phase at $T_{C,R}$, and vanishing macroscopic driving force, due to the underlying Landau coefficients. For the two-dimensional model, the coexistence time is also observed to increase as $T \rightarrow T_{C,R}$. However, the effect is significantly smaller due to the driving force at $T_{C,R}$ not approaching zero in the 2-D case, Figure 4.7(a).

Figure 4.8 illustrates the effect of local electric fields, *i.e.,* solving Equations 4.8 through 4.11, on the transformation kinetics in two-dimensional BZT-40 BCT. Overall, the coexistence time of FE phases increases when the local electric fields within the material are considered. This result can be attributed to the restriction imposed by Coulomb's Equation on the possible domain configurations to minimize the total free energy of the system, which increases the likelihood of extended metastable coexistence. At $T = 41\,°C$, results suggest that the allowed domain configurations are able to better balance the excess energy associated to the different interfaces producing considerably longer coexistence times.

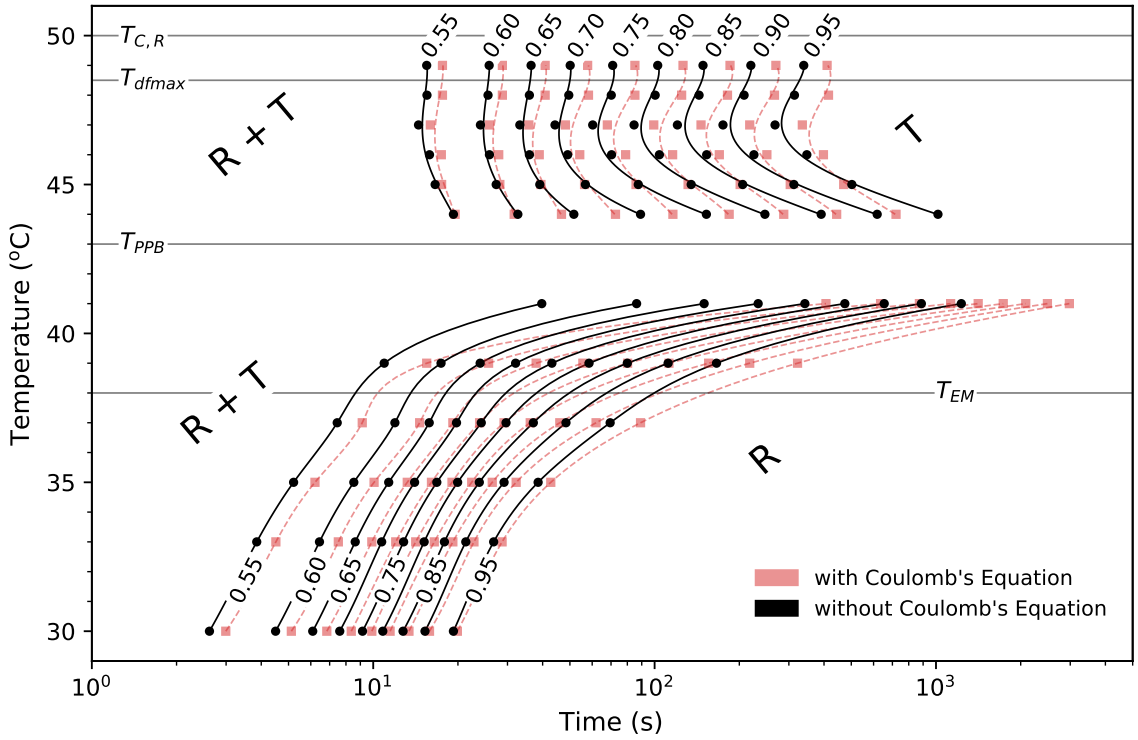

Figure 4.8: TTT diagrams showing the effect of local electric fields in the two-dimensional, coarse-grained BZT-40 BCT system. Both diagrams show transformation from mixed 50%R+50%T state towards stable single phase as $\psi \rightarrow 1$ at each temperature. Markers indicate mean times for constant fraction transformed calculated from fifteen simulations, and splines are included as a guide for the eye. Overall, local electric fields extend R + T metastable coexistence.

The TTT relations were examined for different PPB temperatures using the two-dimensional implementation of the coarse-grained BZT-40 BCT model with local electric fields, Figure 4.9. Results show that the choice of T_{PPB} does not affect qualitatively the overall transformation kinetics of the FE phases. For all cases in Figure 4.9, the T and R phases coexist for longer times as $T \rightarrow T_{PPB}$, a thermodynamic upper coexistence limit is predicted at $T_{C,R} = 49.90\,°C$, and the R + T metastable coexistence is kinetically limited at low temperatures. Quantitative differences are explained by changes in the temperature dependence of the macroscopic driving force for phase transformation, Δf_{min}, Figure 4.10.

4.5.3 Ferroelectric domain structures

Results from the microstructural evolution simulations are used to investigate the domain structure of two-phase FE systems. Figures 4.11 and 4.12 illustrate the effect of local electric fields on the domain structure of the two-phase FE system in the absence of an applied macroscopic electric field. If the local fields within the material are ignored, simulation results show head-to-head and tail-to-tail domain wall configurations that are physically unrealistic. Furthermore, when local electric fields are omitted, the microstructure consists of irregularly shaped FE domains, see Figures 4.11 and 4.12 (left column). This morphology is explained by isotropic domain wall energies, obtained as a consequence of the isotropic polarization gradient energy coefficient K_P.

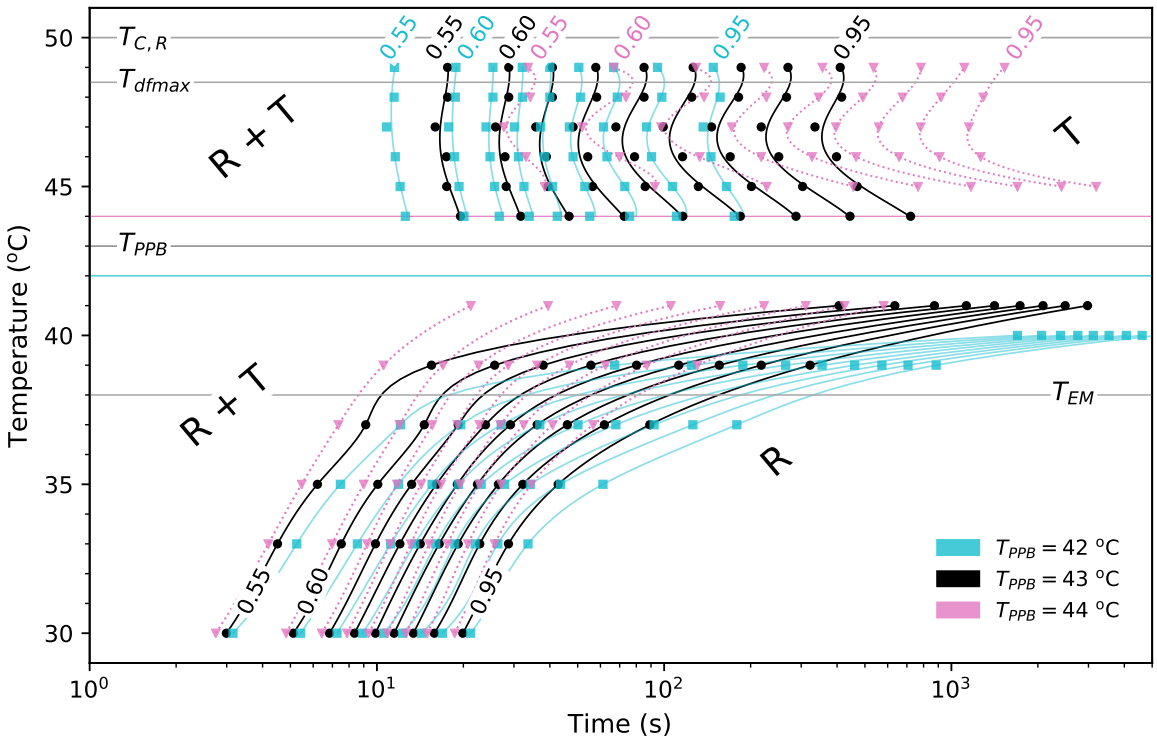

Figure 4.9: TTT diagrams showing the effect of the choice of T_{PPB} in the two-dimensional, coarse-grained BZT-40 BCT system with local electric fields. Each TTT diagram shows the progression from random mixed 50%R+50%T phase conditions towards the stable FE phase as $\psi \rightarrow 1$ at each temperature. Markers indicate mean times for constant fraction transformed calculated from fifteen simulations (for T_{PPB} = 43 °C) and from five simulations (for T_{PPB} = 42 °C and 44 °C). Splines are included as a guide for the eye. Results show qualitative agreement regardless of the selected T_{PPB}.

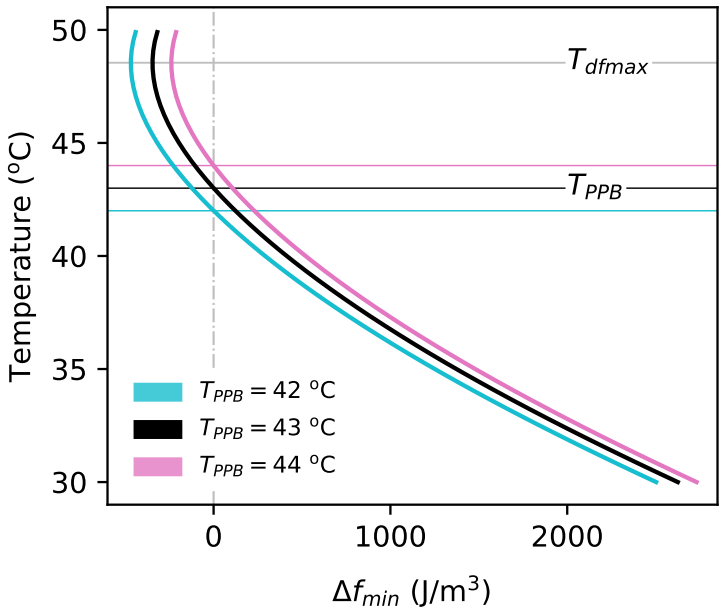

Figure 4.10: Effect of the choice of T_{PPB} on the thermodynamic driving force for transformation of FE phases, Δf_{min}, for the two-dimensional, coarse-grained BZT-40 BCT system. For all cases, there is a local maximum in driving force at T_{dfmax} for the R+T→T transformation.

In contrast, solving for the local electric fields produces predictions that are consistent with polarization patterns typically found in FE systems, as reported in experimental studies[78,86,103–111] and related computational work[39–44,46,112]. Specifically, results show that local electrostatic interactions are responsible for FE domains with head-to-tail polarization configurations, see Figures 4.11 and 4.12 (right column). Including the mechanical coupling into the model to take into account long-range elastic interactions would additionally produce twin-like domain structures in the single-phase regions. This configuration is known to be adopted to accommodate the lattice distortions between structural variants of each FE phase[39,41,43,51].

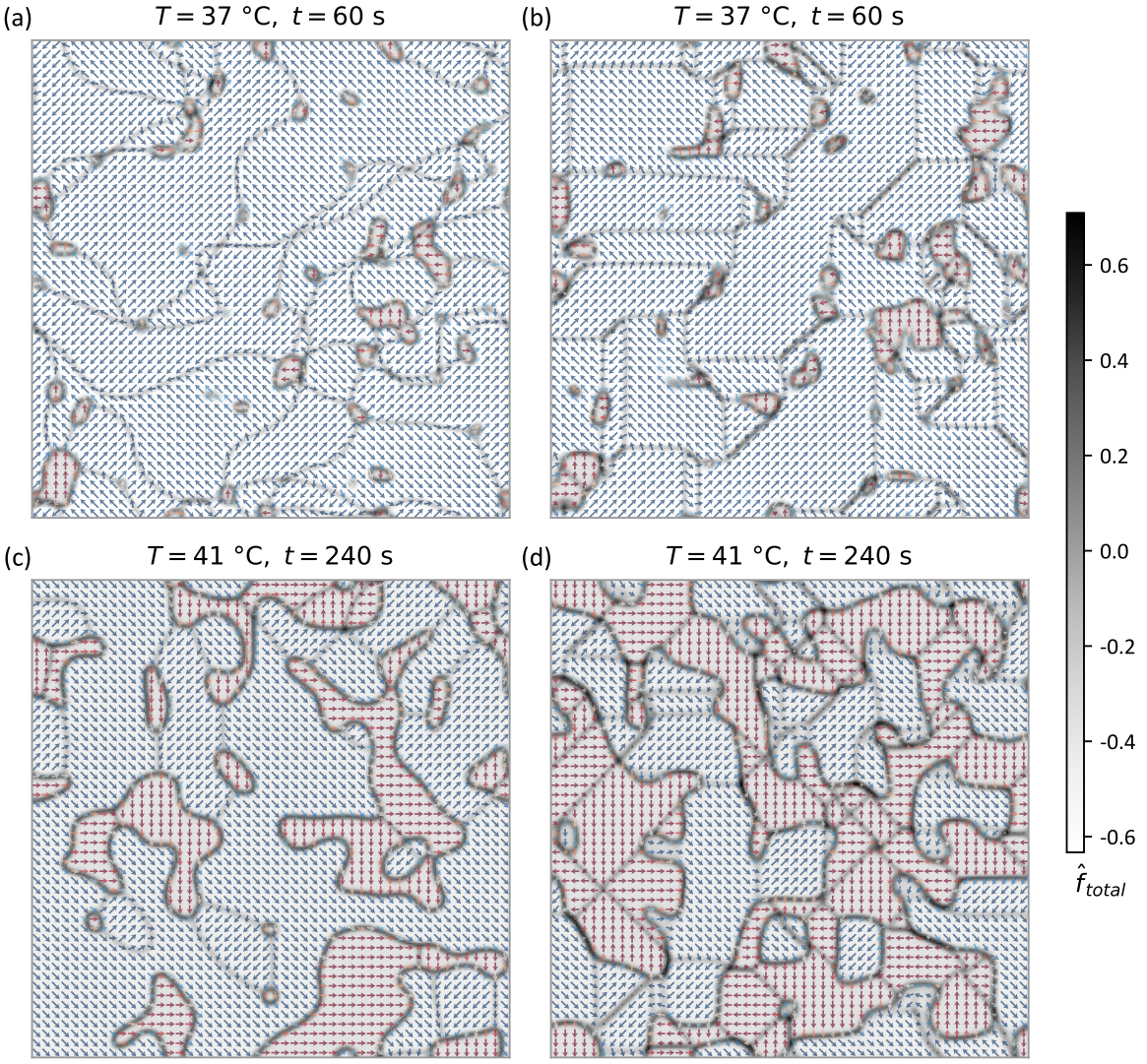

Figure 4.11: Effect of local electric fields on domain morphology for $T < T_{PPB}$ in the two-dimensional BZT-40 BCT system. Left column: results without solving Coulomb's Equation. Right column: results considering local electric fields according to Coulomb's Equation. Subfigures show simulation results at (a)-(b) $T = 37\,°C$, $t = 60\,s$, and (c)-(d) $T = 41\,°C$, $t = 240\,s$. The computational domain size is $223\,nm \times 223\,nm$. For all cases, the contour plot represents the dimensionless total free energy density, $\hat{f}_{total} = f_{total}/(|\alpha_{1,T}|P_{sT}^2)$, and the vector plot represents the dimensionless polarization, $\vec{u} = \vec{P}/|P_{sT}|$. Arrows are coloured by the phase-field value showing, in this case, stable rhombohedral domains (➔) and metastable tetragonal domains (➔).

Moreover, when local electric fields are included, results reveal microstructures consisting of FE

domains with faceted and curved interfaces, Figures 4.11 and 4.12 (right column). Facets correspond to domain walls oriented at specific angles, suggesting highly anisotropic interfacial energies. This is attributed to the system energetics being dominated by the electrostatic free energy contribution, induced by large electrostatic-potential fields that result from $\nabla \cdot \vec{P}$ when domain walls are oriented at angles different from their stable configuration. Hence, facets adopt these low-energy orientations to accommodate non-uniform local electric fields (according to Coulomb's Equation) and minimize the total free energy of the system.

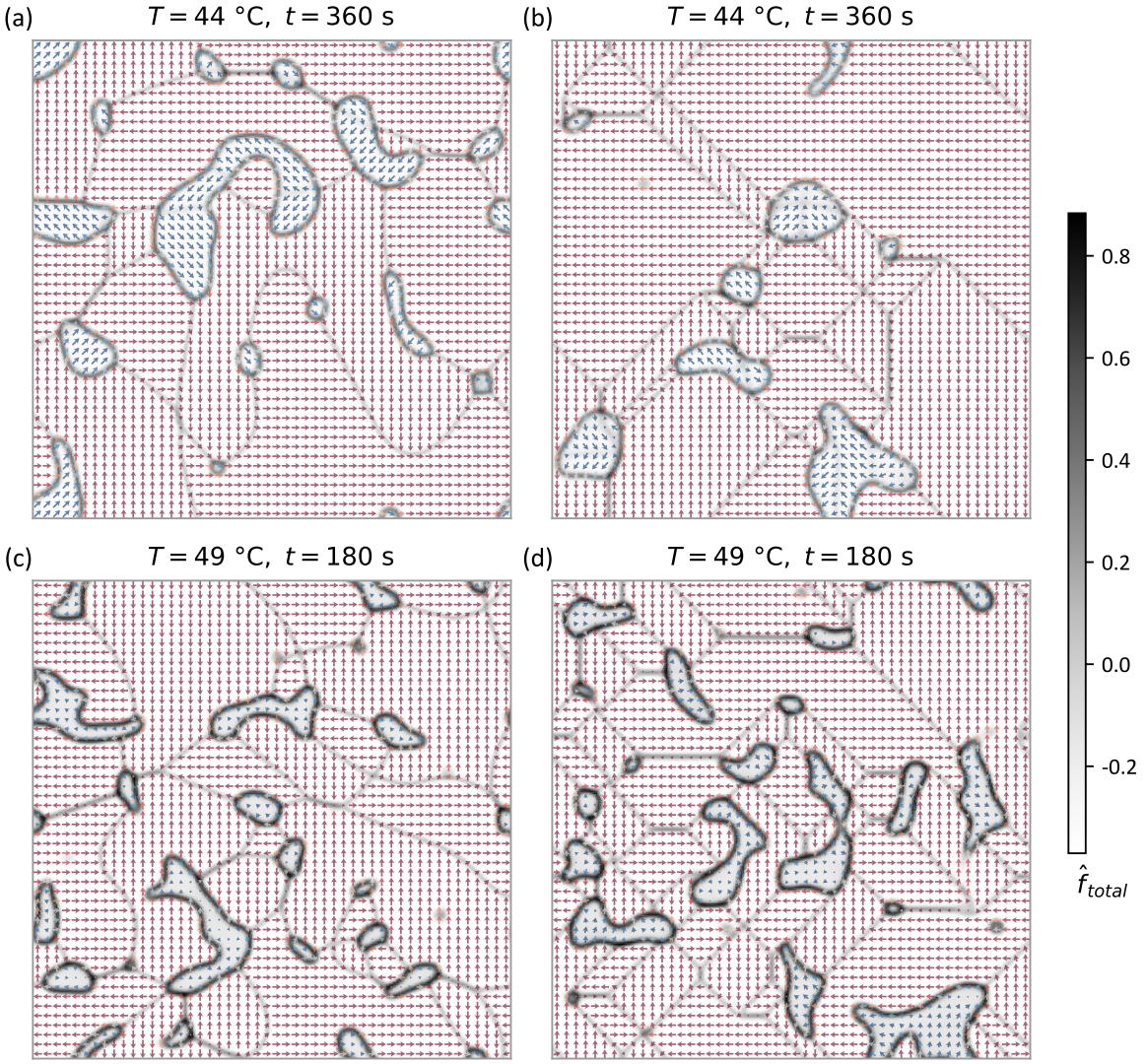

Figure 4.12: Effect of local electric fields on domain morphology for $T > T_{PPB}$ in the two-dimensional BZT-40 BCT system. Left column: results without solving Coulomb's Equation. Right column: results considering local electric fields according to Coulomb's Equation. Subfigures show simulation results at (a)-(b) $T = 44\,°C$, $t = 360\,s$, and (c)-(d) $T = 49\,°C$, $t = 180\,s$. The computational domain size is $223\,nm \times 223\,nm$. For all cases, the contour plot represents the dimensionless total free energy density, $\hat{f}_{total} = f_{total}/(|\alpha_{1,T}|P_{sT}^2)$, and the vector plot represents the dimensionless polarization, $\vec{u} = \vec{P}/|P_{sT}|$. Arrows are coloured by the phase-field value showing, in this case, metastable rhombohedral domains (➔) and stable tetragonal domains (➔).

The angles of the domain walls reveal the orientation relationship between domains in the same FE phase: 90DWs are positioned such that they bisect the angle between the polarization vectors of

the stable domains, and 180DWs are aligned parallel to the stable polarization vectors. For the T phase, 90DWs are oriented parallel to the ⟨11⟩ directions, *i.e.,* at 45°, 135°, 225° and 315° with respect to the global coordinate system; while 180DWs are oriented parallel to the ⟨10⟩ directions. For the R phase, 90DWs are oriented parallel to the ⟨10⟩ directions and 180DWs are oriented parallel to the ⟨11⟩ directions. These domain patterns have been observed experimentally in numerous TEM studies, see Figure 4.13 for an example.

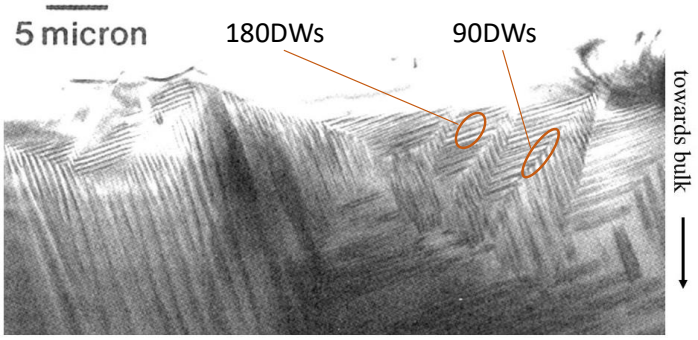

Figure 4.13: TEM image of tetragonal $BaTiO_3$, as reported by Krishnan *et al.*[103], showing typical FE domain structure consisting of faceted 180DWs and 90DWs.

The curved boundaries, observed in Figures 4.11 and 4.12 when local fields are considered, correspond to T-R phase interfaces. This morphology has been observed experimentally near the PPB of the BZT-50 BCT system in TEM studies[108,111]. In order to explain the formation of faceted domain walls and curved phase interfaces in the simulated microstructures, schematic γ-plots are presented in Figure 4.14(a) for a 180TDW and a 45T-R phase interface at $T = T_{PPB} = 43\,^{\circ}\mathrm{C}$. A γ-plot represents a polar plot of interfacial energy as a function of orientation (inclination) of the interface normal. Isotropic interfacial energies have circular γ-plots with radius equal to the interfacial energy, while interfaces with highly anisotropic interfacial energies exhibit cusped minima at low-energy inclinations. Direct calculation of γ-plots was beyond the scope of this work. Here, schematic γ-plots are constructed calculating the interfacial charge density as a proxy, *i.e.,* $\Delta\vec{P}\cdot\hat{n}$, where $\hat{n}$ is the interface normal vector[51].

Figure 4.14(a) shows in black the estimated γ-plot for a 180TDW between a domain with $\vec{P} = (0, P_{sT})$ and another with $\vec{P} = (0, -P_{sT})$, such that $\Delta\vec{P}\cdot\hat{n} = (0, -2P_{sT})\cdot(\cos\theta, \sin\theta)$, where θ is the polar angle. Also, an estimated γ-plot is shown in blue for a 45T-R interface between a rhombohedral domain with $\vec{P} = (P_{sR}/\sqrt{2}, P_{sR}/\sqrt{2})$ and a tetragonal domain with $\vec{P} = (P_{sT}, 0)$, such that $\Delta\vec{P}\cdot\hat{n} = (P_{sT} - P_{sR}/\sqrt{2}, -P_{sR}/\sqrt{2})\cdot(\cos\theta, \sin\theta)$. Figure 4.14(a) indicates that the minimum interfacial energy of 180TDWs is lower than that of 45T-R phase interfaces. However, the energy penalty to form a 180TDW at orientations different from their lowest energy configuration is significantly higher than that associated with 45T-R interfaces. These results suggest that T-R phase interfaces are less anisotropic than domain walls. Hence, in a network of two phases, where the domains in each phase have preferred domain wall orientations, the network is accommodated by curved phase interfaces to minimize the total free energy of the system.

Moreover, Figure 4.14(a) shows that the lowest energy configuration of the 180TDW occurs when the boundary is parallel to the $[0, 1]$ direction, as evidenced by the opposite cusps located at

0°. This orientation is in agreement with the configuration depicted in Figure 4.2(a) and is valid for all temperatures. In addition, Figure 4.14(a) reveals that the lowest energy configuration of the 45T-R phase interface is obtained when its normal is oriented at 12.1°. This result is consistent with the boundary inclination of approximately 12.8° obtained in Figure 4.4(b) at $T = T_{PPB} = 43\,°C$. However, in contrast to domain walls, the orientation associated with the lowest energy configuration of phase interfaces depends on temperature. For the 45T-R phase interface evaluated here, the orientation of the cusps is given by $\theta_{45T-R} = \arctan(\sqrt{2}P_{sT}/P_{sR} - 1)$, where θ_{45T-R} is the angle of the interface normal obtained from $\Delta\vec{P}\cdot\hat{n} = 0$. The temperature dependence of θ_{45T-R} is shown in Figure 4.14(b).

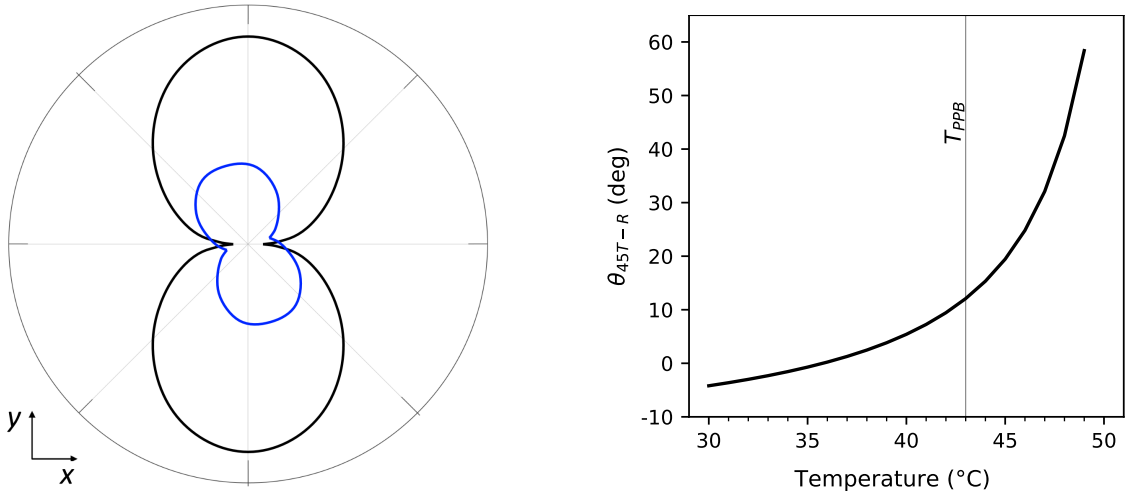

(a) (b)

Figure 4.14: (a) Schematic γ-plots for 180TDWs (—) and 45T-R interfaces (—), showing interfacial energies as a function of orientation of the interface normal at $T = T_{PPB} = 43\,°C$. A 180TDW is considered between two domains with $\vec{P} = (0, P_{sT})$ and $\vec{P} = (0, -P_{sT})$, respectively. A 45T-R phase interface is considered between a rhombohedral domain with $\vec{P} = (P_{sR}/\sqrt{2}, P_{sR}/\sqrt{2})$ and a tetragonal domain with $\vec{P} = (P_{sT}, 0)$. The relatively low anisotropy of phase interfaces compared to that of DWs, along with the smaller energy penalty to form phase boundaries at orientations different from their low-energy configuration, explains the FE domain structures consisting of faceted DWs and curved phase interfaces. (b) Temperature dependence of the lowest energy orientation of 45T-R phase interfaces.

The simulated two-dimensional domain structures also show that domains of the metastable FE phase enable polarization rotation between domains of the stable phase, see Figure 4.11 and Figure 4.12. These results support the phase transformation-induced polarization rotation mechanism, proposed in Section 3.6.3, as a means to extend metastable coexistence of FE phases in the vicinity of the PPB. The proposed mechanism for switching and domain coexistence is favoured at $T > T_{PPB}$ due to the increased thermal energy available in the system and the relatively small energy barrier for polarization switching in the metastable R phase. It is further promoted as $T \rightarrow T_{C,R}$ because of the vanishing Δf_R. The presence of metastable domains has been simulated by Rao and Wang[51] for PZT near its morphotropic phase boundary (MPB). They concluded that domains of the metastable phase spontaneously coexist with and act as bridges for polarization switching between regions of the stable phase in order to minimize the total free energy of the system. In the work presented herein, further insight is provided into the specific mechanism controlling metastable coexistence and phase transformation-induced polarization switching in two-phase FE systems.

4.5.4 Domain size and domain coarsening calculations

Domain size was examined using the simulations for the field-free microstructural evolution of a two-phase FE system considering the spatial variation of local electric fields, *i.e.,* solving Equations 4.8 through 4.11. For each simulation temperature, data was extracted at $t = 100$ s, 200 s and 300 s. Examples of the simulated two-phase microstructure are shown in Figure 4.15 for selected temperatures at $t = 200$ s. For each simulation run and time-temperature combination, the mean domain size (area) was calculated using the package scikit-image[113] for image processing in python. This analysis was performed on rhombohedral domains and tetragonal domains separately, and on the combined data set. Average rhombohedral, tetragonal and overall domain sizes, along with 95 % confidence intervals, were estimated from the fifteen simulations using a non-parametric bootstrap method[114].

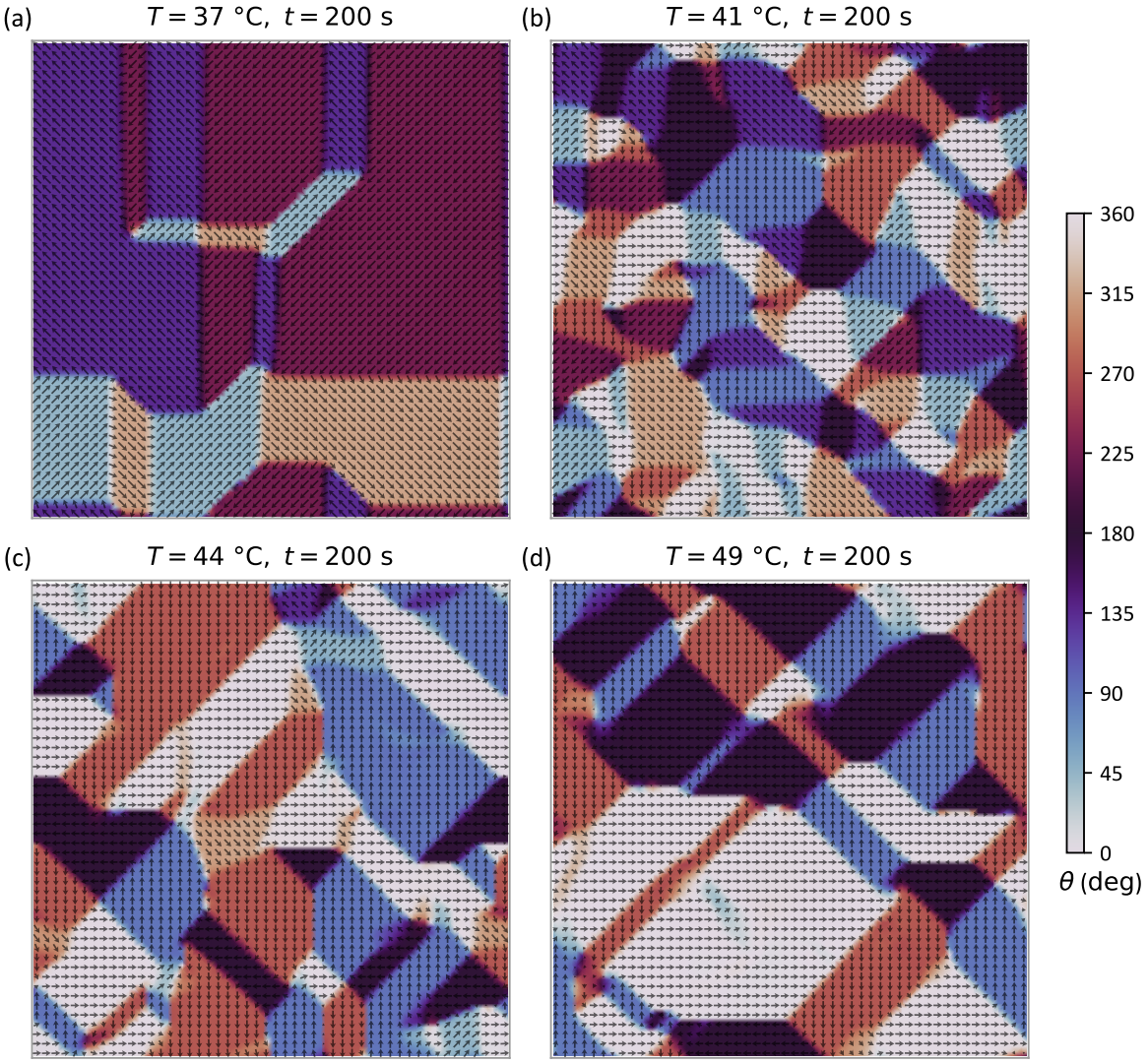

Figure 4.15: Domain structure for two-dimensional, coarse-grained BZT-40 BCT polycrystal at $t = 200$ s and (a) $T = 37\,^{\circ}$C, (b) $T = 41\,^{\circ}$C, (c) $T = 44\,^{\circ}$C, and (d) $T = 49\,^{\circ}$C. The computational domain size is 223 nm × 223 nm. Arrow plots represent the normalized polarization vector, $\vec{u} = \vec{P}/|P_{sT}|$, and contour plots correspond to polarization orientation, $\theta = \text{atan2}(u_y, u_x)$.

For $T = 37\,^{\circ}$C, Figure 4.15(a) shows that the microstructure consists mainly of relatively large domains of the stable R phase. Similarly, for $T = 49\,^{\circ}$C, Figure 4.15(d) shows that the two-phase

microstructure is dominated by large stable tetragonal domains. However, Figure 4.15(b)-(c) show that the overall size of FE domains decreases as $T \rightarrow T_{PPB}$, where the R and T phases metastably coexist for longer periods of time. These observations are consistent with the miniaturization of the domain structure reported experimentally in the BZT-x BCT system near its PPB [86,105,108–111].

The average domain sizes and corresponding volume fraction transformed of FE phases are plotted as a function of temperature for a simulation time of $t = 200$ s, Figure 4.16(a) and Figure 4.16(b). Results confirm that the total average domain size, *i.e.,* considering the rhombohedral and tetragonal

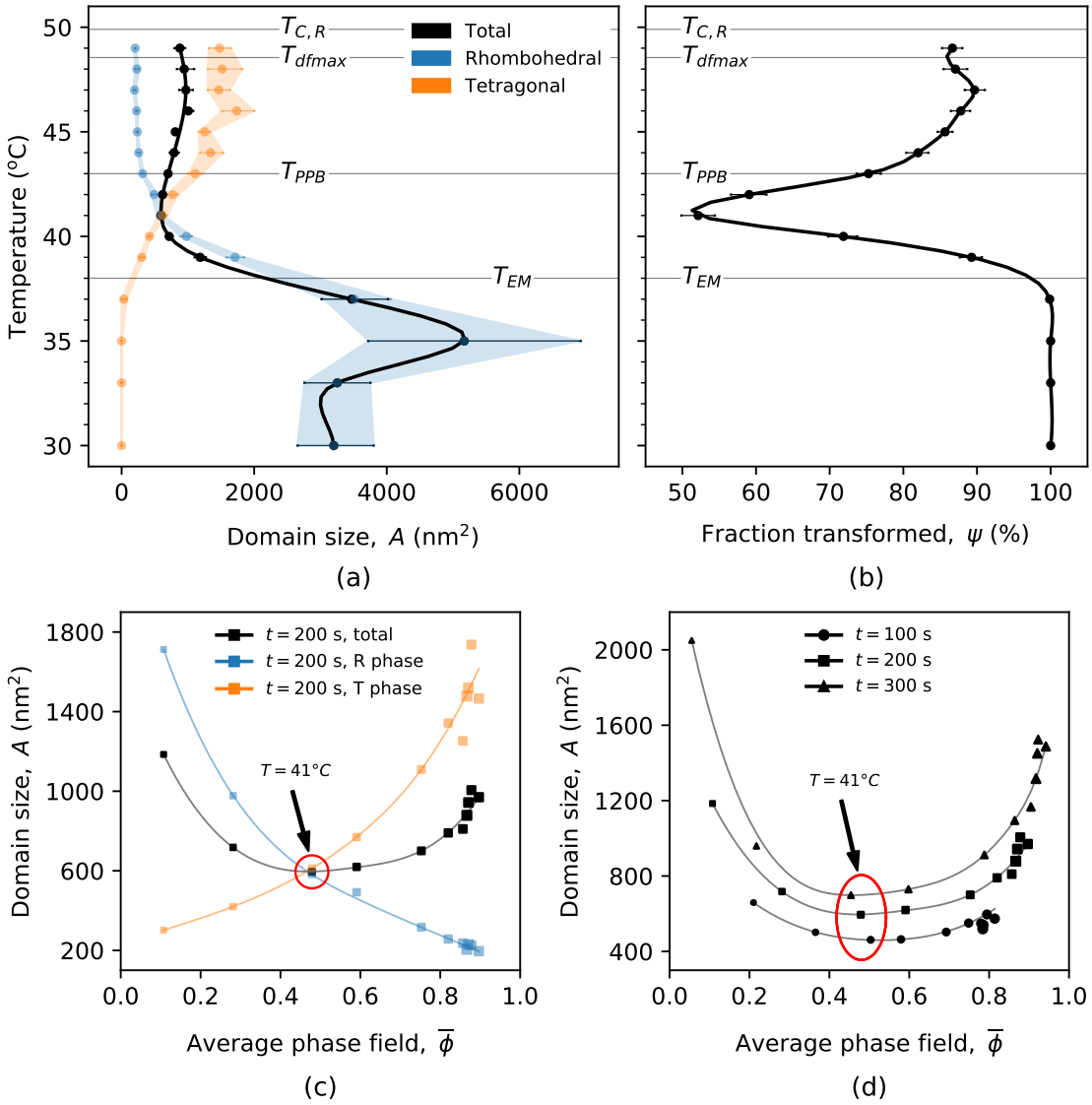

Figure 4.16: Domain size calculations for two-dimensional, coarse-grained BZT-40 BCT polycrystal simulated from mixed 50%R+50%T initial state. Temperature dependence is illustrated at $t = 200$ s for (a) average domain sizes, and (b) volume fraction transformed of FE phases. Error bars correspond to 95 % confidence intervals. (c) Parametric plots of average phase field versus domain size are shown at $t = 200$ s for rhombohedral, tetragonal and combined domains separately. (d) Parametric plots of average phase field versus domain size are shown for combined rhombohedral and tetragonal domains at $t = 100$ s, 200 s and 300 s. The increase in marker size indicates increasing temperature. Data points corresponding to the minimum overall domain size are ringed in red. Splines are included as a guide for the eye.

domains, decreases within the regime where both FE phases coexist. In this study, the average equivalent circle diameter (ECD) of ferroelectric domains in the vicinity of the PPB is 25 – 35 nm, which is within the 10 – 60 nm range observed in experiments for the BZT-x BCT system, as stated by Acosta *et al.* [16].

Figure 4.16(a)-(b) also shows that the minimum total domain size is obtained at $T \sim 41\,°C$, which corresponds to a mixed 50%R+50%T metastable state ($\psi \sim 0.5$). The latter is evidenced by the additional polarization directions that are favoured energetically to minimize the total free energy of the system, see Figure 4.15(b). Gao *et al.* [88] have argued that the vanishing polarization anisotropy is the source of miniaturization of the domain structure observed experimentally near interferroelectric phase boundaries. Further, results for $T < 41\,°C$ indicate that the total average domain size increases rapidly as $\psi \rightarrow 1$ towards the stable R phase; whereas for $T > 41\,°C$, the increase of average domain size is less pronounced as $\psi \rightarrow 1$ towards the stable T phase. This is attributed to the phase transformation-induced polarization rotation mechanism, which is favoured at high temperatures and promotes the formation of minor domains of the metastable R phase between larger domains of stable T phase.

Figure 4.16(c) shows that the average size of tetragonal domains increases with temperature within the coexistence region as the volume fraction of the T phase increases, *i.e.,* as $\overline{\phi} \rightarrow 1$. Similarly, the average size of rhombohedral domains increases with increasing fraction of the R phase as $\overline{\phi} \rightarrow 0$ towards low temperatures. The minimum average domain size of the entire system is obtained when the average size of rhombohedral and tetragonal domains is approximately equal at $\overline{\phi} \approx 0.5$. Further, Figure 4.16(d) shows similar behaviour at different times ($t = 100\,s,\ 200\,s$ and $300\,s$). As the simulations progress, the system relaxes towards the stable single phase, yielding larger domain sizes. However, small changes are noted near the T_{PPB} due to the extended metastable coexistence of the R and T phases.

In this study, domain coarsening rate constants, k, were calculated for the T and R phases using simulation data from mixed- and single-phase initial conditions at $t = 100\,s,\ 200\,s$ and $300\,s$. Despite highly anisotropic domain wall energies, parabolic growth was the simplest model that represented the kinetics of domain coarsening in the single-phase regions reasonably well. The use of parabolic growth kinetics provided a consistent method for extracting coarsening rate constants from mixed- and single-phase simulations to examine the effect of phase coexistence on domain growth. Hence, for each simulation, rhombohedral and tetragonal domain coarsening constants were estimated at each temperature by fitting the equation $A - A_o = kt$ to domain size versus time. Figure 4.17 illustrates the calculation method for a two-FE-phase system using data from three simulations at $T = 42\,°C$, yielding three k values for each phase. Then, mean k values were calculated at each temperature from the fifteen simulations using a non-parametric bootstrap method [114]. Figure 4.18(a) shows the average domain coarsening rate constants as a function of temperature for the R and T phases under mixed-phase initial conditions.

For $T < T_{PPB}$, Figure 4.18(a) shows that the growth rate of stable rhombohedral domains decreases with increasing temperature under mixed-phase conditions. This is explained by the vanishing driving force for R+T $\rightarrow$ R phase transformation as $T \rightarrow T_{PPB}$, see Figure 4.7(a). Similarly, for $T > T_{PPB}$, the coarsening rate constant of stable tetragonal domains decreases as $T \rightarrow T_{PPB}$ due to

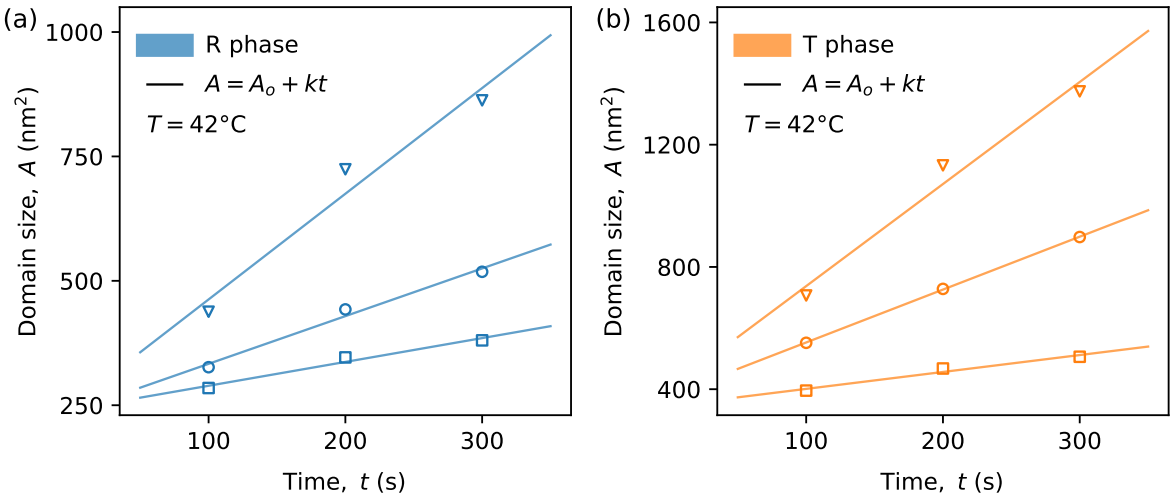

Figure 4.17: Calculation of domain coarsening rate constants, k, for the (a) R (—) and (b) T (—) phases of two-dimensional, coarse-grained BZT-40 BCT polycrystal at $T = 42\,°C$. For each phase, three simulations from mixed-phase initial conditions are used to illustrate the calculation of three different domain coarsening constants.

the corresponding decrease in the driving force for R+T $\rightarrow$ T phase transformation. Figure 4.18(a) also indicates that the coarsening constants of rhombohedral and tetragonal domains under mixed-phase condition are approximately equal at $T = 42\,°C$. This result further explains the occasional relaxation of the metastable T phase discussed in Section 4.5.2, attributed to vanishing driving force for phase transformation, Figure 4.7(a), and equivalent interfacial energies of 180DWs and 90DWs in both phases, Figure 4.5(b).

The analysis described above was also performed for the microstructural evolution on single-phase ferroelectrics to calculate intrinsic domain coarsening constants for each FE phase and isolate the effect of phase coexistence on domain growth. Figure 4.18(b) shows the temperature dependence of domain coarsening constants for the R phase, obtained from single-phase simulations for $T \leq T_{PPB}$; and for the T phase, obtained from single-phase simulations for $T \geq T_{PPB}$. Figure 4.18(b) shows that the intrinsic domain coarsening rates for the stable R phase tend to increase with increasing temperature. This is explained by a rise in mobility values as temperature increases, see Figure 3.13(b). Similarly, results show that the intrinsic domain coarsening rate for the stable T phase generally decreases as the temperature increases due to a corresponding decrease in mobility.

Results from mixed- and single-phase simulation are compared in Figure 4.18(c). It is evident that, for a two-phase FE system, the evolution of domains (single-phase regions) is affected by competing effects of intrinsic domain coarsening and FE phase transformation. Furthermore, the opposite trends of k with respect to temperature under mixed- and single-phase system conditions suggest that, when both FE phases coexist, the effect of phase transformation dominates over the intrinsic domain coarsening.

In single-phase scenarios, all FE domains have the same volumetric free energy and the driving force for domain coarsening is the reduction in total interfacial energy. This situation is analogous to grain growth in single phase alloys. In the mixed-phase FE system, there is additionally a driving force for transformation of the metastable phase to the stable phase. If this transformation occurs by

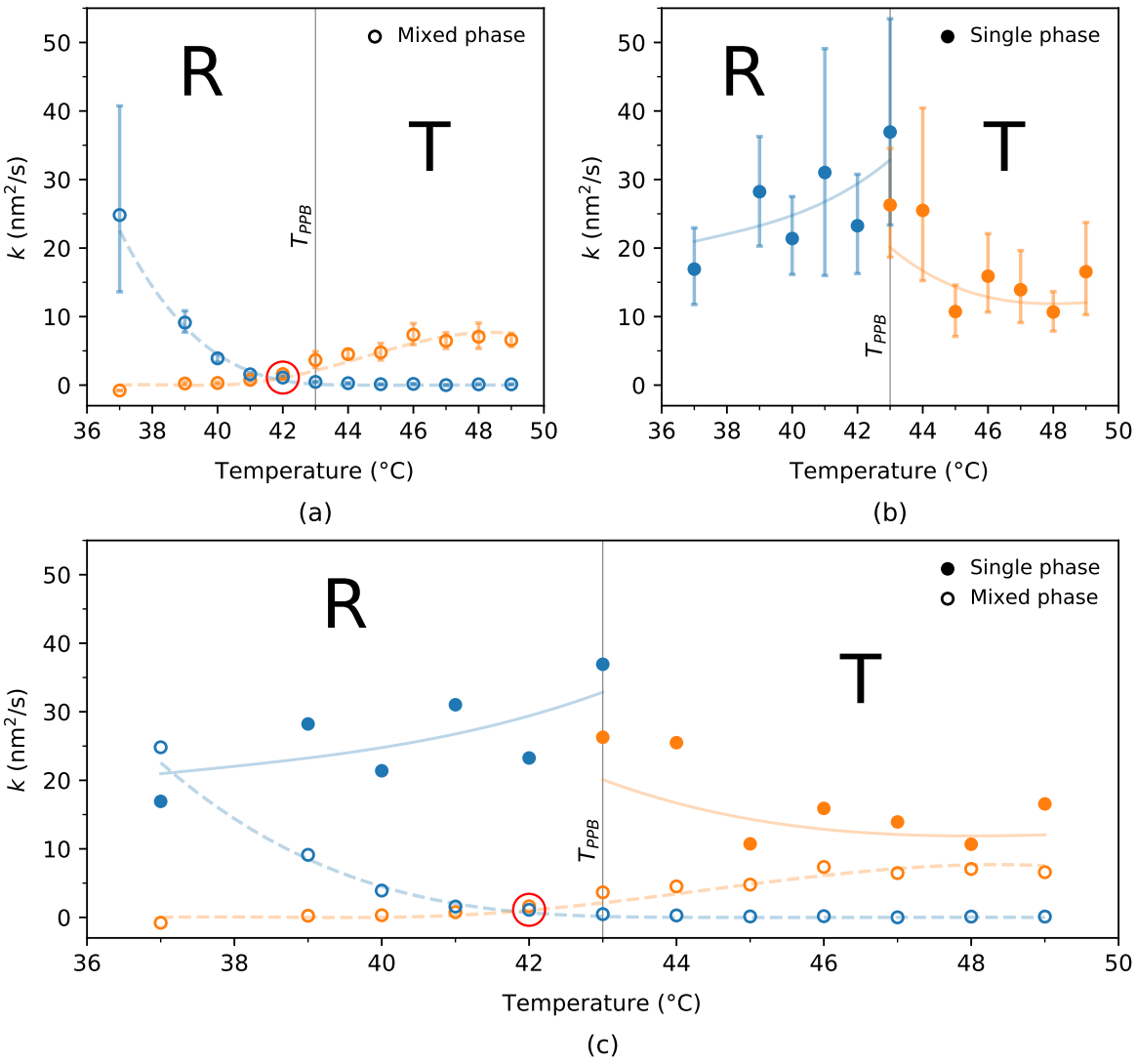

Figure 4.18: Temperature dependence of the domain coarsening constants for the R (—) and T (—) phases under (a) mixed-phase conditions, (b) single-phase conditions, and (c) combined scenarios. Error bars correspond to 95 % confidence intervals. Data points corresponding to approximately equal k values for the R and T phases under mixed-phase conditions are ringed in red. Splines are included as a guide for the eye.

movement of phase interfaces, then it is expected to accelerate the coarsening rate constant of the domains of the stable phase. If, on the other hand, the phase transformation occurs by nucleation of new domains of the stable phase, then it is expected to retard the coarsening rate constant of the domains of the stable phase. Figure 4.18(c) shows that the k values from mixed-phase conditions are generally smaller that those obtained from single-phase simulations at the same temperatures. The latter is consistent with the case of phase transformation by nucleation. However, the JMAK analysis, performed for the ferroelectric phase transformation in one-dimensional BZT-40 BCT, yielded results consistent with site-saturated nucleation, refer to Section 3.6.4 for details. Hence, the decreased coarsening rate constants in the two-phase system are better explained by pinning of domain walls of the stable phase by the domains of the metastable phase, which is analogous to the effect of precipitates on grain growth in two-phase alloys[115], as shown in Figure 4.19.

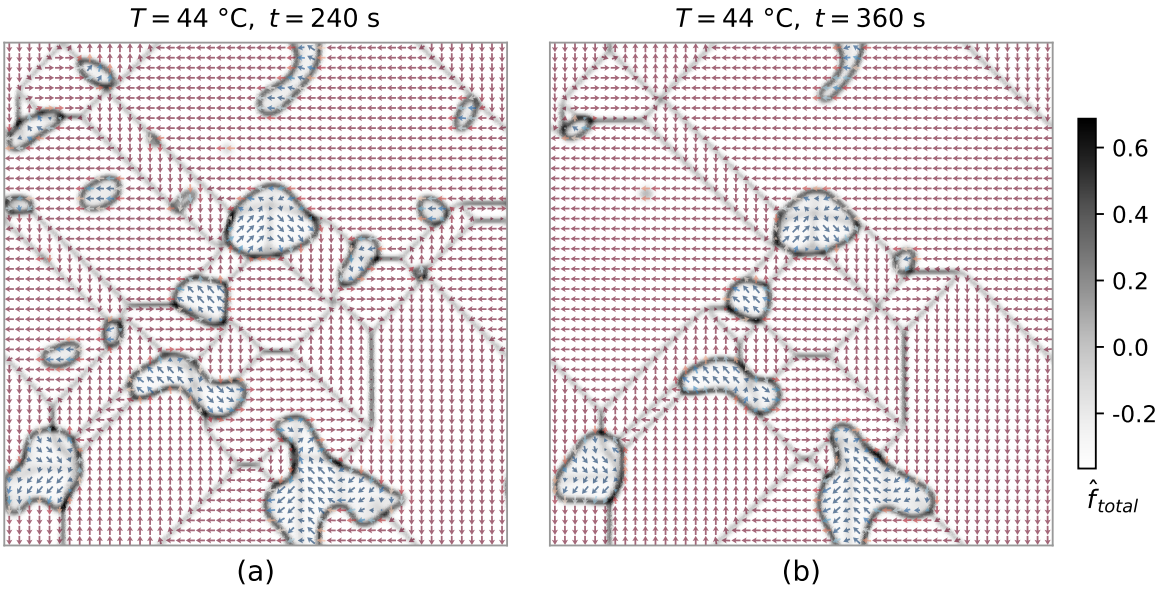

Figure 4.19: Evolution of two-phase microstructure for the two-dimensional, coarse-grained BZT-40 BCT system at $T = 44\,°C$ and (a) $t = 240\,s$, and (b) $t = 360\,s$. The computational domain size is $223\,nm \times 223\,nm$. Contour plots represent the dimensionless total free energy density, $\hat{f}_{total} = f_{total}/(|\alpha_{1,T}|P_{sT}^2)$, and vector plots represent the dimensionless polarization, $\vec{u} = \vec{P}/|P_{sT}|$. Arrows are coloured by the phase-field value showing, in this case, metastable rhombohedral domains (➔) and stable tetragonal domains (➔).

4.6 Summary and conclusions

The MPF model applied to the one-dimensional BZT-40 BCT system in Chapter 3 was extended to a two-dimensional geometry to elucidate, separately, the effects of the additional spatial dimension and the local electric fields within the two-phase FE system. Most parameters of the 2-D model were calculated using the material constants obtained in the one-dimensional study. Additional Landau parameters were estimated to ensure that the volumetric free energy density of each FE phase stabilized the correct polar directions in the temperature range of interest where the phases coexist metastably, while preserving the global stability predictions.

Shorter coexistence times are predicted by the two-dimensional model due to the greater driving force for phase transformation resulting from the selected Landau coefficients in the R phase. For $T_{PPB} < T < T_{C,R}$, coexistence times are significantly shorter because the phase transformation-induced polarization rotation mechanism, reported in Section 3.6.3 as a means to extend metastable coexistence of FE phases, is limited by $\sigma_{RDW} \sim \sigma_{TDW}$ and higher σ_{T-R} values in two dimensions.

When local electric fields are considered, the likelihood of extended R + T metastable coexistence increases due to the restriction imposed by Coulomb's Equation on the possible FE domain configurations to minimize the total free energy of the system. In this case, the two-dimensional model predicts domain structures with head-to-tail polarization patterns that are consistent with the literature. Moreover, the MPF approach naturally reproduces and explains domain morphologies consisting of faceted domain walls and curved T-R interfaces that have been observed experimentally

near the PPB of the BZT-x BCT system. It is shown that the lowest energy orientation of T-R phase interfaces is temperature dependent.

In this work, the metastable coexistence of FE phases is directly connected with the experimentally observed miniaturization of the domain structure to the nanoscale near the PPB, with smaller domains obtained when the volume fractions of the two phases are approximately equal. It is demonstrated that the evolution of FE domains within the two-phase system is dominated by the kinetics of phase transformation over the competing effect of intrinsic domain coarsening. The presence of a metastable FE phase facilitates polarization switching between domains of the stable phase, but also has a pinning effect on the movement of stable domain walls that retard the coarsening rate constant for domains of the stable FE phase.

Chapter 5

Fitting of Landau coefficients for BZT-50 BCT

A version of this chapter is currently under preparation for journal publication as: Oscar A. Torres-Matheus, R. Edwin García and Catherine M. Bishop. Landau expansion parameters for multiphase field formulation of BZT-50 BCT.

5.1 Introduction

In previous chapters, a novel multiphase field model was developed and applied to polycrystalline BZT-40 BCT ceramics, assuming a phase diagram with a single PPB between the T and R phases. The MPF formulation couples the Landau-Devonshire thermodynamic potentials of the coexisting FE phases, each defined separately with its own set of Landau coefficients. Following a coarse-grained approach, macroscopic Helmholtz free energy densities were defined to describe the general ferroelectric behaviour in each region of phase space for a single-crystal sample. Microstructurally averaged Landau parameters were estimated by fitting each set of coefficients to experimental data of polycrystalline samples measured in the single-phase regions of the phase diagram. Application of the model to one-dimensional, coarse-grained BZT-40 BCT enabled detailed analysis of the ferroelectric coexistence, such as the transformation kinetics of coexisting phases, and the energetics associated with the structural FE-FE phase transformation, polarization switching and polarization-phase transformation interactions. Further, extension to two dimensions allowed to elucidate the effects of the additional spatial dimension and local electric fields on the transformation kinetics and the domain morphology and evolution (coarsening) of the two-phase FE system. However, the coarse-grained models do not capture the effects of anisotropy in FE materials.

In polycrystalline FE ceramics, the domain structures and macroscopic response, *i.e.,* due to intrinsic and extrinsic effects, are affected by the grain size and grain orientation distributions [38,47,48,116–118]. Hence, the first step to modelling polycrystalline materials is to model the intrinsic behaviour of single crystals. This implies the definition of Landau-Devonshire potentials with coefficients determined from experimental, single-crystal data [119].

The calculation of required single-crystal Landau coefficients for the BZT-BCT system poses two major challenges. On the one hand, experimental work on single crystals is limited for this chemistry due to TiO_2 volatilization and the segregation of elements during synthesis [120,121]. This causes

large variations in the desired stoichiometry that affect the quality and performance of the crystal. On the other hand, reported electromechanical properties of BZT-BCT ceramics vary considerably depending on raw materials, processing and poling conditions, measurement techniques, among others[16,17]. According to Acosta *et al.*[16], experimental procedures are not well detailed in many research papers and the importance of some of these conditions is often overlooked. Furthermore, the proposed MPF model requires two independent sets of Landau parameters, *i.e.,* one for each FE phase. However, most works on calculation of Landau coefficients are based on a single Landau-Devonshire potential and focus on chemistries with two or more FE phases, *e.g.,* $KNbO_3$[57], PMN-PT[122,123] and $BaTiO_3$-based[58,59,124–126] systems. Thus, these coefficients are commonly fitted over a range of temperatures including the interferroelectric transition temperature(s) and use data from multiple FE phases.

Recently, Yang *et al.*[95] reported Landau parameters for $(1-x)Ba(Zr_{0.2}Ti_{0.8})O_3$-$x(Ba_{0.7}Ca_{0.3})TiO_3$ or BZT-x BCT as a function of temperature and composition (x). Similarly, Zhou *et al.*[124] have determined Landau parameters for the $(1-x)Ba(Zr_{0.2}Ti_{0.8})O_3-x(Ba_{1-y}Ca_y)TiO_3$ system, abbreviated as BZT-xBC$_y$T, as a function of temperature and compositions (x and y). In both studies, the coefficients of the sixth order Landau-Devonshire potential in 3-D were obtained by modifying the Landau parameters for pure $BaTiO_3$ to generate a consistent phase diagram[95,124]. No further details on the fitting procedure were provided in the research papers. Since the Landau coefficients are not based on experimental data from single crystals, the studies are mostly limited to qualitative analysis. No evidence was found in the literature of Landau parameters fitted to experimental, single-crystal data for any composition in the BZT-x BCT system.

In this chapter, a procedure is outlined for estimating the Landau parameters for the R and T phases of single-crystal $(Ba_{0.85}Ca_{0.15})(Zr_{0.10}Ti_{0.90})$, also known as $Ba(Zr_{0.2}Ti_{0.8})O_3$-50 $(Ba_{0.7}Ca_{0.3})TiO_3$ or BZT-50 BCT. This has been the most widely studied composition of this system, which allows comparison of the results with simulations and/or experiments found in the literature on BZT-50 BCT. Each set of Landau coefficients is estimated using data measured in the unambiguously T and R regions of the phase diagram determined by Ehmke[89]. The procedure described hereafter leans heavily on single-crystal and polycrystalline experimental information available in the literature. Equations for calculating the intrinsic electromechanical properties of ceramics are used to relate the single-crystal and polycrystalline data. This allows the use of measurements from polycrystalline samples to complement the required information for the fitting of Landau parameters.

5.2 Intrinsic properties of ferroelectrics ceramics

The properties of FE ceramics essentially consist of two contributions: intrinsic effects, which originate from lattice dynamics and are equivalent to properties obtained from a single domain; and extrinsic effects, which represent non-lattice contributions and arise mainly from changes at domain walls and grain boundaries[5,127]. It has been established in the literature that poled FE ceramics with randomly oriented grains are transversely isotropic around the poling axis regardless of the crystal symmetry[4,8,127]. Hence, for a polycrystalline sample described by global coordinates $[X_1, X_2, X_3]$

with an electric field applied along the [001] direction, the resulting through-thickness polarization and dielectric permittivity have the same non-zero elements as crystals that belong to point group $6mm$, *i.e.,* [4,128]

$$\vec{P} = \begin{pmatrix} 0 \\ 0 \\ P_3 \end{pmatrix} \qquad \overleftrightarrow{\epsilon} = \begin{pmatrix} \epsilon_{11} & 0 & 0 \\ 0 & \epsilon_{11} & 0 \\ 0 & 0 & \epsilon_{33} \end{pmatrix} \tag{5.1}$$

The intrinsic properties given by Equation 5.1 depend on, and are limited by, available domain states, or allowed polarization directions, associated with the crystal symmetry of the FE phase(s) present within the material [4]. The maximum achievable properties of FE ceramics in a saturated poling state have been estimated from single-crystal data via probability density functions of orientation (PDFOs) [5], pole figures [6], inverse pole figures [7] and/or orientation distribution function (ODF) [8–10] methods. In these models, macroscopic properties are estimated as the averaged response of randomly oriented grains over the entire orientation space. A Reuss type approximation [129] is commonly adopted, which neglects the interaction between crystals by assuming that domains are independent of each other and that the internal and external electromechanical loadings are equal.

The saturated remnant polarization of FE ceramics, P_r^*, can be estimated from the magnitude of the spontaneous polarization in the single crystal, $\|\vec{P}_s\| = P_s$, as [4–10]

$$P_{rT}^* = 0.8312 P_{sT} \tag{5.2}$$

$$P_{rR}^* = 0.8660 P_{sR} \tag{5.3}$$

where subscripts T and R represent the tetragonal and rhombohedral phases. Similarly, the saturated macroscopic dielectric permittivity along the polarization direction, ϵ_{33}^*, and in the transverse direction, ϵ_{11}^*, are [5,8]

$$\begin{bmatrix} \epsilon_{11,T}^* \\ \epsilon_{33,T}^* \end{bmatrix} = \frac{1}{3\pi} \begin{bmatrix} 2\pi + \sqrt{3} & \pi - \sqrt{3} \\ 2\pi - 2\sqrt{3} & \pi + 2\sqrt{3} \end{bmatrix} \begin{bmatrix} \epsilon_{11,T} \\ \epsilon_{33,T} \end{bmatrix} \tag{5.4}$$

$$\begin{bmatrix} \epsilon_{11,R}^* \\ \epsilon_{33,R}^* \end{bmatrix} = \frac{1}{3\pi} \begin{bmatrix} 2\pi + 2 & \pi - 2 \\ 2\pi - 4 & \pi + 4 \end{bmatrix} \begin{bmatrix} \epsilon_{11,R} \\ \epsilon_{33,R} \end{bmatrix} \tag{5.5}$$

where ϵ_{33} and ϵ_{11} are the longitudinal and transverse permittivity components in a single FE domain, with local coordinates $[x_1, x_2, x_3]$ [5]. These solutions, which assume a fully saturated poling state, are ideal and provide an upper limit to the properties of polycrystalline ferroelectrics [8,127]. However, FE ceramics rarely reach a fully poled state [4,5,10]. Many domains cannot reorient along available polarization directions due to internal loads associated with grain boundaries, and some domains will switch back after removal of the poling field [4].

Hou *et al.,* [5] have developed a model for unsaturated poling states by incorporating additional parameters into the PDFOs to account for the remnant switching fraction of different types of domain switching, which can be determined using XRD. Thus, the remnant polarization in an unsaturated

state, P_r^{**}, is given by

$$P_{rT}^{**} = \left(1 - \frac{1}{3}t_{180} - \frac{2}{3}t_{90}\right) 0.8312 P_{sT} \tag{5.6}$$

$$P_{rR}^{**} = \left(1 - \frac{3}{8}r_{71} - \frac{3}{8}r_{109} - \frac{1}{4}r_{180}\right) 0.8660 P_{sR} + \frac{\sqrt{3}}{16}\left(r_{71} - r_{109}\right) P_{sR} \tag{5.7}$$

where t_{90} and t_{180} are the remnant fractions of 90° and 180° switching in the T phase; and r_{71}, r_{109} and r_{180} are the remnant fractions of 71°, 109° and 180° switching in the R phase. When all the remnant switching fractions are zero, Equations 5.6 and 5.7 reduce to the saturated poling state; and when all the remnant switching fractions are one, the equations reduce to the randomly-oriented initial state. Similarly, proposed solutions for the dielectric permittivity components under unsaturated poling state, ϵ_{33}^{**} and ϵ_{11}^{**}, are[5]

$$\begin{bmatrix} \epsilon_{11,T}^{**} \\ \epsilon_{33,T}^{**} \end{bmatrix} = \frac{1}{3\pi}\begin{bmatrix} 2\pi + \sqrt{3} & \pi - \sqrt{3} \\ 2\pi - 2\sqrt{3} & \pi + 2\sqrt{3} \end{bmatrix}\begin{bmatrix} \epsilon_{11,T} \\ \epsilon_{33,T} \end{bmatrix} + \frac{t_{90}}{3\pi}\begin{bmatrix} -\sqrt{3} & \sqrt{3} \\ 2\sqrt{3} & -2\sqrt{3} \end{bmatrix}\begin{bmatrix} \epsilon_{11,T} \\ \epsilon_{33,T} \end{bmatrix} \tag{5.8}$$

$$\begin{bmatrix} \epsilon_{11,R}^{**} \\ \epsilon_{33,R}^{**} \end{bmatrix} = \frac{1}{3\pi}\begin{bmatrix} 2\pi + 2 & \pi - 2 \\ 2\pi - 4 & \pi + 4 \end{bmatrix}\begin{bmatrix} \epsilon_{11,R} \\ \epsilon_{33,R} \end{bmatrix} + \frac{r_{71} + r_{109}}{3\pi}\begin{bmatrix} -1 & 1 \\ 2 & -2 \end{bmatrix}\begin{bmatrix} \epsilon_{11,R} \\ \epsilon_{33,R} \end{bmatrix} \tag{5.9}$$

According to Yang *et al.,*[10], 180° domain switching can readily reach saturation in FE ceramics, while other switching types do not, resulting in switching fractions as low as 44 % in PZT. This result agrees with computational simulations performed by Li *et al.,*[130], who reported little domain texture for tetragonal PZT due to a small fraction of 90° domain switching.

The framework described above can be readily extended to estimate the piezoelectric coefficients of FE systems using experimental data from polycrystalline samples in both saturated and unsaturated poling states, see *e.g.,*[5].

5.3 Phenomenological model

According to the MPF model developed in Section 2.3 for a system with a single PPB, the volumetric free energy density of the strain-free, two-phase FE crystal under an external electric field, $\vec{E}$, is defined as

$$f(\vec{P}, \phi; \vec{E}, T) = f_R(\vec{P}; \vec{E}, T)[1 - h(\phi)] + f_T(\vec{P}; \vec{E}, T)h(\phi) + Wg(\phi) \tag{5.10}$$

where the phase field variable, ϕ, specifies the region in (spatial) space where the R and T phases are each locally stable; $h(\phi) = \phi^3(6\phi^2 - 15\phi + 10)$ is a function that interpolates between the free energy densities of the two phases, f_T and f_R; $g(\phi) = \phi^2(1-\phi)^2$ is a double-well potential that prevents unphysical phase transitions; and W is the double-well coefficient that controls the depth of the energy barrier between FE phases. The individual homogeneous free energy densities are defined herein as

$$f_T(\vec{P}; \vec{E}, T) = f_T^{\circ}(\vec{P}; \vec{E}, T) \tag{5.11}$$

$$f_R(\vec{P};\vec{E},T) = f_R^{\circ}(\vec{P};\vec{E},T) + \Delta f_{PPB} \tag{5.12}$$

where f_T° and f_R° are the free energy densities traditionally described by the Helmholtz thermodynamic potential with respect to the cubic paraelectric phase, and $\Delta f_{PPB} = f_T^{\circ}(\vec{P}_{sT};\vec{0},T_{PPB}) - f_R^{\circ}(\vec{P}_{sR};\vec{0},T_{PPB})$, see Chapter 2 for full details.

According to Cao[65,66], the Helmholtz thermodynamic potential up to the sixth-order terms is generally expressed in terms of three polarization components, $\vec{P} = (P_1, P_2, P_3)$, as the following Landau-Devonshire potential

$$\begin{aligned} f^{\circ}(\vec{P};\vec{E},T) = {} & \alpha_1(P_1^2+P_2^2+P_3^2) + \alpha_{11}(P_1^4+P_2^4+P_3^4) \\ & + \alpha_{12}(P_1^2P_2^2+P_2^2P_3^2+P_1^2P_3^2) + \alpha_{111}(P_1^6+P_2^6+P_3^6) \\ & + \alpha_{112}\left[P_1^4(P_2^2+P_3^2)+P_2^4(P_1^2+P_3^2)+P_3^4(P_1^2+P_2^2)\right] \\ & + \alpha_{123}P_1^2P_2^2P_3^2 - P_1E_1 - P_2E_2 - P_3E_3 \end{aligned} \tag{5.13}$$

where the leading coefficient is commonly defined as $\alpha_1 = a_{CW}(T - T_{CW})$, where T_{CW} is the Curie-Weiss temperature and $a_{CW} > 0$ is the Curie-Weiss constant; while the other expansion parameters are considered temperature-independent[1].

In general, the allowed domain states, or polarization directions, for each FE phase depend on its crystal structure. For the T phase, polarizations are along the $\langle 100\rangle_C$ family of directions; while, for the R phase, polarizations are along the $\langle 111\rangle_C$ family of directions. Considering the case of $\vec{P}_T = (0,0,P_3)$ and $\vec{P}_R = (P_3,P_3,P_3)$ in the absence of an applied electric field ($\vec{E} = \vec{0}$), the volumetric free energy densities f_T° and f_R° are obtained from Equation 5.13 as

$$f_T^{\circ} = \alpha_{1,T}P_3^2 + \alpha_{11,T}P_3^4 + \alpha_{111,T}P_3^6 \tag{5.14}$$

$$f_R^{\circ} = 3\alpha_{1,R}P_3^2 + 3(\alpha_{11,R}+\alpha_{12,R})P_3^4 + (3\alpha_{111,R}+6\alpha_{112,R}+\alpha_{123,R})P_3^6 \tag{5.15}$$

where subscripts T and R are used to denote the set of Landau coefficients in the T and R phases. Further, the equilibrium states are obtained from the minimization of Equation 5.13 and substitution of the allowed solutions for polarization in each phase, *i.e.,*

$$\partial f_T^{\circ}/\partial P_3 = \alpha_{1,T} + 2\alpha_{11,T}P_{s3,T}^2 + 3\alpha_{111,T}P_{s3,T}^4 = 0 \tag{5.16}$$

$$\partial f_R^{\circ}/\partial P_3 = \alpha_{1,R} + 2(\alpha_{11,R}+\alpha_{12,R})P_{s3,R}^2 + (3\alpha_{111,R}+6\alpha_{112,R}+\alpha_{123,R})P_{s3,R}^4 = 0 \tag{5.17}$$

where P_{s3} is the component of the spontaneous polarization that stabilizes the system in the absence of applied electric fields. For each FE phase, P_{s3} is defined as $\|\vec{P}_{s,T}\| = P_{s3,T}$ and $\|\vec{P}_{s,R}\| = \sqrt{3}P_{s3,R}$, and its magnitude is obtained from Equations 5.16 and 5.17 as

$$P_{s3,T} = \pm\left[\frac{-\alpha_{11,T} + \sqrt{\alpha_{11,T}^2 - 3\alpha_{1,T}\alpha_{111,T}}}{3\alpha_{111,T}}\right]^{1/2} \tag{5.18}$$

$$P_{s3,R} = \pm\left[\frac{-(\alpha_{11,R}+\alpha_{12,R}) + \sqrt{(\alpha_{11,R}+\alpha_{12,R})^2 - \alpha_{1,R}(3\alpha_{111,R}+6\alpha_{112,R}+\alpha_{123,R})}}{3\alpha_{111,R}+6\alpha_{112,R}+\alpha_{123,R}}\right]^{1/2} \tag{5.19}$$

Similarly, the longitudinal and transverse components of the dielectric permittivity are determined from the second partial derivatives of Equation 5.13. In general,

$$\begin{aligned}\frac{\partial^2 f^\circ}{\partial P_3^2} = \frac{\partial E_3}{\partial P_3} = \frac{1}{\epsilon_{33}} &= 2\alpha_1 + 12\alpha_{11}P_3^2 + 2\alpha_{12}(P_1^2+P_2^2) + 30\alpha_{111}P_3^4 \\ &\quad + 2\alpha_{112}[P_1^4+P_2^4+6P_3^2(P_1^2+P_2^2)] + 2\alpha_{123}P_1^2P_2^2\end{aligned} \tag{5.20}$$

$$\begin{aligned}\frac{\partial^2 f^\circ}{\partial P_1^2} = \frac{\partial E_1}{\partial P_1} = \frac{1}{\epsilon_{11}} &= 2\alpha_1 + 12\alpha_{11}P_1^2 + 2\alpha_{12}(P_2^2+P_3^2) + 30\alpha_{111}P_1^4 \\ &\quad + 2\alpha_{112}[P_2^4+P_3^4+6P_1^2(P_2^2+P_3^2)] + 2\alpha_{123}P_2^2P_3^2\end{aligned} \tag{5.21}$$

$$\frac{\partial^2 f^\circ}{\partial P_1 \partial P_2} = \frac{\partial E_1}{\partial P_2} = \frac{1}{\epsilon_{12}} = 4\alpha_{12}P_1P_2 + 8\alpha_{112}(P_1P_2^3 + P_1^3P_2) + 4\alpha_{123}P_1P_2P_3^2 \tag{5.22}$$

Note that similar expressions can be written for ϵ_{22} and ϵ_{23}. Based on the condition of zero applied field, Equations 5.20 through 5.22 can be simplified in this case by substituting the spontaneous polarization of each phase, $\vec{P}_{s,T} = (0, 0, P_{s3,T})$ and $\vec{P}_{s,R} = (P_{s3,R}, P_{s3,R}, P_{s3,R})$. Hence,

For the T phase:[119]

$$\epsilon_{33,T} = \left(2\alpha_{1,T} + 12\alpha_{11,T}P_{s3,T}^2 + 30\alpha_{111,T}P_{s3,T}^4\right)^{-1} \tag{5.23}$$

$$\epsilon_{11,T} = \epsilon_{22,T} = \left(2\alpha_{1,T} + 2\alpha_{12,T}P_{s3,T}^2 + 2\alpha_{112,T}P_{s3,T}^4\right)^{-1} \tag{5.24}$$

$$\epsilon_{12,T} = \epsilon_{23,T} = \epsilon_{31,T} = 0 \tag{5.25}$$

For the R phase:[131]

$$\begin{aligned}\epsilon_{33,R} = \epsilon_{22,R} = \epsilon_{11,R} = \big[&2\alpha_{1,R} + (12\alpha_{11,R} + 4\alpha_{12,R})P_{s3,R}^2 \\ &+ (30\alpha_{111,R} + 28\alpha_{112,R} + 2\alpha_{123,R})P_{s3,R}^4\big]^{-1}\end{aligned} \tag{5.26}$$

$$\epsilon_{12,R} = \epsilon_{23,R} = \epsilon_{31,R} = \left[4\alpha_{12,R}P_{s3,R}^2 + (16\alpha_{112,R} + 4\alpha_{123,R})P_{s3,R}^4\right]^{-1} \tag{5.27}$$

In the R phase, the spontaneous polarization is assumed to be along the ⟨111⟩ directions of the local pseudocubic axes with coordinates $[x_1, x_2, x_3]$. However, equations presented in Section 5.2 to estimate the dielectric permittivity of poled FE ceramics require that the single-crystal results for the R phase are rotated such that the x_3 axis is parallel to the polarization direction. Rotation of Equations 5.26 and 5.27 to the new local coordinate system $[x_1', x_2', x_3']$ result in a diagonal matrix, similar to that obtained for the T phase, with the following elements[57,58]

$$\begin{aligned}&\epsilon'_{33,R} = \epsilon_{11,R} + 2\epsilon_{12,R} \quad , \quad \epsilon'_{11,R} = \epsilon'_{22,R} = \epsilon_{11,R} - \epsilon_{12,R} \\ &\epsilon'_{12,R} = \epsilon'_{23,R} = \epsilon'_{31,R} = 0\end{aligned} \tag{5.28}$$

5.4 Fitting procedure

The following procedure to estimate the Landau parameters for the R and T phases of the BZT-50 BCT system uses a combination of experimental data from single-crystal and polycrystalline samples found in the literature. The required single-crystal data were taken from Benabdallah *et al.*[132], who successfully grew a single-crystal sample with final composition of $(Ba_{0.838}Ca_{0.162})(Zr_{0.146}Ti_{0.854})$, close to the intended stoichiometry for BZT-50 BCT. Moreover, the authors reported anomalies in the permittivity measurements at 265 K and 366 K, consistent with transition temperatures measured for the BZT-50 BCT system. In particular, the cubic-tetragonal transition obtained at 366 K (93 °C) is within the 91 °C ± 14% range stated by Acosta *et al.*[16]. Available single-crystal data from Benabdallah *et al.*[132] include the spontaneous polarization and dielectric permittivity measured in the $[001]_C$ direction of the single-crystal sample for temperatures from 150 K to 375 K.

In the MPF model, the Landau parameters of each FE phase are estimated independently by fitting to experimental data measured in the unambiguously T and R regions of the phase diagram. For the BZT-x BCT system, an orthorhombic phase (or a region of R + T coexistence) has been speculated, refer to Section 3.1 for a discussion. Particularly, for BZT-50 BCT, this region extends from $T_{R-O} = 274$ K to $T_{O-T} = 302$ K, according to Ehmke[89]. Thus, coefficients for the R phase were fitted to data measured at $T \leq T_{R-O}$; and coefficients for the T phase were fitted to data measured at $T_{O-T} \leq T \leq T_{T-C}$, where $T_{T-C} = 366$ K, as reported by Benabdallah *et al.*[132].

For the R phase, all Landau parameters were estimated by fitting Equation 5.19 to P_s *vs* T single-crystal data from 200 K to 274 K, Figure 5.1. A non-linear least squares fitting was performed using the `lmfit` python package[133]. The initial estimate for the Landau parameters was selected with the same order of magnitude as that of the parameters for $BaTiO_3$, as determined by Bell and Cross[134].

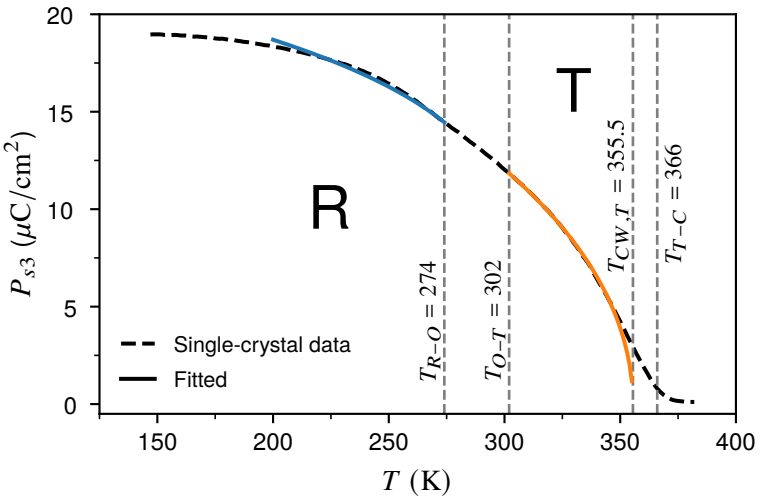

Figure 5.1: Fitting of Landau parameters for the R (—) and T (—) phases of the BZT-50 BCT system to P_s *vs* T single-crystal data, as reported by Benabdallah *et al.*[132]. For the R phase, all the Landau coefficients are found by fitting to data from 200 K to 274 K. For the T phase, coefficients $\alpha_{1,T}$, $\alpha_{11,T}$ and $\alpha_{111,T}$ are obtained by fitting to data from 302 K to 366 K. The R-O and O-T transition temperatures are those measured by Ehmke[89], while the T-C transition temperature corresponds to that reported by Benabdallah *et al.*[132]. A second order P-FE phase transition is observed for the T phase at its calculated Curie-Weiss temperature, $T_{CW,T}$.

Bounds were set for each parameter according to the conditions for stability of the R phase discussed by Smolenskii *et al.*[135]. In this case, data from 270 K to 274 K were given a higher weight, producing a better fit close to the region of interest where the R and T phases coexist. The initial estimate and weight factor were adjusted until the obtained Landau parameters gave a good fit to the experimental P_s *vs* T single-crystal data. The goodness of fit was calculated using RMSE, which measures the residuals between the predicted and experimental values. In addition, the fitted Landau coefficients were used to calculate the Curie temperature, $T_{C,R}$, depending on the order of the P-FE transition. The predicted $T_{C,R} = 301.5$ K was compared with the experimental transition temperature $T_{O-T} = 302$ K to verify that the Landau coefficients correctly reproduce the R phase in the entire region of phase space where it exists stably or metastably.

Similarly, for the T phase, coefficients $\alpha_{1,T}$, $\alpha_{11,T}$ and $\alpha_{111,T}$ were estimated by fitting Equation 5.18 to P_s vs T single-crystal data from 302 K to 366 K, Figure 5.1. Higher weight was given to data at $T \leq 305$ K, yielding a better fit close to the region of interest where the FE phases coexist. In addition, the predicted $T_{CW,T} = 355.5$ K (82.5 °C) is within the 91 °C ± 14% range stated by Acosta *et al.*[16]. Using the fitted values of $\alpha_{1,T}$, $\alpha_{11,T}$ and $\alpha_{111,T}$, the value of Δf_{PPB} was computed and the global stability predictions as a function of temperature were verified, Figure 5.2. The PPB temperature was taken to be $T_{PPB} \sim (T_{R-O} + T_{O-T})/2 = 288$ K, and the minimum volumetric free energy density of each FE phase was calculated by substituting the respective spontaneous polarization, P_{s3}, into Equations 5.14 and 5.15. Then, f_{min} *vs* T curves were plotted using Equations 5.11 and 5.12

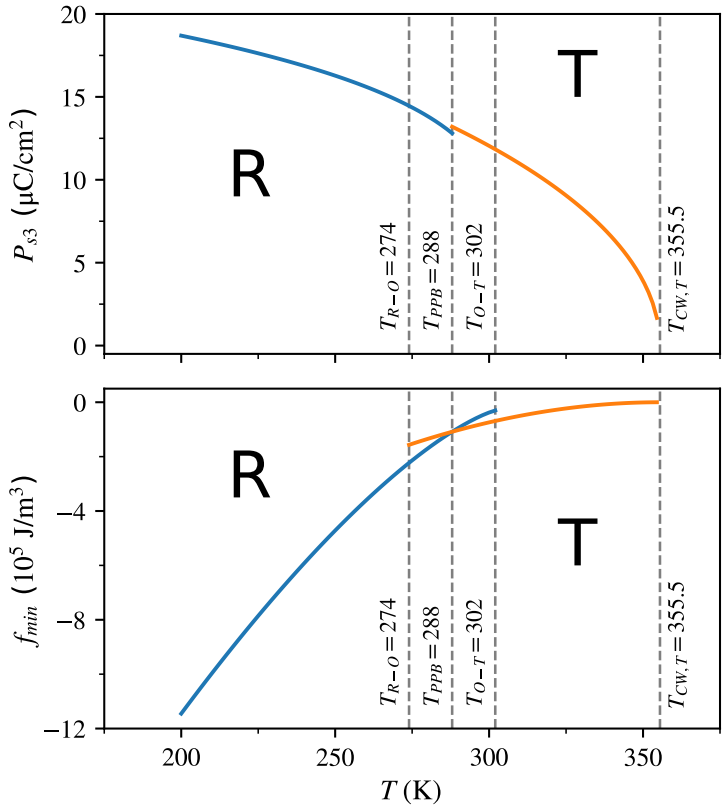

Figure 5.2: Temperature dependence of the spontaneous polarization (P_{s3}) and minimum volumetric free energy density (f_{min}) with fitted Landau coefficients for the R (—) and T (—) phases of BZT-50 BCT. The R-O and O-T transition temperatures are those measured by Ehmke[89]. Results confirm the correct global stability predictions with the fitted Landau coefficients.

to confirm that the R phase is stable for $T < T_{PPB}$ and the T phase is stable for $T > T_{PPB}$. If the volumetric free energies were not suitable, the initial estimate and weight factor were adjusted until appropriate coefficients were found for each FE phase.

Coefficients $\alpha_{12,T}$ and $\alpha_{112,T}$ were fitted to temperature-dependent ϵ_{11} data in the T phase[119,122]. However, for the BZT-50 BCT system, ϵ_{11} *vs* T measurements were not found in the literature. Hence, in this work the required single-crystal $\epsilon_{11,T}$ data were estimated using ϵ_{33} *vs* T measurements from single-crystal and unpoled polycrystalline samples. In order to reproduce the randomly-oriented domains of the unpoled ceramics, the remnant fraction of 90° switching, t_{90}, is set equal to one in the model for unsaturated poling, see Section 5.2. Thus, from Equation 5.8, $\epsilon_{11,T}$ was calculated as

$$\epsilon_{11,T} = (3\epsilon^{**}_{33,T} - \epsilon_{33,T})/2 \tag{5.29}$$

where $\epsilon_{33,T}$ is the longitudinal permittivity in the single-crystal sample and $\epsilon^{**}_{33,T}$ is the longitudinal permittivity in the ceramic sample.

Coefficients $\alpha_{12,T}$ and $\alpha_{112,T}$ were obtained by fitting Equation 5.24 to the estimated single-crystal $\epsilon_{11,T}$ data from 302 K to 355.5 K, Figure 5.3. A non-linear least squares fitting was performed with the `lmfit` python package[133] considering two independent variables, *i.e.*, T and $P_{s3,T}$, taken from Benabdallah *et al.*[132]. Different sources were considered for $\epsilon^{**}_{33,T}$ [85,136–138] until the Landau parameters gave the best fit to the estimated $\epsilon_{11,T}$ data, subjected to $\alpha_{12,T} > 0$ and $\alpha_{112,T} > 0$. The latter was required to ensure stabilization of the T phase. The accuracy of the fitting is limited by the assumption of temperature-independent high-order Landau parameters. However, results are deemed reasonable in this case considering that the underlying data for the fitting is only an estimation that depends on the available ϵ_{33} polycrystalline data.

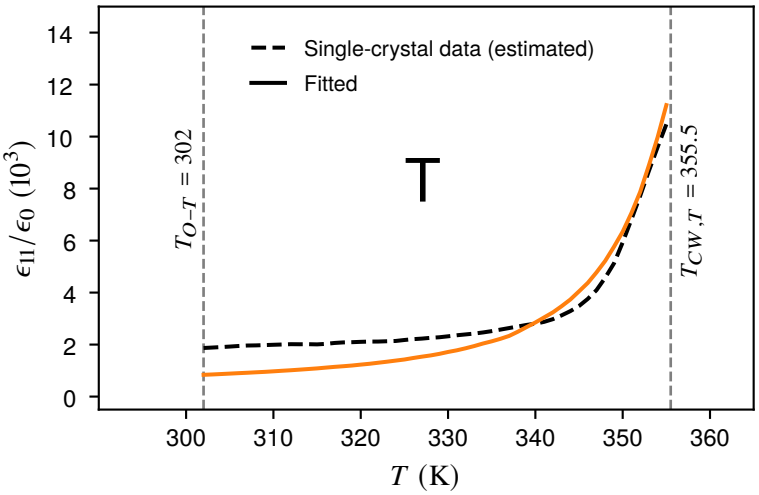

Figure 5.3: Fitting of Landau coefficients $\alpha_{12,T}$ and $\alpha_{112,T}$ to ϵ_{11} *vs* T data from 302 K to 355.5 K for the T phase (—) of the BZT-50 BCT system. The single-crystal ϵ_{11} data were estimated using ϵ_{33} measurements from a single-crystal sample, as measured by Benabdallah *et al.*[132], and from an unpoled polycrystalline sample, as reported by Zhang *et al.*[136].

Finally, we set $\alpha_{123,T} = 0$ following the conditions for stability of the T phase presented by Smolenskii *et al.*[135] in order to prevent spontaneous phase transitions to the R or O phases in the entire temperature range of interest.

5.5 Results and validation

The Landau parameters obtained in this work for the BZT-50 BCT system are summarized in Table 5.1. According to the fitted coefficients, the T phase has a second order P-FE phase transition and the R phase exhibits a weak first order P-FE transition. The latter is evidenced by the similar values for the Curie-Weiss temperature, $T_{CW,R} = 299.0\,\mathrm{K}$, the Curie temperature, $T_{C,R} = 301.5\,\mathrm{K}$[1], and the maximum temperature for metastable coexistence between the cubic and rhombohedral phases, $T_{max,R} = 302.3\,\mathrm{K}$[1]. Table 5.1 also includes existing Landau coefficients found in the literature, calculated using a single Landau-Devonshire potential to describe both FE phases[95,124]. The Curie temperature reported in these works, $T_C = 353\,\mathrm{K}$, is approximately equal to the value predicted in this study for the T-C phase transition at $T_{CW,T} = T_{C,T} = 355.5\,\mathrm{K}$. Further, the Landau parameters reported by all sources exhibit similar order of magnitudes.

Table 5.1: Fitted Landau parameters for the R and T phases of BZT-50 BCT. Landau coefficients found in the literature are also included for comparison. Results reported by Yang *et al.*[95] have been adapted to the form of the Landau-Devonshire potentials used in this work.

	This work				
Coeff.	R phase	T phase	Yang *et al.*[95]	Zhou *et al.*[124]	Unit
α_1	1.450×10^5 $\times(T-299)$	1.800×10^5 $\times(T-355.5)$	2.071×10^5 $\times(T-353)$	4.124×10^5 $\times(T-353)$	$\mathrm{Jm/C^2}$
α_{11}	1.000×10^7	3.225×10^8	$-4.5\times10^6+1.89\times10^5$ $\times(T-335)$	-8.0×10^7	$\mathrm{Jm^5/C^4}$
α_{12}	-1.000×10^8	5.501×10^9	$-4.5\times10^6-1.89\times10^5$ $\times(T-335)$	$2.0\times10^7+3.0\times10^5$ $\times(T-343)$	$\mathrm{Jm^5/C^4}$
α_{111}	3.552×10^9	1.000×10^9	1.304×10^8	1.294×10^9	$\mathrm{Jm^9/C^6}$
α_{112}	-4.582×10^8	1.023×10^7	-5.5×10^6	-2.0×10^7	$\mathrm{Jm^9/C^6}$
α_{123}	9.000×10^9	0.000	$2.5\times10^9+3.5\times10^7$ $\times(T-335)$	8.0×10^7	$\mathrm{Jm^9/C^6}$
Δf_{PPB}	-3.198×10^4		–	–	$\mathrm{J/m^3}$

Figure 5.4 illustrates the thermodynamic conditions for phase coexistence and stability near the PPB in the BZT-50 BCT system, refer to Chapter 2 for details on different scenarios. The predicted upper limit for metastable R + T phase coexistence, $T_{C,R} \sim T_{max,R}$, is approximately equal to $T_{O-T} = 302\,\mathrm{K}$, as reported by Ehmke[89]. Results support the hypothesis of R + T phase coexistence in the vicinity of the PPB, as opposed to a purported intervening O phase. Figure 5.4 also shows that the cubic paraelectric phase is unstable for $T < T_{C,R}$. Hence, no metastable coexistence between the C phase and the R and T ferroelectric phases is predicted for this composition, which is in agreement with experimental observations[77].

[1] For the Landau expansion used in this work, $T_C = T_{CW} + 3(\alpha_{11}+\alpha_{12})^2/[4a_{CW}(3\alpha_{111}+6\alpha_{112}+\alpha_{123})]$, and $T_{max} = T_{CW} + (\alpha_{11}+\alpha_{12})^2/[a_{CW}(3\alpha_{111}+6\alpha_{112}+\alpha_{123})]$.

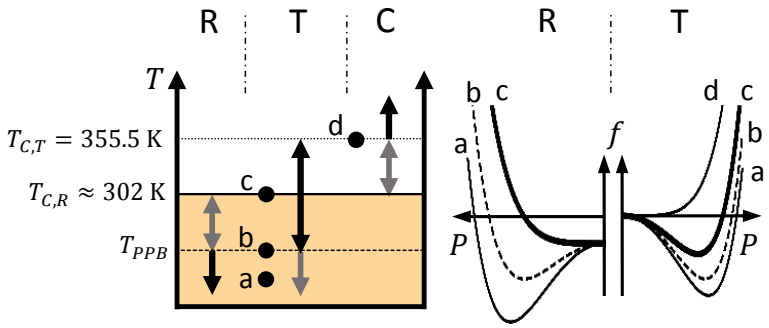

Figure 5.4: Phase coexistence and stability predictions for the BZT-50 BCT system. The T phase has a second order P-FE phase transition, with $T_{C,T} = T_{CW,T}$. The R phase has a weak first order P-FE transition, evidenced by $T_{CW,R} \sim T_{C,R} \sim T_{max,R}$. This case corresponds to the scenario depicted in Figure 2.1(a). A polymorphic phase transition occurs at T_{PPB}. Highlighted area indicates metastable coexistence of the FE phases accessible upon heating or cooling. Black arrows indicate regions where a particular phase is stable and grey arrows indicate regions where the phase is metastable. Free energy curves are sketched on the right for selected temperatures (a, b, c and d).

The Landau coefficients determined for each FE phase were used to verify that the global stability predictions are preserved in the region of interest where the R and T phases coexist, Figure 5.5. At $T = T_{PPB}$, the rhombohedral and tetragonal phases are both stable. Figure 5.5 (c)-(f) show the three-dimensional free energy surface for a specific FE phase at selected temperatures. The shape of each

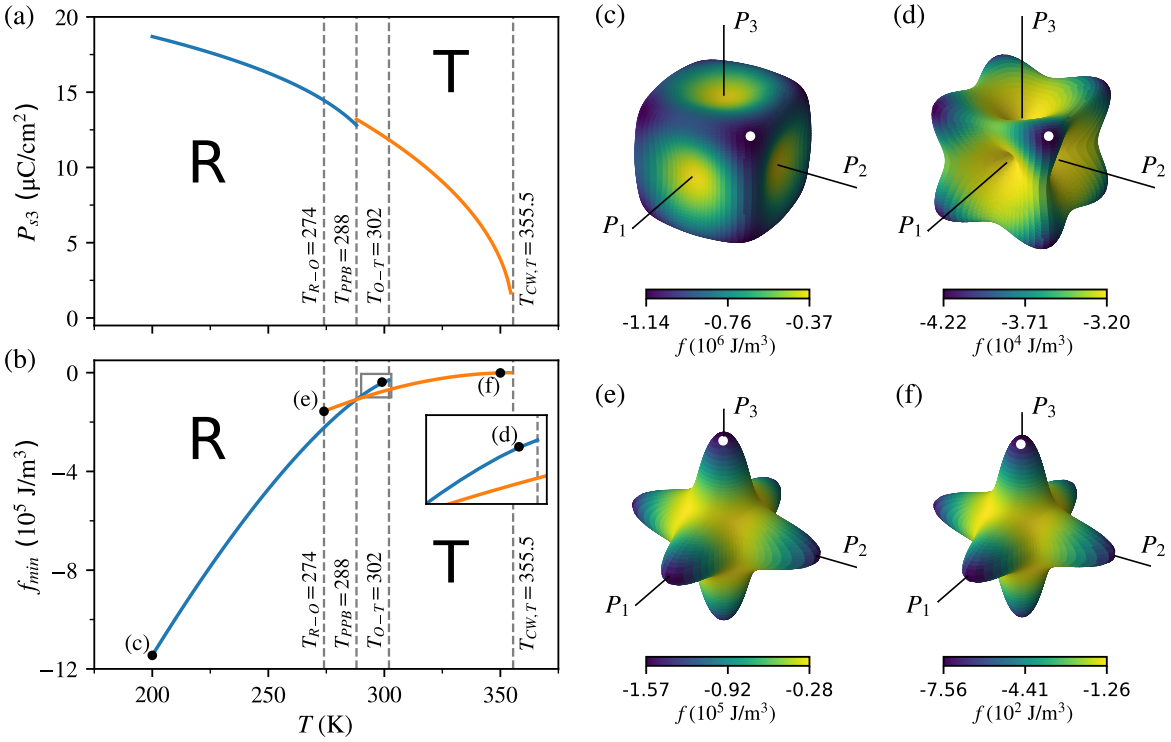

Figure 5.5: Temperature dependence of (a) P_{s3}, and (b) f_{min} for the R (—) and T (—) phases of BZT-50 BCT confirming the correct global stability predictions with selected Landau coefficients. Subfigures (c)-(f) illustrate the volumetric free energy density surface in 3-D for (c) R phase at T = 200 K, (d) R phase at T = 299 K, (e) T phase at T = 274 K, and (f) T phase at T = 350 K. For each case, the surface shape is defined by the polarization vector that minimizes the volumetric free energy density at each spatial orientation. The spontaneous polarization states corresponding to minima in the volumetric free energy density are indicated with a white dot.

surface is defined by plotting the polarization vector that minimizes the homogeneous volumetric free energy density at each spatial orientation, while its colour is given by the corresponding minimum free energy values. Hence, for this field-free scenario, minima in the volumetric free energy density give the orientations of the spontaneous polarization for each case, whose magnitude can be obtained from Figure 5.5(a). For the R phase, Figure 5.5(c)-(d) confirms that selected Landau coefficients give minima along the $\langle 111 \rangle_C$ polarization directions. For the T phase, Figure 5.5(e)-(f) shows that selected Landau coefficients stabilize polarization states along the $\langle 100 \rangle_C$ directions.

Figure 5.6 shows a comparison of predicted properties for single-crystal BZT-50 BCT using the different sets of Landau parameters stated in Table 5.1. Calculated values for the spontaneous polarization component, P_{s3}, and the longitudinal relative permittivity, ϵ_{33}/ϵ_o, are shown in Figure 5.6(a) and Figure 5.6(b), respectively. Considering the ongoing debate on the structural state in the vicinity of the PPB, single-phase calculations are only performed in the temperature ranges corresponding

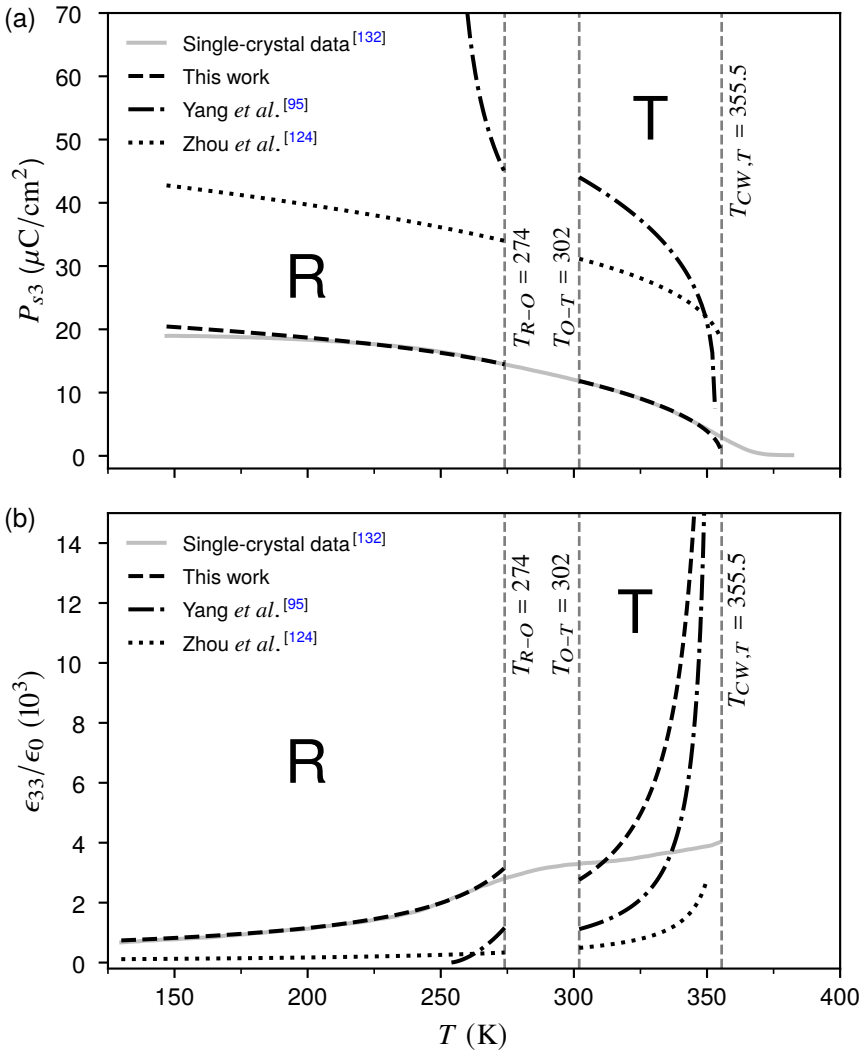

Figure 5.6: (a) P_{s3} *vs* T and (b) ϵ_{33}/ϵ_o *vs* T predicted for single-crystal BZT-50 BCT using the Landau parameters stated in Table 5.1. Experimental data for $[001]_C$-oriented BZT-50 BCT single crystal is also included, as measured by Benabdallah *et al.* [132]. The purported O phase (or region of R + T coexistence) is shown between the interferroelectric transition temperatures T_{R-O} and T_{O-T}, as determined by Ehmke [89]. $T_{CW,T}$ is the calculated Curie-Weiss temperature for the T phase.

to the unambiguously T and R regions of phase space, as determined by Ehmke[89]. Results are compared with experimental data for a $[001]_C$ oriented BZT-50 BCT single crystal, as measured by Benabdallah *et al.*[132].

Figure 5.6(a) shows that the spontaneous polarization predicted using the coefficients fitted in this work gives a better agreement with the single-crystal data than the other sets of coefficients. This result was expected because the Landau parameters obtained herein were fitted to this data. Furthermore, the coefficients reported in the previous studies were not fitted to any experimental measurements. Instead, they were determined by modifying the coefficients of $BaTiO_3$ to generate a consistent phase diagram for the BZT-x BCT system[95,124]. In particular, the coefficients estimated by Yang *et al.*[95] yield P_{s3} values that deviate significantly from the experimental data for the T phase. Moreover, they cannot predict the spontaneous polarization and longitudinal permittivity at $T < 253.5\,\mathrm{K}$ (approximately), where the R phase is stable. Additionally, Figure 5.6(a) shows that the P_{s3} *vs* T curve estimated from Zhou *et al.*[124], despite having the correct shape, also differs significantly from the experimental values.

The Landau coefficients estimated in this work are validated by comparing the predicted relative permittivity, ϵ_{33}/ϵ_o, against experimental values and predictions using existing Landau parameters, Figure 5.6(b). Results show that the values predicted in this study gives the best agreement with the experimental data for all $T \leq T_{R-O}$, where the R phase is stable. Similarly, for the T phase, the calculated values near the region of interest, *i.e.,* close to T_{O-T}, fit the experimental data reasonably well compared to the predictions using Landau coefficients found in the literature. However, divergence is evident as $T \rightarrow T_{CW,T}$ for all the permittivity predictions. For the values calculated in this work, the divergence from experimental measurements is explained by the use of Equation 5.23, which involves only the direct coefficients of the Landau expansion, *i.e.,* $\alpha_{1,T}$, $\alpha_{11,T}$ and $\alpha_{111,T}$. These parameters were determined independently of any permittivity data and only $\alpha_{1,T}$ is allowed to vary with temperature.

The poor agreement of the longitudinal relative permittivity as $T \rightarrow T_{CW,T}$ can also be partly attributed to a weak relaxor behaviour observed in the single-crystal sample. According to Damjanovic[4], relaxor ferroelectrics display a diffuse P-FE phase transition with a broad peak in the dielectric permittivity and strong frequency dispersion in the FE phase. Although the $T_{T-C} = 366\,\mathrm{K}$ measured by Benabdallah *et al.*[132] was essentially frequency independent, they observed a strong dispersion in the permittivity of the T phase and a relatively broad permittivity peak. Additionally, the weak relaxor behaviour is also evidenced in the P_s *vs* T measurements, see Figure 5.1, where a diffuse P-FE phase transition is observed as the spontaneous polarizarion decreases continuously to zero but exhibits a finite value at $T_{T-C} = 366\,\mathrm{K}$. These observations were attributed to the extrinsic effects of FE domain wall motion or to local chemical heterogeneities[132].

The fitted Landau coefficients were also used to predict the longitudinal relative permittivity in an unpoled polycrystalline BZT-50 BCT sample, Figure 5.7. All the remnant domain switching fractions, included in Equations 5.8 and 5.9, were set to one in order to reproduce the randomly-oriented domains of an unpoled sample. Results were compared with experimental dielectric permittivity data measured from polycrystalline BZT-50 BCT samples in unpoled state at 1 kHz[85,136–138]. Overall, the

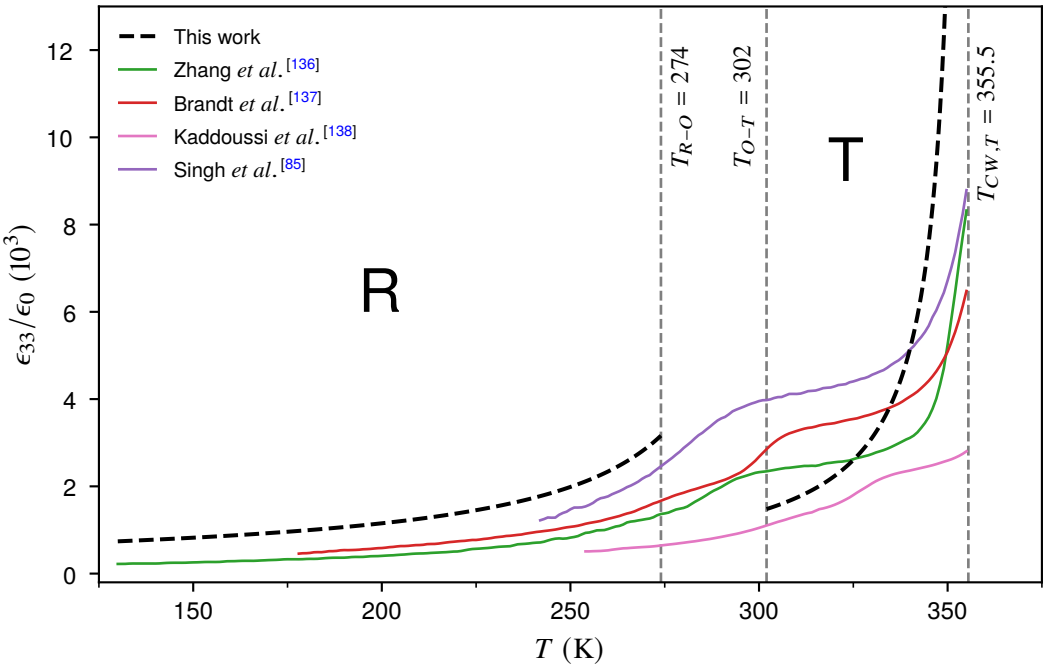

Figure 5.7: Predicted ϵ_{33}/ϵ_o *vs* T in unpoled BZT-50 BCT ceramic using the Landau parameters estimated for each FE phase. Experimental measurements from unpoled polycrystalline samples are also included for comparison. The purported O phase (or region of R + T coexistence) is shown between the interferroelectric transition temperatures T_{R-O} and T_{O-T}, as determined by Ehmke[89]. $T_{CW,T}$ is the predicted Curie-Weiss temperature for the T phase.

predictions show good agreement with respect to the general trends observed in experiments. These results further validate the Landau coefficients fitted in this study for each FE phase. However, near the interferroelectric transition temperatures (T_{R-O} and T_{O-T}), results yield lower permittivity values in the T phase than those predicted in the R phase. This can be explained by the fitting of coefficients $\alpha_{12,T}$ and $\alpha_{112,T}$ to single-crystal ϵ_{11} data estimated using a combination of ϵ_{33} values from a single-crystal and a polycrystalline sample. The latter was necessary due to the lack of available direct experimental ϵ_{11} data in the literature.

5.6 Summary and conclusions

A procedure was established to estimate the Landau parameters of FE systems using a combination of single-crystal and polycrystalline experimental data. The procedure can be readily extended to determine the Landau (and piezoelectric) coefficients based purely on a complete dataset of properties collected from a polycrystalline sample, which was not available in the literature. In particular, a better estimation of transverse permittivity data in the single crystal is possible from polycrystalline longitudinal and transverse permittivity measurements. However, for samples in saturated or unsaturated poling state, this requires additional information about the remnant switching fraction of the FE domains, which can be obtained via XRD experiments.

The fitting procedure developed was applied to obtain the Landau coefficients for the R and T phases of BZT-50 BCT. To the best of the author's knowledge, the estimated parameters correspond to

the first experimentally-fitted Landau coefficients reported for the BZT-50 BCT system. Results were used to predict the dielectric permittivity in single-crystal and polycrystalline samples yielding good agreement with experimental data. The fitted Landau parameters can be used in further theoretical and computational research to validate competing hypotheses regarding the structural state near the PPB of BZT-50 BCT. This would shed light upon the mechanisms responsible for the enhanced electromechanical properties reported experimentally for this system. These coefficients are used in Chapter 6 to model the intrinsic ferroelectric behaviour of BZT-50 BCT single crystals and explore the phase coexistence and domain structures.

Chapter 6

Application to BZT-50 BCT single crystal in 2-D

A version of this chapter is currently under preparation for journal publication as: Oscar A. Torres-Matheus, R. Edwin García and Catherine M. Bishop. Two-dimensional phase coexistence in multiphase field model of BZT-50 BCT single crystal.

6.1 Introduction

In previous chapters, a novel multiphase field model was developed for FE materials with a single polymorphic phase boundary. The model was applied to the BZT-40 BCT system assuming a phase diagram with a single PPB between the T and R phases. Analysis was performed in one and two spatial dimensions on coarse-grained BZT-40 BCT polycrystals to study the essential physics of phase coexistence in FE systems. This included the thermodynamic conditions for the stable and metastable coexistence of the FE phases, and the energetics associated with ferroelectric phase transformation, polarization switching and polarization-phase transformation interactions. In addition, the phase transformation kinetics and the domain structure and evolution (coarsening) were investigated taking into account the local electric fields arising from the dipole-dipole interactions within the two-phase FE material. However, the coarse-grained models do not capture the effects of anisotropy in these crystalline materials, which is required to study their intrinsic ferroelectric behaviour. Also, the macroscopic properties and domain morphology of polycrystalline ceramics are affected by extrinsic effects, such as the grain size and grain orientation distributions [38,47,48,116–118]. Hence, the detailed modelling of polycrystalline ferroelectrics depends on a correct description of the intrinsic FE behaviour in a single crystal using the anisotropic Landau coefficients calculated from single-crystal properties.

In this chapter, the MPF model is applied to a BZT-50 BCT single crystal to examine the intrinsic effects of ferroelectric coexistence on the phase transformation kinetics and domain morphology. A phase diagram with a single PPB between the T and R phases is assumed for the BZT-50 BCT system. The anisotropic Landau coefficients determined in Chapter 5 are used. Although the model is suitable for three-dimensional analysis, two-dimensional simulations are performed herein following similar works [51,52] due to limitations in the computational capacity.

6.2 Model formulation

The formulation described herein is based on the theoretical multiphase field framework presented in Section 2.3 for FE systems with a single PPB. For a single-crystal FE sample, characterized by the spatial distribution of the polarization vector $\vec{P} = (P_1, P_2, P_3)$, we define a 2-D computational domain described by coordinates $[x_1, x_2]$ parallel to the (001) plane of the pseudocubic crystal structure, Figure 6.1. For the selected computational domain, there are four in-plane and two fully out-of-plane tetragonal variants, while all eight rhombohedral variants are out of plane. In this work, an in-plane applied electric field is defined as $\vec{E} = (E_1, E_2) = -\nabla V_E$, where $\nabla = (\partial/\partial x_1, \partial/\partial x_2)$ and V_E is the electrostatic potential.

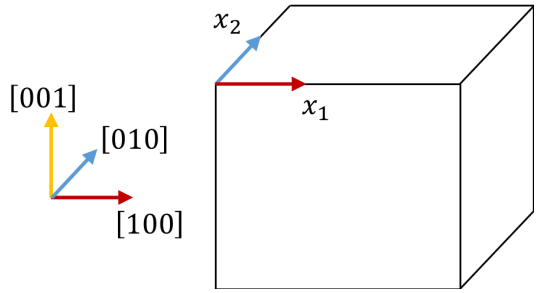

Figure 6.1: 2-D computational domain parallel to the (001) plane of the pseudocubic crystal structure.

The volumetric free energy density of the T and R phases, given by Equations 2.6 and 2.7, transform into[65,66]

$$\begin{aligned} f_T(\vec{P};\vec{E},T) = {} & \alpha_{1,T}(P_1^2+P_2^2+P_3^2) + \alpha_{11,T}(P_1^4+P_2^4+P_3^4) \\ & + \alpha_{12,T}(P_1^2P_2^2+P_2^2P_3^2+P_1^2P_3^2) + \alpha_{111,T}(P_1^6+P_2^6+P_3^6) \\ & + \alpha_{112,T}\left[P_1^4(P_2^2+P_3^2)+P_2^4(P_1^2+P_3^2)+P_3^4(P_1^2+P_2^2)\right] \\ & + \alpha_{123,T}P_1^2P_2^2P_3^2 - P_1E_1 - P_2E_2 \end{aligned} \tag{6.1}$$

$$\begin{aligned} f_R(\vec{P};\vec{E},T) = {} & \alpha_{1,R}(P_1^2+P_2^2+P_3^2) + \alpha_{11,R}(P_1^4+P_2^4+P_3^4) \\ & + \alpha_{12,R}(P_1^2P_2^2+P_2^2P_3^2+P_1^2P_3^2) + \alpha_{111,R}(P_1^6+P_2^6+P_3^6) \\ & + \alpha_{112,R}\left[P_1^4(P_2^2+P_3^2)+P_2^4(P_1^2+P_3^2)+P_3^4(P_1^2+P_2^2)\right] \\ & + \alpha_{123,R}P_1^2P_2^2P_3^2 - P_1E_1 - P_2E_2 + \Delta f_{PPB} \end{aligned} \tag{6.2}$$

where α_1, α_{11}, α_{12}, α_{111}, α_{112} and α_{123} are the Landau coefficients of each FE phase. As in the previous models, the leading coefficient is $\alpha_1 = a_{CW}(T - T_{CW})$, where T_{CW} is the Curie-Weiss temperature and $a_{CW} > 0$.

The free energy densities due to gradients in polarization and phase field are calculated as

$$\frac{1}{2}\sum_{k,l=1}^{3}\sum_{i,j=1}^{3} K_{ijkl}\frac{\partial P_k}{\partial x_i}\frac{\partial P_l}{\partial x_j} = \frac{1}{2}K_P(P_{1,1}^2 + P_{2,2}^2 + P_{1,2}^2 + P_{2,1}^2 + P_{3,2}^2 + P_{3,1}^2) \tag{6.3}$$

$$\frac{1}{2}\sum_{i,j=1}^{3} K_{ij}\frac{\partial \phi}{\partial x_i}\frac{\partial \phi}{\partial x_j} = \frac{1}{2}K_\phi\left(\frac{\partial \phi}{\partial x_1} + \frac{\partial \phi}{\partial x_2}\right)^2 \tag{6.4}$$

where $P_{i,j} = \partial P_i/\partial x_j$, $K_\phi = K_{11}$ and $K_P = K_{1111}$ assuming an isotropic gradient energy penalty for the formation of a polarization domain wall[47,48].

The spatial distribution and temporal evolution of the polarization order parameter are controlled by the following four coupled Allen-Cahn equations

$$\frac{\partial P_1}{\partial t} = -M_P \left\{ \frac{\partial f_R(\vec{P};T)}{\partial P_1}[1-h(\phi)] + \frac{\partial f_T(\vec{P};T)}{\partial P_1}h(\phi) + \frac{\partial V_E}{\partial x_1} - K_P\nabla^2 P_1 \right\} \tag{6.5}$$

$$\frac{\partial P_2}{\partial t} = -M_P \left\{ \frac{\partial f_R(\vec{P};T)}{\partial P_2}[1-h(\phi)] + \frac{\partial f_T(\vec{P};T)}{\partial P_2}h(\phi) + \frac{\partial V_E}{\partial x_2} - K_P\nabla^2 P_2 \right\} \tag{6.6}$$

$$\frac{\partial P_3}{\partial t} = -M_P \left\{ \frac{\partial f_R(\vec{P};T)}{\partial P_3}[1-h(\phi)] + \frac{\partial f_T(\vec{P};T)}{\partial P_3}h(\phi) - K_P\nabla^2 P_3 \right\} \tag{6.7}$$

$$\frac{\partial \phi}{\partial t} = -M_\phi \left\{ [f_T(\vec{P};T) - f_R(\vec{P};T)]\frac{\mathrm{d}h(\phi)}{\mathrm{d}\phi} + W\frac{\mathrm{d}g(\phi)}{\mathrm{d}\phi} - K_\phi\nabla^2\phi \right\} \tag{6.8}$$

where $\nabla^2 = \partial^2/\partial x_1^2 + \partial^2/\partial x_2^2$ and $M_P = M_\phi = M(\phi;T) = M_R(T)[1-h(\phi)] + M_T(T)h(\phi)$, with M_R and M_T defined as $M(T) = M_o \exp(-Q/RT)$, see Section 3.3.2 for full details on the definition of mobilities.

As in the previous models, the electrostatic field distribution is calculated using Coulomb's Equation. By assuming zero free electric charge density and considering the constitutive relation $\vec{D} = \vec{P} + \epsilon_o \vec{E}$[90], Coulomb's Equation becomes

$$\nabla \cdot \vec{P} - \epsilon_o \nabla^2 V_E = 0 \tag{6.9}$$

The model is normalized following a procedure similar to that detailed in Section 4.2. We define $\hat{x_i} = x_i/L$, $\hat{t} = t/\tau$, $u_i = P_i/|P_{sT}|$, and $\hat{E}_i = E_i/|E_{cT}|$; where L is the size of a square crystal, P_{sT} is the spontaneous polarization of the T phase, E_{cT} is the coercive field of the T phase, $\tau = 1/\left(\left|\alpha_{1,T}\right| M_T\right)$ and $i = 1, 2$. Thus, Equations 6.5 through 6.9 are cast in dimensionless form as

$$\frac{1}{\mu}\frac{\partial u_1}{\partial \hat{t}} = \gamma\hat{\nabla}^2 u_1 - \left\{ \frac{\partial \hat{f}_R(\vec{u};T)}{\partial u_1}[1-h(\phi)] + \frac{\partial \hat{f}_T(\vec{u};T)}{\partial u_1}h(\phi) + \hat{E}_{cT}\frac{\partial \hat{V}_E}{\partial \hat{x}_1} \right\} \tag{6.10}$$

$$\frac{1}{\mu}\frac{\partial u_2}{\partial \hat{t}} = \gamma\hat{\nabla}^2 u_2 - \left\{ \frac{\partial \hat{f}_R(\vec{u};T)}{\partial u_2}[1-h(\phi)] + \frac{\partial \hat{f}_T(\vec{u};T)}{\partial u_2}h(\phi) + \hat{E}_{cT}\frac{\partial \hat{V}_E}{\partial \hat{x}_2} \right\} \tag{6.11}$$

$$\frac{1}{\mu}\frac{\partial u_3}{\partial \hat{t}} = \gamma\hat{\nabla}^2 u_3 - \left\{ \frac{\partial \hat{f}_R(\vec{u};T)}{\partial u_3}[1-h(\phi)] + \frac{\partial \hat{f}_T(\vec{u};T)}{\partial u_3}h(\phi) \right\} \tag{6.12}$$

$$\frac{1}{\nu}\frac{\partial \phi}{\partial \hat{t}} = \gamma\lambda\hat{\nabla}^2\phi - \left\{ [\hat{f}_T(\vec{u};T) - \hat{f}_R(\vec{u};T)]\frac{\mathrm{d}h(\phi)}{\mathrm{d}\phi} + \hat{W}\frac{\mathrm{d}g(\phi)}{\mathrm{d}\phi} \right\} \tag{6.13}$$

$$0 = \hat{\nabla} \cdot \vec{u} - \hat{\epsilon}_o \hat{\nabla}^2 \hat{V}_E \tag{6.14}$$

where the following dimensionless parameters are defined: $\mu = M/M_T$, $\nu = P_{sT}^2\mu$, $\gamma = K_P/(|\alpha_{1,T}|L^2)$, $\lambda = K_\phi/(K_P P_{sT}^2)$, $\hat{W} = W/(|\alpha_{1,T}|P_{sT}^2)$, $\hat{E}_{cT} = \left|E_{cT}/(\alpha_{1,T}P_{sT})\right|$, and $\hat{\epsilon}_o = \epsilon_o\,|E_{cT}/P_{sT}|$.

Furthermore, $\hat{f}_T(\vec{u};T) = f_T(\vec{u};T)/(|\alpha_{1,T}|P_{sT}^2)$ and $\hat{f}_R(\vec{u};T) = f_R(\vec{u};T)/(|\alpha_{1,T}|P_{sT}^2)$ are calculated as

$$\begin{aligned}\hat{f}_T(\vec{u};T) =& \frac{\alpha'_{1,T}}{2}(u_1^2+u_2^2+u_3^2) + \frac{\alpha'_{11,T}}{4}(u_1^4+u_2^4+u_3^4) + \frac{\alpha'_{12,T}}{2}(u_1^2u_2^2+u_2^2u_3^2+u_1^2u_3^2)\\ &+ \frac{\alpha'_{111,T}}{6}(u_1^6+u_2^6+u_3^6) + \frac{\alpha'_{112,T}}{2}[u_1^4(u_2^2+u_3^2)+u_2^4(u_1^2+u_3^2)+u_3^4(u_1^2+u_2^2)]\\ &+ \frac{\alpha'_{123,T}}{2}u_1^2u_2^2u_3^2\end{aligned} \tag{6.15}$$

$$\begin{aligned}\hat{f}_R(\vec{u};T) =& \frac{\alpha'_{1,R}}{2}(u_1^2+u_2^2+u_3^2) + \frac{\alpha'_{11,R}}{4}(u_1^4+u_2^4+u_3^4) + \frac{\alpha'_{12,R}}{2}(u_1^2u_2^2+u_2^2u_3^2+u_1^2u_3^2)\\ &+ \frac{\alpha'_{111,R}}{6}(u_1^6+u_2^6+u_3^6) + \frac{\alpha'_{112,R}}{2}[u_1^4(u_2^2+u_3^2)+u_2^4(u_1^2+u_3^2)+u_3^4(u_1^2+u_2^2)]\\ &+ \frac{\alpha'_{123,R}}{2}u_1^2u_2^2u_3^2 + \Delta\hat{f}_{PPB}\end{aligned} \tag{6.16}$$

where the following dimensionless Landau coefficients are defined: $\alpha'_{1,T} = 2\alpha_{1,T}/|\alpha_{1,T}| = -2$, $\alpha'_{11,T} = 4\alpha_{11,T}P_{sT}^2/|\alpha_{1,T}|$, $\alpha'_{12,T} = 2\alpha_{12,T}P_{sT}^2/|\alpha_{1,T}|$, $\alpha'_{111,T} = 6\alpha_{111,T}P_{sT}^4/|\alpha_{1,T}|$, $\alpha'_{112,T} = 2\alpha_{112,T}P_{sT}^4/|\alpha_{1,T}|$, $\alpha'_{123,T} = 2\alpha_{123,T}P_{sT}^4/|\alpha_{1,T}|$, $\alpha'_{1,R} = 2\alpha_{1,R}/|\alpha_{1,T}|$, $\alpha'_{11,R} = 4\alpha_{11,R}P_{sT}^2/|\alpha_{1,T}|$, $\alpha'_{12,R} = 2\alpha_{12,R}P_{sT}^2/|\alpha_{1,T}|$, $\alpha'_{111,R} = 6\alpha_{111,R}P_{sT}^4/|\alpha_{1,T}|$, $\alpha'_{112,R} = 2\alpha_{112,R}P_{sT}^4/|\alpha_{1,T}|$, $\alpha'_{123,R} = 2\alpha_{123,R}P_{sT}^4/|\alpha_{1,T}|$ and $\Delta\hat{f}_{PPB} = \Delta f_{PPB}/(|\alpha_{1,T}|P_{sT}^2)$.

The tetragonal polarizations states are along the $\langle 100\rangle$ family of directions, while the rhombohedral variants are along the $\langle 111\rangle$ directions. Considering the case of $\vec{P}_T = (P,0,0)$, the magnitude of the coercive field in the tetragonal phase, $\vec{E}_{cT} = (E_{cT},0,0)$, is

$$E_{cT} = \left.\frac{\partial f_T(\vec{P}_T;T)}{\partial P}\right|_{P=P_{cT}} = 2\alpha_{1,T}P_{cT} + 4\alpha_{11,T}P_{cT}^3 + 6\alpha_{111,T}P_{cT}^5 \tag{6.17}$$

where P_{cT} represents the magnitude of the polarization at the coercive field, which can be calculated from $\partial^2 f_T(\vec{P}_T;T)/\partial P^2\big|_{P=P_{cT}} = 0$. Moreover, the magnitudes of the spontaneous polarization for each FE phase, $\vec{P}_{sT} = P_{sT}(1,0,0)$ and $\vec{P}_{sR} = P_{sR}(1/\sqrt{3},1/\sqrt{3},1/\sqrt{3})$, are calculated as

$$P_{sT} = \pm\left[\frac{-\alpha_{11,T} + \sqrt{\alpha_{11,T}^2 - 3\alpha_{1,T}\alpha_{111,T}}}{3\alpha_{111,T}}\right]^{1/2} \tag{6.18}$$

$$P_{sR} = \pm\sqrt{3}\left[\frac{-(\alpha_{11,R}+\alpha_{12,R}) + \sqrt{(\alpha_{11,R}+\alpha_{12,R})^2 - \alpha_{1,R}(3\alpha_{111,R}+6\alpha_{112,R}+\alpha_{123,R})}}{3\alpha_{111,R}+6\alpha_{112,R}+\alpha_{123,R}}\right]^{1/2} \tag{6.19}$$

6.3 Model parameters

The dimensionless parameters of the BZT-50 BCT model are calculated using the physical constants stated in Table 6.1. In this model, the PPB temperature is estimated as $T_{PPB} \sim (T_{O-T} + T_{R-O})/2 = 288\,\text{K}$, where $T_{R-O} = 274\,\text{K}$ and $T_{O-T} = 302\,\text{K}$ according to Ehmke[89].

Table 6.1: Physical parameters of the MPF model for a BZT-50 BCT single crystal. The anisotropic Landau coefficients are repeated from Table 5.1 for completeness.

Symbol	R phase ($\phi = 0$)	T phase ($\phi = 1$)	Units
a_{CW}	1.450×10^5	1.800×10^5	$\mathrm{Jm/C^2K}$
α_{11}	1.000×10^7	3.225×10^8	$\mathrm{Jm^5/C^4}$
α_{12}	-1.000×10^8	5.501×10^9	$\mathrm{Jm^5/C^4}$
α_{111}	3.552×10^9	1.000×10^9	$\mathrm{Jm^9/C^6}$
α_{112}	-4.582×10^8	1.023×10^7	$\mathrm{Jm^9/C^6}$
α_{123}	9.000×10^9	0.000	$\mathrm{Jm^9/C^6}$
T_{CW}	299.0	355.5	K
T_C	301.5	$T_{CW,T}$	K
T_{max}	302.3	$T_{CW,T}$	K
M_o	1.809×10^{-4}	3.349×10^{-4}	S/m
Q	8561	13 250	J/mol
K_P	1.962×10^{-11}		$\mathrm{Jm^3/C^2}$
K_ϕ	9.000×10^{-13}		J/m
W	3.000×10^6		$\mathrm{J/m^3}$
Δf_{PPB}	-3.198×10^4		$\mathrm{J/m^3}$

The gradient energy coefficients, K_P and K_ϕ, and the double-well coefficient, W, are established via numerical evaluation such that the widths of phase interfaces, measured in $\vec{P}$ and in ϕ, are similar at T_{PPB}, where both phases are stable. In addition, the parameters are estimated so that all interfaces are resolved and their width is two orders of magnitude smaller than the computational domain. The latter allows analysis of bulk domains and their interfaces. The width of in-plane 180TDWs, *i.e.,* a 180TDW between domains with in-plane polarizations, is set to 3 nm. It is worth noting that the evaluation is carried out using the in-plane 180TDWs to capture the entire energetics of the interface. Then, the size of the single-crystal sample is calculated as $L = 232$ nm. This is smaller than typical grain sizes achieved during standard processing of $29 \pm 6\,\mu$m for BZT-50 BCT[89]. However, the estimated sample size is sufficiently large to enable multiple domains to be investigated. Finally, the value for K_P is back-calculated from $\gamma = K_P/(L^2 \left|\alpha_{1,T}\right|_{T_{PPB}})$, while K_ϕ and W are established to adjust the interfacial energy of T-R phase boundaries and prevent unphysical relaxation of the FE phases.

The constants M_o and Q, which define the mobility of each FE phase as $M(T) = M_o \exp(-Q/RT)$, are calculated using data obtained from experiments, Figures 6.2(a) and (c). The procedure for estimating mobility values from experimental data is detailed in Section 3.3.2. It is worth noting that measurements from polycrystalline samples are used in this work due to the lack of single-crystal information in the literature. For the T phase, $M_{o,T}$ and Q_T are calculated directly from

BZT-50 BCT data by fitting the equation $\ln(M) = \ln(M_o) - (Q/R)(1/T)$ to five data points, Figure 6.2(d). For the R phase, no experimental data was available at $T < 274$ K, where the R phase is unambiguously stable for the BZT-50 BCT composition. Hence, the constants $M_{o,R}$ and Q_R, obtained from BZT-40 BCT data, are used in this study, Figure 6.2(b).

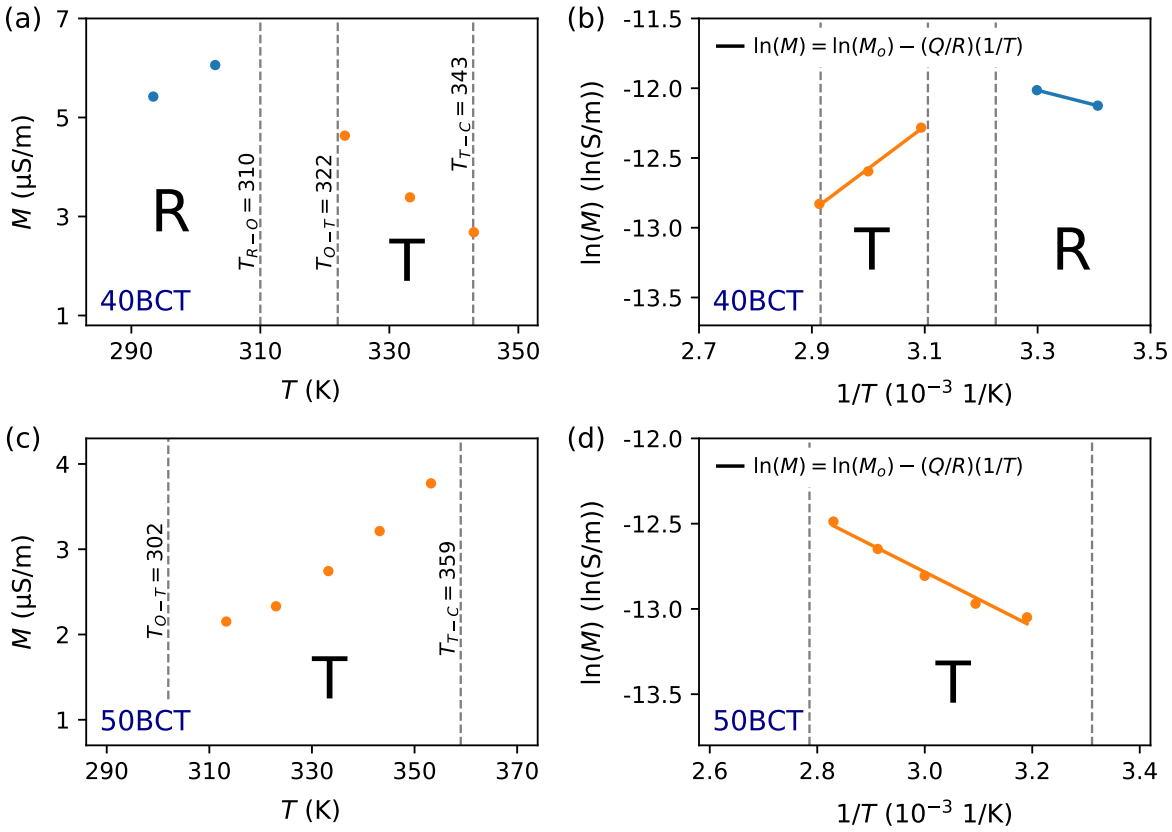

Figure 6.2: Calculation of mobility constants for the R (—) and T (—) phases of the BZT-50 BCT single-crystal model from experimental hysteresis data, as reported by Ehmke[89]. Subfigures (a) and (c) show mobility values extracted using experimental hysteresis data at selected temperatures from BZT-40 BCT and BZT-50 BCT polycrystalline samples, respectively. Subfigures (b) and (d) illustrate the fitting of equation $\ln(M) = \ln(M_o) - (Q/R)(1/T)$ to estimate parameters Q and M_o using BZT-40 BCT and BZT-50 BCT data, respectively. The transition temperatures T_{R-O}, T_{O-T} and T_{T-C} are also shown, as measured by Ehmke[89].

The estimated mobility constants are shown in Table 6.1. These parameters yield mobilities with the same order of magnitude as those reported by Zhao, Cao and García[93] for stress-free, lanthanum-doped PZT. Moreover, Table 6.1 shows that the tetragonal mobility, calculated using data directly from the BZT-50 BCT composition, has a positive activation energy, *i.e.*, $Q_T > 0$, see Figure 6.2(d). In contrast, calculations for the BZT-40 BCT system yielded $Q_T < 0$ (Table 3.1), which was attributed to the proximity of experiments to the T-C phase transition, see Figure 6.2(b). It can be shown that the mobility in the T phase, calculated for the BZT-60 BCT and BZT-45 BCT compositions using data measured by Ehmke[89], also has $Q_T > 0$, see Appendix A. Similarly, calculations performed on the $K_{0.5}Na_{0.5}NbO_3$ (KNN)-modified $(1-x)Bi_{0.5}Na_{0.5}TiO_3$-$x(Ba_{0.7}Ca_{0.3})TiO_3$ (BNT-BT) system, known as BNT-BT-KNN, found a positive activation energy[93].

6.4 Simulation cases and numerical implementation

The MPF model for a BZT-50 BCT single crystal described by a three-component polarization order parameter was implemented using FEM in COMSOL Multiphysics® [94]. A square computational domain of side L was defined with coordinates x and y. All simulations were performed on a mesh with 120×120 elements and using second-order Lagrange shape functions.

The interfacial widths and energies were calculated for different types of TDWs, RDWs and T-R phase interfaces at selected temperatures. For all cases, Equations 6.10 through 6.14 were solved considering a computational domain with a single interface between two homogeneous FE domains, with $\hat{V}_E(\hat{x}, \hat{y}, \hat{t}=0) = 0$. All boundaries were electrically grounded ($\hat{V}_E = 0$), while zero flux conditions were applied for u_x, u_y, u_z and ϕ.

The microstructural evolution of two-phase FE systems was simulated upon quenching for selected temperatures in the absence of applied electric fields. The effect of dipole-dipole interactions within the material was included by solving Equations 6.10 through 6.14. Results were used to investigate the intrinsic effects of phase coexistence on the domain configurations and transformation dynamics of the coexisting FE phases. Five simulations were performed at each temperature, with ten additional cases at $T = 286\,\text{K}$, $287\,\text{K}$ and $288\,\text{K}$ to examine the long-term phase coexistence in the vicinity of the PPB. Different mixed 50%R+50%T initial conditions were considered using a uniform random distribution function, {mean, range}, for the phase field $\{0.5, 0.5\}$ and for each polarization component $\{0, 2\}$. Further, $\hat{V}_E(\hat{x}, \hat{y}, \hat{t}=0) = 0$ for all cases. The boundaries of the computational domain were electrically grounded, with periodic boundary conditions for u_x, u_y, u_z and ϕ.

Additional simulations at selected temperatures were performed for the microstructural evolution of a particular two-phase FE sample in the absence of applied electric fields. Two different mixed 50%R+50%T initial states (samples) were considered. For each case, only one simulation was performed at each selected temperature. In the first scenario, the simulations were initialized using $\hat{V}_E(\hat{x}, \hat{y}, \hat{t}=0) = 0$ and the same random conditions for u_x, u_y, u_z and ϕ. These initial conditions were identified as RIC1. In the second scenario, a specific microstructure with well-developed ferroelectric domains, labelled DIC1, was selected as the initial condition for all simulations. Results were used to study the evolution of different types of interfaces and the effect of the interfacial energies on the stabilization of FE phases at different temperatures. For both scenarios, Equations 6.10 through 6.14 were solved in a computational domain with electrically grounded boundaries and periodic conditions for u_x, u_y, u_z and ϕ.

For all microstructural evolution simulations, a scalar variable was created to output the average phase field $\overline{\phi}$ at every $\hat{t} = 1$. The solution fields of u_x, u_y, u_z and ϕ were stored at selected times for detailed analysis of FE domain structures and interfaces.

6.5 Results and analysis

6.5.1 Interfacial calculations

Values for the interfacial width and energy, ξ and σ, were calculated for the different types of interfaces identified in this study. Domain walls are described by the polarization rotation between variants that occurs across the interface. Similarly, T-R phase interfaces are described by the polarization rotation from one phase to the other. These descriptions do not specify the interface normal or inclination. The interfacial energy is a function of both polarization rotation and interface inclination in ferroelectric systems. Hence, the lowest energy configuration reported for each type of interface is determined by the interfacial energy as it is principally anisotropic.

In this model, four different domain walls were distinguished in the T phase: 180TDW$_1$, 90TDW$_1$, 180TDW$_2$ and 90TDW$_2$. The interfaces denoted as 180TDW$_1$ and 90TDW$_1$ are those characterized by 180° and 90° in-plane polarization switchings between tetragonal domains, Figure 6.3(a). Further, the 2-D implementation produces additional, different TDWs that involve domain(s) with out-of-plane polarization, Figure 6.3(b). An 180TDW$_2$ represents an interface between two tetragonal domains with out-of-plane polarizations, while a 90TDW between one in-plane domain and one out-of-plane domain is labelled 90TDW$_2$.

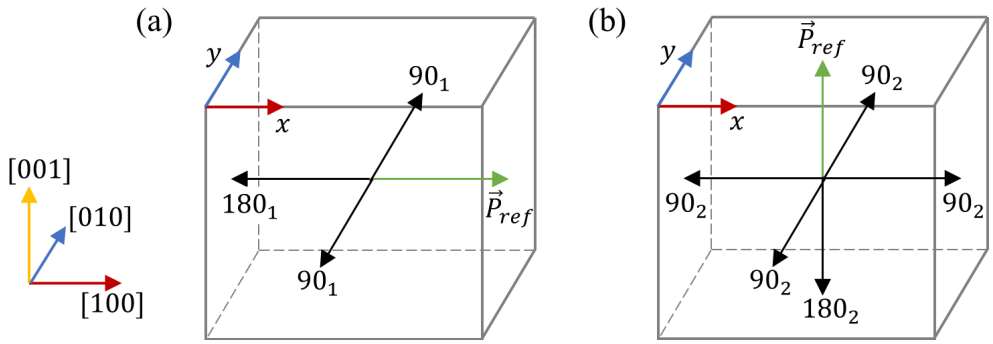

Figure 6.3: Types of TDWs identified in the two-dimensional MPF model for a BZT-50 BCT single crystal described by a three-component polarization order parameter. Subfigure (a) illustrates the in-plane tetragonal domain walls: 180TDW$_1$ and 90TDW$_1$. Subfigure (b) describes TDWs involving out-of-plane polarization switching: 180TDW$_2$ and 90TDW$_2$. For both cases, directions of spontaneous polarization in the tetragonal phase are represented by arrows. Also, the switching angles between a reference polarization direction, $\vec{P}_{ref}$, and its variants are indicated. Subscripts 1 and 2 correspond to the types of 180TDWs and 90TDWs identified in this study.

Similarly, for the R phase, the following domain walls were observed: 180RDW, 109RDW$_1$, 71RDW$_1$, 109RDW$_2$ and 71RDW$_2$. Figure 6.4 shows that all the rhombohedral variants are partially contained in the selected 2-D computational domain. In this case, the selected plane resulted in two energetically different 109RDWs and 71RDWs.

For the T-R phase boundaries, four different interfaces were distinguished, namely: 55T-R$_1$, 125T-R$_1$, 55T-R$_2$ and 125T-R$_2$. In this case, the two types of 55T-R and 125T-R interfaces depend on the polarization direction in the T phase. The first type (with subscript 1) involves a tetragonal

domain with in-plane polarization, Figure 6.5(a); while the second type (with subscript 2) involves a tetragonal domain with out-of-plane polarization, Figure 6.5(b).

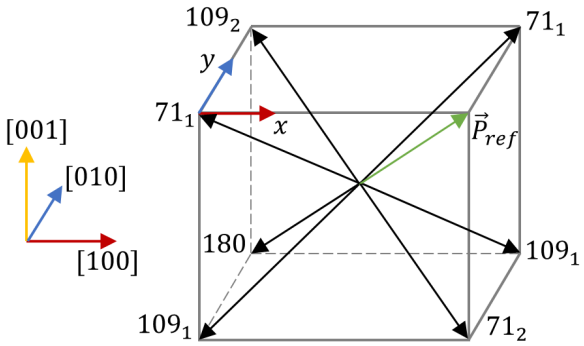

Figure 6.4: Types of RDWs identified in the two-dimensional MPF model for a BZT-50 BCT single crystal described by a three-component polarization order parameter. Directions of spontaneous polarization in the rhombohedral phase are represented by arrows. Also, the switching angles between a reference polarization direction, $\vec{P}_{ref}$, and its variants are indicated. Subscripts 1 and 2 correspond to the types of 109RDWs and 71RDWs identified in this study.

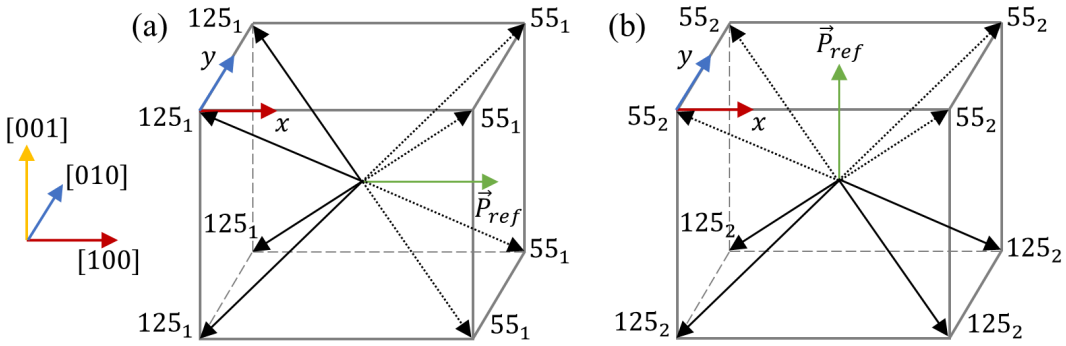

Figure 6.5: Types of T-R phase interfaces identified in the two-dimensional MPF model for a BZT-50 BCT single crystal described by a three-component polarization order parameter. Subfigure (a) depicts the T-R interfaces involving in-plane polarization in the T phase: 55T-R_1 and 125T-R_1. Subfigure (b) shows the T-R interfaces involving out-of-plane polarization in the T phase: 55T-R_2 and 125T-R_2. Black arrows represent directions of spontaneous polarization in the R phase and the green arrow represents a reference polarization direction, $\vec{P}_{ref}$, in the T phase. Switching angles are indicated, with subscripts 1 and 2 referring to the types of 55T-R (⋯▶) and 125T-R (⟶) phase interfaces identified in this study.

In the cases of 180TDW_1 and 90TDW_1, where the polarization of both domains lies in the (001) plane, the normal to the interfaces at their lowest energy inclination is also in the (001) plane. Thus, the 2-D model captures the 3-D energetics of the interfaces. For a 180TDW_2, where the polarization of both domains is perpendicular to the (001) plane, the normal to the interface lies in the (001) plane and can have any orientation in that plane. In this case, the 2-D model also reproduces the interfacial energy in 3-D. For all other cases, the energetics of interfaces in the 2-D implementation differ from those in a 3-D scenario.

Figures 6.6 through 6.8 illustrate the interfacial calculations discussed in this section, and show simulation results at $T = T_{PPB} = 288\,\mathrm{K}$. In the left column of these figures, the lowest energy

configurations for FE systems with a single interface are shown. In the right column, $\hat{f}$, ϕ and $u_{y'}$ (or $u_{z'}$) are plotted along a line normal to the resolved interface. For all cases, a local coordinate system is defined with respect to the interface of interest, with x' as the normal direction, y' as the tangential direction and $z' = z$ is parallel to the [001] direction.

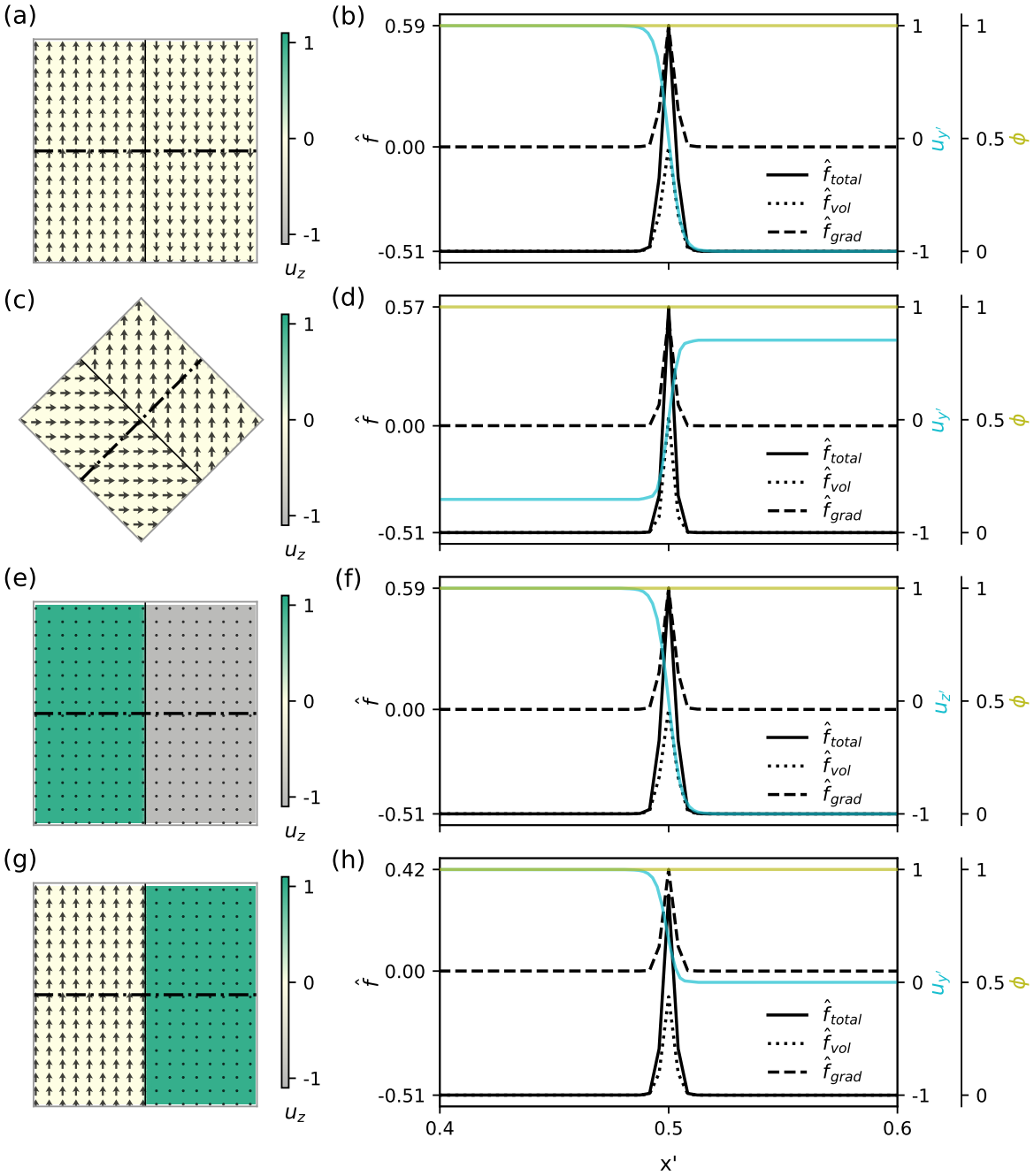

Figure 6.6: Interfacial width and energy calculations at $T = T_{PPB} = 288\,\mathrm{K}$ for (a)-(b) 180TDW$_1$, (c)-(d) 90TDW$_1$, (e)-(f) 180TDW$_2$, and (g)-(h) 90TDW$_2$. Left column: vector plot of (u_x, u_y) and contour plot of u_z showing the lowest energy configurations for each case, with local coordinates x' and y' in the normal and tangential directions to the interface and $z' = z$. Right column: line plot of calculated $\hat{f} = f/(|\alpha_{1,T}|P_{sT}^2)$, $u_{y'} = P_{y'}/|P_{sT}|$ (or $u_{z'} = P_{z'}/|P_{sT}|$) and ϕ along interface normal, showing results for $0.4 \leq x' \leq 0.6$.

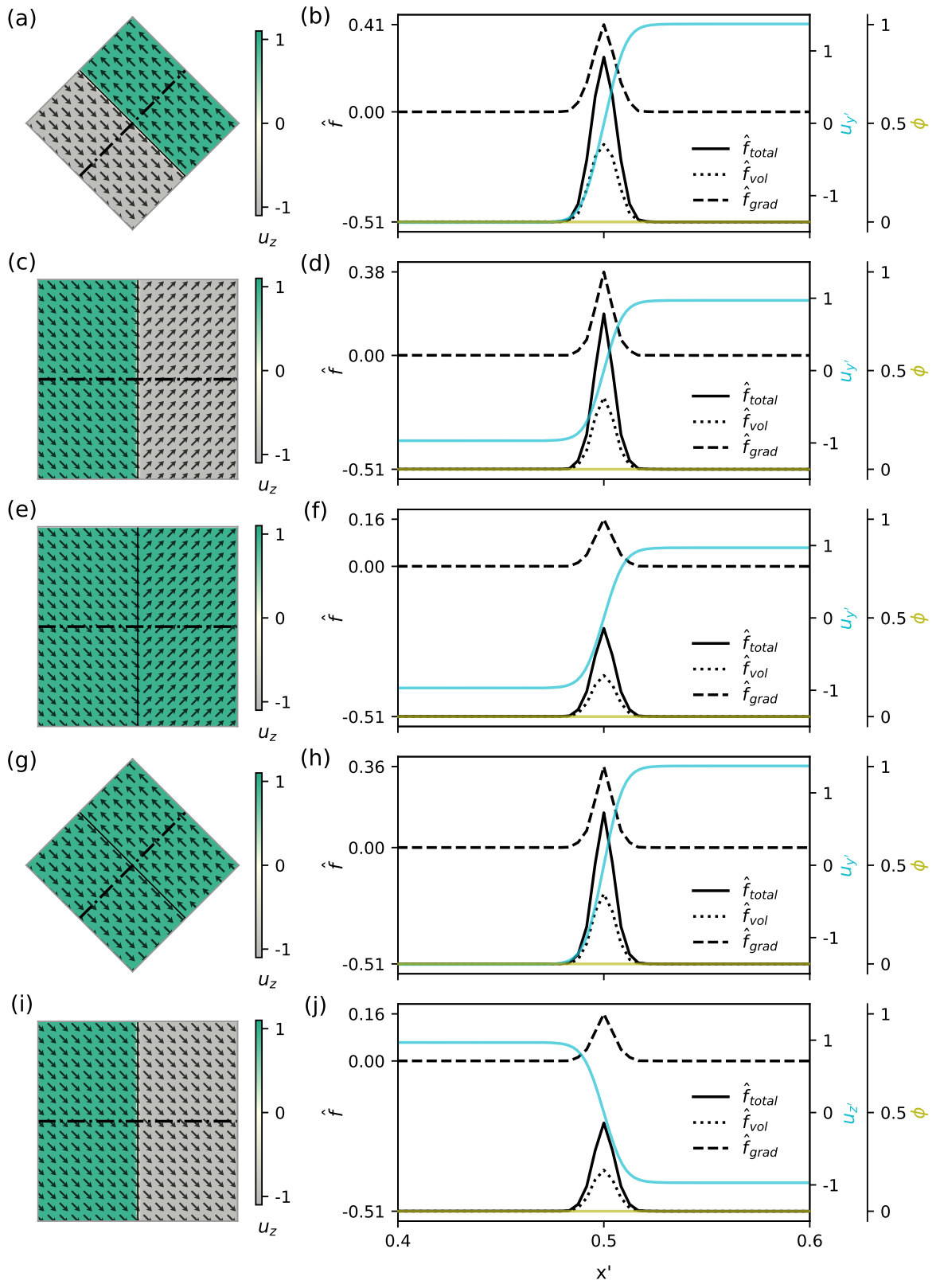

Figure 6.7: Interfacial width and energy calculations at $T = T_{PPB} = 288\,\mathrm{K}$ for (a)-(b) 180RDW, (c)-(d) 109RDW$_1$, (e)-(f) 71RDW$_1$, (g)-(h) 109RDW$_2$, and (i)-(j) 71RDW$_2$. Left column: vector plot of (u_x, u_y) and contour plot of u_z showing the lowest energy configurations for each case, with local coordinates x' and y' in the normal and tangential directions to the interface and $z' = z$. Right column: line plot of calculated $\hat{f} = f/(|\alpha_{1,T}|P_{sT}^2)$, $u_{y'} = P_{y'}/|P_{sT}|$ (or $u_{z'} = P_{z'}/|P_{sT}|$) and ϕ along interface normal, showing results for $0.4 \leq x' \leq 0.6$.

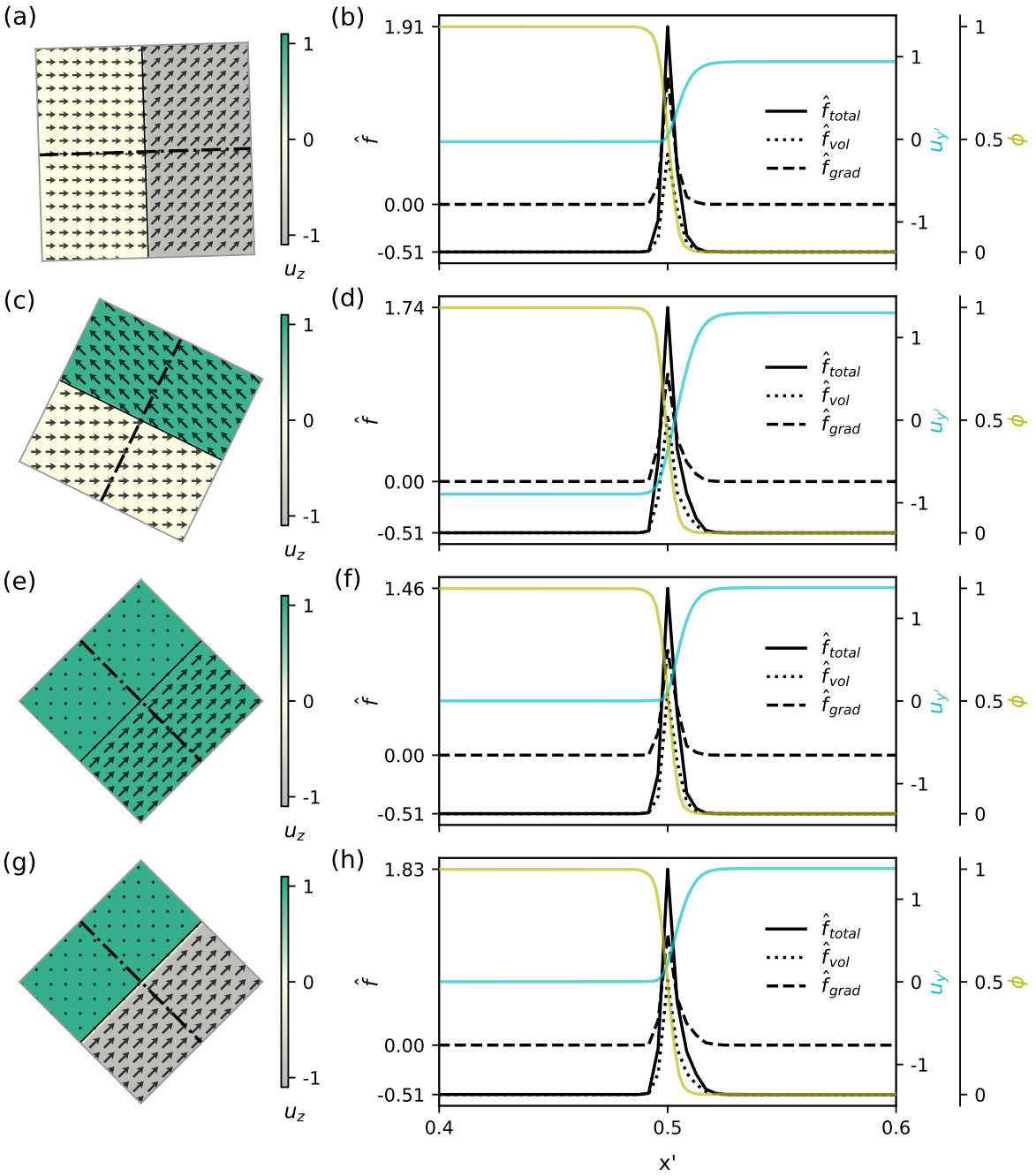

Figure 6.8: Interfacial width and energy calculations at $T = T_{PPB} = 288\,\text{K}$ for (a)-(b) 55T-R_1, (c)-(d) 125T-R_1, (e)-(f) 55T-R_2, and (g)-(h) 125T-R_2. Left column: vector plot of (u_x, u_y) and contour plot of u_z showing the lowest energy configurations for each case, with local coordinates x' and y' in the normal and tangential directions to the interface and $z' = z$. Right column: line plot of calculated $\hat{f} = f/(|\alpha_{1,T}|P_{sT}^2)$, $u_{y'} = P_{y'}/|P_{sT}|$ and ϕ along interface normal for $0.4 \leq x' \leq 0.6$.

The interfacial calculations were performed only for planar interfaces, where $\partial u_{x'}/\partial y' = \partial u_{y'}/\partial y' = \partial u_{z'}/\partial y' = \partial \hat{V}_E/\partial y' = 0$. Further, assuming that there is no free charge in the system, Coulomb's Equation is cast as $\hat{\nabla} \cdot \vec{u} - \hat{\epsilon}_o \hat{\nabla}^2 \hat{V}_E = 0$ (Equation 6.14), where $\hat{\nabla} = (\partial/\partial x', \partial/\partial y')$ and $\hat{\nabla}^2 = \partial^2/\partial x'^2 + \partial^2/\partial y'^2$. Since $\hat{\epsilon}_o$ values are negligible, it can be shown that $\partial u_{x'}/\partial x' \approx 0$. Thus, only the out-of-plane polarization component, $u_{z'} = u_z$, and the polarization component perpendicular to the interface normal, $u_{y'}$, can change across the boundary, *i.e.*, $\partial u_{z'}/\partial x' \neq 0$ and $\partial u_{y'}/\partial x' \neq 0$.

The methods for calculating the interfacial widths and energies were the same described in Sections 3.3 and 4.5.1. For this particular model, the interfacial widths were calculated using, where possible, the profile of $u_{y'}$ across the interface. However, the width of 180TDW$_2$ and 71RDW$_2$, where $\partial u_{y'}/\partial x' \approx 0$, was calculated using the profile of $u_{z'}$. Results are summarized in Table 6.2 for all interfaces at $T = T_{PPB} = 288\,\mathrm{K}$. The same procedure described above was repeated for calculations at different temperatures.

Table 6.2: Interfacial widths and energies calculated at $T = T_{PPB} = 288\,\mathrm{K}$ in the two-dimensional MPF model for a BZT-50 BCT single crystal described by a three-component polarization order parameter.

Interface type	Width, ξ (nm)	Interfacial energy, σ (J/m^2)
180TDW$_1$	3.000	3.543×10^{-4}
90TDW$_1$	2.432	2.456×10^{-4}
180TDW$_2$	3.000	3.543×10^{-4}
90TDW$_2$	2.659	2.193×10^{-4}
180RDW	5.163	5.520×10^{-4}
109RDW$_1$	4.566	4.067×10^{-4}
71RDW$_1$	4.855	1.916×10^{-4}
109RDW$_2$	4.654	4.023×10^{-4}
71RDW$_2$	4.855	1.916×10^{-4}
55T-R$_1$	2.986	7.067×10^{-4}
125T-R$_1$	4.259	8.304×10^{-4}
55T-R$_2$	3.042	6.419×10^{-4}
125T-R$_2$	3.353	8.428×10^{-4}

Table 6.2 shows that the calculated interfacial widths for BZT-50 BCT single crystals are similar to the values obtained for coarse-grained BZT-40 BCT polycrystals, see Table 4.2. This is explained by the equivalent procedures used to establish K_P, K_ϕ and W for both FE systems. Essentially, numerical evaluation was used in both cases until the dimensionless parameters gave a reasonable size of the computational model to investigate multiple FE domains, while still resolving their interfaces. For BZT-40 BCT, the width of one-dimensional 180RDWs was then set to 4 nm, yielding a simulated crystal size of $L = 190\,\mathrm{nm}$, as described in Section 3.3. For BZT-50 BCT, the width of in-plane 180TDWs (denoted herein as 180TDW$_1$) was set to 3 nm, giving $L = 232\,\mathrm{nm}$, see Section 6.3.

Although the above procedure leads to comparable ξ values, the estimated model parameters for single-crystal BZT-50 BCT ($K_P = 1.962 \times 10^{-11}\,\mathrm{Jm^3/C^2}$, $K_\phi = 9.000 \times 10^{-13}\,\mathrm{J/m}$ and $W = 3.000 \times 10^6\,\mathrm{J/m^3}$) are one or two orders of magnitude greater than those obtained for coarse-grained BZT-40 BCT ($K_P = 8.051 \times 10^{-13}\,\mathrm{Jm^3/C^2}$, $K_\phi = 2.150 \times 10^{-14}\,\mathrm{J/m}$ and $W = 1.444 \times 10^4\,\mathrm{J/m^3}$). This is attributed to the use of anisotropic Landau coefficients fitted to experimental single-crystal data

for the BZT-50 BCT composition. Moreover, higher values for K_P, K_ϕ and W yield greater calculated interfacial energies. Table 6.2 shows that the σ values are two orders of magnitude higher that those calculated for the BZT-40 BCT system, see Table 4.2.

The interfacial widths estimated herein are similar to those reported for 90TDWs in $BaTiO_3$ using TEM (4-6 nm[139] and 7-12 nm[140]), electron holography (1-2.5 nm[141] and 2-5 nm[142]) and XRD (4-6 nm[143]). Moreover, the estimated ξ values have the same orders of magnitude as the widths reported in phenomenological studies for $BaTiO_3$[68,71]. In these models, the authors used a six-order Landau-Devonshire expansion, with Landau coefficients and anisotropic gradient energy coefficient estimated from single-crystal properties, to study mechanically compatible and electrically neutral DWs. At T = 298 K, calculated widths of 3.6 nm and 0.6 nm were reported for 90TDWs and 180TDWs, respectively[68]. Additionally, ξ values were estimated in temperature ranges where the T and R phases are stable in $BaTiO_3$. The following approximate results were obtained: 3.4-6.2 nm for 90TDWs, 0.6-1.2 nm for 180TDWs, 1.8-2.6 nm for 180RDWs, and 0.6-0.9 nm for 109RDWs and 71RDWs[71].

Domain wall energies of FE systems remain largely unavailable in the literature, with the few reported values spanning a wide range, *e.g.,* 0.012 mJ/m^2 for 180° walls in Rochelle salt and 10 mJ/m^2 for 180° walls in $BaTiO_3$[1]. The calculated interfacial energies for the BZT-50 BCT single crystal are between one and two orders of magnitude smaller than those predicted for $BaTiO_3$, the archetype of FE materials. Phenomenological results in the T and R phases of $BaTiO_3$ yield approximately: 1.5-7.5 mJ/m^2 for 90TDWs, 1.5-6.0 mJ/m^2 for 180TDWs, 25-50 mJ/m^2 for 180RDWs, 5.0-11 mJ/m^2 for 109RDWs and 2.0-7.0 mJ/m^2 for 71RDWs[71].

Figure 6.9 illustrates the temperature dependence of the calculated widths and energies of domain walls for two-dimensional BZT-50 BCT single crystals. For all types of domain walls, the ξ values increase with temperature, Figure 6.9(a). The same behaviour was observed for coarse-grained BZT-40 BCT polycrystals in agreement with Equation 4.17 and phenomenological results for $BaTiO_3$[71], see Section 4.5.1. Also, a similar, significant increase in the ξ values of RDWs is observed as $T \rightarrow T_{CW,R}$ (299 K). This is associated with the near vanishing spontaneous polarization close to the weak first order P-FE transition that occurs for the R phase at $T_{CW,R}$, see Section 5.5.

For all types of domain walls, the interfacial energy decreases with increasing temperature, Figure 6.9(b). As discussed in Section 4.5.1, this is caused by a decrease in the energy barrier between stable FE domains as temperature rises, following Equation 4.18. Further, in both FE phases, higher σ values are observed for 180DWs as a consequence of greater energy barriers and polarization switching between anti-parallel polarization states.

Figure 6.9 also shows that $\xi_{180TDW_1} = \xi_{180TDW_2}$ and $\xi_{71RDW_1} = \xi_{71RDW_2}$, and $\sigma_{180TDW_1} = \sigma_{180TDW_2}$ and $\sigma_{71RDW_1} = \sigma_{71RDW_2}$ at their lowest energy configuration. However, an analysis of the interfacial charge density, $\Delta\vec{P} \cdot \hat{n}$, for different angles of the interfaces normal, $\hat{n}$, revealed that $180TDW_2$ and $71RDW_2$ have isotropic interfacial energies. This is explained by $180TDW_2$ and $71RDW_2$ being characterized in this model by constant in-plane u_x and u_y values across the interface; while the spatial distribution of the out-of-plane polarization component, u_z, is unconstrained, see

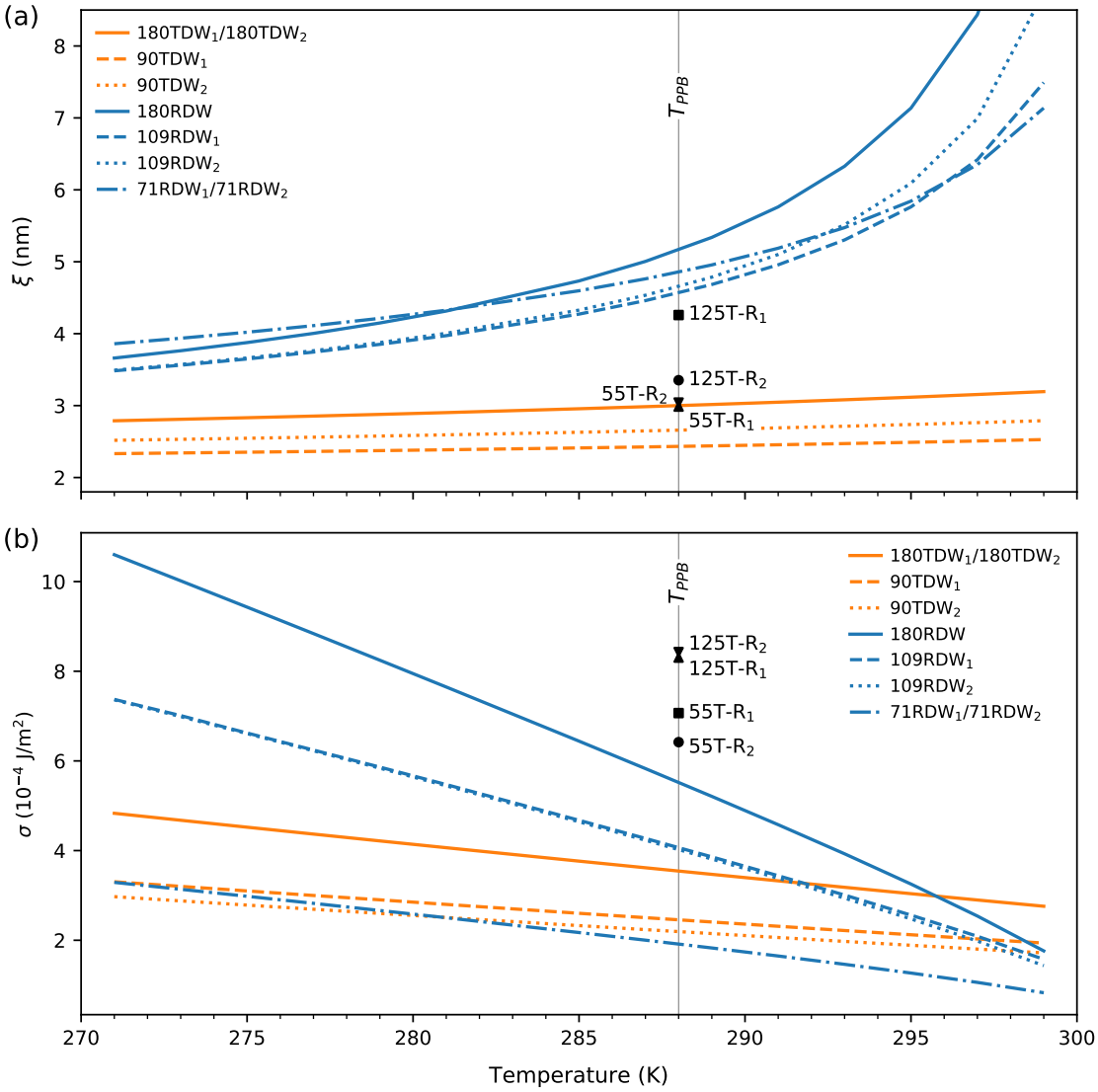

Figure 6.9: Temperature dependence of the calculated (a) widths and (b) energies of DWs for a two-dimensional BZT-50 BCT single crystal. Calculations were performed at 2 K increments between 271 K and 299 K. The width and energy of T-R phase interfaces are also included at $T = T_{PPB} = 288$ K, the only temperature where both phases are stable.

Figure 6.3(e) and Figure 6.4(i). Consequently, for 180TDW$_2$ and 71RDW$_2$, any orientation of the interface normal satisfies Coulomb's Equation, yielding microstructures with curved domain walls or straight walls with arbitrary inclinations. In contrast, faceted 180TDW$_1$ and 71RDW$_1$ with specific orientations are expected due to the anisotropic nature of their interfacial energies. This is illustrated in Figure 6.10, where schematic γ-plots are constructed for a 180TDW$_1$ and a 180TDW$_2$ using $\Delta\vec{P} \cdot \hat{n}$ as a proxy. It is observed that the interfacial energy of a 180TDW$_2$ is the same for any orientation, *i.e.,* it is isotropic; while there is a large energy penalty to form a 180TDW$_1$ at orientations different from its lowest energy configuration. Hence, Figure 6.10 suggests that observing a 180TDW$_2$ (or a 71RDW$_2$) in the microstructure is more likely than observing a 180TDW$_1$ (or a 71RDW$_1$).

The analysis shown in Figure 6.10 was applied to all interfaces. Calculations showed that all TDWs and RDWs, with the exception of 180TDW$_2$ and 71RDW$_2$, have anisotropic interfacial

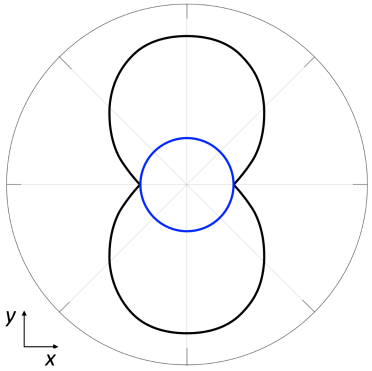

Figure 6.10: Schematic γ-plots for 180TDW$_1$ (—) and 180TDW$_2$ (—), showing interfacial energies as a function of orientation of the interface normal. A 180TDW$_1$ is considered between a domain with $\vec{P} = (0, P_{sT}, 0)$ and another with $\vec{P} = (0, -P_{sT}, 0)$, such that $\Delta\vec{P} \cdot \hat{n} = (0, -2P_{sT}, 0) \cdot (\cos\theta, \sin\theta, 0)$, where θ is the polar angle measured from [100] in the (001) plane. This configuration is illustrated in Figure 6.6(a). The isotropic 180TDW$_2$ has the same interfacial energy as the anisotropic 180TDW$_1$ at its lowest energy orientation.

energies with minima at specific, temperature-independent orientations, see Figures 6.6 and 6.7. Similar results were obtained for 55T-R$_2$ and 125T-R$_2$ phase interfaces. In Figures 6.8(e) and (g), for example, the 55T-R$_2$ and 125T-R$_2$ phase interfaces are oriented at 45° with respect to [100] in the (001) plane. Equivalent orientations would be obtained for 55T-R$_2$ and 125T-R$_2$ interfaces between domains with different polarization variants.

In contrast, for 55T-R$_1$ and 125T-R$_1$ phase interfaces, the orientation associated with the energy cusp in their γ-plots depends on temperature. For a 55T-R$_1$ between a tetragonal domain with $\vec{P} = (P_{sT}, 0, 0)$ and a rhombohedral domain with $\vec{P} = (P_{sR}/\sqrt{3}, P_{sR}/\sqrt{3}, -P_{sR}/\sqrt{3})$, such that $\Delta\vec{P} \cdot \hat{n} = (P_{sR}/\sqrt{3} - P_{sT}, P_{sR}/\sqrt{3}, -P_{sR}/\sqrt{3}) \cdot (\cos\theta, \sin\theta, 0)$, the lowest energy configuration is given by $\theta_{55T\text{-}R_1} = \arctan(\sqrt{3}P_{sT}/P_{sR} - 1)$. Here, $\theta_{55T\text{-}R_1}$ is the angle of the interface normal obtained from $\Delta\vec{P} \cdot \hat{n} = 0$. A similar expression governs the lowest energy orientations of 125T-R$_1$ phase interfaces. These results are consistent with the observations made in Section 4.5.3 for coarse-grained BZT-40 BCT polycrystals, which further validates the earlier use of a coarse-grained approach for the analysis of FE domain structures.

It should be noted that Coulomb's Equation does not restrict the values adopted by $u_{z'}$ in this model. Consequently, although the orientations of all interfaces, shown in Figures 6.6 through 6.8 (left column), correspond to their lowest energy configuration according to Coulomb's Equation, the interfaces are not electrically neutral in principle. Only the in-plane 180TDW$_1$ and 90TDW$_1$ interfaces, characterized by $u'_z = 0$ and $\partial u'_z/\partial x' = 0$, are strictly neutral. Moreover, the restriction imposed by the 2-D geometry produces interfaces that are not mechanically compatible, such as 90TDW$_2$, 109RDW$_2$, 55T-R$_2$ and 125T-R$_2$. In the T phase, for example, mechanical compatibility would force 90TDWs with either charged head-to-head or tail-to-tail configurations, or neutral head-to-tail configurations[71], neither of which is observed in Figure 6.6(g) for the case of 90TDW$_2$. Similar observations can be made for 109RDW$_2$, 55T-R$_2$ and 125T-R$_2$. Despite these limitations, the calculations described in this section allow for an analysis of results from the microstructural simulations, and for a comparison with future modelling on different crystallographic planes.

6.5.2 Time-temperature-transformation (TTT) diagram

A TTT diagram was constructed using data from the simulations for the microstructural evolution of two-phase FE systems, Figure 6.11. The volume fraction transformed of FE phases was measured by ψ, where $\psi = \overline{\phi}$ at $T > T_{PPB}$ and $\psi = 1 - \overline{\phi}$ at $T < T_{PPB}$. Markers correspond to transformation times for constant fraction transformed, calculated as the average from five simulations at each selected temperature. The calculations were performed in the absence of applied electric fields and considering the dipole-dipole interactions within the material.

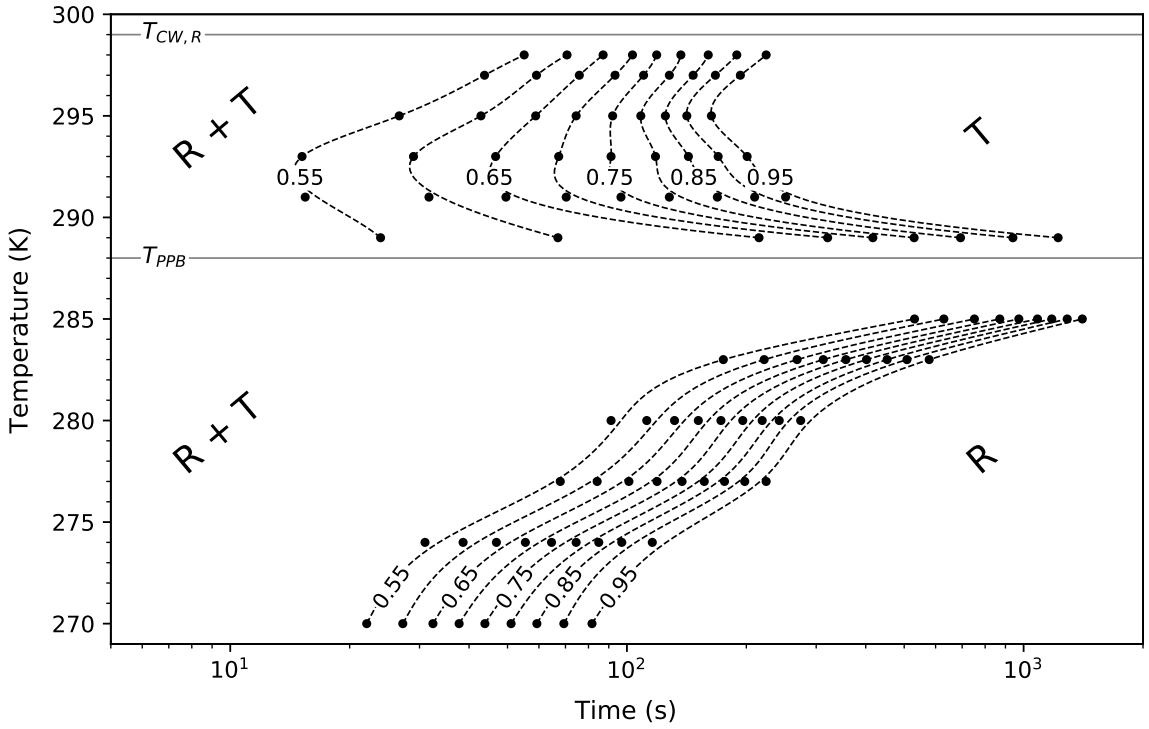

Figure 6.11: TTT diagram for a two-dimensional BZT-50 BCT single crystal. The diagram shows transformation from a mixed 50%R+50%T state towards the stable single phase as $\psi \rightarrow 1$ at each temperature. Markers indicate mean times for constant fraction transformed calculated from five simulations. Splines are included as a guide for the eye. Results at $T = 286$ K, 287 K and 288 K are not included due to the observation of long-term phase coexistence, stagnation of microstructures and occasional relaxation of the metastable phase.

Figure 6.11 shows that metastable coexistence between the R and T phases is possible for all $T < T_{CW,R} = 299$ K. In this case, $T_{CW,R} \approx T_{C,R} \approx T_{max,R}$ due to the weak first order P-FE transition that occurs in the R phase for BZT-50 BCT. This temperature corresponds to the thermodynamic upper limit for FE coexistence predicted by the MPF model, above which the R phase becomes unstable and coexistence is not possible. Furthermore, calculations indicate that both FE phases are more likely to coexist as $T \rightarrow T_{PPB}$. Meanwhile, for $T < T_{PPB}$, coexistence time decreases considerably at low temperatures, with complete R + T $\rightarrow$ R transformation occurring on the order of seconds. The latter suggests that FE coexistence in BZT-x BCT, and similar systems, is kinetically limited at low temperatures. For BZT-50 BCT, the results explain the phase transition observed experimentally at 274 K by Ehmke[89]. This supports the hypothesis of R + T phase coexistence in the vicinity of the PPB, as opposed to a purported intervening O phase.

The results depicted in Figure 6.11 are partly explained by the thermodynamic driving force for transformation of FE phases, Δf_{min}, and the system mobility, M, illustrated in Figure 6.12 as a function of temperature. For $T < T_{PPB}$, Figure 6.12(a) shows that the thermodynamic driving force increases significantly with decreasing temperature. This explains the rapid kinetics of R + T → R transformation observed at low temperatures, in spite of a decreasing phase-averaged mobility, see Figure 6.12(b). For temperatures below the PPB, Figure 6.12(b) also shows that the mobility of the two-phase system increases as the transformation progresses towards the stable R phase. This further promotes rapid rates of R + T → R transformation at $T < T_{PPB}$.

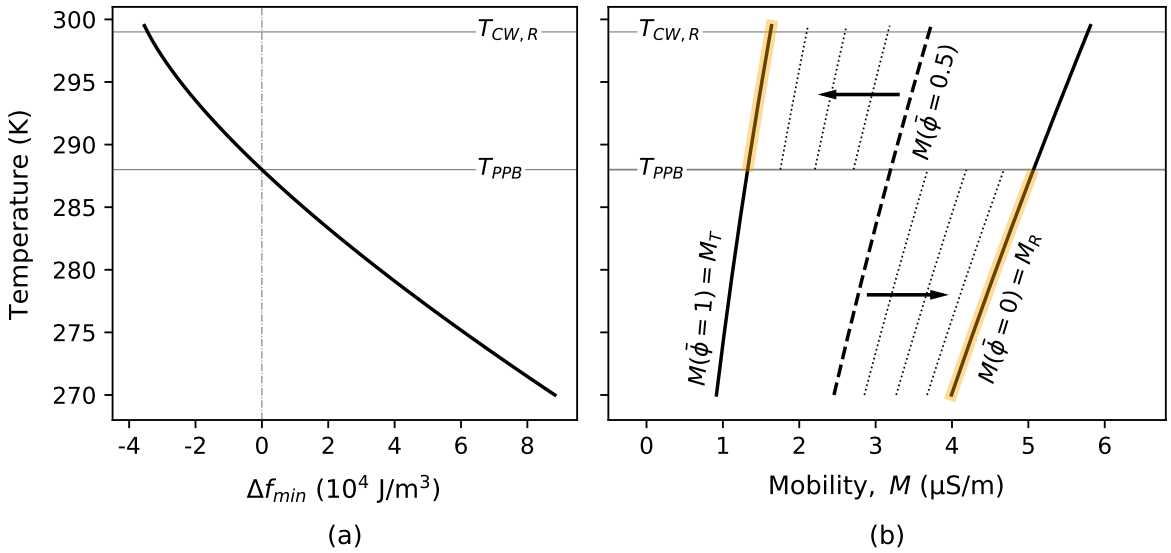

Figure 6.12: Temperature dependence of (a) thermodynamic driving force for transformation of FE phases, $\Delta f_{min} = f_T(P = P_{sT}; E = 0, T) - f_R(P = P_{sR}; E = 0, T)$, and (b) mobility, M, for the two-dimensional BZT-50 BCT system.

For $T > T_{PPB}$, Figure 6.12(a) indicates that the macroscopic driving force for R + T → T transformation increases with increasing temperature. Furthermore, Figure 6.12(b) shows that the phase-averaged mobility also increases with temperature; although, in this case, the rate of transformation is limited by the low mobility of the stable T phase. Consequently, the kinetics of R + T → T transformation tend to increase with increasing temperature away from the PPB. However, calculations reveal that the coexistence time of FE phases increases as $T \to T_{CW,R}$, see Figure 6.11. This results in C-shaped lines for constant fraction transformed that do not correspond with the temperature dependence of Δf_{min} and M, shown in Figure 6.12 for $T > T_{PPB}$.

The above observations are supported by an analysis of the rates of phase transformation, calculated as $r = 1/t_{\bar{\phi}=0.55}$ at each selected temperature. Here, $t_{\bar{\phi}=0.55}$ is the mean time for 0.55 fraction transformed from five simulations. Figure 6.13(a) shows the temperature dependence of the calculated transformation rates. For $T < T_{PPB}$, calculations confirm that the rate of R + T → R transformation increases with decreasing temperature. In addition, Figure 6.13(b) features a parametric plot that demonstrates a direct correlation between Δf_{min} and r (dashed line). Similarly, for $T > T_{PPB}$, a direct correlation between Δf_{min} and r is observed from the T_{PPB} to approximately 293 K. This explains the increasing rates of R + T → T transformation as temperature increases away from the PPB. However, for $293\,\text{K} \gtrsim T > T_{CW,R}$, the transformation rates drop significantly

as $T \rightarrow T_{CW,R}$, while the macroscopic driving force continuously increases. The reason for this reduction in the rates of R + T → T transformation, associated with an increase in the coexistence time of the FE phases at 293 K $\gtrsim T > T_{CW,R}$, is not clear here. This will be explored in Section 6.5.5.

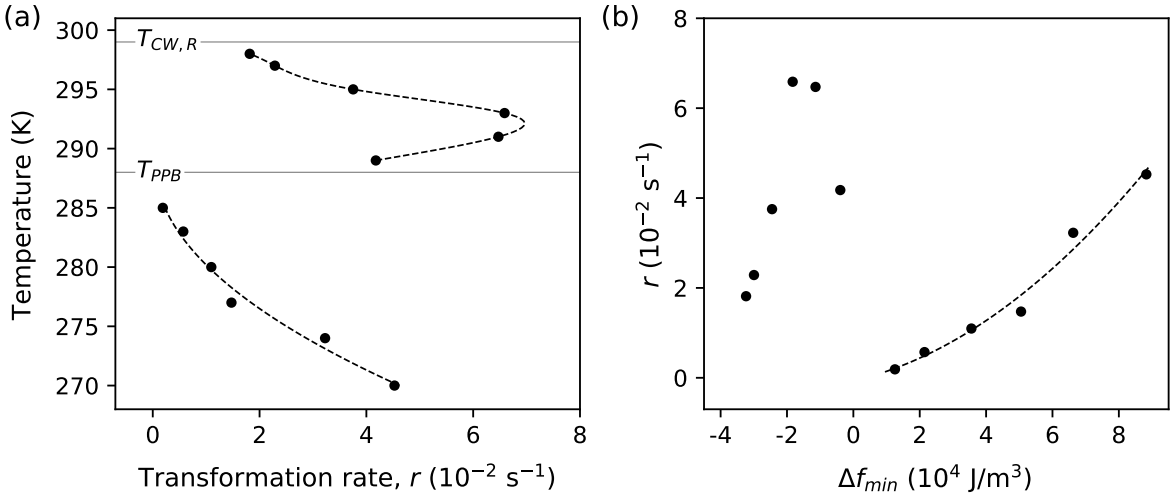

Figure 6.13: (a) Rate of phase transformation, $r = 1/t_{\bar{\phi}=0.55}$, as a function of temperature, and (b) parametric plot of Δf_{min} versus r for the two-dimensional BZT-50 BCT system. Dashed lines are included as a guide for the eye. In the parametric plot, a direct correlation is shown between Δf_{min} and r at $T < T_{PPB}$.

It should be noted that the restriction imposed by the 2-D implementation of this model produces additional types of interfaces and limits the solution of Coulomb's Equation. The latter is evidenced, for example, by the isotropic interfacial energy obtained for 180TDW_2 and 71RDW_2. However, this limitation is not expected to significantly change the observations in Figure 6.11, considering the similar results observed in Figure 4.8, where the effect of including local electric fields was analysed for the BZT-40 BCT system.

6.5.3 Avrami (JMAK) analysis

The kinetics of isothermal R + T → R and R + T → T phase transformations can be fitted to the JMAK model, $\psi = 1 - \exp(-kt^n)$ [98]. For each selected temperature, the parameters n and k are obtained by plotting $\ln(-\ln(1-\psi))$ versus $\ln(t)$ and fitting the equation of a line with slope n. The method is illustrated in Figure 6.14 for $T = 274$ K. The estimated n and k values are shown for different temperatures in Table 6.3.

According to Bordeaux *et al.* [99], Avrami exponents are generally reported to explain the nucleation condition and the growth mechanism/dimensionality of transformation processes. However, Pradell *et al.* [100] have indicated that the correct interpretation of these exponents must consider possible changes in the driving mechanism during the transformation and, hence, it requires appropriate understanding of the underlying kinetics.

In this study, Avrami exponents of $0.31 \leq n \leq 1.28$ were found, Table 6.3. These results are similar to those obtained for coarse-grained BZT-40 BCT polycrystals, see Table 3.4. Two-

dimensional analysis of the BZT-40 BCT system demonstrated that domain growth in two-phase FE systems is dominated by the kinetics of phase transformation, rather than by the competing effect of intrinsic domain coarsening, Section 4.5.4. In addition, coarsening rate constants, calculated for the two-phase system, were smaller than those obtained from single-phase simulations. Hence, for the two-dimensional BZT-50 BCT single crystal, estimated values of $n \sim 1$ can be explained by a case of site-saturated nucleation and interface-controlled domain growth, with a pinning effect caused by the presence of metastable domains, see Section 4.5.4.

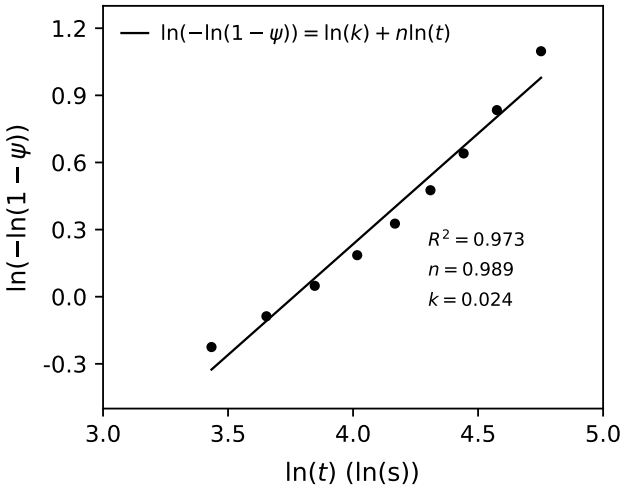

Figure 6.14: JMAK analysis for two-dimensional BZT-50 BCT single crystals at $T = 274$ K. Average transformation times are calculated from five simulations.

Table 6.3: Estimated n and k values of the JMAK equation for the BZT-50 BCT system.

$T < T_{PPB}$				$T > T_{PPB}$			
T (K)	n	K	R^2	T (K)	n	K	R^2
285	1.284	2.25×10^{-4}	0.941	289	0.312	2.43×10^{-1}	0.838
283	1.084	2.59×10^{-3}	0.955	291	0.453	1.95×10^{-1}	0.919
280	1.171	3.60×10^{-3}	0.962	293	0.478	1.83×10^{-1}	0.897
277	1.068	7.89×10^{-3}	0.959	295	0.697	6.76×10^{-2}	0.903
274	0.989	2.42×10^{-2}	0.973	297	0.859	2.70×10^{-2}	0.942
270	0.995	3.39×10^{-2}	0.983	298	0.936	1.69×10^{-2}	0.975

6.5.4 Metastable equilibrium regime

In this section, the simulation results for microstructural evolution at temperatures close to the PPB are analysed. In the TTT diagram shown in Figure 6.11, no data was reported at $T =$ 286 K, 287 K and 288 K. This was due to the occasional relaxation of the metastable phase, stagnation of microstructures and long-term coexistence between the R and T phases (incomplete transformation). These results are illustrated in Figure 6.15, which shows $\overline{\phi}$ *vs* t line plots from fifteen different simulations at each temperature.

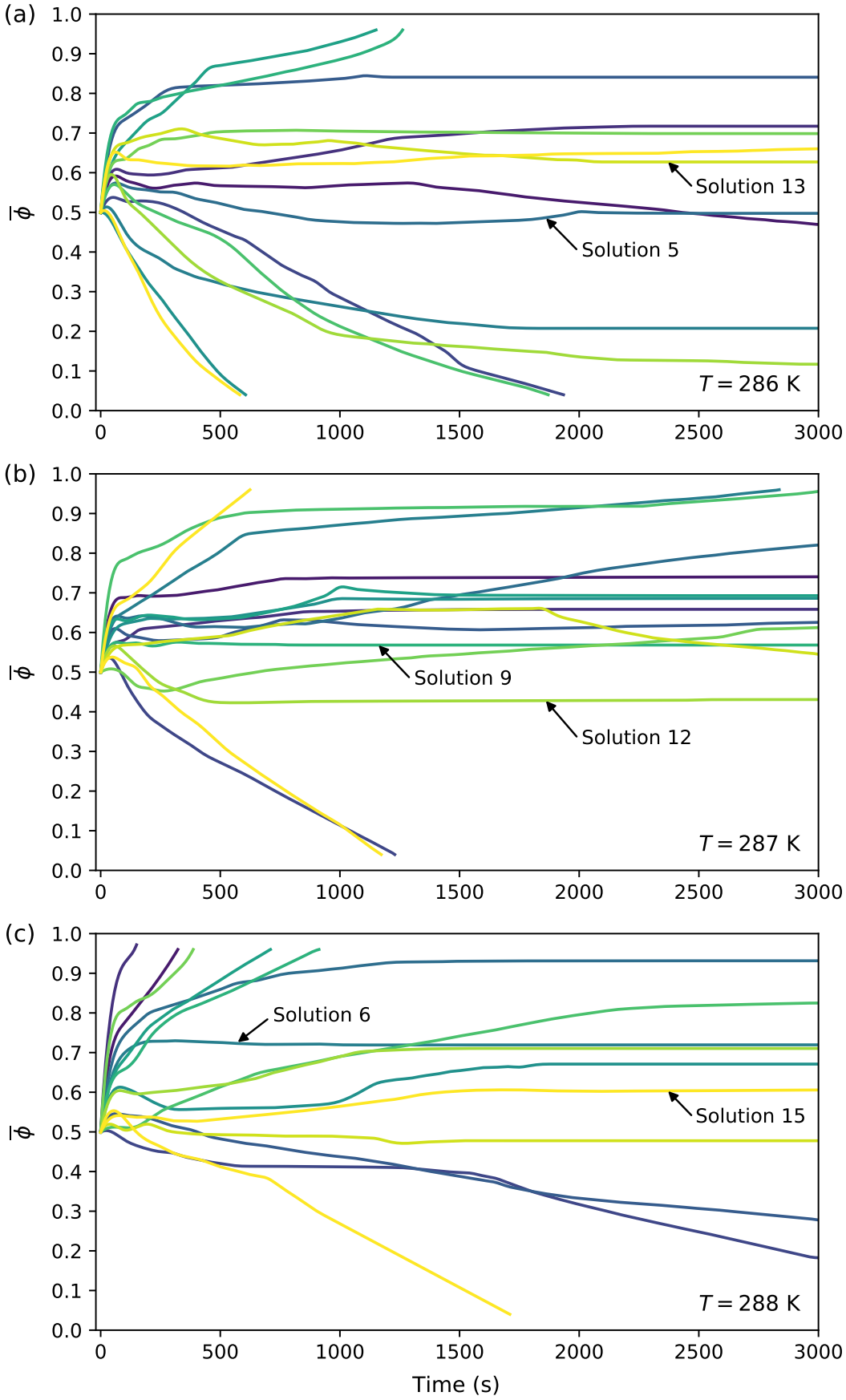

Figure 6.15: Line plots of mean phase field, $\overline{\phi}$, versus time, t, for each of fifteen 2-D simulations for a BZT-50 BCT single crystal at (a) $T = 286$ K, (b) $T = 287$ K, and (c) $T = 288$ K. Select solution labels were added for future reference.

For T = 286 K, Figure 6.15(a) shows relaxation to the stable R phase (4 solutions), relaxation to the metastable T phase (2 solutions), stagnation of microstructure (6 solutions), and long-term phase coexistence (3 solutions). Similarly, for T = 287 K, Figure 6.15(b) shows relaxation to the stable R phase (2 solutions), relaxation to the metastable T phase (3 solutions), stagnation of microstructure (8 solutions), and long-term phase coexistence (2 solutions). Finally, for T = 288 K = T_{PPB}, Figure 6.15(c) shows relaxation to the R phase (1 solution), relaxation to the T phase (5 solutions), stagnation of microstructure (7 solutions), and long-term phase coexistence (2 solutions).

The observations at T = 286 K, 287 K and 288 K can be explained by the vanishing driving force for phase transformation, Δf_{min}, as $T \rightarrow T_{PPB}$, Figure 6.12(a). This means that the volumetric free energy density in the R and T phases are approximately equal at these temperatures. Consequently, the driving force for microstructural evolution is the reduction in total interfacial energy. This situation is akin to grain growth in duplex alloys.

Based on the above, the stagnation of FE microstructures can be elucidated by comparing it with the stabilization of grain boundaries in polycrystalline materials. Generally, all grain boundaries represent high-energy regions that increase the free energy of the system with respect to a single crystal, moving it away from thermodynamic equilibrium. However, during the annealing process, grain boundaries can adopt configurations that produce a metastable equilibrium at the intersections[144]. Thus, in the current study, a metastable equilibrium regime can be defined within the R + T coexistence region in the vicinity of the PPB. It is characterized by vanishing Δf_{min} that leads to long-term R + T coexistence, stagnation of microstructures, or relaxation of the stable or metastable phase depending on the temperature-dependent interfacial energies and the initial conditions. For BZT-50 BCT, the metastable equilibrium regime occurs in a temperature range that includes 286 K, 287 K and 288 K (T_{PPB}).

Moreover, visual inspection of microstructures can help to determine which interfaces or domain patterns are favoured to stabilize these systems. It also allows identification of mechanisms controlling the metastable coexistence of the FE phases. Figure 6.16 shows the domain morphologies corresponding to the solutions annotated on Figure 6.15. In all these cases, the metastable coexistence of FE phases allows access to additional polarization states, which facilitates polarization rotation in the FE system upon application of external fields. The existence of a path for easy polarization rotation has been linked to enhanced electromechanical properties near the PPB[55,96]. For T = 286 K and 287 K, Figures 6.16(a)-(d) show that metastable tetragonal domains act as bridges for polarization rotation between stable rhombohedral domains. For $T = T_{PPB} = 288$ K, Figures 6.16(e) and (f) also show polarization rotation that is facilitated, in this case, by the existence of fourteen equilibrium polarization states (eight variants in the R phase and six in the T phase).

Figures 6.16(c) and (d) reveal the formation of vortex and twin-like (or lamellar) domain structures with head-to-tail configurations. These patterns play a crucial role in the stabilization of FE microstructures. Lamellar structures are commonly observed, for example, in atomic force microscopy (AFM) studies on $PbTiO_3$[104], and in TEM studies on $BaTiO_3$[103] and BZT-50 BCT[106–108,110]. In addition, vortex and twin patterns have been reported extensively in other computational works, see *e.g.,*[39–41,45].

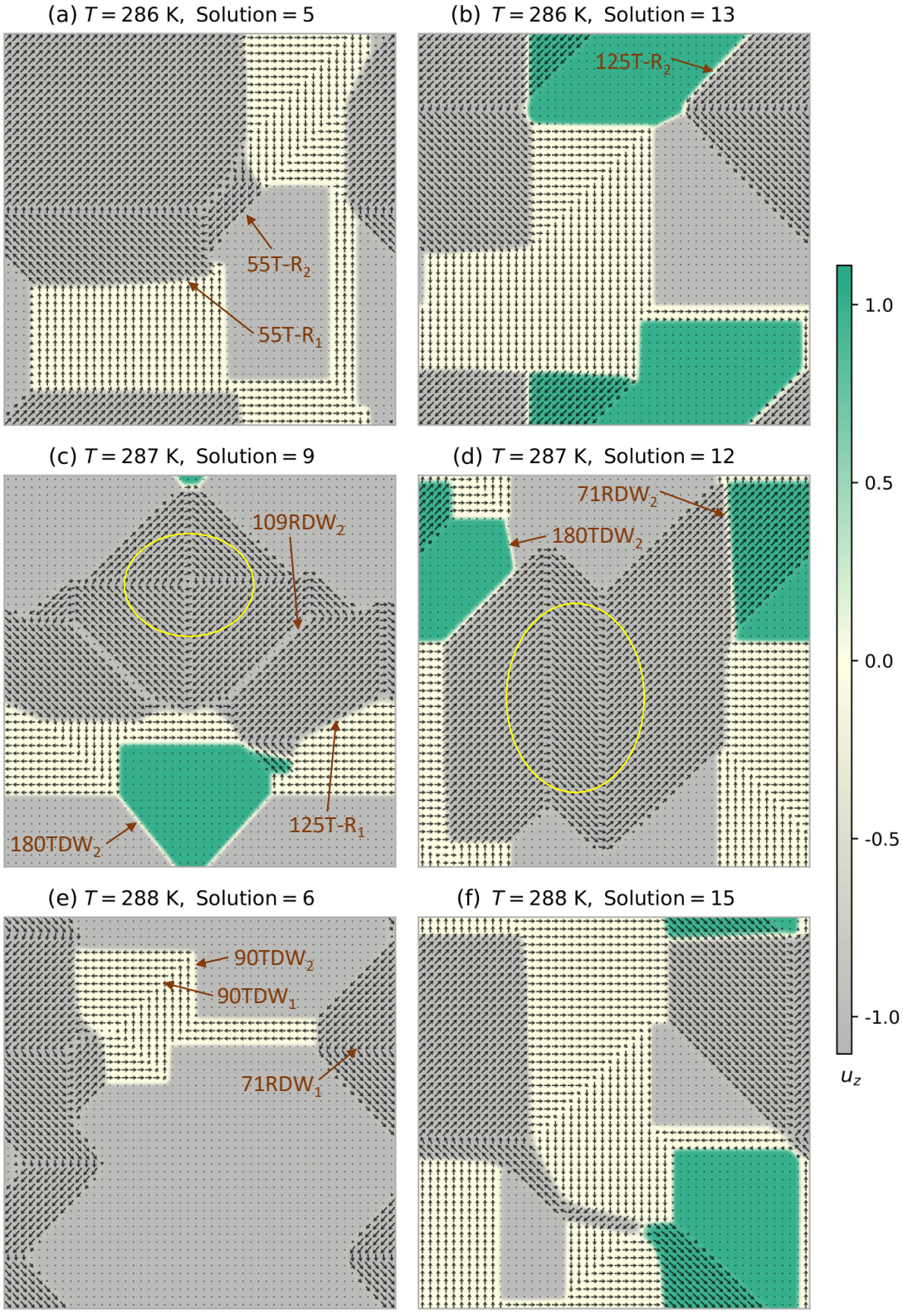

Figure 6.16: Two-phase microstructures corresponding to solutions annotated on Figure 6.15 for two-dimensional BZT-50 BCT single crystals at (a)-(b) $T = 286$ K, (c)-(d) $T = 287$ K, and (e)-(f) $T = 288$ K. The computational domain size is 232 nm × 232 nm. Vector plots correspond to in-plane polarization $\vec{u} = \vec{P}/|P_{sT}| = (u_x, u_y)$. Contour plots correspond to the out-of-plane polarization component, u_z. A vortex and a twin-like (or lamellar) domain structures are ringed in yellow. Different types of interfaces are annotated for discussion. The 90TDW$_1$, 90TDW$_2$, 71RDW$_1$, 109RDW$_2$, 55T-R$_2$ and 125T-R$_2$ interfaces appear faceted; while the 71RDW$_2$, 55T-R$_1$ and 125T-R$_1$ interfaces appear curved. Straight 180TDW$_2$ boundaries appear with different orientations.

Figure 6.16 also confirms the presence of interfaces with the configurations predicted in Section 6.5.1. Faceted 90TDW$_1$, 90TDW$_2$ and 71RDW$_1$ appear in all microstructures due to their low minimum interfacial energies, see *e.g.,* Figure 6.16(e). In contrast, faceted 180TDW$_1$, 180RDW and 109RDW$_1$ do not appear in any microstructure because of their relatively high minimum interfacial energy at $T = 286$ K, 287 K and 288 K, see Figure 6.9. Additionally, Figure 6.16(c) demonstrates the formation of a 109RDW$_2$, whose faceted nature is also explained by its anisotropic interfacial energy. For phase interfaces, faceted 55T-R$_2$ boundaries are observed in all cases, see *e.g.,* Figure 6.16(a); while faceted 125T-R$_2$ boundaries are demonstrated in Figure 6.16(b).

Further, Figures 6.16(c) and (d) demonstrate the formation of two 180TDW$_2$ with different (arbitrary) orientations due to the isotropic nature of their interfacial energy. Similarly, Figure 6.16(d) shows a slightly curved 71RDW$_2$, explained by its isotropic interfacial energy.

According to Section 6.5.1, 55T-R$_1$ and 125T-R$_1$ phase interfaces are expected to be faceted and oriented at angles that depend on temperature. However, these interfaces appear slightly curved in Figures 6.16(a) and (c). For the BZT-40 BCT system, highly curved 45T-R and 135T-R phase interfaces were obtained despite their anisotropic interfacial energy, Section 4.5.3. The results were attributed to small energy penalty to form phase interfaces at orientations different from their lowest energy configurations compared to the penalty associated with DWs, see Figure 4.14(a). Similarly, results for BZT-50 BCT suggest that the interfacial energy of 55T-R$_1$ and 125T-R$_1$ phase interfaces is less anisotropic than that associated to DWs. This causes the formation of curved 55T-R$_1$ and 125T-R$_1$ phase interfaces in order to accommodate FE domains with preferred DW orientations and minimize the total free energy of the system. This morphology has been observed experimentally near the PPB of the BZT-50 BCT system in TEM studies[108,111].

6.5.5 Evolution of domain structures from fixed initial conditions

In this section, the kinetics of phase transformation and evolution of domain structures are investigated for two particular mixed 50%R+50%T phase initial states: a random initial condition and a nano-domain initial condition.

First, calculations were performed from the same random initial conditions, known hereafter as **RIC1**, at different temperatures. Physically, this situation corresponds to the microstructural evolution of a two-phase FE system upon quenching from the paraelectric phase. Figure 6.17(a) depicts $\overline{\phi}$ *vs* t line plots obtained at each simulation temperature. Overall, results show a behaviour consistent with the TTT diagram illustrated in Figure 6.11. For $T < T_{PPB}$ and $T > T_{PPB}$, Figure 6.17(a) demonstrates relaxation to the stable FE phase in each temperature range, with coexistence times increasing as $T \rightarrow T_{PPB}$. However, Figure 6.17(b) reveals that the fraction of metastable phase increases significantly at very short times for all temperatures. The temporary rise in the metastable phase fraction is larger at the extreme temperatures. This could be related to coupled spinodal decomposition, caused by the random initial conditions for polarization and phase field that yield regions of locally stable FE phases. A similar phenomenon has been reported during the growth of BZT-x BCT single crystals at high temperatures due to compositional fluctuations[145]. The classical treatment shows that the

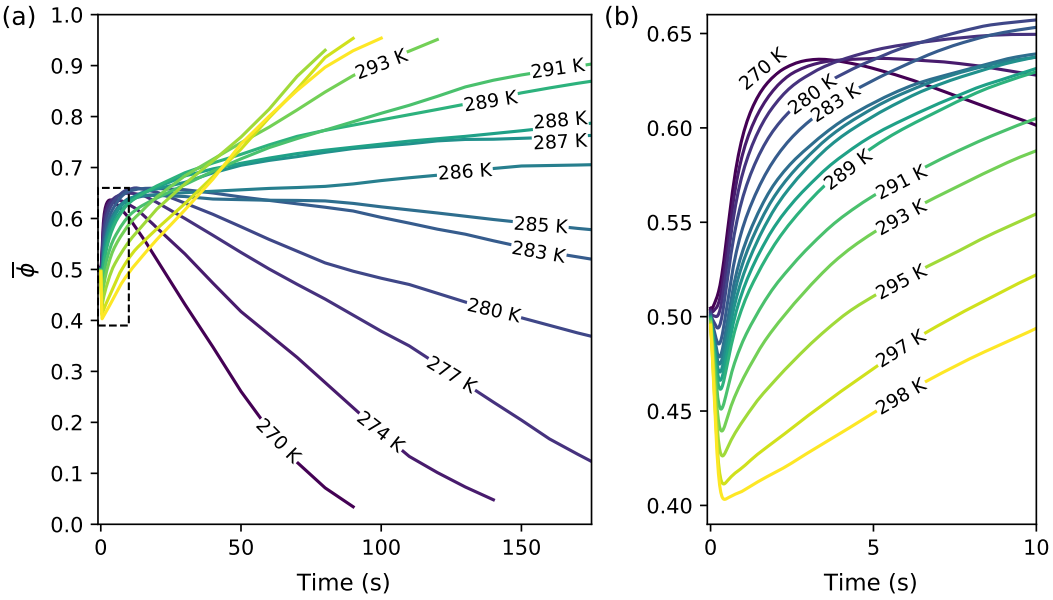

Figure 6.17: (a) Line plots of $\overline{\phi}$ *vs* t at selected temperatures for a two-dimensional BZT-50 BCT single crystal from initial conditions RIC1, and (b) magnified view of the first ten seconds.

local curvature of the free energy with respect to polarization should dictate the rate of spinodal decomposition[146]. This relates to the first Landau coefficient for each phase, which are functions of temperature. A recent article has proposed a phenomenological treatment of coupled spinodal decomposition for martensitic phase transformations in multi-component polycrystals[147]. However, no theoretical treatment of this phenomenon has been found in the literature for FE systems.

Calculations were also carried out for the microstructural evolution of a two-phase system with developed FE domains. The initial microstructure, known hereafter as **DIC1**, was selected from previous simulations such that all types of interfaces are represented and $\overline{\phi} \approx 0.5$. From a practical point of view, this situation corresponds to the microstructural analysis at selected temperatures of a sample held at T_{PPB} until the complete set of domains have formed. Figure 6.18 shows $\overline{\phi}$ *vs* t line

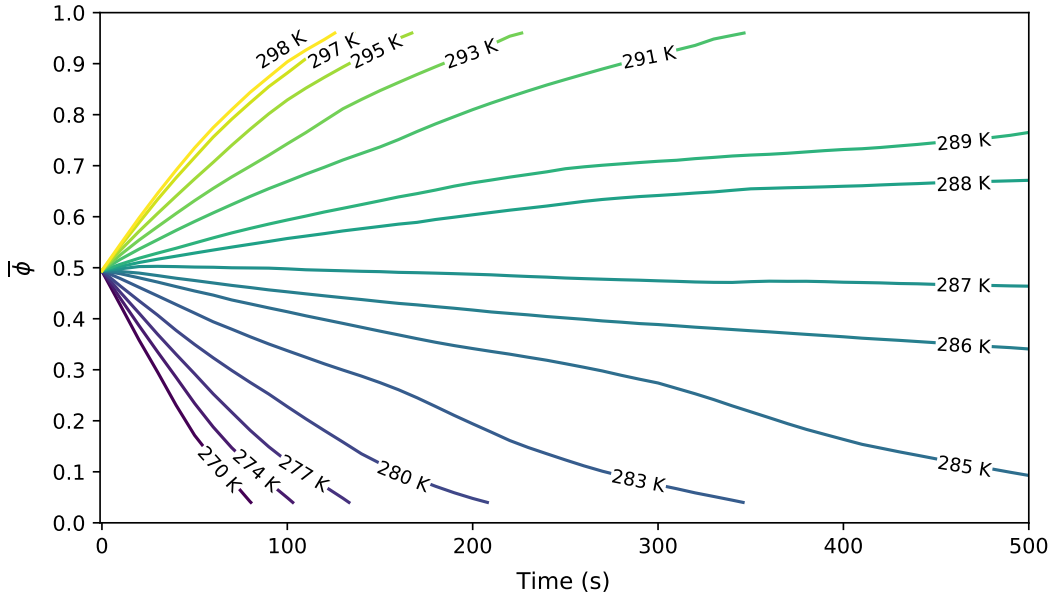

Figure 6.18: Line plots of $\overline{\phi}$ *vs* t at selected temperatures for a two-dimensional BZT-50 BCT single crystal from initial conditions DIC1.

plots obtained from each simulation. Results are similar to those depicted in Figure 6.17(a) over long times. However, in this case, there is a continuous increase in the fraction of the stable phase rather than an initial decrease found in Figure 6.17(b). This shows that the short time behaviour from random initial conditions is dominated by the first stages of domain formation. This is the subject of future work.

Further, a TTT diagram was constructed using the simulations from initial conditions DIC1, Figure 6.19(a). Results can be contrasted with the TTT diagram illustrated in Figure 6.19(b), calculated from five different random initial conditions at each temperature. Figure 6.19(a) shows that transformation towards the stable FE phase starts at shorter times for all $T < T_{PPB}$. This is

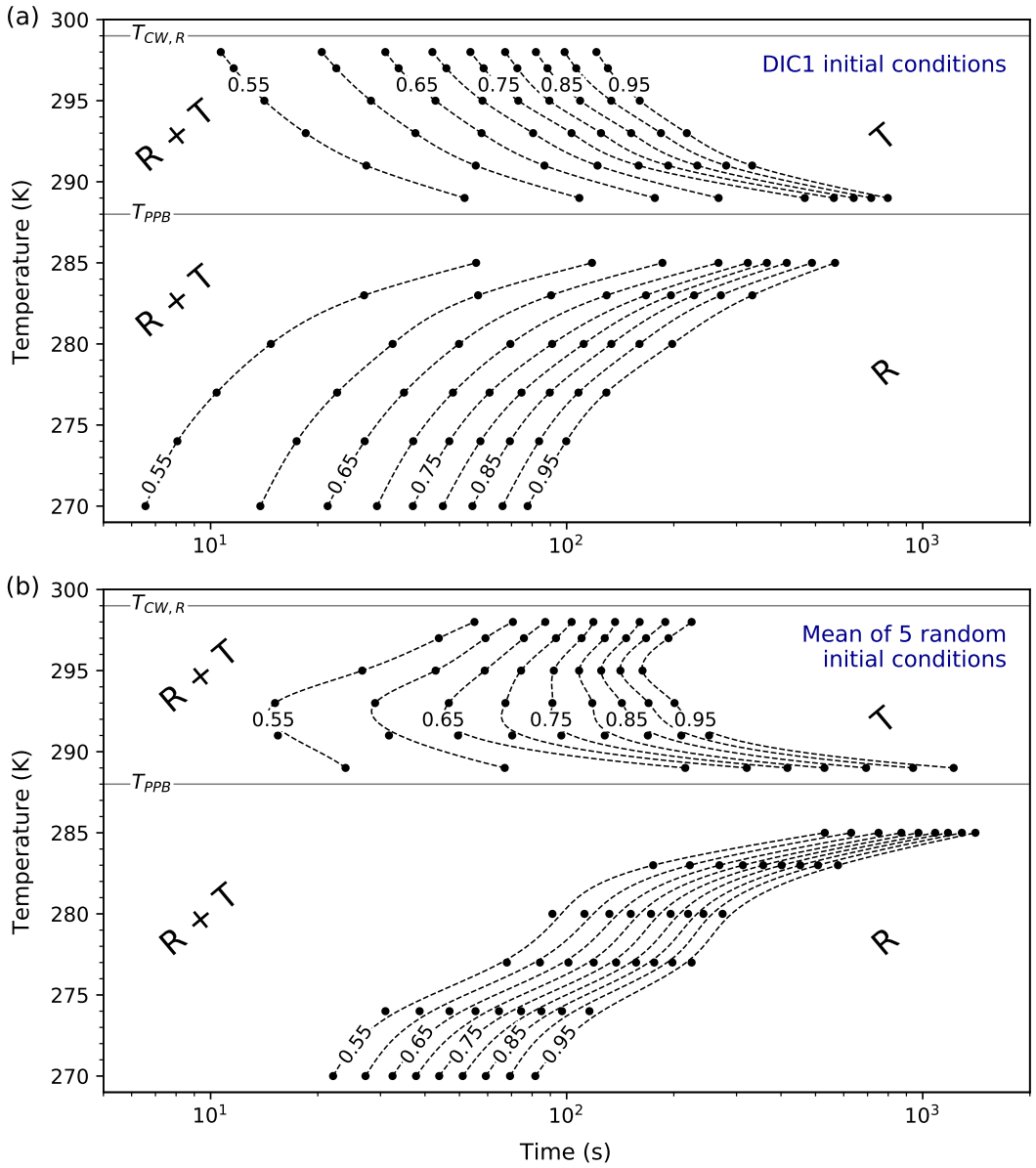

Figure 6.19: (a) TTT diagram for a two-dimensional BZT-50 BCT single crystal from initial conditions DIC1. (b) TTT diagram shown in Figure 6.11, included here for ease of comparison. Markers in subfigure (a) indicate times for constant fraction transformed obtained from a single simulation at each temperature. Markers in subfigure (b) indicate mean times for constant fraction transformed calculated from five simulations at each temperature. Splines are included as a guide for the eye.

explained by the time required for domain formation when random initial conditions are adopted, as opposed to a developed microstructure.

Most notably, for $T > T_{PPB}$, Figure 6.19(a) reveals that the kinetics for R + T → T transformation increases steadily with increasing temperature. A similar behaviour is also observed for $T < T_{PPB}$. This behaviour is consistent with the increasing driving force for phase transformation, Δf_{min}, away from the PPB temperature, see Figure 6.12(a). In contrast, Figure 6.19(b) shows C-shaped lines for constant fraction transformed at $T > T_{PPB}$. The C-shapes are caused by an increase in the phase coexistence time as $T \rightarrow T_{CW,R}$ that do not correspond with the thermodynamic driving force. Their origin can now be attributed to the rise in metastable phase fraction during initial domain formation, as shown in Figure 6.17(b), which delays the transformation towards the stable FE phase.

The results presented above are supported by Figure 6.20. In Figure 6.20(a), the rates of phase transformation, calculated as $r = 1/t_{\bar{\phi}=0.55}$, are plotted with respect to temperature. It is observed that the transformation rates, obtained from initial conditions DIC1, decrease as $T \rightarrow T_{PPB}$. Further, Figure 6.20(b) shows a direct correlation between these transformation rates and the thermodynamic driving force at $T < T_{PPB}$ and $T > T_{PPB}$. Hence, higher rates of R + T → R and R + T → T transformations are explained by the increasing Δf_{min} values away from the PPB temperature.

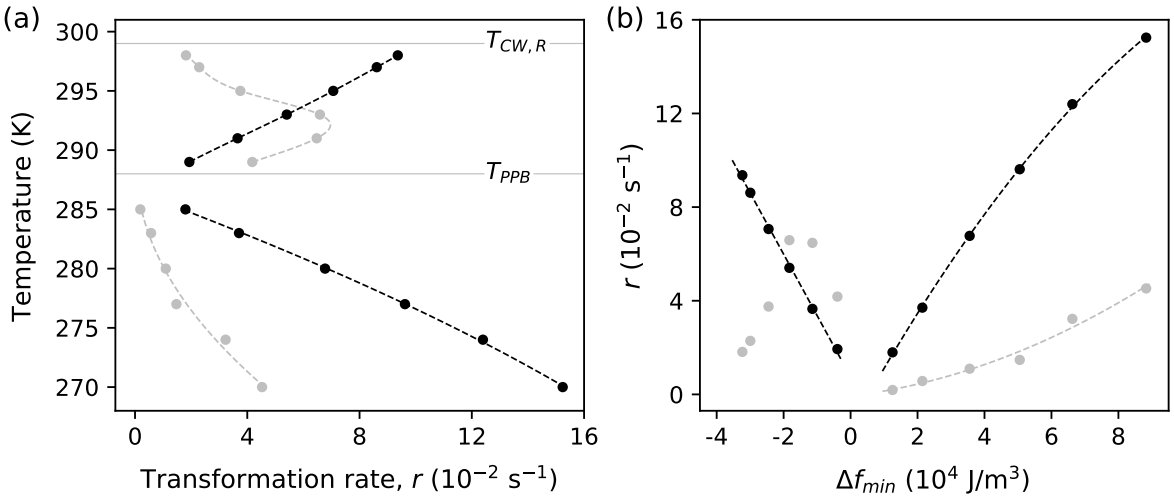

Figure 6.20: (a) Rate of phase transformation, $r = 1/t_{\bar{\phi}=0.55}$, as a function of temperature, and (b) parametric plot of Δf_{min} versus r for a two-dimensional BZT-50 BCT single crystal from initial conditions DIC1 (■). Results from Figure 6.13 are included here for ease of comparison (■). Dashed lines are included as a guide for the eye. In the parametric plot, direct correlations are shown between Δf_{min} and r. Overall, results from initial conditions DIC1 are explained by the temperature dependence of Δf_{min} at $T <_{PPB}$ and $T > T_{PPB}$.

6.5.6 Quantitative analysis in MATLAB

Initial conditions DIC1 were also used to investigate the evolution of interfaces in the microstructures as a function of temperature. The corresponding initial microstructure is represented

in Figure 6.21. In this figure, vector plots correspond to the in-plane polarization, $\vec{u} = \vec{P}/|P_{sT}| = (u_x, u_y)$. Different contour plots were used to identify the FE domains and their interfaces. In Figure 6.21(a), the contour colour corresponds to the out-of-plane polarization component, u_z, which allows better visualization of domain types. In Figure 6.21(b), the contour colour corresponds to the total free energy density, $\hat{f}_{total} = f_{total}/(|\alpha_{1,T}|P_{sT}^2)$, which allows better analysis of the interfaces. The total free energy density, shown in Figure 6.21(b), was calculated at $T = T_{PPB}$, where both FE phases are stable. Hence, the rhombohedral and tetragonal domains have the same total free energy density, which corresponds to the global minimum. All interfaces represent high-energy regions. In particular, Figure 6.21(b) shows that the T-R phase interfaces have the highest total free energy density and adopt faceted and curved configurations, as discussed in Sections 6.5.1 and 6.5.4. The formation of faceted and curved domain walls is also confirmed.

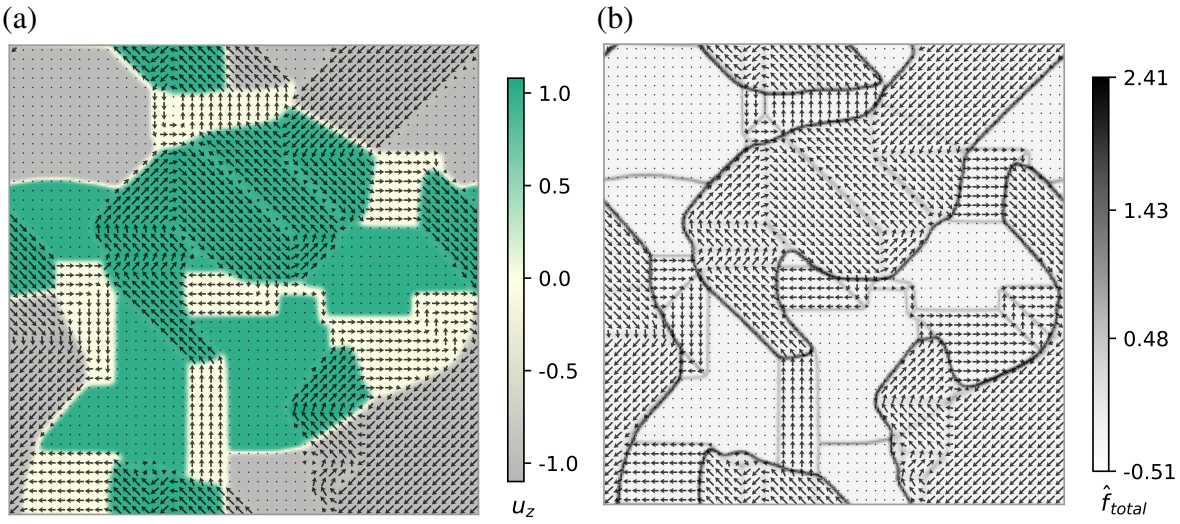

Figure 6.21: Microstructure corresponding to initial conditions DIC1. The computational domain size is 232 nm × 232 nm. Contour plots correspond to (a) out-of-plane polarization component, $u_z = P_z/|P_{sT}|$, and (b) total free energy density, $\hat{f}_{total} = f_{total}/(|\alpha_{1,T}|P_{sT}^2)$, at $T = T_{PPB}$. Vector plots represent the in-plane polarization, (u_x, u_y).

For all the analysed microstructures, the MATLAB™ toolbox MTEX[148,149] was utilized to calculate the length of each type of interface. MTEX is a well-established tool for texture analysis and grain detection by post-processing of electron back scatter diffraction (EBSD) or pole figure data. In this work, a method was developed to convert the polarization fields into orientation measurements that could be processed by MTEX as if they were EBSD data. The method is demonstrated by describing its application to the initial microstructure.

For the DIC1 microstructure, the polarization field, extracted directly from COMSOL Multiphysics, is discretized into fourteen possible polarization variants for the combined R + T system. A discrete field variable is defined using values between 1 and 14 to represent the eight rhombohedral variants (1-8), Figure 6.22(a), and the six tetragonal variants (9-14), Figure 6.22(b). Its spatial distribution allows easy identification of all FE domains, see *e.g.,* Figure 6.23(a). Then, a field with individual orientations (rotations) is calculated by mapping each polarization onto a reference vector. In this study, rotations are defined with respect to the [100] direction.

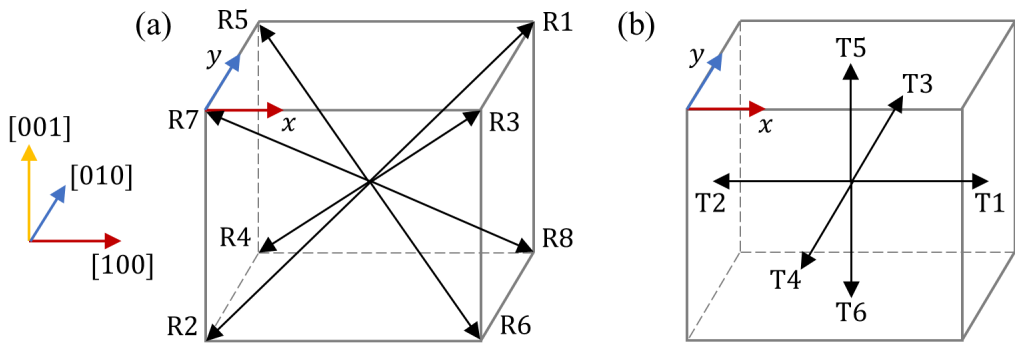

Figure 6.22: Definition of (a) eight rhombohedral variants, and (b) six tetragonal variants.

In principle, these calculated orientations can be readily imported to MTEX as EBSD data. However, in this case, fourteen different 'rotated' crystal symmetries (or textures) are first created in MTEX for the polarization variants, using the above definition for the rotations. This yields more control to identify, select and perform calculations on specific domains or domain boundaries. Moreover, the domain reconstruction depends on a threshold misorientation angle that indicates the location of each domain boundary. This parameter was set to the default value of 10° for all cases. Similarly, after visual inspection, small domains formed by less than five pixels were removed from all microstructures. Figure 6.23(b) demonstrates reasonable accuracy in the detection of FE domains after processing the calculated orientations.

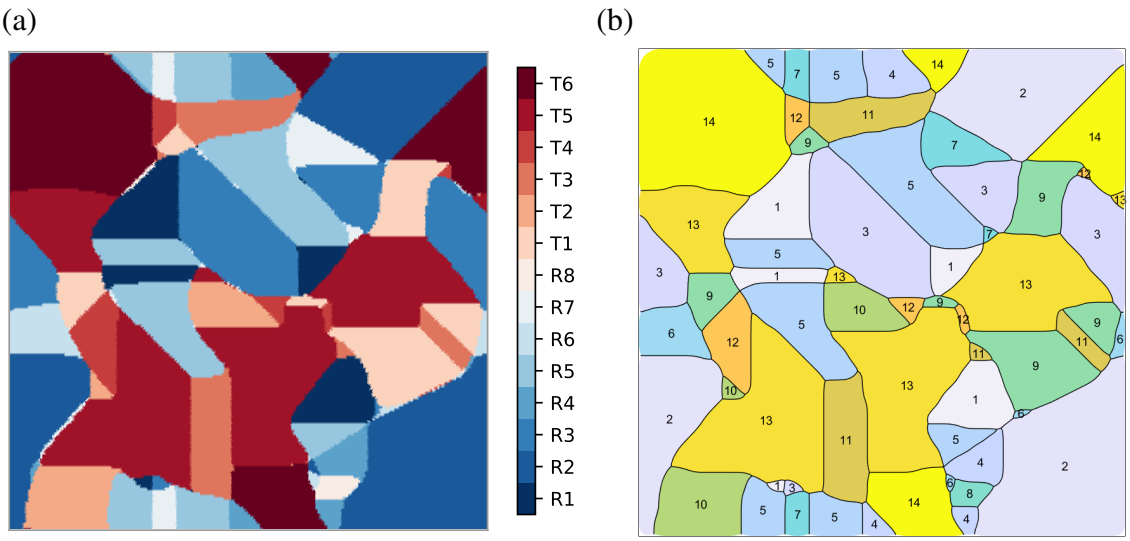

Figure 6.23: (a) Spatial distribution of the discrete field variable showing FE domains coloured by the fourteen polarization variants. (b) MTEX results showing detection of FE domains after processing the calculated orientations. The computational domain size is 232 nm × 232 nm. Annotated numbers correspond to the eight rhombohedral variants (1-8) and the six tetragonal variants (9-14). The colours represent the 'rotated' crystal symmetries (or textures) created in MTEX to identify each polarization variant.

Once the ferroelectric domains are successfully detected, the MTEX toolbox can be readily used to visualize the data using phase plots, orientation plots, pole figures and inverse pole figures, among others. Moreover, several calculations can be performed on the entire microstructure or on a selection of specific domains or interfaces. In particular, MTEX has multiple, well-documented

functions for misorientation analysis. Furthermore, the software provides access to properties that facilitate calculations. For domains, available properties include domain size, area, diameter, centroid, perimeter, aspect ratio, and mean orientation. Similarly, properties such as length and misorientation between two specific domains are stored for all interfaces. In this work, MTEX is used to calculate the length fraction of all interfaces.

Figure 6.24 shows the results from the application of the method explained above to the DIC1 microstructure. These values are used as a reference for further calculations of the microstructural evolution at different times and temperatures.

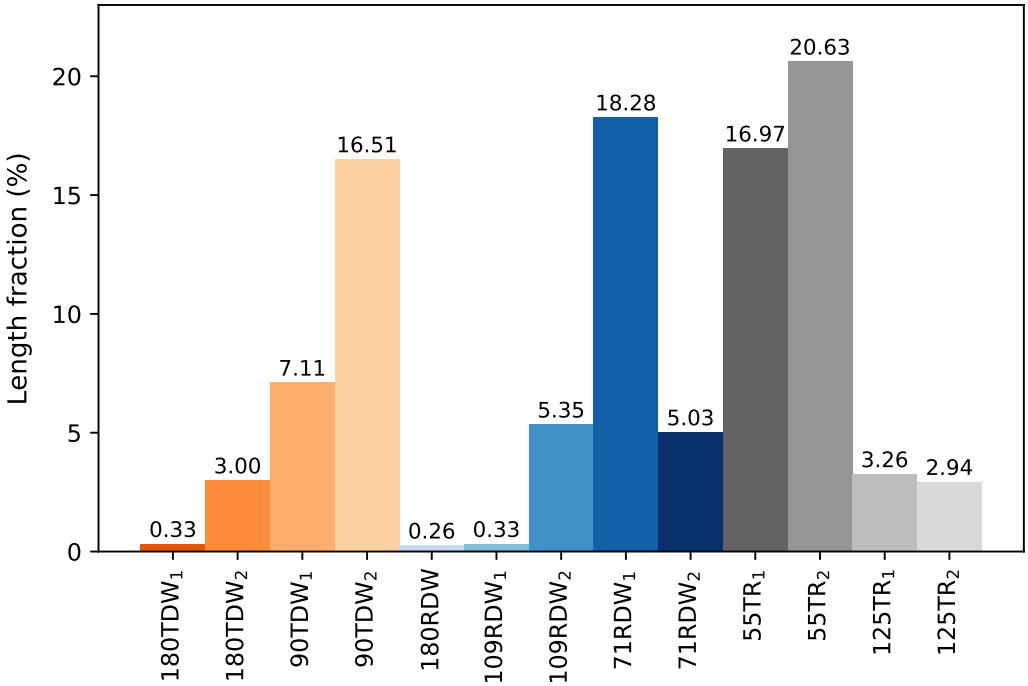

Figure 6.24: Length fraction of all domain walls and phase interfaces for the microstructure shown in Figure 6.23, corresponding to initial conditions DIC1.

The method developed herein enables visual inspection of domain structures and their evolution. This is demonstrated in Figures 6.25 and 6.26, where the MTEX toolbox was used to process snapshots of the microstructure at t = 50 s, 100 s, 150 s and 200 s for two different temperatures. For $T = 280\,\mathrm{K} < T_{PPB}$, Figure 6.25 shows relaxation to the stable R phase, as evidenced by the decreasing mean phase field with time. Further, the microstructural evolution depicted in Figures 6.25(a)-(d) shows that R + T $\rightarrow$ R transformation occurs by movement of phase interfaces, rather than by nucleation. The latter is demonstrated by the coarsening of the rhombohedral domains ringed in red in Figures 6.25(a)-(d). This result is consistent with the conclusions from the JMAK analysis performed in Section 6.5.3. Accordingly, Figure 6.25 also shows that the size of domains of the metastable T phase decreases with time. This is illustrated by the shrinking of the tetragonal domain ringed in blue in Figures 6.25(a)-(c), until it completely disappears in Figure 6.25(d).

Similarly, for $T = 293\,\mathrm{K} > T_{PPB}$, Figures 6.26(a)-(d) show relaxation to the stable T phase and R + T $\rightarrow$ T transformation by movement of phase interfaces, see tetragonal domain ringed in

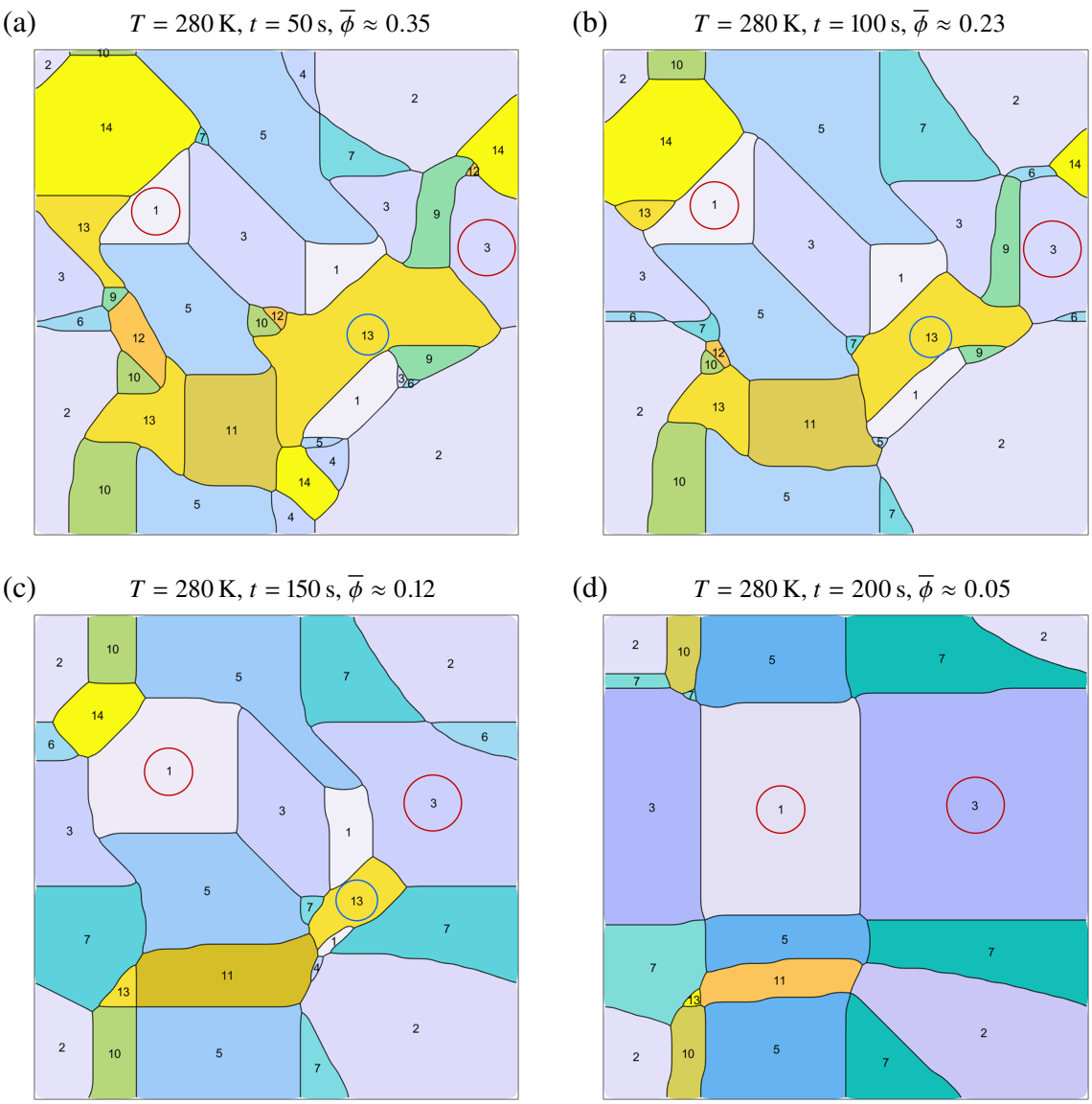

Figure 6.25: MTEX orientation plots for $T = 280\,\mathrm{K}$ showing evolution of microstructure at (a) $t = 50\,\mathrm{s}$, (b) $t = 100\,\mathrm{s}$, (c) $t = 150\,\mathrm{s}$, and (d) $t = 200\,\mathrm{s}$. The computational domain size is $232\,\mathrm{nm} \times 232\,\mathrm{nm}$. For each case, the mean phase field is indicated and the polarization variants of domains are annotated (1-8 for the R phase and 9-14 for the T phase). Coarsening of two stable rhombohedral domains, ringed in red, is demonstrated. A shrinking metastable tetragonal domain, ringed in blue, is also shown.

blue. Also, they show shrinking domains of the metastable R phase, see *e.g.,* the rhombohedral domain ringed in red in Figures 6.26(a)-(b). In this case, however, the final microstructure consists of relatively elongated domains, Figure 6.26(d). In contrast, for $T < T_{PPB}$ and the same time (200 s), Figure 6.25(d) shows a final microstructure with more equiaxed domains.

In addition, the MTEX toolbox was used to obtain quantitative results of all interfaces for selected temperatures and times of interest. In Figure 6.27, two extreme microstructures are analysed: Figure 6.27(a) corresponds to a case of 96 % R + T $\rightarrow$ R transformation at $T = 270\,\mathrm{K}$, and Figure 6.27(b) corresponds to a case of 96 % R + T $\rightarrow$ T transformation at $T = 298\,\mathrm{K}$. For $T = 270\,\mathrm{K}$, Figure 6.27(a) shows the presence of faceted and curved RDWs and phase interfaces, in

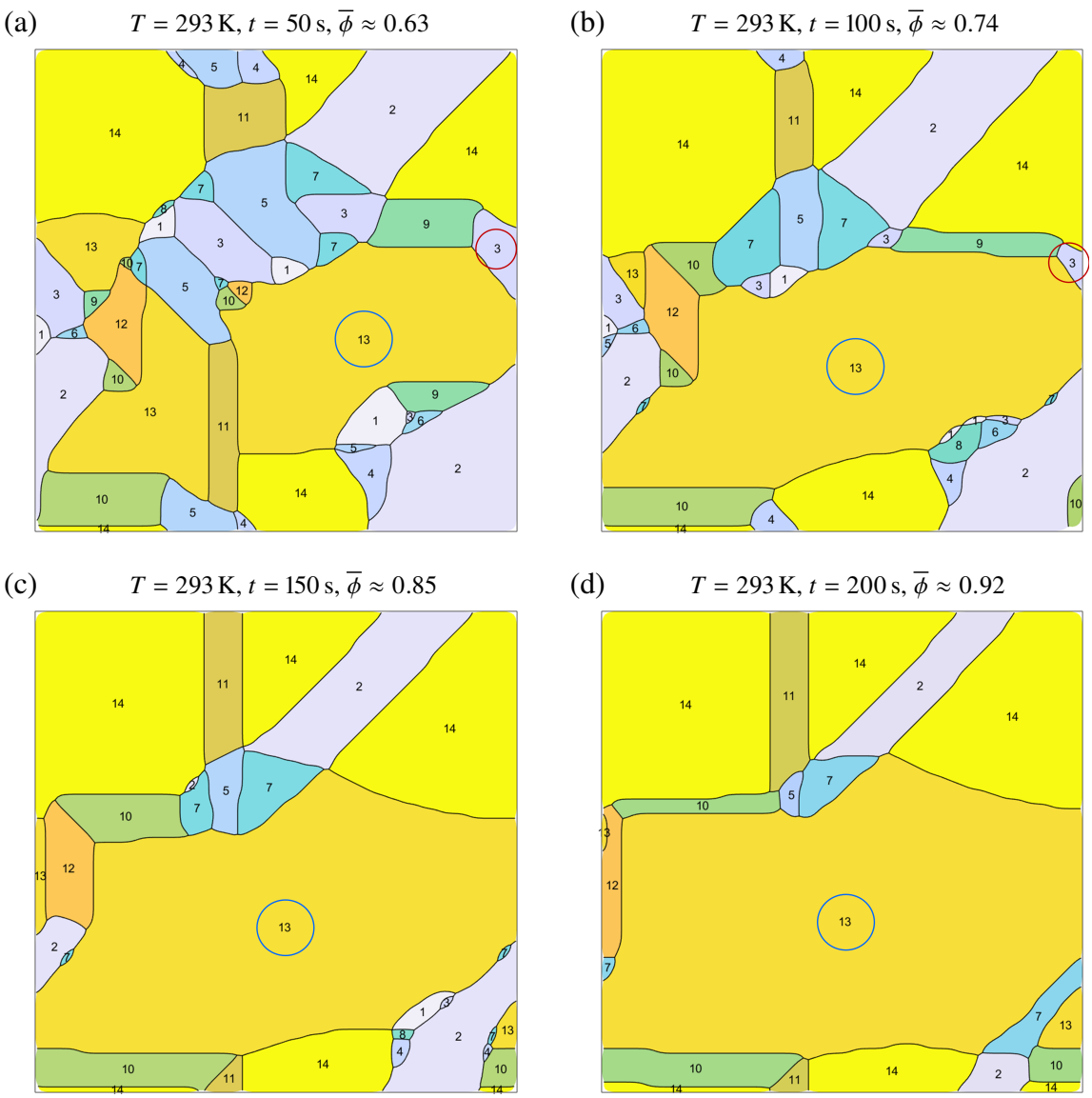

Figure 6.26: MTEX orientation plots for $T = 293\,\mathrm{K}$ showing evolution of microstructure at (a) $t = 50\,\mathrm{s}$, (b) $t = 100\,\mathrm{s}$, (c) $t = 150\,\mathrm{s}$, and (d) $t = 200\,\mathrm{s}$. The computational domain size is $232\,\mathrm{nm} \times 232\,\mathrm{nm}$. For each case, the mean phase field is indicated and the polarization variants of domains are annotated (1-8 for the R phase and 9-14 for the T phase). Coarsening of a stable tetragonal domain, ringed in blue, is demonstrated. A shrinking metastable rhombohedral domain, ringed in red, is also shown.

agreement with predictions made in Section 6.5.1. In particular, the formation of curved 71RDW$_2$ boundaries, due to their isotropic interfacial energy, is more evident than in Figure 6.16(d). Similarly, for $T = 298\,\mathrm{K}$, Figure 6.27(b) demonstrates the formation of curved 180TDW$_2$ boundaries due to their isotropic interfacial energy, in accordance with Section 6.5.1.

Moreover, Figure 6.27(b) also shows that domains of the stable T phase at $T = 298\,\mathrm{K}$ are significantly larger than domains of the stable R phase at $T = 270\,\mathrm{K}$. This can be explained by the relatively low interfacial energies estimated at $T = 298\,\mathrm{K}$ ($0.83 \times 10^{-4}\,\mathrm{J/m^2}$ to $2.76 \times 10^{-4}\,\mathrm{J/m^2}$), see Figure 6.9(b). The latter results in a comparatively small increase in the total free energy of the system for high aspect ratio domains. In contrast, all interfacial energies are greater at $T = 270\,\mathrm{K}$

(3.30×10^{-4} J/m^2 to 10.6×10^{-4} J/m^2), which causes a larger increase in the total free energy for the same initial conditions.

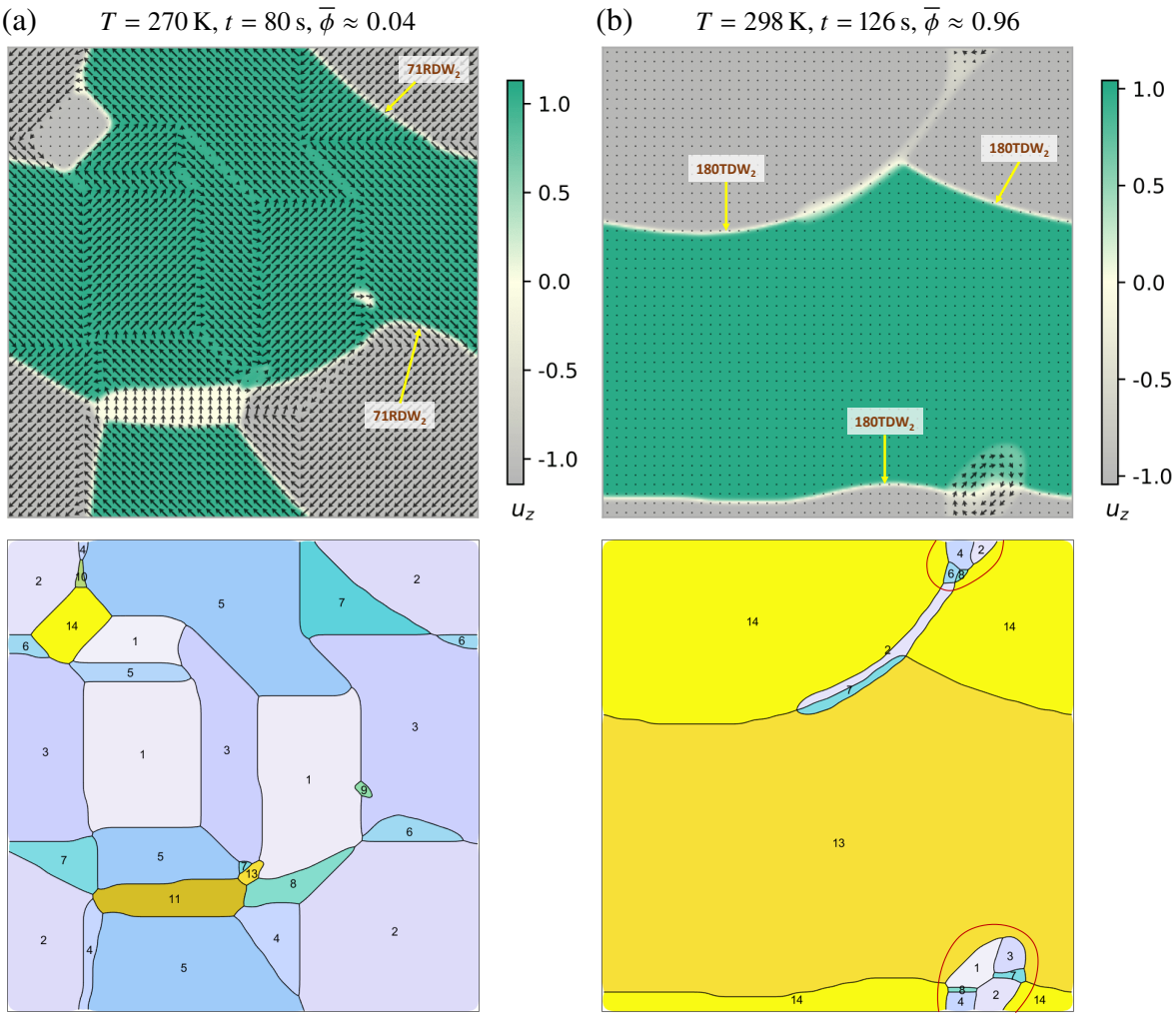

Figure 6.27: Analysis of microstructures corresponding to (a) 96 % R + T → R transformation at T = 270 K, and (b) 96 % R + T → T transformation at T = 298 K. The computational domain size is 232 nm × 232 nm. Small nano-domains of the metastable R phase are ringed in red.

Notably, Figure 6.27(b) also shows formation of small nano-domains of the metastable R phase at T = 298 K. This can be attributed to the near vanishing energy barrier between rhombohedral variants close to the first order P-FE transition that occurs at $T_{CW,R}$ (299 K). The vanishing energy barrier between rhombohedral domains is responsible for the negligible interfacial energy associated to RDWs. According to classical ferroelectric theory[1], the domain size is proportional to the square root of the interfacial energy. Hence, the small σ values partly explain the miniaturization of the domain structure observed experimentally in the BZT-x BCT system near its PPB[86,105,108–111]. Additionally, the vanishing energy barrier generates flattening of the homogeneous free energy density that facilitates polarization switching in the R phase. Thus, the small nano-domains of metastable R phase provide an easy path for polarization switching between stable tetragonal domains through a phase transformation-induced polarization rotation mechanism. This interfacial stabilization of the metastable R phase was also reported in Section 3.6.3 for the BZT-40 BCT system near its $T_{CW,R}$. These results explain experimental observations on BZT-x BCT ceramics,

reported by Acosta *et al.*[72], who found that the highest electromechanical response was along the orthorhombic-tetragonal phase boundary. For BZT-40 BCT and BZT-50 BCT, this boundary corresponds to the upper thermodynamic limit for R + T coexistence predicted by the MPF model at each $T_{CW,R}$.

Figure 6.28 shows the calculated length fraction of all interfaces for the microstructures depicted in Figure 6.27. Results are compared to those obtained in Figure 6.24 for the initial microstructure. For $T = 270\,\mathrm{K}$, Figure 6.28(a) indicates that the total fraction of RDWs increases with respect to initial conditions DIC1. This is consistent with the rise in the fraction of the stable R phase to approximately 96 %. In particular, a greater increase is observed in the length fraction of $71\mathrm{RDW}_1$ and $71\mathrm{RDW}_2$. These RDWs have the lowest interfacial energy and, hence, their formation is favoured to minimize the total free energy of the system, see Figure 6.9(b). Further, Figure 6.27(a) shows that the remaining fraction of the metastable T phase (4 %) manifests as isolated domains surrounded by the R phase. Accordingly, the fraction of TDWs becomes negligible, while the fraction of phase interfaces only decreases slightly.

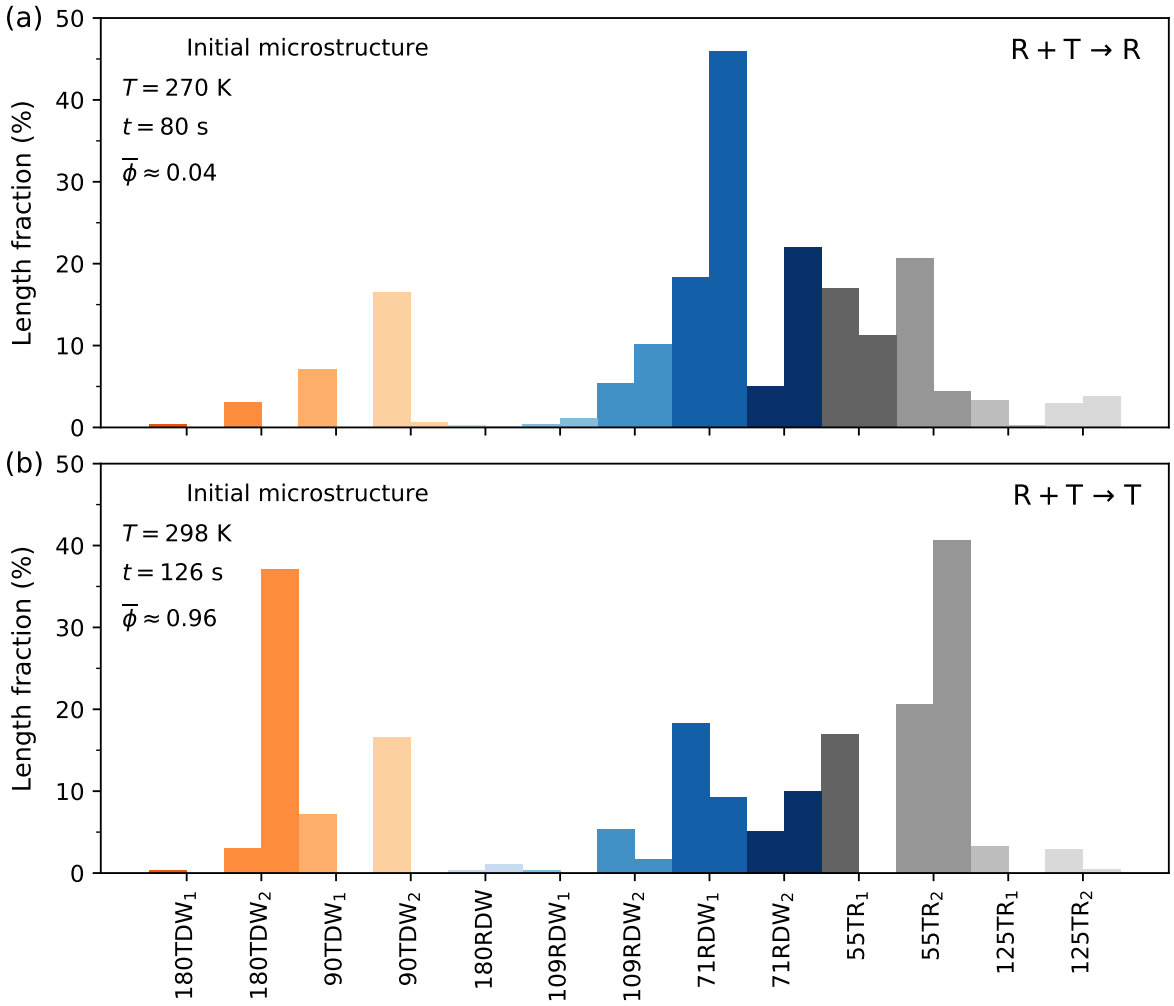

Figure 6.28: Combined bar plots showing the calculated length fraction of all interfaces for microstructures corresponding to (a) 96 % R + T → R transformation at $T = 270\,\mathrm{K}$, and (b) 96 % R + T → T transformation at $T = 298\,\mathrm{K}$. The dashed columns are results from the initial DIC1 microstructure.

For $T = 298\,\mathrm{K}$, Figure 6.28(b) shows that the total length fraction of TDWs increases in accordance with the rise in the fraction of the stable T phase. However, this increase is relatively small compared to that observed in Figure 6.28(a) for the stable RDWs. This is explained by the formation of only a few, large tetragonal domains, as shown in Figure 6.27(b). Remarkably, Figure 6.28(b) also reveals that only the 180TDW$_2$ and 55T-R$_2$ interfaces are present in the final microstructure, while the rest of the TDWs and T-R phase interfaces disappear. This relates to the formation of tetragonal domains oriented only perpendicularly to the (001) plane, *i.e.,* domains with T5 or T6 polarization variants according to Figure 6.22(b). It is worth noting that these tetragonal variants correspond to the crystallographic textures labelled as 13 and 14 in MTEX, see Figure 6.27(b). Moreover, Figure 6.28(b) shows a modest reduction in the length fraction of RDWs, despite the small fraction of the metastable R phase in the final microstructure (4 %). This is explained by the formation of particularly small rhombohedral domains at $T = 298\,\mathrm{K}$, as shown in Figure 6.27(b) and discussed above.

While the relative length fractions of the various interfaces change, the total interface length should also change during the microstructural evolution. In Figure 6.29, the total length of all interfaces was calculated for microstructures simulated at selected temperatures. To begin with, the total interface length of the initial microstructure was calculated as 3554 nm. Then, for each temperature, two microstructural states were considered. First, calculations were carried out at $t = 50\,\mathrm{s}$ for each selected temperature, Figure 6.29(a). For all cases, the total interface length decreases with time from the initial state. For $T < T_{PPB}$, results show that the expected decrease in the total length of interfaces is less with increasing temperature. Assuming equiaxed domains, similar to those observed in Figure 6.25(a) for $T = 280\,\mathrm{K}$ and $t = 50\,\mathrm{s}$, the behaviour can be attributed to the expected miniaturization of the domain structure as $T \rightarrow T_{PPB}$. For the BZT-40 BCT system, calculations showed that the size of FE domains decreases in the vicinity of the PPB due to the R + T metastable coexistence, with smaller domains obtained when the volume fractions of both phases are approximately equal, Section 4.5.4.

For $T > T_{PPB}$, Figure 6.29(a) shows that the total length of interfaces remains relatively constant for $T_{PPB} < T \lesssim 295\,\mathrm{K}$, with a maximum at 293 K, before dropping drastically as $T \rightarrow T_{CW,R}$. This is likely due to a trade off between the driving force for phase transformation and the formation of small nano-domains of the metastable R phase. Moreover, Figure 6.26 revealed that domains at $T = 293\,\mathrm{K}$ are relatively elongated compared to those at $T < T_{PPB}$, see *e.g.,* Figure 6.25 and Figure 6.27(a). The presence of elongated domains would further increase the total length of interfaces.

Calculations were also performed for each selected temperature at $\psi = 96\,\%$, Figure 6.29(b). For $T < T_{PPB}$, results show that the total length of interfaces decreases with increasing temperature at the same fraction transformed. This can be explained by the longer time required to reach $\psi = 96\,\%$ as $T \rightarrow T_{PPB}$, and the intrinsic coarsening of domains during that time. Similarly, for $T > T_{PPB}$, the total length generally decreases as the required time to reach $\psi = 96\,\%$ increases. However, in this case, the trend is much less pronounced than for $T < T_{PPB}$, yielding smaller values. Also, the total length drops as $T \rightarrow T_{CW,R}$. These results can be attributed to the

formation of larger domains of the stable T phase at $T > T_{PPB}$, which are favoured due to the relatively low interfacial energies, see *e.g.,* Figure 6.27(b).

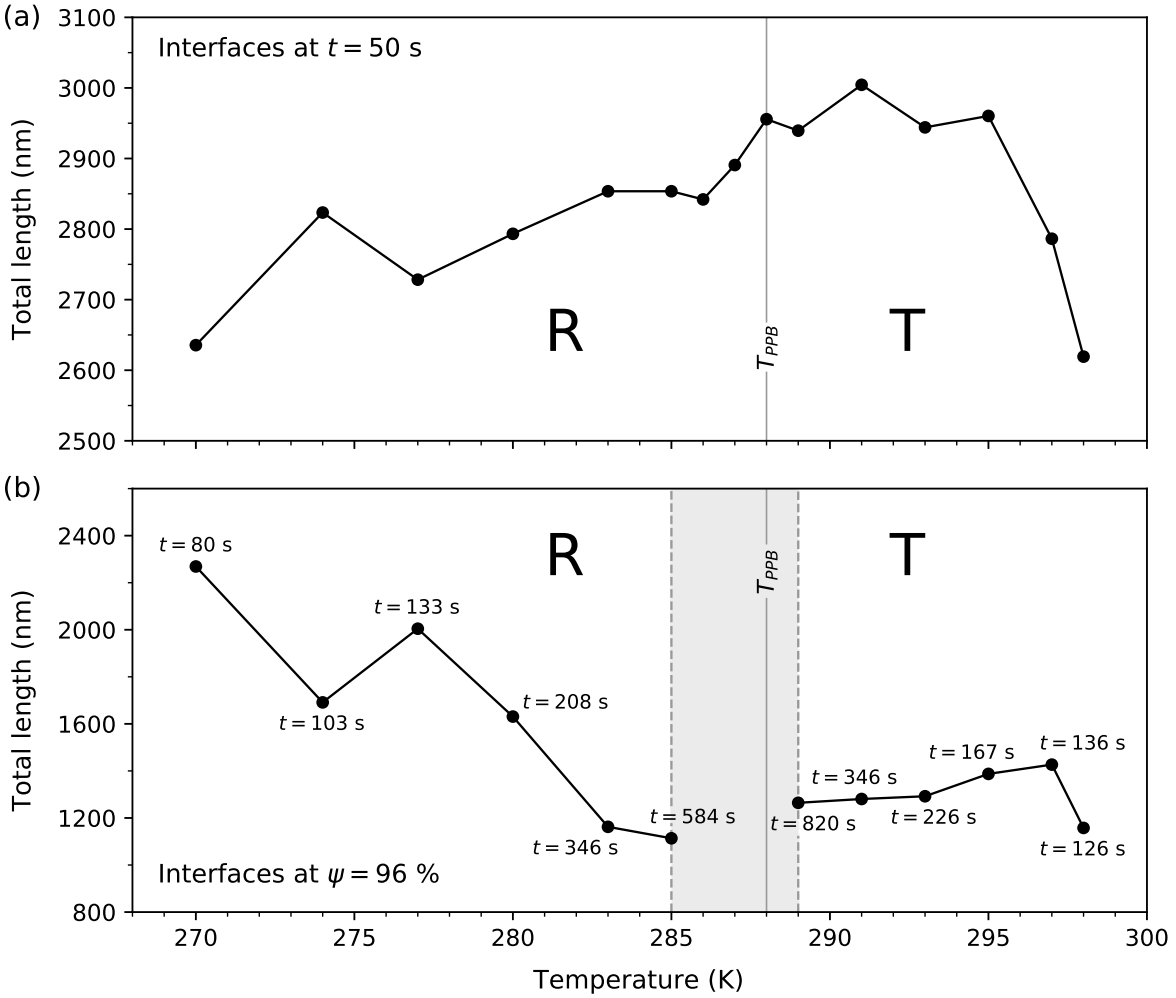

Figure 6.29: Total length of all interfaces as a function of temperature at (a) $t = 50$ s, and (b) $\psi = 96$ %. For all cases, the total interface length of the initial microstructure is 3554 nm. The metastable equilibrium regime, defined in this study, occurs within the temperature range delimited by the dashed lines.

In this thesis, no domain size / coarsening analysis has been performed on the BZT-50 BCT simulations. The codes developed with MTEX are suitable for this analysis. This is the subject of future work.

6.6 Summary and conclusions

A two-dimensional MPF model was developed for a BZT-50 BCT single crystal, characterized by the spatial distribution of a three-component polarization vector. In particular, anisotropic Landau coefficients were used for each FE phase to investigate the intrinsic effects of R + T coexistence on the kinetics of phase transformation and domain morphology. The 2-D computational domain was selected parallel to the (001) plane of the pseudocubic crystal structure. The analysis

of [001]-oriented single-crystal samples is of particular interest because they exhibit relatively high piezoelectric response in similar FE systems, including PZT[55]. The restriction imposed by the 2-D geometry limits the solution of Coulomb's Equation and produces additional interfaces that do not correspond with real three-dimensional scenarios. However, these limitations are not expected to significantly change the results reported in this chapter. Future work is required to study the intrinsic ferroelectric behaviour of BZT-*x* BCT, or similar systems, in other two-dimensional planes or in the three-dimensional space. For example, if the simulation domain were chosen to be a pseudocubic (1$\bar{1}$0) plane, it would contain four R in-plane variants and two T in-plane variants. The effect of geometry on the detailed results of two-phase coexistence could then be investigated.

The TTT diagram constructed for a BZT-50 BCT single crystal shows qualitative agreement with those constructed in previous chapters for coarse-grained BZT-40 BCT polycrystals. A thermodynamic upper limit for R + T metastable coexistence is predicted by the MPF model, while a lower limit is determined by the rapid kinetics of phase transformation. These results are consistent with, and provide a rationale for, the experimentally observed phase transitions in the BZT-*x* BCT system. Further, in this study, a metastable equilibrium regime is defined within the R + T coexistence region. It is characterized by vanishing driving force for phase transformation that leads to possible long-term R + T coexistence, stagnation of microstructures, or relaxation to one phase depending on the interfacial energies and initial conditions. For BZT-50 BCT, the metastable equilibrium regime occurs in a temperature range that includes 286 K, 287 K and 288 K (T_{PPB}).

In this work, a method is presented for converting the polarization fields into individual orientation measurements that can be post-processed by the MATLAB™ toolbox MTEX as EBSD data. It represents a powerful tool for the quantitative analysis of ferroelectric domain structures and their evolution. For $T > T_{PPB}$, results show formation of small nano-domains of the metastable R phase in the vicinity of $T_{CW,R}$. These observations are explained by the vanishing energy barrier between rhombohedral variants as $T \rightarrow T_{CW,R}$, which in turn generates the vanishing interfacial energy of RDWs and flattening of the homogeneous free energy density. The latter leads to a reduced barrier for polarization switching in the R phase, facilitating polarization rotation between stable tetragonal domains. The enabled polarization rotation can be linked to the origin of enhanced electromechanical properties in the BZT-*x* BCT system[55,96]. Furthermore, its appearance in the vicinity of $T_{CW,R}$ explains the higher piezoelectric response along the orthorhombic-tetragonal phase boundary reported in experiments[72].

Chapter 7

Conclusions and future work

The primary objective of this project was to develop a novel multiphase field (MPF) model for the description of ferroelectric (FE) materials with at least one polymorphic phase boundary (PPB). The MPF approach was demonstrated for the $(1-x)\mathrm{Ba}(\mathrm{Zr}_{0.2}\mathrm{Ti}_{0.8})\mathrm{O}_3$-$x(\mathrm{Ba}_{0.7}\mathrm{Ca}_{0.3})\mathrm{TiO}_3$, or BZT-$x$ BCT, system assuming a phase diagram with a single PPB between the tetragonal (T) and rhombohedral (R) phases. This chapter summarizes the main findings and predictions of the developed model, as well as their implications for the analysis of similar FE systems. The chapter also outlines a potential trajectory for future work in the field. This includes possible applications of the MPF model and recommendations for its further development.

7.1 Review of objectives and findings

At the core of this project, a new theory based on a MPF formulation is proposed to describe systems with multiple FE phases. This approach considers the homogeneous free energy density of the individual FE phases, with their own Landau coefficients, enabling a better description of the single-phase regions of the material. A thermodynamically correct analysis in the vicinity of the interferroelectric phase transitions is then possible.

Based on the proposed MPF framework, a model was developed to describe FE systems with a single PPB. It naturally identifies thermodynamic conditions for the coexistence and stability of phases near the PPB, based on the order of the two paraelectric-ferroelectric (P-FE) transitions. The MPF model was demonstrated in 1-D for the BZT-40 BCT system, assuming a phase diagram with a single PPB between the T and R phases. For this objective, Landau coefficients were estimated separately for both FE phases using a coarse-grained approach. The 1-D model allowed the detailed study of the energetics related to FE phase transformation, polarization switching, and polarization-phase transformation interactions. Further, a time-temperature-transformation (TTT) diagram was constructed to investigate the kinetics of FE phase transformation. The combined energetic and kinetic analysis of the metastable coexistence of the T and R phases can explain the stabilization of the apparent orthorhombic (O) phase in the vicinity of the T-R boundary. At high temperatures, the R + T metastable coexistence is thermodynamically limited, while at low temperatures, it is kinetically limited. The apparent O phase reported experimentally can be explained by adaptive diffraction of the nano-domain structure of T and R phases that characterize compositions near

the PPB. In addition, the 1-D analysis allowed the identification of a phase transformation-induced polarization rotation mechanism that can explain the enhanced electromechanical properties near the PPB. This mechanism is facilitated at $T > T_{PPB}$ due to higher thermal energy in the system, and a relatively low energy barrier between variants in the R phase.

The one-dimensional MPF model was then extended to two spatial dimensions and demonstrated for the coarse-grained BZT-40 BCT system. The 2-D analysis enabled the additional study of transformation kinetics and domain morphologies considering local dipole-dipole interactions. Two TTT diagrams were constructed to investigate the effects of the additional spatial dimension and local electric fields on the transformation kinetics of the coexisting FE phases. Overall, results confirmed that R + T metastable coexistence is thermodynamically limited at high temperatures and kinetically limited at low temperatures. Further, the MPF model confirmed the formation of FE domains with head-to-tail polarization configurations that have been observed in other computational works. It also predicted microstructures with faceted domain walls (DWs) and curved T-R phase interfaces that are consistent with experiments. The formation of curved interfaces to accommodate domains of different phases was explained by the relatively low anisotropy of the interfacial energy compared to that of DWs.

Domain size and coarsening calculations were performed for BZT-40 BCT in the temperature range where the T and R phases coexist. Results yielded average domain sizes of $25-35$ nm, within the $10-60$ nm range observed experimentally for the BZT-x BCT system[16]. Miniaturization of the domain structure to the nanoscale is generally explained by low interfacial energy values. In this analysis, the nano-domain structure was additionally linked to the metastable coexistence of FE phases. Results showed that, when both FE phases coexist, the evolution of domains is dominated by the kinetics of phase transformation over the competing effect of intrinsic domain coarsening. They also suggested that the presence of metastable domains has a pinning effect on the motion of stable DWs, which retards the coarsening rate for domains of the stable FE phase. This explains the smaller average domain sizes obtained near the PPB, where the volume fractions of the two phases are approximately equal. Further, for $T > T_{PPB}$, results revealed the formation of small nano-domains of the metastable R phase, due to the relatively low interfacial energy of RDWs. The latter was attributed to the reduced energy barrier between variants in the R phase, which is also responsible for facilitation of the polarization rotation observed in the 1-D model.

For the next objective, anisotropic Landau coefficients were determined for the T and R phases of the BZT-50 BCT system. Each phase was described by a sixth order Landau-Devonshire potential with a three-component polarization vector as the order parameter. A fitting procedure that uses a combination of single-crystal and polycrystalline experimental data was developed. To the best of the author's knowledge, the estimated parameters correspond to the first experimentally-fitted Landau coefficients reported for the BZT-50 BCT system. The use of anisotropic Landau coefficients enables the analysis of the FE phenomenon due to intrinsic effects of the lattice, and is the first step towards modelling polycrystalline ferroelectrics.

Finally, the MPF model was applied to a [001]-oriented BZT-50 BCT single crystal using the estimated anisotropic Landau coefficients. A metastable equilibrium regime was identified in

the vicinity of the PPB temperature. It is characterized by a vanishing driving force for phase transformation that leads to possible long-term R + T coexistence, stagnation of microstructures, or relaxation to one FE phase depending on the interfacial energies and initial conditions. Visual inspection of stagnated microstructures revealed the formation of vortex and twin-like (or lamellar) domain structures with head-to-tail polarization configurations. These patterns help to stabilize the metastable FE microstructures and are consistent with reports from experimental and computational works on BZT-BCT and similar FE systems. For the BZT-50 BCT system, the metastable equilibrium regime occurs in a temperature range that includes 286 K, 287 K and 288 K (T_{PPB}). In addition, two TTT diagrams were constructed to investigate the effects of different initial conditions on the transformation kinetics of the FE phases. In particular, two mixed 50 %R + 50 %T phase states were considered: a random initial condition and a microstructure with developed nano-domains. Results revealed possible coupled spinodal decomposition during the first stages of domain formation upon cooling from the paraelectric phase. This phenomenon affects the macroscopic kinetics of phase transformation, especially at $T > T_{PPB}$. No theoretical treatment of this phenomenon has been found in the literature for FE systems.

Furthermore, a method was developed for the quantitative analysis of domain structures and their evolution using the MATLAB™ toolbox MTEX. The developed tool was applied to calculate the length of all interfaces for selected times and temperatures of interest. Results showed that the lowest-energy interfaces of the stable FE phase are favoured to minimize the total free energy of the system, hence they persist for a longer time. In addition, visual inspection and an analysis of the relative interface length fractions revealed the formation of small nano-domains of the metastable R phase near the predicted thermal limit for coexistence, $T_{CW,R}$. This was again attributed to the vanishing energy barrier between R variants, which produces (a) vanishing RDWs energies and (b) flattening of the homogeneous free energy density for the R phase. The former automatically predicts the formation of small nano-domains according to classical FE theory, which relates domain size and interfacial energy. The latter facilitates rhombohedral polarization switching, enabling polarization rotation between stable T domains via phase transformation. The origin of superior electromechanical properties in the BZT-*x* BCT system has been associated with easy polarization rotation. In this case, it also explains the higher piezoelectric response along the purported O-T phase boundary measured in experiments.

7.2 Summary of key contributions

– A novel multiphase field theory was developed for FE materials.

– For ferroelectrics with a single PPB, the MPF model identifies conditions for the coexistence and stability of phases near the PPB based on the order of the two P-FE transitions.

– The MPF model predicts a thermodynamic upper limit for the metastable coexistence of FE phases. For the BZT-*x* BCT system, predictions are consistent with the experimentally observed transition temperatures. These results support the hypothesis of R + T metastable coexistence, as opposed to an intervening O phase.

– A novel TTT diagram was proposed for the analysis of transformations in two-FE-phase systems. These diagrams have been extensively used to understand transformations in alloys and glasses, but the use of this technique has not been found in the literature for FE systems.

– The TTT diagrams constructed for the BZT-*x* BCT system suggest that the metastable coexistence of the T and R phases is kinetically limited at low temperatures.

– For the BZT-40 BCT system, the MPF model predicts microstructures with faceted DWs and curved T-R phase interfaces, which are consistent with recent transmission electron microscopy (TEM) studies carried out near the PPB of the BZT-*x* BCT system.

– Miniaturization of the domain structure to the nanoscale was linked to low interfacial energy values and the volume fraction of the metastable FE phase. The latter produces a pinning effect on the motion of stable DWs that retards the coarsening rate for domains of the stable FE phase.

– A procedure was developed to determine the anisotropic Landau parameters for the T and R phases of the BZT-50 BCT system, using a combination of single-crystal and polycrystalline experimental data. The estimated parameters constitute the first experimentally-fitted Landau coefficients reported for the BZT-50 BCT system.

– A metastable equilibrium regime, characterized by a vanishing driving force for phase transformation, was identified in the vicinity of the PPB. It explains the formation of typical domain configurations or patterns that produce a metastable equilibrium at the interface intersections and stabilize the microstructure.

– A method was developed for the quantitative analysis of domain structures using the MATLAB™ toolbox MTEX.

– Near the coexistence thermal limit, the MPF model predicts a vanishing energy barrier between variants in the metastable R phase. This automatically predicts the formation of small metastable domains that provide an easy path for polarization switching between stable tetragonal domains through a phase transformation-induced polarization rotation mechanism. For the BZT-*x* BCT system, this interfacial stabilization of the metastable R phase can explain the higher electromechanical response reported experimentally along the purported O-T phase boundary.

7.3 Implications and future work

In this research project, a framework has been established for the modelling and analysis of FE systems with multiple phases. The MPF approach enables a thermodynamically correct analysis of interferroelectric phase transitions subjected to different external fields. It also allows direct assessment of the transformation kinetics of the multiple coexisting FE phases during all the stages of microstructure evolution. Further, the developed method for the quantitative analysis of FE domain structures in MATLAB™ constitutes a powerful tool for the detailed study of domain interfaces and bulk domains, *e.g.,* domain size and coarsening.

The MPF model developed in this work can be readily applied to systems with two or more FE phases to validate competing theories regarding the structural state and enhanced properties near the PPB(s) in the search for lead-free materials. The model can also be used to analyse complex microstructures in 2-D or 3-D, including the effect of grain boundaries, local elastic strains, and charged species, among others. Finally, the MPF formulation can be extended to account for compositionally driven phase transitions. In the limiting case, the latter would allow the study of FE systems with a morphotropic phase boundary (MPB), such as PZT.

Appendix A

Mobility calculations for the BZT-x BCT system

This appendix contains mobility calculations for different compositions of the BZT-x BCT system. The calculation method is detailed in Section 3.3.2. However, the procedure is summarized here for completeness.

In the MPF models developed herein, the interface mobilities, $M_P = M_\phi$, are defined as an interpolation function that combines the mobilities of the FE phases, M_T and M_R; each one described by an Arrhenius expression, $M(T) = M_o \exp(-Q/RT)$. The constants M_o and Q are estimated by fitting the equation $\ln(M) = \ln(M_o) - (Q/R)(1/T)$ to mobility values extracted from experimental hysteresis data at selected temperatures. In this work, measurements from polycrystalline samples at different compositions are used, as reported by Ehmke[89]. Following Zhao, Cao and García[93], the mobility values are calculated using

$$M = 2\pi\omega\chi_c\epsilon_o\sqrt{\left(\frac{E_o}{E_c}\right)^2 - 1} \tag{A.1}$$

where $\omega = 0.1\,\mathrm{Hz}$ is the experimental cycling frequency, $E_o = 1\,\mathrm{MV/m}$ is the maximum applied field during the experiment, χ_c is the electric susceptibility at the experimentally observed coercive field, and $\chi_c\epsilon_o$ corresponds to the slope of the P vs E curve at the coercive field. This calculation is illustrated in Figure 3.6 for the BZT-40 BCT composition.

The method described above is applied to different compositions of the BZT-x BCT system, Figure A.1. The calculated M_o and Q constants are stated in Table A.1. For the R phase, mobility

Table A.1: Calculated mobility constants for different compositions of the BZT-x BCT system

	R phase		T phase	
Composition	M_o (S/m)	Q (J/mol)	M_o (S/m)	Q (J/mol)
BZT-40 BCT	1.809×10^{-4}	8561	3.806×10^{-10}	−25 260
BZT-45 BCT	–	–	1.671×10^{-5}	5382
BZT-50 BCT	–	–	3.349×10^{-4}	13 250
BZT-60 BCT	–	–	8.283×10^{-4}	16 920

constants are only reported for the BZT-40 BCT composition. For all other compositions, no experimental data was available at low temperatures where the R phase is unambiguously stable. Further, Table A.1 shows that the tetragonal mobility in BZT-40 BCT has negative activation energy, *i.e.,* $Q_T < 0$. This can be attributed to the proximity of the experiments to the T-C transition, and the relatively narrow temperature range where the T phase is stable compared to other compositions, see Figure A.1. For all other compositions, the mobility in the T phase has positive activation energy.

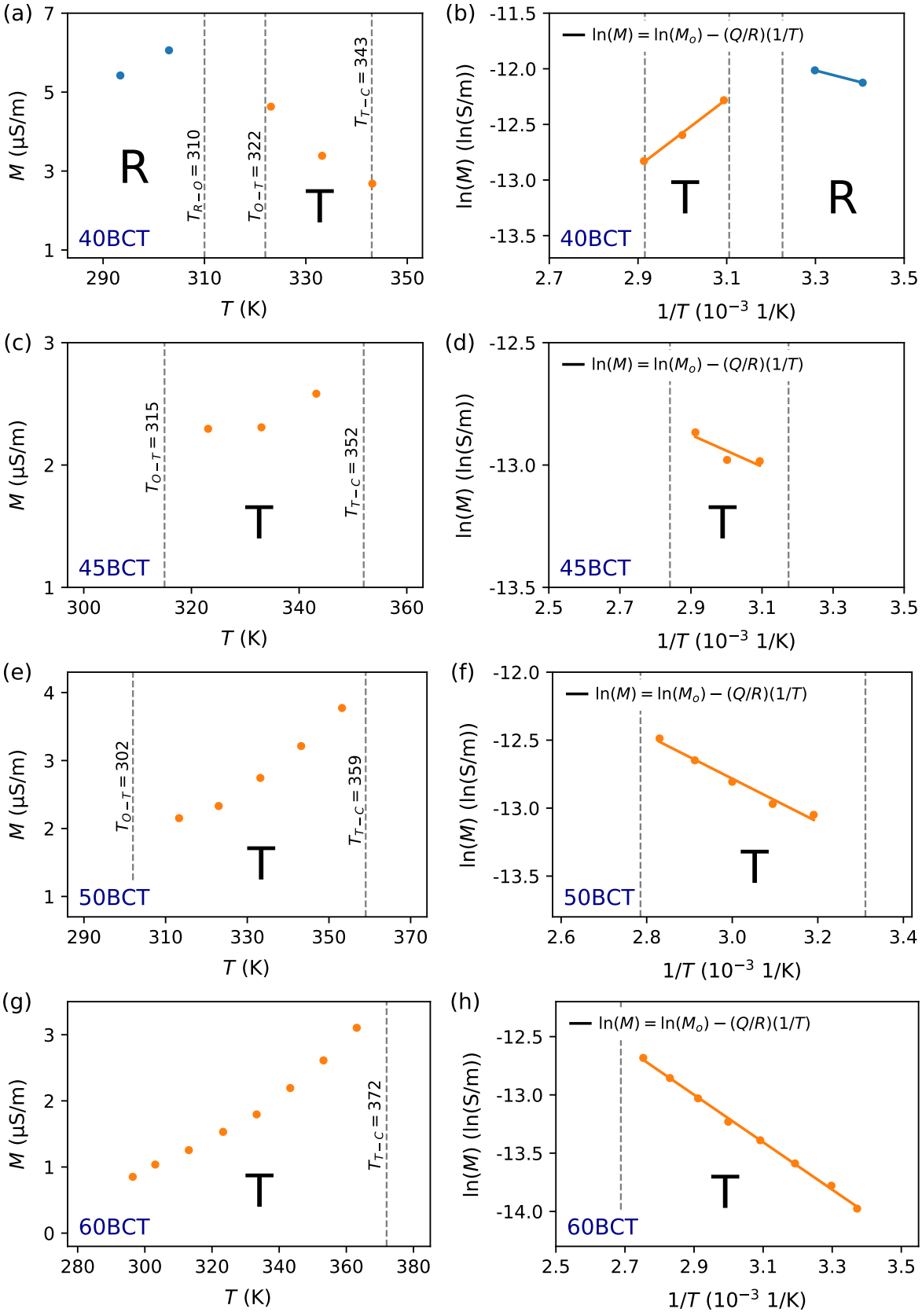

Figure A.1: Calculation of mobility constants for the R (—) and T (—) phases of the (a)-(b) BZT-40 BCT, (c)-(d) BZT-45 BCT, (e)-(f) BZT-50 BCT, and (g)-(h) BZT-60 BCT compositions. Left column: mobility values calculated at selected temperatures using experimental hysteresis data from polycrystalline samples, as measured by Ehmke[89]. Right column: fitting of equation $\ln(M) = \ln(M_o) - (Q/R)(1/T)$ to estimate parameters Q and M_o.

Appendix B

Publications

This appendix provides a copy of an article published during the course of this research. The article was published in the journal Acta Materialia and was adapted in this work for non-commercial use only. Specifically, its content was included and further developed in Chapters 2 and 3. The article has the following citation:

– Oscar A. Torres-Matheus, R. Edwin García and Catherine M. Bishop. Phase coexistence near the polymorphic phase boundary. *Acta Materialia*, 164: 577-585, 2019, DOI: 10.1016/j.actamat.2018.10.041.

Acta Materialia 164 (2019) 577–585

Contents lists available at ScienceDirect

Acta Materialia

journal homepage: www.elsevier.com/locate/actamat

Full length article

Phase coexistence near the polymorphic phase boundary

Oscar A. Torres-Matheus [a], R. Edwin García [b], Catherine M. Bishop [a, *]

[a] Department of Mechanical Engineering, University of Canterbury, Private Bag 4800, Christchurch, 8140, New Zealand
[b] School of Materials Engineering, Purdue University, West Lafayette, IN, 47907, USA

ARTICLE INFO

Article history:
Received 27 July 2018
Received in revised form
18 October 2018
Accepted 21 October 2018
Available online 27 October 2018

MSC:
00–01
99-00

Keywords:
Ferroelectric
Interferroelectric transitions
Phase field model
Phase coexistence
Phase stability

ABSTRACT

A novel multiphase field theory for ferroelectric systems in the vicinity of a polymorphic phase boundary (PPB) is developed by coupling the Landau-Devonshire thermodynamic potentials of the individual phases. The model naturally predicts metastable coexistence of the rhombohedral (R) and tetragonal (T) phases near the PPB temperature, $T_{PPB} = 43^{\circ}C$, for the BZT-40BCT system, and provides a maximum temperature of coexistence, $T_{C,0} = 49.9^{\circ}C$, in agreement with experiments. For $T > T_{PPB}$, results show that metastable coexistence of two ferroelectric phases is a result of a phase transformation-induced polarization rotation plus switching mechanism. Metastable domains of the low-temperature R phase coexist with the high-temperature, thermodynamically stable T phase for long periods of time, from minutes to hours. For $T < T_{PPB}$, the coexistence time is on the order of tens of seconds due to a decreased thermal energy that suppresses the polarization rotation plus switching mechanism. Further, the kinetics of macroscopic T→R phase transformation is accelerated by a large thermodynamic driving force and high mobility.

1. Introduction

Ferroelectric (FE) materials span a wide range of applications, including high-dielectric-constant capacitors [1]; electromechanical devices, such as sensors, actuators, transducers, micro-positioning systems, piezoelectric fuel injectors and printing machines [2]; and, more recently, non-volatile memories [1]. In particular, $Pb(Zr,Ti)O_3$ or PZT has been the most widely used piezoelectric material due to its wide range of composition-dependent properties [3] and high electromechanical performance near its morphotropic phase boundary (MPB) [1–3]. However, recent environmental restrictions on the use of lead have resulted in the identification of alternate chemistries, with equal or higher response [2,4,5].

The search for new lead-free materials depends on understanding the origin of electromechanical performance in the vicinity of the transition temperature where two different FE phases coexist [3], commonly termed the interferroelectric phase transition temperature to differentiate it from the paraelectric-ferroelectric transition temperature [4]. The phase transformation regimes are traditionally summarized in composition-temperature maps, or phase diagrams (*e.g.*, Fig. 1). A phase boundary representing a compositionally driven interferroelectric transition is referred to as an MPB [4,5]. A phase boundary representing an interferroelectric transition driven by changes in temperature is referred to as a polymorphic phase boundary (PPB) [4,5]. Because the focus is on understanding the effect of temperature on material behaviour, the remainder of this paper will describe the equilibrium and phase transition kinetics in the vicinity of a PPB.

One promising lead-free candidate is $(1-x)Ba(Zr_{0.2}Ti_{0.8})O_3$-$x(Ba_{0.7}Ca_{0.3})TiO_3$ or BZT-xBCT, which exhibits a PPB between the tetragonal (T) and rhombohedral (R) phases [6], Fig. 1. Recently, the existence of an additional orthorhombic (O) phase has been speculated via high-resolution XRD and Rietveld refinement [7], Raman spectroscopy [8], and elastic, dielectric and piezoelectric measurements [9]. Gao et al. [5] have argued that the presence of the orthorhombic phase is inconclusive due to the narrow region of phase space in which the purported O phase appears and the negligible difference in lattice parameter of the surrounding rhombohedral and tetragonal phases. Moreover, a region of R + T phase coexistence has been reported by experiments based on temperature-dependent dielectric permittivity and XRD measurements [10], micro-Raman scattering [11], CBED [12], and high-resolution XRD and Rietveld analysis [13].

* Corresponding author.
E-mail address: catherine.bishop@canterbury.ac.nz (C.M. Bishop).

https://doi.org/10.1016/j.actamat.2018.10.041
1359-6454/

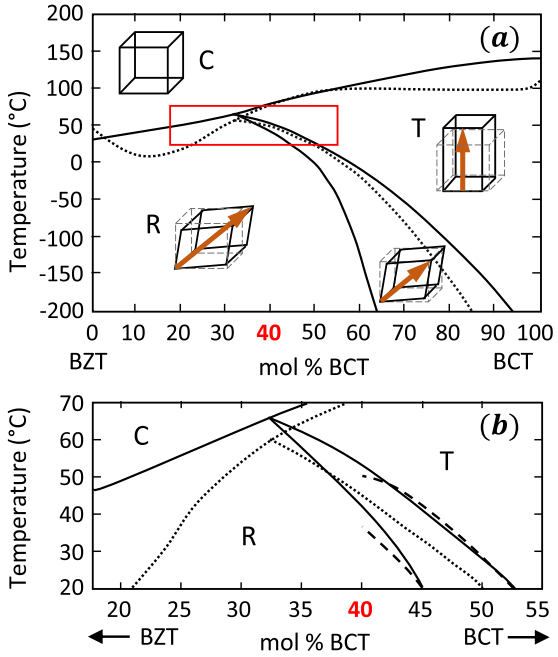

Fig. 1. (a) BZT-*x*BCT pseudo-binary phase diagram, and (b) region of interest. Dotted lines correspond to single PPB between R and T phases, as reported by Liu and Ren [6]. Continuous lines indicate a purported O phase between the R and T phases (or the region of R + T coexistence), as reported by Keeble et al. [7]. Dashed lines are detailed phase boundaries depicted in region of interest, according to Ehmke [49].

The identification of three FE phases, R, O and T, would imply the existence of two PPBs in the system as opposed to one, see Fig. 1. Nevertheless, the presence of any one PPB is the origin of enhanced material properties [5], commonly associated with free energy flattening and low polarization anisotropy [14–16]. The latter results in minimal domain wall energy that causes miniaturization of the domain structure near the interferroelectric phase boundaries [17], and facilitates polarization rotation/extension [18]. Even though beyond the scope of this work, it should be noted that the classic Gibbs phase rule is violated for R + O + T + C coexistence, as proposed by Keeble et al. [7] and indicated on Fig. 1 at the intersection of the two PPBs.

Theoretical work on ferroelectrics includes first-principles [19–24], atomic-level [25–30], and phase field modelling and simulations [14–16,31–44]. First-principles approaches are typically based on density functional theory [19], and have been successfully used to determine intrinsic material properties [19,20], as well as to study domain walls [21] and domain patterns in nanowires [22], ultrathin films [23] and single-crystals [24]. Shell model molecular dynamics have been used to investigate domain nucleation and switching dynamics in single-crystals [25], size and strain effects on electric field-induced domain evolution in ultrathin films [28], and energetics of surfaces and domain walls [29]. Further, molecular dynamics simulations based on effective Hamiltonians have been employed to investigate the mechanisms of polarization switching [27]. Nanoscale domain configurations and their evolution have also been studied by combining the shell model and the atomic-scale finite element method to improve computational performance [30].

Phase field formulations are traditionally built upon the Landau-Devonshire thermodynamic potential to describe the paraelectric-ferroelectric phase transition, and a polarization gradient energy penalty to account for domain walls [31]. Phase field descriptions have been extensively used for single-phase ferroelectrics to investigate microstructural evolution and domain configurations in single-crystals [32–37], polycrystals [38,39], as well as in thin films [40,41]. For the region near the interferroelectric phase boundary, phenomenological approaches commonly split the Landau coefficients into isotropic and anisotropic contributions to facilitate the thermodynamic analysis [14–16]. Structure symmetry is determined by identifying the easy polarization directions [15]. Landau coefficients are commonly fitted to experimental data of specific FE phases, and the accuracy of predicted properties is limited near interferroelectric transitions and bulk phases, *e.g.*, [45–47].

In spite of the great progress, the thermodynamic state and the material properties in the vicinity of the interferroelectric phase boundary remain under considerable debate [14]. Existing approaches cannot assess directly the impact of the transformation dynamics of multiple coexisting FE phases. This limitation can be overcome by considering the homogeneous free energy density of multiple coexisting FE phases separately [48], each with independent Landau coefficients obtained from experimental data for the respective phase. In this paper, a new theory based on a multiphase field formulation is proposed to consider the thermodynamics of the two neighbouring phases. The model is applied to the BZT-40BCT system to demonstrate the mechanisms controlling the stabilization of the apparent O phase in the vicinity of the T-R phase boundary and to elucidate the driving forces that determine their long term dynamics.

2. Theoretical framework

We define the total Helmholtz free energy of a strain-free, two-phase FE system, where a polymorphic phase transition occurs at $T = T_{PPB}$ for a specific composition, as

$$F[\vec{P},\phi;\vec{E},T] = \int_V \left\{ f(\vec{P},\phi;\vec{E},T) + \frac{1}{2}\sum_{k,l=1}^{3}\sum_{i,j=1}^{3} K_{ijkl}\frac{\partial P_k}{\partial x_i}\frac{\partial P_l}{\partial x_j} + \frac{1}{2}\sum_{i,j=1}^{3} K_{ij}\frac{\partial \phi}{\partial x_i}\frac{\partial \phi}{\partial x_j} \right\} dV \quad (1)$$

where T is the temperature of interest, $\vec{P}$ is the polarization, $\vec{E}$ is the electric field, and ϕ is a phase field variable that specifies the region in space where each FE phase is locally stable. We set $\phi = 0$ as the low-temperature phase and $\phi = 1$ as the high-temperature phase. The first term on the right side of Equation (1) is the volumetric free energy density of the FE system, a continuous function of the controlling variables at the temperature of interest. The second term is the gradient energy penalty to create a domain wall (a polarization domain interface). K_{ijkl} is the *ijkl*-th gradient energy coefficient contribution for a polarization domain wall. The third term is the phase gradient energy penalty to create an interface between two phases. K_{ij} is the *ij*-th gradient energy coefficient contribution for a phase boundary.

The volumetric free energy density of the system is defined as

$$f(\vec{P},\phi;\vec{E},T) = f_0(\vec{P};\vec{E},T)[1-h(\phi)] + f_1(\vec{P};\vec{E},T)h(\phi) + Wg(\phi) \quad (2)$$

where $h(\phi) = \phi^3(6\phi^2 - 15\phi + 10)$ is a function that interpolates between the free energy densities of the two phases, f_0 and f_1; and $g(\phi) = \phi^2(1-\phi)^2$ is a double-well potential that prevents unphysical phase transitions, see *e.g.*, [50].

For each phase, the volumetric free energy density is described by the Helmholtz thermodynamic potential, A, (a Landau-Devonshire potential) with respect to the cubic paraelectric phase, *i.e.*, [51]

$$A\left(\vec{P};\vec{E},T\right)=A\left(\vec{0};\vec{0},T\right)+\frac{1}{2}\alpha_i P_i^2+\frac{1}{4}\alpha_{ij}P_i^2P_j^2+\frac{1}{6}\alpha_{ijk}P_i^2P_j^2P_k^2-P_iE_i \quad (3)$$

where P_i is the ith polarization component (with $i,j,k=1,2,3$), and α_i, α_{ij}, and α_{ijk} are the Landau coefficients. The leading coefficient is $\alpha_i=a_{CW}(T-T_{CW})$, where T_{CW} is the Curie-Weiss temperature and $a_{CW}>0$ [51].

The free energy density is defined herein as $f(\vec{P};\vec{E},T)=A(\vec{P};\vec{E},T)-A(\vec{0};\vec{0},T_{CW,1})$, where $A(\vec{0};\vec{0},T_{CW,1})$ is the Helmholtz free energy of the reference state. Thus,

$$f_1\left(\vec{P};\vec{E},T\right)=\frac{1}{2}\alpha_{i,1}(T)P_i^2+\frac{1}{4}\alpha_{ij,1}P_i^2P_j^2+\frac{1}{6}\alpha_{ijk,1}P_i^2P_j^2P_k^2-P_iE_i \quad (4)$$

$$f_0\left(\vec{P};\vec{E},T\right)=\frac{1}{2}\alpha_{i,0}(T)P_i^2+\frac{1}{4}\alpha_{ij,0}P_i^2P_j^2+\frac{1}{6}\alpha_{ijk,0}P_i^2P_j^2P_k^2-P_iE_i+\Delta f_{PPB} \quad (5)$$

For a first order interferroelectric phase transition [14], $\Delta f_{PPB}=A_1(\vec{P}_{s1};\vec{0},T_{PPB})-A_0(\vec{P}_{s0};\vec{0},T_{PPB})$, where $\vec{P}_{s1}$ is the spontaneous polarization of the high-temperature phase and $\vec{P}_{s0}$ is the spontaneous polarization of the low-temperature phase.

The proposed model is reference frame invariant and can be readily extended to describe polycrystalline systems, see *e.g.*, [39]. The model can also be adapted to include strain effects, see *e.g.*, [40]; and charged defects, see *e.g.*, [52].

Overall, the formulation naturally captures the structural R↔T phase transformation energetics, polarization energetics, and polarization-structural phase transformation interactions. Further, the coexistence and stability of phases near the PPB depend on the order of the two paraelectric-ferroelectric (P-FE) transitions, independently described by the free energy density of the individual FE phases with their own Landau coefficients, Fig. 2.

Fig. 2 predicts a thermal upper limit for the metastable coexistence of the two FE phases. Its extent is a function of the underlying Landau coefficients. When both FE phases display the possibility of a second order P-FE transition, the paraelectric phase is always unstable within the PPB region where the FE phases coexist, Fig. 2(a). However, if one of the phases presents a first order P-FE transition, the paraelectric phase will be metastable for temperatures as low as $T=T_{CW}$, Fig. 2(b)-(d), allowing the possibility of metastable coexistence of the FE and C phases, which enables polarization switching mechanisms that have been associated with the enhancement of electromechanical properties [3,18]. For the BZT-xBCT system, coexistence of the R and T ferroelectric phases and the cubic paraelectric phase has been experimentally reported [10].

3. Application to one-dimensional BZT-xBCT

For a system that undergoes polarization switching events along one direction, say $\hat{\imath}$, with an electric field applied along the same direction, we define $\vec{P}=P\hat{\imath}$ and $\vec{E}=E\hat{\imath}=-\partial V_E/\partial x$, where V_E is the electrostatic potential [53]. The polarization switching dynamics are described by two coupled Allen-Cahn equations,

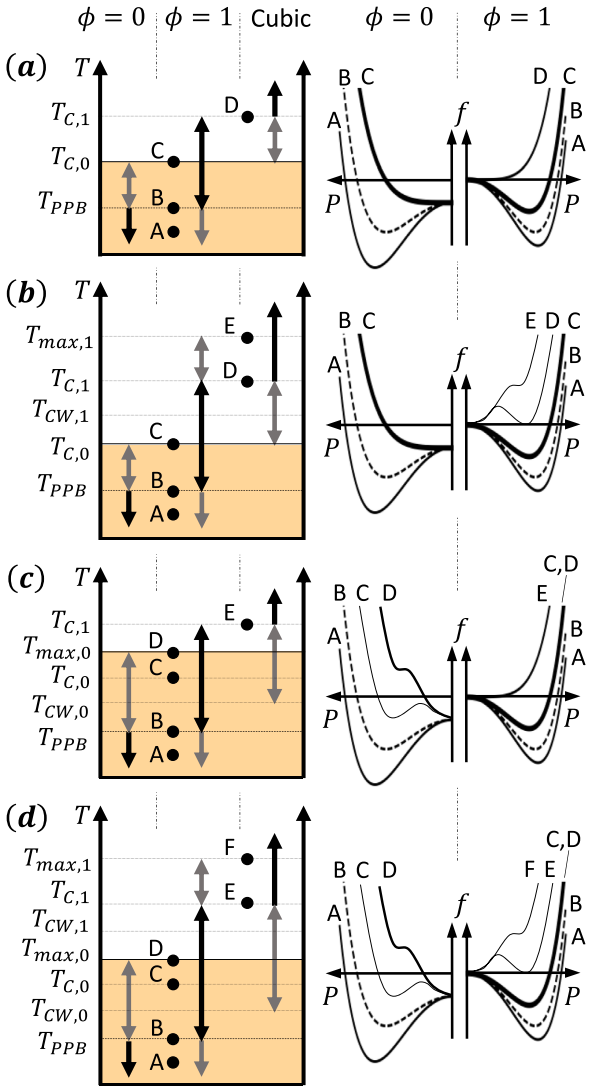

Fig. 2. Phase coexistence and stability as a function of P-FE phase transition. Two FE phases are shown: a low-temperature FE phase ($\phi=0$) and a high-temperature FE phase ($\phi=1$). Subfigures show (a) second order–second order, (b) second order–first order, (c) first order–second order, and (d) first order–first order interactions. Highlighted area indicates metastable coexistence of the FE phases accessible upon heating or cooling. Free energy curves are sketched on the right for selected temperatures.

$$\frac{\partial P}{\partial t}=-M_P\left\{\frac{\partial f_0(P;T)}{\partial P}[1-h(\phi)]+\frac{\partial f_1(P;T)}{\partial P}h(\phi)+\frac{\partial V_E}{\partial x}-K_P\frac{\partial^2 P}{\partial x^2}\right\} \quad (6)$$

$$\frac{\partial \phi}{\partial t}=-M_\phi\left\{[f_1(P;T)-f_0(P;T)]\frac{\mathrm{d}h(\phi)}{\mathrm{d}\phi}+W\frac{\mathrm{d}g(\phi)}{\mathrm{d}\phi}-K_\phi\frac{\partial^2\phi}{\partial x^2}\right\} \quad (7)$$

where $K_P=K_{1111}$, $K_\phi=K_{11}$, M_P is the polarization mobility, and M_ϕ is the phase mobility. We set $M_P=M_\phi=M(\phi;T)=M_0(T)[1-h(\phi)]+M_1(T)h(\phi)$, with the mobility of each phase given by $M(T)=M_o\exp(-Q/RT)$.

The electrostatic field distribution is given by Coulomb's Equation in its differential form, $\partial D/\partial x = 0$. The electric displacement is related to the total polarization via the constitutive relation $D = \varepsilon_o E + P$, where ε_o is the vacuum permittivity [53]. Therefore,

$$-\varepsilon_o \frac{\partial^2 V_E}{\partial x^2} + \frac{\partial P}{\partial x} = 0 \tag{8}$$

The model is normalized using $\hat{x} = x/L$, $\hat{t} = t/\tau$, $u = P/|P_{s1}|$, and $\hat{E} = E/|E_{c1}|$, where L is the size of the bulk sample, E_{c1} is the coercive field of the high-temperature phase, and $\tau = 1/(\alpha_{111,1} P_{s1}^4 M_1(T))$. Thus, Equation (6) through (8) are cast in dimensionless form as

$$\frac{1}{\mu}\frac{\partial u}{\partial \hat{t}} = \gamma \hat{\nabla}^2 u - \left\{ \frac{\partial \hat{f}_0(u;T)}{\partial u}[1 - h(\phi)] + \frac{\partial \hat{f}_1(u;T)}{\partial u} h(\phi) + \hat{E}_{c1}\frac{\partial \hat{V}_E}{\partial \hat{x}} \right\} \tag{9}$$

$$\frac{1}{\nu}\frac{\partial \phi}{\partial \hat{t}} = \gamma \lambda \hat{\nabla}^2 \phi - \left\{ [\hat{f}_1(u;T) - \hat{f}_0(u;T)]\frac{\mathrm{d}h(\phi)}{\mathrm{d}\phi} + \widehat{W}\frac{\mathrm{d}g(\phi)}{\mathrm{d}\phi} \right\} \tag{10}$$

$$0 = -\hat{\varepsilon}_o \frac{\partial^2 \hat{V}_E}{\partial \hat{x}^2} + \frac{\partial u}{\partial \hat{x}} \tag{11}$$

where the following dimensionless parameters are identified: $\mu = M(\phi;T)/M_1(T)$, $\nu = P_{s1}^2 \mu$, $\gamma = K_P/(L^2 \alpha_{111,1} P_{s1}^4)$, $\lambda = K_\phi/(K_P P_{s1}^2)$, $\widehat{W} = W/(\alpha_{111,1} P_{s1}^6)$, $\hat{E}_{c1} = E_{c1}/(\alpha_{111,1} P_{s1}^5)$, and $\hat{\varepsilon}_o = \varepsilon_o E_{c1}/P_{s1}$.

Further, $\hat{f}_0(u;T)$ and $\hat{f}_1(u;T)$ are given by

$$\hat{f}_1(u;T) = \frac{1}{6}u^6 + \frac{B_1 - 1}{4}u^4 - \frac{B_1}{2}u^2 \tag{12}$$

$$\hat{f}_0(u;T) = \rho\left[\frac{1}{6}u^6 + \frac{B_0 - \eta^2}{4}u^4 - \frac{B_0 \eta^2}{2}u^2\right] + \Delta\hat{f}_{PPB} \tag{13}$$

where $B_1 = 1 + \alpha_{11,1}/(\alpha_{111,1} P_{s1}^2)$, $B_0 = \eta^2 + \alpha_{11,0}/(\alpha_{111,0} P_{s1}^2)$, $\eta = P_{s0}/P_{s1}$, $\rho = \alpha_{111,0}/\alpha_{111,1}$, and $\Delta\hat{f}_{PPB} = \Delta f_{PPB}/(\alpha_{111,1} P_{s1}^6)$. In this model, the order of the P-FE phase transitions depends on the values of B_1, B_0 and η.

Values for the microstructurally averaged Landau coefficients are determined from experimental hysteresis loops for polycrystalline BZT-40BCT ceramics, measured at selected temperatures by Ehmke [49]. While the approach presented herein can be readily extended to estimate the Landau parameters for a single-crystal BZT-40BCT sample, such information was unavailable [54]. The equation $\partial f/\partial P = E = \alpha_1 P + \alpha_{11} P^3 + \alpha_{111} P^5$ is fitted to the stable and metastable parts of the hysteresis loops for the unambiguously rhombohedral and tetragonal regions of the phase diagram, see Appendix A for details. Mobilities are calculated directly from the BZT-40BCT data at each temperature using $M = 2\pi\omega\chi_c\varepsilon_o\sqrt{(E_o/E_c)^2 - 1}$, [55], where $\omega = 0.1$ Hz is the experimental cycling frequency and $E_o = 1$ MV/m is the maximum applied field. Fitted parameters are summarized in Table 1. Mobility values have the same order of magnitude as those reported by Zhao, Cao and García [55] for stress-free, lanthanum-doped PZT.

The PPB temperature is estimated as $T_{PPB} \sim (T_{O-T} + T_{R-O})/2 = 43\,^\circ$C, using $T_{R-O} = 37\,^\circ$C and $T_{O-T} = 49\,^\circ$C, as reported by Ehmke [49]. The estimated T_{PPB} is approximately equal to the value determined by Liu and Ren [6], Fig. 1(b). The dimensionless gradient energy coefficients, $\gamma = 3 \times 10^{-5}$ and $\lambda = 5.5$, and the double-well coefficient, $\widehat{W} = 4$, are established via numerical evaluation such that the widths of the rhombohedral domain wall and the phase interfaces measured in ϕ are approximately equal at $T = T_{PPB}$, the only temperature where both phases are stable. In qualitative agreement with Jona and Shirane [56], the width (ξ) of the rhombohedral domain walls is set to 4 nm, *i.e.,* ten times the characteristic lattice parameter. The size of the bulk sample was found to be $L = 190$ nm, which is smaller than typical grain sizes of 27±3 μm for BZT-40BCT [49]. The estimated values for the gradient energy coefficients and the interfacial widths and energies of domain walls, ξ_{DW} and σ_{DW}, and T-R interfaces, ξ_{T-R} and σ_{T-R}, are included in Table 1.[1]

Table 1
Fitted Landau coefficients and mobilities for BZT-40BCT, after experimental data reported by Ehmke [49], and estimated gradient energy coefficients and interfacial widths and energies calculated at $T = T_{PPB} = 43\,^\circ$C.

Symbol	R phase ($\phi = 0$)	T phase ($\phi = 1$)	Units
a_{CW}	5.000×10^4	2.063×10^4	Jm/C^{2}K
α_{11}	6.314×10^7	-4.229×10^7	Jm^5/C^4
α_{111}	1.263×10^{10}	3.154×10^{10}	Jm^9/C^6
T_{CW}	49.90	69.08	$^\circ$C
T_C	$T_{CW,0}$	69.60	$^\circ$C
T_{max}	$T_{CW,0}$	69.77	$^\circ$C
M_o	1.809×10^{-4}	3.806×10^{-10}	S/m
Q	8561	−25260	J/mol
K_P	8.922×10^{-13}	8.922×10^{-13}	Jm^3/C^2
K_ϕ	2.383×10^{-14}	2.383×10^{-14}	J/m
σ_{DW}	1.876×10^{-6}	4.063×10^{-6}	J/m^2
σ_{T-R}	4.445×10^{-6}	4.445×10^{-6}	J/m^2
ξ_{DW}	4.000	2.867	nm
ξ_{T-R}	2.834	2.834	nm

For BZT-40BCT, with the Landau coefficients stated in Table 1, the T phase has a weak first order P-FE transition and the R phase has a second order P-FE transition, *i.e.,* the case illustrated in Fig. 2(a). The predicted upper limit for metastable coexistence between the R and T phases is $T_{C,0} = 49.9\,^\circ$C, which is approximately equal to $T_{O-T} \sim 49\,^\circ$C, as determined by Ehmke [49], see Fig. 1(b). This supports the hypothesis of R + T phase coexistence near the PPB, based on data acquired in the unambiguously single phase regions. Interfacial energies are in agreement with Gao et al. [17] and Damjanovic [18].

Fig. 3 shows contour plots of the volumetric free energy density of the system at different temperatures and normalized polarization states. In all cases, $u = \pm 1$ is the dimensionless spontaneous polarization of the T phase and $u = \pm\eta$ is the dimensionless spontaneous polarization of the R phase at each temperature. For $\hat{E} = 0$, the global minima in the bulk free energy of the system are located at $u = \pm 1, \phi = 1$, for $T > T_{PPB}$; and at $u = \pm\eta, \phi = 0$, for $T < T_{PPB}$. Results show that direct R↔T transformation between domains with opposing polarization states is inaccessible because of the large energy barrier between antiparallel polarization states. Instead, this transformation is achieved by a combination of 180° polarization reversals and R↔T reversible transformations, *i.e.,* polarization rotations, thus defining a mechanism for switching and ferroelectric domain coexistence in the vicinity of the PPB.

For $T < T_{PPB}$, the T phase is metastable, see Fig. 3(a). Thus, both T and R phases coexist through formation of domains of opposite polarization and a weak intervening built-in electric field. Energy

[1] Each interfacial energy is calculated via numerical evaluation of $\sigma = \int_0^L [f_{total}(x) - f_{min}]dx$ across a computational domain with a single interface, where f_{total} is the total free energy density and f_{min} is the volumetric free energy density corresponding to the stable polarization state(s).

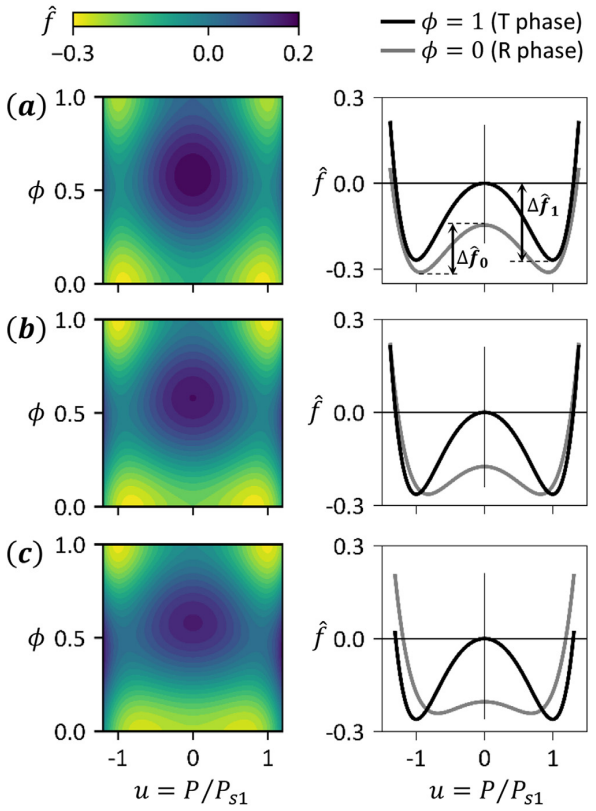

Fig. 3. Left column: contour plots of the volumetric free energy density, $\hat{f}(u, \phi; \hat{E} = 0, T) = f/(\alpha_{111,1} P_{s1}^6)$. Right column: volumetic free energy density of R (——) and T (▬▬) phases. Subfigures correspond to (a) $T = 39^\circ$C, (b) $T = T_{PPB} = 43^\circ$C, and (c) $T = 46^\circ$C. In the absence of an applied electric field, both FE phases are equally stable at $T = T_{PPB}$, but metastably persist for a finite range of temperatures away from the PPB line on the phase diagram.

barriers for polarization switching are different in each phase; for example, at $T = 39^\circ$C the energy barrier between $u = \pm 1$ in the T phase, $\Delta\hat{f}_1$, is 1.6 times larger than the energy barrier between $u = \pm\eta$ in the R phase, $\Delta\hat{f}_0$. Consequently, switching between rhombohedral domains is possible through two mechanisms, namely: a) via direct 180° polarization reversals; or b) by performing a R→T transformation (rotation), followed by a 180° reversal while in the tetragonal phase, and finally by transforming back to the rhombohedral phase (rotation), *i.e.,* T→R. The second mechanism favours rotation of the polarization order parameter, but requires the thermal energy of the system to be greater than both $\Delta\hat{f}_1$ and the R→T energy of transformation in order to be accessible.

For $T = T_{PPB}$, four thermodynamic equilibrium states are available, see Fig. 3(b). The existence of additional polarization directions results in a decrease in polarization anisotropy. At the PPB, the domain switching mechanisms described for the R phase at $T < T_{PPB}$ are possible for both phases, *i.e.,* direct 180° polarization reversal or phase transformations plus 180° reversal (polarization rotation mechanism). As temperature increases, the energy barrier in the R phase decreases such that $\Delta\hat{f}_0 \approx \Delta\hat{f}_1/3$, favouring the formation of rhombohedral domain walls via the direct 180° reversal mechanism. Since $\Delta\hat{f}_1$ and the T→R energy of transformation are equivalent, the likelihood of observing tetragonal domain walls and T→R transformations is equal. Further, while the polarization rotation mechanism can occur in both phases, the decrease in $\Delta\hat{f}_0$ favours this mechanism in the T phase.

For $T > T_{PPB}$, the R phase becomes metastable, Fig. 3(c), and the energy barrier of the R phase further decreases such that $\Delta\hat{f}_0 \approx \Delta\hat{f}_1/7$ at $T = 46^\circ$C. Here, the additional thermal energy and the low energy barrier will enable the polarization switching plus rotation mechanism proposed herein, allowing the R phase to persist for very long periods of time.

4. Numerical implementation

The multiphase field model was implemented using FEM in COMSOL Multiphysics® [57]. A 200-element mesh with second-order Lagrange shape functions was used. Simulations took on the order of 25 s in an i7-6700 3.4 GHz Quad Core 64 bit processor, with 16 GB of RAM and a Microsoft Windows 7 Enterprise operating system version 6.1.7601.

Hysteretic cycling of BZT-40BCT was simulated at $T = 40.2^\circ$C to validate the model. Equation (9) through (11) were solved with a mixed 50%R + 50%T initial state. A time-dependent electric field was applied through the boundary conditions $\hat{V}_E(0, \hat{t}) = 0$ and $\hat{V}_E(1, \hat{t}) = \hat{V}_{E,max}\sin(2\pi\hat{\omega}\hat{t})$, where $\hat{V}_{E,max} = -E_o/E_{c1}$ and $\hat{\omega} = \omega\tau$. Zero flux boundary conditions were applied for polarization and for phase field.

The field-free microstructural evolution was simulated at $T = T_{PPB}$ to investigate the phase coexistence of FE phases. Equations (9) and (10) were solved with initial conditions generated from a uniform random distribution, with {mean, range}, for u {0, 2} and ϕ {0.5, 1}. Periodic boundary conditions were applied for both variables (polarization and phase field).

A time-temperature-transformation (TTT) diagram was constructed for the microstructural evolution of the two-phase ferroelectric towards a stable single phase. The fraction transformed of FE phases was measured by ψ, where $\psi = \bar{\phi}$ at $T > T_{PPB}$, and $\psi = 1 - \bar{\phi}$ at $T < T_{PPB}$. Average transformation times for constant fraction transformed were calculated from fifteen computational simulations at selected temperatures. The Johnson-Mehl-Avrami-Kolmogorov (JMAK) equation [58] was fitted to the kinetics of isothermal R + T→T and R + T→R transformations, $\psi = 1 - \exp(-kt^n)$, yielding Avrami exponents $0.29 \leq n \leq 0.55$.

5. Results and discussion

The model was directly compared against polycrystalline experimental data, as reported by Ehmke [49] for $T = 40.2^\circ\text{C} < T_{PPB}$ and $\omega = 0.1$ Hz, Fig. 4(a). Very good agreement was found between experiments and the numerical results. Differences near the tails of the hysteresis loops are a result of the slow polarization switching of the last set of domains pinned by grain boundaries, as discussed by Zhao, Bowman and García [59]. Additional comparisons can be found in Figure S2, see Appendix A. Further, Fig. 4(b) shows that the application of a cyclic electric field accelerates the R + T→R transformation, measured by the average phase field $\bar{\phi}$, when $\hat{E} \neq 0$.

In a 1D system, the spatial distribution of polarization u is dominated by Coulomb's Equation where $\partial u/\partial\hat{x} \approx 0$. This forces a uniform polarization configuration over the entire system, Fig. 4(c)-(e). In 2D and 3D systems, polarization configuration enables access to additional degrees of freedom and will be the subject of future work.

For $T = T_{PPB}$, Fig. 5 shows that rhombohedral and tetragonal domains stably coexist. The average domain size of 20 nm, within the 10 – 60 nm range as reported by Acosta et al. [4], is consistent with miniaturization of the domain structure associated with the decrease in polarization anisotropy [17] and interfacial energy [51] in the vicinity of the PPB. In the absence of an applied electric field, Fig. 5 demonstrates that the low energy barrier between variants in

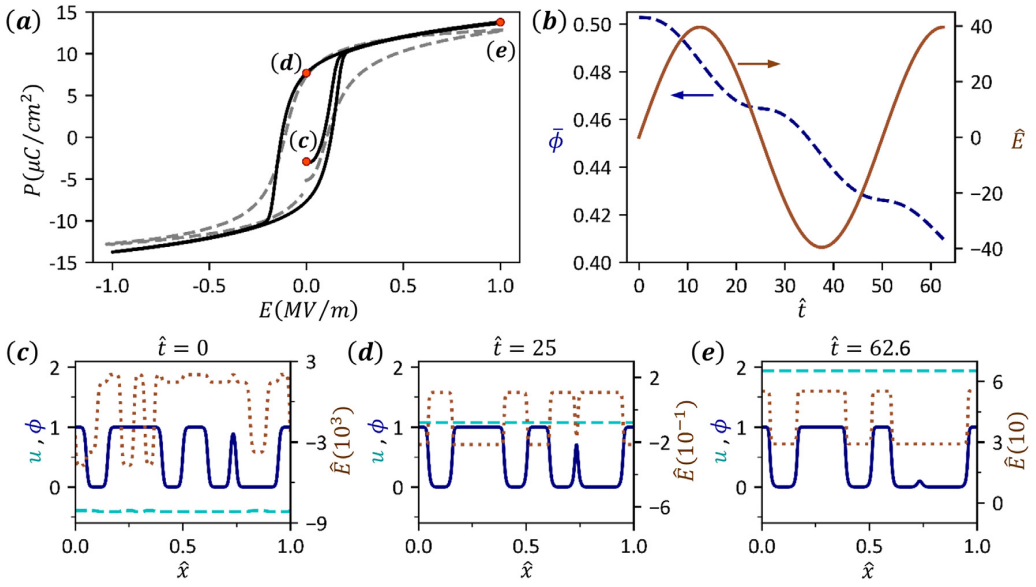

Fig. 4. (a) Experimental [49] (- - -) and calculated (——) hysteresis loops at $T = 40.2^{\circ}$C with $\omega = 0.1$ Hz and mixed 50%R + 50%T initial condition. (b) Effect of sinusoidal electric field (——) on the average phase field, $\bar{\phi}$ (- - -). Insets (c) through (e) show the spatial distributions of $u = P/P_{s1}$ (- - -, left axis), ϕ (——, left axis), and $\hat{E} = E/E_{c1}$ (·····, right axis) at selected normalized instants $\hat{t} = t/\tau$. Inset (c) shows initial condition ($t = 0$), (d) shows $\hat{t} = 25$ ($t = 5$ s), and (e) shows $\hat{t} = 62.6$ ($t = 12.5$ s) after one full cycle.

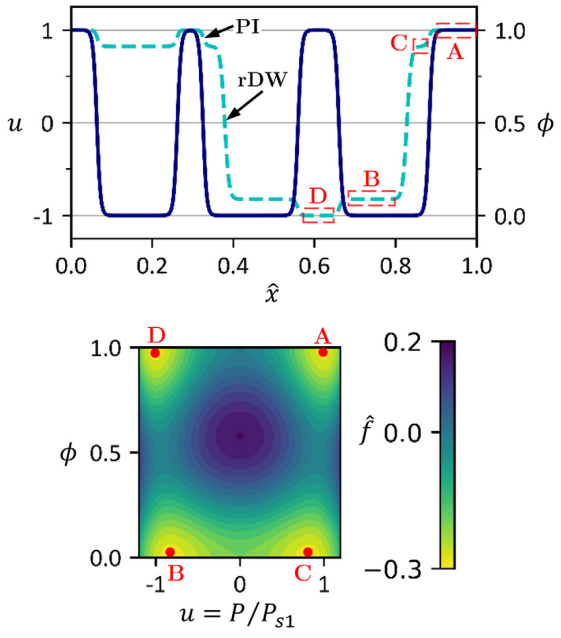

Fig. 5. Above: spatial distribution of normalized polarization, $u = P/P_{s1}$ (- - -), and phase field, ϕ (——), at dimensionless time, $\hat{t} = t/\tau = 40000$, at $T = T_{PPB} = 43^{\circ}$C. Below: contour plot of the volumetric free energy density, $\hat{f}(u, \phi; \hat{E} = 0, T) = f/(\alpha_{111,1}P_{s1}^6)$, at $T = T_{PPB} = 43^{\circ}$C. Rhombohedral domain walls (rDW) and phase interfaces (PI) are noted. A, B, C and D represent four equilibrium states. Long term coexistence of R and T phases is observed at the PPB.

the R phase facilitates the formation of rhombohedral domain walls between states B and C, and enables the polarization rotation as it transitions between states A and D. This is consistent with theoretical results reported by Yang et al. [44] that link the small energy barrier for direct 180° polarization reversal in one phase to the small energy barrier for phase transformation and polarization rotation, identified as the main origin of the enhanced electromechanical properties near the PPB in lead-free materials [43,60]. Fig. 5 also shows that R↔T transformations between domains with opposing polarization states, *e.g.,* between states A and B, occur through a phase transformation, from state A to state C, followed by a 180° polarization reversal, from state C to state B. The presence of local metastable domains, such as those reported herein, have also been simulated by Rao and Wang [42] revealing their role in reducing the total free energy of the system by bridging stable domains.

The formulation developed herein can be readily extended to 2D and include the effects of mechanical compatibility from the individual ferroelectric variants and interfaces between coexisting phases. This is the subject of future work.

Fig. 6 shows the macroscopic volume fraction transformed from a mixed 50%R + 50%T state as a function of time at fixed temperature, *i.e.,* a Time-Temperature-Transformation (TTT) diagram. Calculations show that as $T \rightarrow T_{PPB}$ both phases are more likely to coexist. For $T_{PPB} < T < T_{C,0}$, the low-temperature rhombohedral phase coexists metastably with the high-temperature, thermodynamically stable tetragonal phase as a result of the local R↔T phase transformations that are favoured to accommodate local switching events and metastable domains. In contrast, for $T < T_{PPB}$, a decrease in thermal energy suppresses phase transformations and, hence, suppresses the polarization switching plus rotation mechanism. The phase transformation and polarization reversal pathway between domains is possible at all temperatures where the two FE phases can coexist metastably $T < T_{C,0}$. It is favoured at $T > T_{PPB}$ due to the high domain wall energy of the stable phase. Further, the likelihood of observing R + T coexistence decreases with temperature as the driving force for transformation to the most stable phase increases.

The time to reach 55% transformed volume fraction is one to

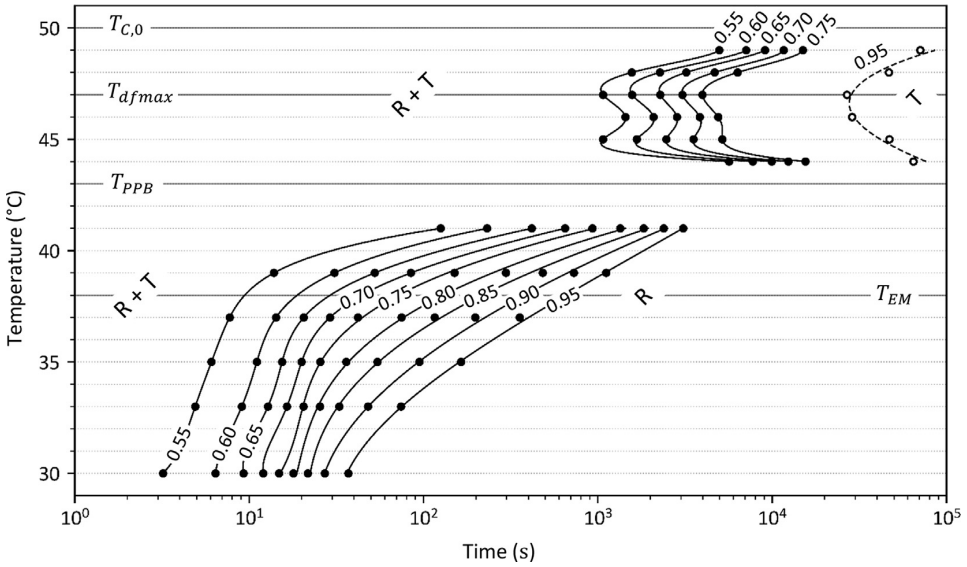

Fig. 6. TTT diagram for transformation of mixed R + T phase towards stable single phase as $\psi \rightarrow 1$, starting from $\psi = 0.5$ at $t = 0$ at each temperature. Markers represent mean times for constant fraction of phase transformation calculated from 15 computational simulations. Splines are included as a guide for the eye. Estimated times for 0.95 fraction transformed to T phase (▬ ▬ ▪) are extrapolated from a JMAK analysis at each $T > T_{PPB}$. T_{dfmax} is the temperature at which the driving force for formation of T phase is maximal, and T_{EM} corresponds to a temperature where mobilities of the FE phases are equal. Metastable coexistence persists for longer times at high temperatures compared to shorter times for R + T→R transformation at lower temperatures.

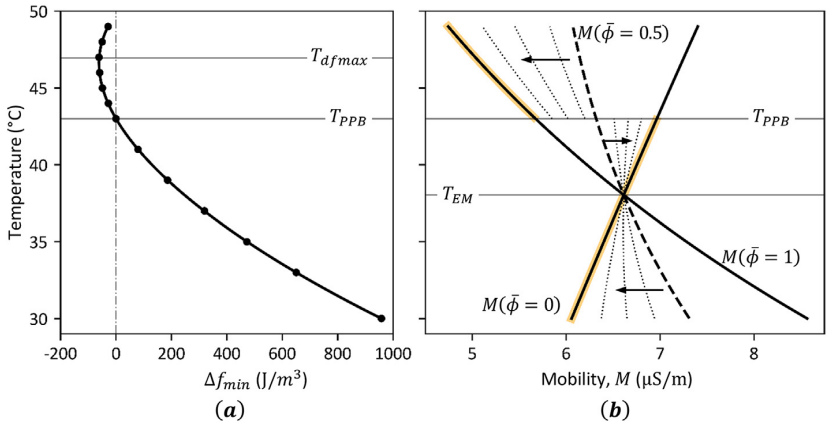

Fig. 7. (a) Thermodynamic driving force for transformation of FE phases, $\Delta f_{min} = f_1(P = P_{s1}; E = 0, T) - f_0(P = P_{s0}; E = 0, T)$, and (b) mobility as a function of temperature. There is a local maximum in driving force at T_{dfmax} for the R + T→T transformation. The mobilities of the two phases are equal at T_{EM}. Above T_{PPB} and below T_{EM}, the phase-averaged mobility decreases as $\psi \rightarrow 1$, but increases in the range $T_{EM} < T < T_{PPB}$. Metastable coexistence is expected to persist for longer times above T_{PPB} due to smaller driving force and lower mobility.

three orders of magnitude greater for $T > T_{PPB}$ because the available thermal energy enables the polarization switching of the individual phases to accommodate opposing polarization states. This favours the phase transformation-induced polarization rotation mechanism as a means to extend domain coexistence.[2]

Macroscopically, for $T < T_{PPB}$, the predicted driving force for transformation to the most stable phase is very large, providing a rationale for the rapid kinetics of phase transformation, Fig. 7(a). In addition, the phase-averaged mobility of the system increases with decreasing temperature for $\phi = 0.5$, further promoting fast phase transformation at T<T_{PPB}, Fig. 7(b). For $T_{PPB} > T > T_{EM}$, mobility increases as the transformation progresses and so does the rate of phase transformation; for $T < T_{EM}$, phase transformation kinetics are limited by the mobility of the stable R phase being the lowest of the two phases. For $T > T_{PPB}$, comparatively slow transformation kinetics correspond to a much smaller driving force for R→T transformation, which reaches a maximum at $T = T_{dfmax}$. The rate of phase transformation is again limited by the low mobility of the stable phase, in this case the T phase, with smaller values of mobility being attained than at $T < T_{PPB}$.

The coexistence time increases as $T \rightarrow T_{C,0}$ for $T_{dfmax} < T < T_{C,0}$. This is attributed to the vanishing R phase domain wall energy, σ^R_{DW}, and the vanishing macroscopic driving force, Δf_{min}, Fig. 7(a). The

[2] The large differences in coexistence time above and below $T = T_{PPB}$, suggest that the true polymorphic phase boundary temperature in the BZT-xBCT system is lower than that suggested by experiments.

first is a consequence of the second order P-FE transition that occurs for R phase at $T_{C,0}$. The second is a consequence of the fitted Landau coefficients and the selection of a constant Δf_{PPB}.

For $T > T_{C,0}$, the R phase is no longer metastable and any superheated, mixed R + T state is expected to relax to the equilibrium T phase rapidly, in agreement with the phase diagram. No simulations were carried out in this temperature range.

While the quantitative results reported in this study for BZT-40BCT might shift for different gradient energy parameters, the general conclusions would remain the same for this system. Moreover, if the low temperature phase had a first order P-FE transition, then the domain wall energy would not approach zero as temperature approached the maximum metastable coexistence temperature, in that case $T = T_{max,0}$. Thus, the coexistence time would be unlikely to increase for $T \rightarrow T_{max,0}$, as predicted for BZT-40BCT. This predicted behaviour must be explored for material chemistries exhibiting an interferroelectric transition and appropriate FE behaviours.

6. Summary and conclusions

A phase field theory for ferroelectric systems in the vicinity of the polymorphic phase boundary is proposed. Based on a multiphase field formulation, the model considers the thermodynamics of individual phases independently, in order to assess equilibrium states and phase transformation dynamics of two competing ferroelectric phases. The model was applied to the BZT-40BCT system and identifies conditions for the stable and metastable coexistence of the rhombohedral and tetragonal phases, as well as an upper limit for metastability, $T_{C,0} = 49.9^{\circ}$C. While there is no thermodynamic limit on metastability for $T < T_{PPB}$, results demonstrate that coexistence is short lived (on the order of tens of seconds), whereas coexistence persists from minutes to hours for $T > T_{PPB}$. Further, metastable coexistence of phases provides access to additional polarization directions, which enables a phase transformation-induced polarization rotation mechanism near the interferroelectric phase boundary. The proposed polarization rotation mechanism is a local intervening kinetic step that is partially responsible for the enhancement of ferroelectric properties.

Acknowledgements

This work was supported by the University of Canterbury (College of Engineering PhD Scholarship). REG thanks the Erskine Fellowship, and the partial support from NSF grant 1734763. The authors thank M. C. Ehmke and J. E. Blendell for sharing their experimental data.

Appendix A. Supplementary data

Supplementary data to this article can be found online at https://doi.org/10.1016/j.actamat.2018.10.041.

References

[1] A.J. Bell, Ferroelectrics: the role of ceramic science and engineering, J. Eur. Ceram. Soc. 28 (7) (2008) 1307–1317, https://doi.org/10.1016/j.jeurceramsoc.2007.12.014.
[2] J. Rödel, W. Jo, K.T.P. Seifert, E.-M. Anton, T. Granzow, D. Damjanovic, Perspective on the development of lead-free piezoceramics, J. Am. Ceram. Soc. 92 (6) (2009) 1153–1177, https://doi.org/10.1111/j.1551-2916.2009.03061.x.
[3] D. Damjanovic, N. Klein, J. Li, V. Porokhonskyy, What can be expected from lead-free piezoelectric materials? Funct. Mater. Lett. 3 (1) (2010) 5–13, https://doi.org/10.1142/S1793604710000919.
[4] M. Acosta, N. Novak, V. Rojas, S. Patel, R. Vaish, J. Koruza, G.A. Rossetti, J. Rödel, $BaTiO_3$-based piezoelectrics: fundamentals, current status, and perspectives, Appl. Phys. Rev. 4 (4) (2017), 041305. https://doi.org/10.1063/1.4990046.
[5] J. Gao, D. Xue, W. Liu, C. Zhou, X. Ren, Recent progress on $BaTiO_3$-based piezoelectric ceramics for actuator applications, Actuators 6 (3) (2017) 24, https://doi.org/10.3390/act6030024.
[6] W. Liu, X. Ren, Large piezoelectric effect in Pb-free ceramics, Phys. Rev. Lett. 103 (25) (2009) 257602, https://doi.org/10.1103/PhysRevLett.103.257602.
[7] D.S. Keeble, F. Benabdallah, P.A. Thomas, M. Maglione, J. Kreisel, Revised structural phase diagram of $(Ba_{0.7}Ca_{0.3}TiO_3)$-$(BaZr_{0.2}Ti_{0.8}O_3)$, Appl. Phys. Lett. 102 (9) (2013), 092903, https://doi.org/10.1063/1.4793400.
[8] L. Zhang, M. Zhang, L. Wang, C. Zhou, Z. Zhang, Y.G. Yao, L.X. Zhang, D.Z. Xue, X.J. Lou, X.B. Ren, Phase transitions and the piezoelectricity around morphotropic phase boundary in $Ba(Zr_{0.2}Ti_{0.8})O_3$-$x(Ba_{0.7}Ca_{0.3})TiO_3$ lead-free solid solution, Appl. Phys. Lett. 105 (16) (2014) 162908, https://doi.org/10.1063/1.4899125.
[9] D. Damjanovic, A. Biancoli, L. Batooli, A. Vahabzadeh, J. Trodahl, Elastic, dielectric, and piezoelectric anomalies and Raman spectroscopy of $0.5Ba(Ti_{0.8}Zr_{0.2})O_3$-$0.5(Ba_{0.7}Ca_{0.3})TiO_3$, Appl. Phys. Lett. 100 (19) (2012) 192907, https://doi.org/10.1063/1.4714703.
[10] M.C. Ehmke, S.N. Ehrlich, J.E. Blendell, K.J. Bowman, Phase coexistence and ferroelastic texture in high strain $(1-x)Ba(Zr_{0.2}Ti_{0.8})O_3$-$x(Ba_{0.7}Ca_{0.3})TiO_3$ piezoceramics, J. Appl. Phys. 111 (12) (2012) 124110, https://doi.org/10.1063/1.4730342.
[11] G. Singh, V. Sathe, V.S. Tiwari, Investigation of rhombohedral-to-tetragonal phase transition in $0.5Ba(Ti_{0.8}Zr_{0.2})$-$0.5(Ba_{0.7}Ca_{0.3})TiO_3$ lead-free ferroelectric using micro-Raman scattering, J. Electron. Mater. 46 (8) (2017) 4976–4980, https://doi.org/10.1007/s11664-017-5512-y.
[12] J.H. Gao, L.X. Zhang, D.Z. Xue, T. Kimoto, M.H. Song, L.S. Zhong, X.B. Ren, Symmetry determination on Pb-free piezoceramic $0.5Ba(Zr_{0.2}Ti_{0.8})O_3$-$0.5(Ba_{0.7}Ca_{0.3})TiO_3$ using convergent beam electron diffraction method, J. Appl. Phys. 115 (5) (2014), 054108, https://doi.org/10.1063/1.4864130.
[13] A.B. Haugen, J.S. Forrester, D. Damjanovic, B.Z. Li, K.J. Bowman, J.L. Jones, Structure and phase transitions in $0.5(Ba_{0.7}Ca_{0.3}TiO_3)$-$0.5(BaZr_{0.2}Ti_{0.8}O_3)$ from -100 °C to 150 °C, J. Appl. Phys. 113 (1) (2013), 014103, https://doi.org/10.1063/1.4772741.
[14] A.A. Heitmann, G.A. Rossetti, Thermodynamics of ferroelectric solid solutions with morphotropic phase boundaries, J. Am. Ceram. Soc. 97 (6) (2014) 1661–1685, https://doi.org/10.1111/jace.12979.
[15] G.A. Rossetti Jr., A.G. Khachaturyan, G. Akcay, Y. Ni, Ferroelectric solid solutions with morphotropic boundaries: vanishing polarization anisotropy, adaptive, polar glass, and two-phase states, J. Appl. Phys. 103 (11) (2008) 114113, https://doi.org/10.1063/1.2930883.
[16] M. Acosta, N. Khakpash, T. Someya, N. Novak, W. Jo, H. Nagata, G.A. Rossetti, J. Rödel, Origin of the large piezoelectric activity in $(1-x)Ba(Zr_{0.2}Ti_{0.8})O_3$-$x(Ba_{0.7}Ca_{0.3})TiO_3$ ceramics, Phys. Rev. B 91 (10) (2015) 104108, https://doi.org/10.1103/PhysRevB.91.104108.
[17] J.H. Gao, X.H. Hu, Y.B. Liu, Y. Wang, X.Q. Ke, D. Wang, L.S. Zhong, X.B. Ren, Ferroelectric domain walls approaching morphotropic phase boundary, J. Phys. Chem. C 121 (4) (2017) 2243–2250, https://doi.org/10.1021/acs.jpcc.6b11595.
[18] D. Damjanovic, A morphotropic phase boundary system based on polarization rotation and polarization extension, Appl. Phys. Lett. 97 (6) (2010), 062906, https://doi.org/10.1063/1.3479479.
[19] R. Cohen, Theory of ferroelectrics: a vision for the next decade and beyond, J. Phys. Chem. Solids 61 (2) (2000) 139–146, https://doi.org/10.1016/S0022-3697(99)00272-3.
[20] B. Völker, P. Marton, C. Elsässer, M. Kamlah, Multiscale modeling for ferroelectric materials: a transition from the atomic level to phase-field modeling, Continuum Mech. Therm. 23 (5) (2011) 435–451, https://doi.org/10.1007/s00161-011-0188-7.
[21] B. Meyer, D. Vanderbilt, *Ab Initio* study of ferroelectric domain walls in $PbTiO_3$, Phys. Rev. B 65 (10) (2002) 104111, https://doi.org/10.1103/PhysRevB.65.104111.
[22] G. Pilania, R. Ramprasad, Complex polarization ordering in $PbTiO_3$ nanowires: a first-principles computational study, Phys. Rev. B 82 (15) (2010) 155442, https://doi.org/10.1103/PhysRevB.82.155442.
[23] T. Shimada, S. Tomoda, T. Kitamura, *Ab Initio* study of ferroelectric closure domains in ultrathin $PbTiO_3$ films, Phys. Rev. B 81 (14) (2010) 144116, https://doi.org/10.1103/PhysRevB.81.144116.
[24] A. Grünebohm, M.E. Gruner, P. Entel, Domain structure in the tetragonal phase of $BaTiO_3$ - from bulk to nanoparticles, Ferroelectrics 426 (1) (2012) 21–30, https://doi.org/10.1080/00150193.2012.671090.
[25] V. Boddu, F. Endres, P. Steinmann, Molecular dynamics study of ferroelectric domain nucleation and domain switching dynamics, Sci. Rep. 7 (1) (2017) 806, https://doi.org/10.1038/s41598-017-01002-0.
[26] M. Sepliarsky, A. Asthagiri, S. Phillpot, M. Stachiotti, R. Migoni, Atomic-level simulation of ferroelectricity in oxide materials, Curr. Opin. Solid State Mater. Sci. 9 (3) (2005) 107–113, https://doi.org/10.1016/j.cossms.2006.05.002.
[27] J. Paul, T. Nishimatsu, Y. Kawazoe, U.V. Waghmare, Polarization rotation, switching, and electric-field–temperature phase diagrams of ferroelectric $BaTiO_3$: a molecular dynamics study, Phys. Rev. B 80 (2) (2009), 024107, https://doi.org/10.1103/PhysRevB.80.024107.
[28] Y. Sang, B. Liu, D. Fang, The size and strain effects on the electric-field-induced domain evolution and hysteresis loop in ferroelectric $BaTiO_3$ nanofilms, Comput. Mater. Sci. 44 (2) (2008) 404–410, https://doi.org/10.1016/j.commatsci.2008.04.001.

[29] T. Shimada, K. Wakahara, Y. Umeno, T. Kitamura, Shell model potential for $PbTiO_3$ and its applicability to surfaces and domain walls, J. Phys. Condens. Matter 20 (32) (2008) 325225, https://doi.org/10.1088/0953-8984/20/32/325225.
[30] Y. Zhang, R. Xu, B. Liu, D. Fang, An electromechanical atomic-scale finite element method for simulating evolutions of ferroelectric nanodomains, J. Mech. Phys. Solids 60 (8) (2012) 1383–1399, https://doi.org/10.1016/j.jmps.2012.04.012.
[31] P. Marton, I. Rychetsky, J. Hlinka, Domain walls of ferroelectric $BaTiO_3$ within the Ginzburg-Landau-Devonshire phenomenological model, Phys. Rev. B 81 (14) (2010) 144125, https://doi.org/10.1103/PhysRevB.81.144125.
[32] W. Zhang, K. Bhattacharya, A computational model of ferroelectric domains. Part I: model formulation and domain switching, Acta Mater. 53 (1) (2005) 185—198, https://doi.org/10.1016/j.actamat.2004.09.016.
[33] J. Wang, S.-Q. Shi, L.-Q. Chen, Y. Li, T.-Y. Zhang, Phase-field simulations of ferroelectric/ferroelastic polarization switching, Acta Mater. 52 (3) (2004) 749–764, https://doi.org/10.1016/j.actamat.2003.10.011.
[34] Y.C. Song, Y. Ni, J.Q. Zhang, Phase field model of polarization evolution in a finite ferroelectric body with free surfaces, Acta Mech. 224 (6) (2013) 1309–1313, https://doi.org/10.1007/s00707-013-0858-6.
[35] H.-L. Hu, L.-Q. Chen, Three-dimensional computer simulation of ferroelectric domain formation, J. Am. Ceram. Soc. 81 (1998) 492–500.
[36] T. Koyama, H. Onodera, Phase-field simulation of ferroelectric domain microstructure changes in $BaTiO_3$, Mater. Trans. 50 (5) (2009) 970–976, https://doi.org/10.2320/matertrans.MC200806.
[37] W.D. Dong, D.M. Pisani, C.S. Lynch, A finite element based phase field model for ferroelectric domain evolution, Smart Mater. Struct. 21 (9) (2012), 094014, https://doi.org/10.1088/0964-1726/21/9/094014.
[38] W. Zhang, K. Bhattacharya, A computational model of ferroelectric domains. Part II: grain boundaries and defect pinning, Acta Mater. 53 (1) (2005) 199–209, https://doi.org/10.1016/j.actamat.2004.09.015.
[39] S. Choudhury, Y.L. Li, C.E. Krill, L.-Q. Chen, Phase-field simulation of polarization switching and domain evolution in ferroelectric polycrystals, Acta Mater. 53 (20) (2005) 5313–5321, https://doi.org/10.1016/j.actamat.2005.07.040.
[40] L.-Q. Chen, Phase-field method of phase transitions/domain structures in ferroelectric thin films: a review, J. Am. Ceram. Soc. 91 (6) (2008) 1835–1844, https://doi.org/10.1111/j.1551-2916.2008.02413.x.
[41] X.L. Wang, B. Li, X.L. Zhong, Y. Zhang, J.B. Wang, Y.C. Zhou, Effects of space charge distribution on ferroelectric hysteresis loops considering the inhomogeneous built-in electric field: a phase field simulation, J. Appl. Phys. 112 (11) (2012) 114103, https://doi.org/10.1063/1.4767702.
[42] W.-F. Rao, Y.U. Wang, Bridging domain mechanism for phase coexistence in morphotropic phase boundary ferroelectrics, Appl. Phys. Lett. 90 (18) (2007) 182906, https://doi.org/10.1063/1.2736276.
[43] X.Q. Ke, D. Wang, Y. Wang, Origin of ultrahigh piezoelectric activity of [001]-oriented ferroelectric single crystals at the morphotropic phase boundary, Appl. Phys. Lett. 108 (1) (2016), 012904, https://doi.org/10.1063/1.4939626.
[44] T. Yang, X. Ke, Y. Wang, Mechanisms responsible for the large piezoelectricity at the tetragonal-orthorhombic phase boundary of (1-x)$BaZr_{0.2}Ti_{0.8}O_3$-x$Ba_{0.7}Ca_{0.3}TiO_3$ system, Sci. Rep. 6 (2016) 33392, https://doi.org/10.1038/srep33392.
[45] L. Liang, Y.L. Li, L.-Q. Chen, S.Y. Hu, G.-H. Lu, Thermodynamics and ferroelectric properties of $KNbO_3$, J. Appl. Phys. 106 (10) (2009) 104118, https://doi.org/10.1063/1.3260242.
[46] Z. Ma, L. Xi, H. Liu, F. Zheng, H. Gao, Z. Chen, H. Chen, Ferroelectric phase transition of $BaTiO_3$ single crystal based on a tenth order Landau-Devonshire potential, Comput. Mater. Sci. 135 (2017) 109—118, https://doi.org/10.1016/j.commatsci.2017.04.011.
[47] Y.L. Wang, A.K. Tagantsev, D. Damjanovic, N. Setter, V.K. Yarmarkin, A.I. Sokolov, I.A. Lukyanchuk, Landau thermodynamic potential for $BaTiO_3$, J. Appl. Phys. 101 (10) (2007) 104115, https://doi.org/10.1063/1.2733744.
[48] F. Xue, Y. Ji, L.-Q. Chen, Theory of strain phase separation and strain spinodal: applications to ferroelastic and ferroelectric systems, Acta Mater. 133 (2017) 147–159, https://doi.org/10.1016/j.actamat.2017.05.028.
[49] M.C. Ehmke, Ferroelastic Domains in Lead-free Barium Zirconate Titanate - Barium Calcium Titanate Piezoceramics, Ph.D. thesis, ProQuest, UMI Dissertations Publishing, 2014.
[50] J.A. Warren, W.J. Boettinger, Prediction of dendritic growth and microsegregation patterns in a binary alloy using the phase-field method, Acta Metall. Mater. 43 (2) (1995) 689–703, https://doi.org/10.1016/0956-7151(94)00285-P.
[51] M.E. Lines, A.M. Glass, Principles and Applications of Ferroelectrics and Related Materials, Oxford University Press, Oxford, 2001.
[52] K.S.N. Vikrant, W.C. Chueh, R.E. Garcia, Charged interfaces: electrochemical and mechanical effects, Energy Environ. Sci. (2018), https://doi.org/10.1039/C7EE03400H.
[53] J.D. Jackson, Classical Electrodynamics, third Edition, Wiley, New York, 1999.
[54] J. Hou, Y. Wu, Z. Wang, Analytical intrinsic electromechanical properties of ferroelectric ceramics under the saturated and unsaturated poling states, Comput. Mater. Sci. 96 (2015) 327–335, https://doi.org/10.1016/j.commatsci.2014.08.046.
[55] Z. Zhao, Y. Cao, R.E. Garcia, Kinetically stabilized metastable polarization states in ferroelectric ceramics, J. Eur. Ceram. Soc. 37 (2) (2017) 573–581, https://doi.org/10.1016/j.jeurceramsoc.2016.08.022.
[56] F. Jona, G. Shirane, Ferroelectric Crystals, Vol. 1 of International Series of Monographs on Solid State Physics, The Macmillan Company, New York, 1962.
[57] COMSOL Multiphysics® v. 5.2. www.comsol.com. COMSOL AB, Stockholm, Sweden.
[58] R.E. Reed-Hill, R. Abbaschian, Physical metallurgy principles, in: The PWS-Kent Series in Engineering, third Edition, PWS-Kent Pub, Boston, 1992.
[59] Z. Zhao, K. Bowman, R.E. Garcia, Modeling 180° domain switching population dynamics in polycrystalline ferroelectrics, J. Am. Ceram. Soc. 95 (5) (2012) 1619–1627, https://doi.org/10.1111/j.1551-2916.2011.05023.x.
[60] F. Rubio-Marcos, R. López-Juárez, R.E. Rojas-Hernandez, A. del Campo, N. Razo-Pérez, J.F. Fernandez, Lead-free piezoceramics: revealing the role of the rhombohedral-tetragonal phase coexistence in enhancement of the piezoelectric properties, Appl. Mater. Interfaces 7 (41) (2015) 23080–23088, https://doi.org/10.1021/acsami.5b06747.

Bibliography

[1] M. E. Lines and A. M. Glass. *Principles and Applications of Ferroelectrics and Related Materials*. Oxford University Press, Oxford, 2001.

[2] Hans-Günther Unruh. Ferroelectrics. In *Ullmann's Encyclopedia of Industrial Chemistry*. Wiley-VCH Verlag GmbH & Co. KGaA, Weinheim, Germany, 2000.

[3] Sei-Joo Jang. Ferroelectrics. In *Kirk-Othmer Encyclopedia of Chemical Technology*. John Wiley & Sons, Inc., Hoboken, NJ, USA, 2000.

[4] Dragan Damjanovic. Ferroelectric, dielectric and piezoelectric properties of ferroelectric thin films and ceramics. *Reports on Progress in Physics*, 61(9):1267–1324, 1998.

[5] J. Hou, Y. Wu, and Z. Wang. Analytical intrinsic electromechanical properties of ferroelectric ceramics under the saturated and unsaturated poling states. *Computational Materials Science*, 96:327–335, 2015.

[6] K. Bowman, M. Hoffman, and J. Jones. Saturated domain switching textures and strains in ferroelastic ceramics. *Journal of Applied Physics*, 98(2):024115–024115, 2005.

[7] H.-S. Ryo and I.-G. Ryo. A generalized inverse-pole-figure method to analyze domain switching in polycrystalline ferroelectrics. *Applied Physics A*, 122(8):745, 2016.

[8] F. X. Li and R. K. N. D. Rajapakse. Analytical saturated domain orientation textures and electromechanical properties of ferroelectric ceramics due to electric/mechanical poling. *Journal of Applied Physics*, 101(5):054110, 2007.

[9] W. Lu, D.-N. Fang, C. Q. Li, and K.-C. Hwang. Nonlinear electric–mechanical behavior and micromechanics modelling of ferroelectric domain evolution. *Acta Materialia*, 47(10):2913–2926, 1999.

[10] F. Yang, Y. Wu, H. Li, and J. Jiang. Estimation of intrinsic contribution of piezoelectric properties in ferroelectric ceramics. *Ferroelectrics*, 408(1):62–70, 2010.

[11] Andrew J. Bell. Ferroelectrics: The role of ceramic science and engineering. *Journal of the European Ceramic Society*, 28(7):1307–1317, 2008.

[12] Jürgen Rödel, Wook Jo, Klaus T. P. Seifert, Eva-Maria Anton, Torsten Granzow, and Dragan Damjanovic. Perspective on the development of lead-free piezoceramics. *Journal of the American Ceramic Society*, 92(6):1153–1177, 2009.

[13] Gene H. Haertling. Ferroelectric Ceramics: History and Technology. *Journal of the American Ceramic Society*, 82(4):797–818, 1999.

[14] A. A. Heitmann and G. A. Rossetti. Polar Anisotropy and Inter-Ferroelectric Transitions in Barium Titanate and its Solid Solutions. *Integrated Ferroelectrics*, 126(1):155–165, 2011.

[15] A. A. Heitmann and G. A. Rossetti Jr. Thermodynamics of ferroelectric solid solutions with morphotropic phase boundaries. *Journal of the American Ceramic Society*, 97(6):1661–1685, 2014.

[16] M. Acosta, N. Novak, V. Rojas, S. Patel, R. Vaish, J. Koruza, G. A. Rossetti Jr., and J. Rödel. $BaTiO_3$-based piezoelectrics: Fundamentals, current status, and perspectives. *Applied Physics Reviews*, 4(4):041305, 2017.

[17] Jinghui Gao, Dezhen Xue, Wenfeng Liu, Chao Zhou, and Xiaobing Ren. Recent progress on $BaTiO_3$-based piezoelectric ceramics for actuator applications. *Actuators*, 6(3):24, 2017.

[18] Dragan Damjanovic, Naama Klein, Jin Li, and Viktor Porokhonskyy. What can be expected from lead-free piezoelectric materials? *Functional Materials Letters*, 3(1):5–13, 2010.

[19] Thomas R. Shrout and Shujun J. Zhang. Lead-free piezoelectric ceramics: Alternatives for PZT? *Journal of Electroceramics*, 19(1):113–126, 2007.

[20] G. A. Rossetti Jr., A. G. Khachaturyan, G. Akcay, and Y. Ni. Ferroelectric solid solutions with morphotropic boundaries: Vanishing polarization anisotropy, adaptive, polar glass, and two-phase states. *Journal of Applied Physics*, 103(11):114113, 2008.

[21] Dragan Damjanovic. Contributions to the Piezoelectric Effect in Ferroelectric Single Crystals and Ceramics. *Journal of the American Ceramic Society*, 88(10):2663–2676, 2005.

[22] Dragan Damjanovic. A morphotropic phase boundary system based on polarization rotation and polarization extension. *Applied Physics Letters*, 97, 2010.

[23] P. K. Panda. Review: Environmental friendly lead-free piezoelectric materials. *Journal of Materials Science*, 44(19):5049–5062, 2009.

[24] W. Liu and X. Ren. Large Piezoelectric Effect in Pb-Free Ceramics. *Physical Review Letters*, 103(25), 2009.

[25] Dean S. Keeble, Feres Benabdallah, Pam A. Thomas, Mario Maglione, and Jens Kreisel. Revised structural phase diagram of $(Ba_{0.7}Ca_{0.3}TiO_3)$-$(BaZr_{0.2}Ti_{0.8}O_3)$. *Applied Physics Letters*, 102(9):092903, 2013.

[26] R.E. Cohen. Theory of ferroelectrics: A vision for the next decade and beyond. *Journal of Physics and Chemistry of Solids*, 61(2):139–146, 2000.

[27] B. Völker, P. Marton, C. Elsässer, and M. Kamlah. Multiscale modeling for ferroelectric materials: A transition from the atomic level to phase-field modeling. *Continuum Mechanics and Thermodynamics*, 23(5):435–451, 2011.

[28] B. Meyer and David Vanderbilt. *Ab Initio* study of ferroelectric domain walls in $PbTiO_3$. *Physical Review B*, 65(10), 2002.

[29] G. Pilania and R. Ramprasad. Complex polarization ordering in $PbTiO_3$ nanowires: A first-principles computational study. *Physical Review B*, 82(15), 2010.

[30] T. Shimada, S. Tomoda, and T. Kitamura. *Ab Initio* study of ferroelectric closure domains in ultrathin $PbTiO_3$ films. *Physical Review B*, 81(14), 2010.

[31] A. Grünebohm, M. E. Gruner, and P. Entel. Domain Structure in the Tetragonal Phase of $BaTiO_3$ – from Bulk to Nanoparticles. *Ferroelectrics*, 426(1):21–30, 2012.

[32] Vishal Boddu, Florian Endres, and Paul Steinmann. Molecular dynamics study of ferroelectric domain nucleation and domain switching dynamics. *Scientific Reports*, 7(1), 2017.

[33] M. Sepliarsky, A. Asthagiri, S.R. Phillpot, M.G. Stachiotti, and R.L. Migoni. Atomic-level simulation of ferroelectricity in oxide materials. *Current Opinion in Solid State and Materials Science*, 9(3):107–113, 2005.

[34] Jaita Paul, Takeshi Nishimatsu, Yoshiyuki Kawazoe, and Umesh V. Waghmare. Polarization rotation, switching, and electric-field–temperature phase diagrams of ferroelectric $BaTiO_3$: A molecular dynamics study. *Physical Review B*, 80(2), 2009.

[35] Yongliang Sang, Bin Liu, and Daining Fang. The size and strain effects on the electric-field-induced domain evolution and hysteresis loop in ferroelectric $BaTiO_3$ nanofilms. *Computational Materials Science*, 44(2):404–410, 2008.

[36] T. Shimada, K. Wakahara, Y. Umeno, and T. Kitamura. Shell model potential for $PbTiO_3$ and its applicability to surfaces and domain walls. *Journal of Physics: Condensed Matter*, 20(32):325225, 2008.

[37] Yihui Zhang, Ran Xu, Bin Liu, and Daining Fang. An electromechanical atomic-scale finite element method for simulating evolutions of ferroelectric nanodomains. *Journal of the Mechanics and Physics of Solids*, 60(8):1383–1399, 2012.

[38] W. Zhang and K. Bhattacharya. A computational model of ferroelectric domains. Part I: Model formulation and domain switching. *Acta Materialia*, 53(1):185–198, 2005.

[39] Jie Wang, San-Qiang Shi, Long-Qing Chen, Yulan Li, and Tong-Yi Zhang. Phase-field simulations of ferroelectric/ferroelastic polarization switching. *Acta Materialia*, 52(3):749–764, 2004.

[40] Y. C. Song, Y. Ni, and J. Q. Zhang. Phase field model of polarization evolution in a finite ferroelectric body with free surfaces. *Acta Mechanica*, 224(6):1309–1313, 2013.

[41] Hong-Liang Hu and Long-Qing Chen. Three-dimensional computer simulation of ferroelectric domain formation. *Journal of the American Ceramic Society*, 81:492–500, 1998.

[42] Hong-Liang Hu and Long-Qing Chen. Computer simulation of 90 degrees ferroelectric domain formation in two-dimensions. *Materials Science and Engineering A*, 238(1):182–191, 1997.

[43] T. Koyama and H. Onodera. Phase-Field Simulation of Ferroelectric Domain Microstructure Changes in $BaTiO_3$. *Materials Transactions*, 50(5):970–976, 2009.

[44] Wen D. Dong, David M. Pisani, and Christopher S. Lynch. A finite element based phase field model for ferroelectric domain evolution. *Smart Materials and Structures*, 21(9):094014, 2012.

[45] Jie Wang, Marc Kamlah, and Tong-Yi Zhang. Phase field simulations of ferroelectric nanoparticles with different long-range-electrostatic and -elastic interactions. *Journal of Applied Physics*, 105(1):014104, 2009.

[46] W. Zhang and K. Bhattacharya. A computational model of ferroelectric domains. Part II: Grain boundaries and defect pinning. *Acta Materialia*, 53(1):199–209, 2005.

[47] S. Choudhury, Y. L. Li, C. E. Krill III, and L.-Q. Chen. Phase-field simulation of polarization switching and domain evolution in ferroelectric polycrystals. *Acta Materialia*, 53(20):5313–5321, 2005.

[48] S. Choudhury, Y. L. Li, C. E. Krill III, and L.-Q. Chen. Effect of grain orientation and grain size on ferroelectric domain switching and evolution: Phase field simulations. *Acta Materialia*, 55(4):1415–1426, 2007.

[49] L.-Q. Chen. Phase-field method of phase transitions/domain structures in ferroelectric thin films: A review. *Journal of the American Ceramic Society*, 91(6):1835–1844, 2008.

[50] X. L. Wang, B. Li, X. L. Zhong, Y. Zhang, J. B. Wang, and Y. C. Zhou. Effects of space charge distribution on ferroelectric hysteresis loops considering the inhomogeneous built-in electric field: A phase field simulation. *Journal of Applied Physics*, 112(11):114103, 2012.

[51] Wei-Feng Rao and Yu U. Wang. Bridging domain mechanism for phase coexistence in morphotropic phase boundary ferroelectrics. *Applied Physics Letters*, 90(18):182906, 2007.

[52] Wei-Feng Rao and Yu U. Wang. Microstructures of coherent phase decomposition near morphotropic phase boundary in lead zirconate titanate. *Applied Physics Letters*, 91(5):052901, 2007.

[53] Yu U. Wang. Field-induced inter-ferroelectric phase transformations and domain mechanisms in high-strain piezoelectric materials: Insights from phase field modeling and simulation. *Journal of Materials Science*, 44(19):5225–5234, 2009.

[54] X. Q. Ke, D. Wang, X. Ren, and Y. Wang. Formation of monoclinic nanodomains at the morphotropic phase boundary of ferroelectric systems. *Physical Review B*, 88(21):214105, 2013.

[55] X. Q. Ke, D. Wang, and Y. Wang. Origin of ultrahigh piezoelectric activity of [001]-oriented ferroelectric single crystals at the morphotropic phase boundary. *Applied Physics Letters*, 108(1):012904, 2016.

[56] Yong Ni and Armen G. Khachaturyan. Giant anhysteretic response of ferroelectric solid solutions with morphotropic boundaries: The role of polar anisotropy. *Acta Mechanica Solida Sinica*, 25(4):429–440, 2012.

[57] L. Liang, Y. L. Li, L.-Q. Chen, S. Y. Hu, and G.-H. Lu. Thermodynamics and ferroelectric properties of $KNbO_3$. *Journal of Applied Physics*, 106(10):104118, 2009.

[58] Z. Ma, L. Xi, H. Liu, F. Zheng, H. Gao, Z. Chen, and H. Chen. Ferroelectric phase transition of $BaTiO_3$ single crystal based on a tenth order Landau-Devonshire potential. *Computational Materials Science*, 135:109–118, 2017.

[59] Y. L. Wang, A. K. Tagantsev, D. Damjanovic, N. Setter, V. K. Yarmarkin, A. I. Sokolov, and I. A. Lukyanchuk. Landau thermodynamic potential for $BaTiO_3$. *Journal of Applied Physics*, 101(10):104115, 2007.

[60] Nele Moelans, Bart Blanpain, and Patrick Wollants. An introduction to phase-field modeling of microstructure evolution. *Calphad*, 32:268–294, 2008.

[61] Long-Qing Chen. Phase-Field Models for Microstructure Evolution. *Annual Review of Materials Research*, 32(1):113–140, 2002.

[62] J.Z. Zhu, T. Wang, S.H. Zhou, Z.K. Liu, and L.Q. Chen. Quantitative interface models for simulating microstructure evolution. *Acta Materialia*, 52(4):833–840, 2004.

[63] Ingo Steinbach. Phase-field models in materials science. *Modelling and Simulation in Materials Science and Engineering*, 17(7):073001, 2009.

[64] R. S. Qin and H. K. Bhadeshia. Phase field method. *Materials Science and Technology*, 26(7):803–811, 2010.

[65] W. Cao. Phenomenological theories of ferroelectric phase transitions. *British Ceramic Transactions*, 103(2):71–75, 2004.

[66] W. Cao. Constructing Landau-Ginzburg-Devonshire type models for ferroelectric systems based on symmetry. *Ferroelectrics*, 375(1):28–39, 2008.

[67] Wenwu Cao and L. E. Cross. Theory of tetragonal twin structures in ferroelectric perovskites with a first-order phase transition. *Physical Review B*, 44(1):5–12, 1991.

[68] J. Hlinka and P. Márton. Phenomenological model of a 90° domain wall in $BaTiO_3$-type ferroelectrics. *Physical Review B*, 74(10), 2006.

[69] K. S. N. Vikrant, William C. Chueh, and R. Edwin García. Charged interfaces: Electrochemical and mechanical effects. *Energy & Environmental Science*, 2018.

[70] Zizhao Zhao, Keith Bowman, and R. Edwin García. Modeling 180° Domain Switching Population Dynamics in Polycrystalline Ferroelectrics. *Journal of the American Ceramic Society*, 95(5):1619–1627, 2012.

[71] P. Marton, I. Rychetsky, and J. Hlinka. Domain walls of ferroelectric $BaTiO_3$ within the Ginzburg-Landau-Devonshire phenomenological model. *Physical Review B*, 81(14):144125, 2010.

[72] Matias Acosta, Nasser Khakpash, Takumi Someya, Nikola Novak, Wook Jo, Hajime Nagata, George A. Rossetti, and Jürgen Rödel. Origin of the large piezoelectric activity in (1-x)$Ba(Zr_{0.2}Ti_{0.8})O_3$ - x$(Ba_{0.7}Ca_{0.3})TiO_3$ ceramics. *Physical Review B*, 91(10):104108, 2015.

[73] Fei Xue, Yanzhou Ji, and Long-Qing Chen. Theory of strain phase separation and strain spinodal: Applications to ferroelastic and ferroelectric systems. *Acta Materialia*, 133:147–159, 2017.

[74] I. Steinbach, F. Pezzolla, B. Nestler, M. Seeßelberg, R. Prieler, G.J. Schmitz, and J.L.L. Rezende. A phase field concept for multiphase systems. *Physica D: Nonlinear Phenomena*, 94(3):135–147, 1996.

[75] Britta Nestler and Adam A. Wheeler. Phase-field modeling of multi-phase solidification. *Computer Physics Communications*, 147(1-2):230–233, 2002.

[76] J. A. Warren and W. J. Boettinger. Prediction of dendritic growth and microsegregation patterns in a binary alloy using the phase-field method. *Acta Metallurgica et Materialia*, 43(2):689–703, 1995.

[77] Matthias C. Ehmke, Steven N. Ehrlich, John E. Blendell, and Keith J. Bowman. Phase coexistence and ferroelastic texture in high strain (1-x)$Ba(Zr_{0.2}Ti_{0.8})O_3$ – x$(Ba_{0.7}Ca_{0.3})TiO_3$ piezoceramics. *Journal of Applied Physics*, 111(12):124110, 2012.

[78] Jinghui Gao, Yan Wang, Yongbin Liu, Xinghao Hu, Xiaoqin Ke, Lisheng Zhong, Yuting He, and Xiaobing Ren. Enhancing dielectric permittivity for energy-storage devices through tricritical phenomenon. *Scientific Reports*, 7(1), 2017.

[79] Yongshang Tian, Yansheng Gong, Dawei Meng, Hao Deng, and Boya Kuang. Low-temperature sintering and electric properties of BCT–BZT and BCZT lead-free ceramics. *Journal of Materials Science: Materials in Electronics*, 26(6):3750–3756, 2015.

[80] Le Zhang, Ming Zhang, Liang Wang, Chao Zhou, Zhen Zhang, Yonggang Yao, Lixue Zhang, Dezhen Xue, Xiaojie Lou, and Xiaobing Ren. Phase transitions and the piezoelectricity around morphotropic phase boundary in $Ba(Zr_{0.2}Ti_{0.8})O_3$ - x$(Ba_{0.7}Ca_{0.3})TiO_3$ lead-free solid solution. *Applied Physics Letters*, 105(16):162908, 2014.

[81] Dragan Damjanovic, Alberto Biancoli, Leili Batooli, Amirhossein Vahabzadeh, and Joe Trodahl. Elastic, dielectric, and piezoelectric anomalies and Raman spectroscopy of 0.5$Ba(Ti_{0.8}Zr_{0.2})O_3$ - 0.5$(Ba_{0.7}Ca_{0.3})TiO_3$. *Applied Physics Letters*, 100(19):192907, 2012.

[82] F. Cordero, F. Craciun, M. Dinescu, N. Scarisoreanu, C. Galassi, W. Schranz, and V. Soprunyuk. Elastic response of (1-x)$Ba(Ti_{0.8}Zr_{0.2})O_3$ – x$(Ba_{0.7}Ca_{0.3})TiO_3$ (x = 0.45–0.55) and the role of the intermediate orthorhombic phase in enhancing the piezoelectric coupling. *Applied Physics Letters*, 105(23):232904, 2014.

[83] Venkata Sreenivas Puli, Dhiren K. Pradhan, W. Pérez, and R.S. Katiyar. Structure, dielectric tunability, thermal stability and diffuse phase transition behavior of lead free BZT–BCT ceramic capacitors. *Journal of Physics and Chemistry of Solids*, 74(3):466–475, 2013.

[84] Venkata Sreenivas Puli, Dhiren K. Pradhan, Shiva Adireddy, R. Martínez, Punam Silwal, J. F. Scott, C. V. Ramana, Douglas B. Chrisey, and Ram S. Katiyar. Nanoscale polarisation switching and leakage currents in $(Ba_{0.955}Ca_{0.045})(Zr_{0.17}Ti_{0.83})O_3$ epitaxial thin films. *Journal of Physics D: Applied Physics*, 48(35):355502, 2015.

[85] G. Singh, V. Sathe, and V. S. Tiwari. Investigation of rhombohedral-to-tetragonal phase transition in $0.5Ba(Ti_{0.8}Zr_{0.2})$ - $0.5(Ba_{0.7}Ca_{0.3})TiO_3$ lead-free ferroelectric using micro-Raman scattering. *Journal of Electronics Materials*, 46(8):4976–4980, 2017.

[86] Jinghui Gao, Lixue Zhang, Dezhen Xue, Takayoshi Kimoto, Minghui Song, Lisheng Zhong, and Xiaobing Ren. Symmetry determination on Pb-free piezoceramic $0.5Ba(Zr_{0.2}Ti_{0.8})O_3$ - $0.5(Ba_{0.7}Ca_{0.3})TiO_3$ using convergent beam electron diffraction method. *Journal of Applied Physics*, 115(5):054108, 2014.

[87] Astri Bjørnetun Haugen, Jennifer S. Forrester, Dragan Damjanovic, Binzhi Li, Keith J. Bowman, and Jacob L. Jones. Structure and phase transitions in $0.5(Ba_{0.7}Ca_{0.3}TiO_3)$ - $0.5(BaZr_{0.2}Ti_{0.8}O_3)$ from -100 °C to 150 °C. *Journal of Applied Physics*, 113(1):014103, 2013.

[88] Jinghui Gao, Xinghao Hu, Yongbin Liu, Yan Wang, Xiaoqin Ke, Dong Wang, Lisheng Zhong, and Xiaobing Ren. Ferroelectric domain walls approaching morphotropic phase boundary. *Journal of Physical Chemistry C*, 121(4):2243–2250, 2017.

[89] Matthias C. Ehmke. *Ferroelastic Domains in Lead-Free Barium Zirconate Titanate - Barium Calcium Titanate Piezoceramics*. PhD thesis, Purdue University, 2014.

[90] John David Jackson. *Classical Electrodynamics*. Wiley, New York, 3rd edition, 1999.

[91] Franco Jona and G. Shirane. *Ferroelectric Crystals*, volume 1 of *International Series of Monographs on Solid State Physics*. The Macmillan Company, New York, 1962.

[92] D. Schrade, R. Muller, and D. Gross. On the physical interpretation of material parameters in phase field models for ferroelectrics. *Archive of Applied Mechanics*, 83:1393–1413, 2013.

[93] Z. Zhao, Y. Cao, and R. Edwin García. Kinetically stabilized metastable polarization states in ferroelectric ceramics. *Journal of the European Ceramic Society*, 37(2):573–581, 2017.

[94] COMSOL Multiphysics® v. 5.2. www.comsol.com. COMSOL AB, Stockholm, Sweden.

[95] T. Yang, X. Ke, and Y. Wang. Mechanisms responsible for the large piezoelectricity at the tetragonal-orthorhombic phase boundary of $(1\text{-}x)BaZr_{0.2}Ti_{0.8}O_3$ - $xBa_{0.7}Ca_{0.3}TiO_3$ system. *Scientific reports*, 6:33392, 2016.

[96] Fernando Rubio-Marcos, Rigoberto López-Juárez, Rocio E. Rojas-Hernandez, Adolfo del Campo, Neftalí Razo-Pérez, and Jose F. Fernandez. Lead-Free Piezoceramics: Revealing the Role of the Rhombohedral–Tetragonal Phase Coexistence in Enhancement of the Piezoelectric Properties. *ACS Applied Materials & Interfaces*, 7(41):23080–23088, 2015.

[97] Y. M. Jin, Y. U. Wang, A. G. Khachaturyan, J. F. Li, and D. Viehland. Adaptive ferroelectric states in systems with low domain wall energy: Tetragonal microdomains. *Journal of Applied Physics*, 94(5):3629–3640, 2003.

[98] Robert E. Reed-Hill and R. Abbaschian. *Physical Metallurgy Principles*. The PWS-Kent Series in Engineering. PWS-Kent Pub, Boston, 3rd edition, 1992.

[99] N. Bordeaux, A.M. Montes-Arango, J. Liu, K. Barmak, and L.H. Lewis. Thermodynamic and kinetic parameters of the chemical order–disorder transformation in L1 0 FeNi (tetrataenite). *Acta Materialia*, 103:608–615, 2016.

[100] T. Pradell, D. Crespo, N. Clavaguera, and M. T. Clavaguera-Mora. Diffusion controlled grain growth in primary crystallization: Avrami exponents revisited. *Journal of Physics: Condensed Matter*, 10(17):3833–3844, 1998.

[101] Daniel J. Franzbach, Bai-Xiang Xu, Ralf Mueller, and Kyle G. Webber. The effects of polarization dynamics and domain switching energies on field induced phase transformations of perovskite ferroelectrics. *Applied Physics Letters*, 99(16):162903, 2011.

[102] Fei Xue, Yijia Gu, Linyun Liang, Yi Wang, and Long-Qing Chen. Orientations of low-energy domain walls in perovskites with oxygen octahedral tilts. *Physical Review B*, 90(22), 2014.

[103] A. Krishnan, M.E. Bisher, and M.M.J. Treacy. In-Situ TEM Study of Domain Propagation in Ferroelectric Barium Titanate, and Its Role in Fatigue. *MRS Proceedings*, 541, 1998.

[104] Ch. Loppacher, F. Schlaphof, S. Schneider, U. Zerweck, S. Grafström, L.M. Eng, A. Roelofs, and R. Waser. Lamellar ferroelectric domains in $PbTiO_3$ grains imaged and manipulated by AFM. *Surface Science*, 532-535:483–487, 2003.

[105] Jinghui Gao, Dezhen Xue, Yu Wang, Dong Wang, Lixue Zhang, Haijun Wu, Shengwu Guo, Huixin Bao, Chao Zhou, Wenfeng Liu, Sen Hou, Ge Xiao, and Xiaobing Ren. Microstructure basis for strong piezoelectricity in Pb-free $Ba(Zr_{0.2}Ti_{0.8})O_3$ - $(Ba_{0.7}Ca_{0.3})TiO_3$ ceramics. *Applied Physics Letters*, 99(9):092901, 2011.

[106] Hanzheng Guo, Brian K. Voas, Shujun Zhang, Chao Zhou, Xiaobing Ren, Scott P. Beckman, and Xiaoli Tan. Polarization alignment, phase transition, and piezoelectricity development in polycrystalline $0.5Ba(Zr_{0.2}Ti_{0.8})O_3$ - $0.5(Ba_{0.7}Ca_{0.3})TiO_3$. *Physical Review B*, 90(1), 2014.

[107] Hanzheng Guo, Chao Zhou, Xiaobing Ren, and Xiaoli Tan. Unique single-domain state in a polycrystalline ferroelectric ceramic. *Physical Review B*, 89(10):100104(R), 2014.

[108] Shengbo Lu, Zhengkui Xu, Shi Su, and Ruzhong Zuo. Temperature driven nano-domain evolution in lead-free $Ba(Zr_{0.2}Ti_{0.8})O_3$ - $50(Ba_{0.7}Ca_{0.3})TiO_3$ piezoceramics. *Applied Physics Letters*, 105(3):032903, 2014.

[109] M. Zakhozheva, L. A. Schmitt, M. Acosta, W. Jo, J. Rödel, and H.-J. Kleebe. *In Situ* electric field induced domain evolution in $Ba(Zr_{0.2}Ti_{0.8})O_3$ - $0.3(Ba_{0.7}Ca_{0.3})TiO_3$ ferroelectrics. *Applied Physics Letters*, 105(11):112904, 2014.

[110] M. Zakhozheva, L. A. Schmitt, M. Acosta, H. Guo, W. Jo, R. Schierholz, H.-J. Kleebe, and X. Tan. Wide compositional range *in situ* electric field investigations on lead-free $Ba(Zr_{0.2}Ti_{0.8})O_3$ - $x(Ba_{0.7}Ca_{0.3})TiO_3$ piezoceramic. *Physical Review Applied*, 3(6):064018, 2015.

[111] Jinghui Gao, Ye Dai, Xinghao Hu, Xiaoqin Ke, Lisheng Zhong, Shengtao Li, Lixue Zhang, Yu Wang, Dong Wang, Yan Wang, Yongbin Liu, Hu Xiao, and Xiaobing Ren. Phase transition behaviours near the triple point for Pb-free $(1-x)Ba(Zr_{0.2}Ti_{0.8})O_3$ - $x(Ba_{0.7}Ca_{0.3})TiO_3$ piezoceramics. *Europhysics Letters*, 115(3):37001, 2016.

[112] William S. Oates, Aurelian Malbec, Scott L. Herdic, and Christopher S. Lynch. Phase field modeling of domain structures in ferroelectric materials. In Dimitris C. Lagoudas, editor, *Smart Structures and Materials*, page 314, San Diego, CA, 2004.

[113] Stéfan van der Walt, Johannes L. Schönberger, Juan Nunez-Iglesias, François Boulogne, Joshua D. Warner, Neil Yager, Emmanuelle Gouillart, and Tony Yu. Scikit-image: Image processing in Python. *PeerJ*, 2:e453, 2014.

[114] Douglas C. Montgomery and George C. Runger. *Applied Statistics and Probability for Engineers*. John Wiley and Sons, Inc, Hoboken, NJ, sixth edition, 2014.

[115] V. Seetharaman and S. L. Semiatin. Analysis of grain growth in a two-phase gamma titanium aluminide alloy. *Metallurgical and Materials Transactions A*, 28(4):947–954, 1997.

[116] W. Shu, J. Wang, and T.-Y. Zhang. Effect of grain boundary on the electromechanical response of ferroelectric polycrystals. *Journal of Applied Physics*, 112(6):064108, 2012.

[117] J. Wang, W. Shu, T. Shimada, T. Kitamura, and T.-Y. Zhang. Role of grain orientation distribution in the ferroelectric and ferroelastic domain switching of ferroelectric polycrystals. *Acta Materialia*, 61(16):6037–6049, 2013.

[118] X. Li and J. Wang. Effect of grain size on the domain structures and electromechanical responses of ferroelectric polycrystal. *Smart Materials and Structures*, 26(1):015013, 2017.

[119] M. J. Haun, E. Furman, S. J. Jang, H. A. McKinstry, and L. E. Cross. Thermodynamic theory of $PbTiO_3$. *Journal of Applied Physics*, 62(8):3331–3338, 1987.

[120] Philippe Veber, Feres Benabdallah, Hairui Liu, Gabriel Buse, Michael Josse, and Mario Maglione. Growth and Characterization of Lead-free Piezoelectric Single Crystals. *Materials*, 8(11):7962–7978, 2015.

[121] Yiming Zeng, Yanqing Zheng, Xiaoniu Tu, Zhiping Lu, and Erwei Shi. Growth and characterization of lead-free $Ba_{(1-x)}Ca_xTi_{(1-y)}Zr_yO_3$ single crystal. *Journal of Crystal Growth*, 343(1):17–20, 2012.

[122] H. Zhang, X. Lu, C. Wang, L. Zheng, B. Yang, and W. Cao. Landau expansion parameters and the *O-T* phase transition of a $0.64Pb(Mg_{1/3}Nb_{2/3})O_3$ - $0.36PbTiO_3$ single crystal. *Physical Review B*, 97(5):054114, 2018.

[123] H. Zhang, X. Lu, R. Wang, C. Wang, L. Zheng, Z. Liu, C. Yang, R. Zhang, B. Yang, and W. Cao. Phase coexistence and Landau expansion parameters for a $0.70Pb(Mg_{1/3}Nb_{2/3})O_3$ - $0.30PbTiO_3$ single crystal. *Physical Review B*, 96(5):054109, 2017.

[124] C. Zhou, X. Ke, Y. Yao, S. Yang, Y. Ji, W. Liu, Y. Yang, L. Zhang, Y. Hao, S. Ren, L. Zhang, and X. Ren. Evolution from successive phase transitions to “morphotropic phase boundary” in $BaTiO_3$ -based ferroelectrics. *Applied Physics Letters*, 112(18):182903, 2018.

[125] X. Lu, H. Li, and W. Cao. Landau expansion parameters for $BaTiO_3$. *Journal of Applied Physics*, 114(22):224106, 2013.

[126] Y. L. Li, L. E. Cross, and L.-Q. Chen. A phenomenological thermodynamic potential for $BaTiO_3$ single crystals. *Journal of Applied Physics*, 98(6):064101, 2005.

[127] Y. Wu and J. Hou. Intrinsic electromechanical properties of ferroelectric ceramics with the coexistence of tetragonal and rhombohedral phases near the morphotropic phase boundary. *Journal of Applied Physics*, 116(11):114104, 2014.

[128] J. F. Nye. *Physical Properties of Crystals: Their Representation by Tensors and Matrices*. Clarendon Press, Oxford, 1957.

[129] R. Hill. Elastic properties of reinforced solids: Some theoretical principles. *Journal of the Mechanics and Physics of Solids*, 11(5):357–372, 1963.

[130] F. X. Li, X. L. Zhou, and A. K. Soh. An optimization-based "phase field" model for polycrystalline ferroelectrics. *Applied Physics Letters*, 96(15):152905, 2010.

[131] J. A. Pérez, M. R. Soares, F. A. A. Paz, J. Klinowski, A. M. R. Senos, and P. Q. Mantas. Structural and electrical characteristics of rhombohedral lead zirconate titanate single crystals. *Journal of Materials Science*, 50(12):4232–4243, 2015.

[132] F. Benabdallah, P. Veber, M. Prakasam, O. Viraphong, K. Shimamura, and M. Maglione. Continuous cross-over from ferroelectric to relaxor state and piezoelectric properties of $BaTiO_3$ - $BaZrO_3$ - $CaTiO_3$ single crystals. *Journal of Applied Physics*, 115(14):144102, 2014.

[133] M. Newville, T. Stensitzki, D. B. Allen, and A. Ingargiola. LMFIT: Non-linear least-square minimization and curve-fitting for python. Zenodo, 2014.

[134] A. J. Bell and L. E. Cross. A phenomenological gibbs function for $BaTiO_3$ giving correct e field dependence of all ferroelectric phase changes. *Ferroelectrics*, 59(1):197–203, 1984.

[135] G. A. Smolenskii, V. A. Isupov, S. A. Ktitorov, V. A. Trepakov, and N. K. Yushin. The state of ferroelectric physics. *Soviet Physics Journal*, 22(1):3–30, 1979.

[136] L. Zhang, X. Ren, and M. A. Carpenter. Influence of local strain heterogeneity on high piezoelectricity in $0.5Ba(Zr_{0.2}Ti_{0.8})O_3$ - $0.5(Ba_{0.7}Ca_{0.3})TiO_3$ ceramics. *Physical Review B*, 95(5):054116, 2017.

[137] D. R. J. Brandt, M. Acosta, J. Koruza, and K. G. Webber. Mechanical constitutive behavior and exceptional blocking force of lead-free BZT-xBCT piezoceramics. *Journal of Applied Physics*, 115(20):204107, 2014.

[138] H. Kaddoussi, A. Lahmar, Y. Gagou, B. Manoun, J. N. Chotard, J. L. Dellis, Z. Kutnjak, H. Khemakhem, B. Elouadi, and M. El Marssi. Sequence of structural transitions and electrocaloric properties in $(Ba_{1-x}Ca_x)(Zr_{0.1}Ti_{0.9})O_3$ ceramics. *Journal of Alloys and Compounds*, 713:164–179, 2017.

[139] SI Yakunin, VV Shakmanov, GV Spivak, and NV Vasil'eva. Microstructure of domains and domain walls in single-crystal films of barium titanate. *Soviet Physics-Solid State*, 14(2), 1972.

[140] M. D. Dennis and R. C. Bradt. Thickness of 90° ferroelectric domain walls in (Ba,Pb)TiO_3 single crystals. *Journal of Applied Physics*, 45(5):1931–1933, 1974.

[141] X. Zhang, T. Hashimoto, and D. C. Joy. Electron holographic study of ferroelectric domain walls. *Applied Physics Letters*, 60(6):784–786, 1992.

[142] Xiao Zhang, D.C. Joy, Y. Zhang, T. Hashimoto, L. Allard, and T.A. Nolan. Electron holography techniques for study of ferroelectric domain walls. *Ultramicroscopy*, 51(1-4):21–30, 1993.

[143] N. Floquet, C. M. Valot, M. T. Mesnier, J. C. Niepce, L. Normand, A. Thorel, and R. Kilaas. Ferroelectric Domain Walls in $BaTiO_3$: Fingerprints in XRPD Diagrams and Quantitative HRTEM Image Analysis. *Journal de Physique III*, 7(6):1105–1128, 1997.

[144] David A. Porter and K. E. Easterling. *Phase Transformations in Metals and Alloys*. Van Nostrand Reinhold, New York, 1981.

[145] Gabriel Buse, Cong Xin, Pascal Marchet, Ana Borta-Boyon, Mai Pham-Thi, Hughes Cabane, Emmanuel Veron, Michael Josse, Matias Velazquez, Michel Lahaye, Eric Lebraud, Mario Maglione, and Philippe Veber. Spinodal Decomposition in Lead-free Piezoelectric $BaTiO_3$ – $CaTiO_3$ – $BaZrO_3$ Crystals. *Crystal Growth & Design*, 18(10):5874–5884, 2018.

[146] E.L. Huston, John W. Cahn, and J.E. Hilliard. Spinodal decomposition during continuous cooling. *Acta Metallurgica*, 14(9):1053–1062, 1966.

[147] Shiva Rudraraju, Anton Van der Ven, and Krishna Garikipati. Mechanochemical spinodal decomposition: A phenomenological theory of phase transformations in multi-component, crystalline solids. *npj Computational Materials*, 2(1):16012, 2016.

[148] F. Bachmann, Ralf Hielscher, and Helmut Schaeben. Texture Analysis with MTEX – Free and Open Source Software Toolbox. *Solid State Phenomena*, 160:63–68, 2010.

[149] Florian Bachmann, Ralf Hielscher, and Helmut Schaeben. Grain detection from 2d and 3d EBSD data—Specification of the MTEX algorithm. *Ultramicroscopy*, 111(12):1720–1733, 2011.